In Situ Methods to Characterize Zeolite Growth by Nonclassical Pathway

A Dissertation

Presented to

the Faculty of the Department of Chemical and Biomolecular Engineering

University of Houston

In Partial Fulfillment

of the Requirements for the Degree

Doctor of Philosophy

in Chemical Engineering

by

Madhuresh K. Choudhary

August 2019

In Situ Methods to Characterize Zeolite Growth by Nonclassical Pathway

Madhuresh K. Choudhary

Approved:

Chair of the Committee
Jeffrey D. Rimer, Professor
Chemical and Biomolecular Engineering

Committee Members:

Megan L. Robertson, Associate Professor
Chemical and Biomolecular Engineering

Praveen Bollini, Assistant Professor
Chemical and Biomolecular Engineering

Allan J. Jacobson, Professor
Chemistry

Jakoah Brgoch, Assistant Professor
Chemistry

Suresh K. Khator, Associate Dean
Cullen College of Engineering

Michael P. Harold, Professor and Chair
Chemical and Biomolecular Engineering

ACKNOWLEDGEMENTS

The last five years at the University of Houston have been an incredible experience. It has been a challenging, yet rewarding time that I could not have successfully passed through without the support of several people. I want to start by thanking the Chemical Engineering Department for allowing me to pursue my doctoral degree. Foremost, I am obliged to my Ph.D. advisor, Dr. Jeffrey D. Rimer, who gave me the opportunity to work on this project and gave valuable suggestions and advice along the way. I am grateful to him for his foresight, patience and mentorship.

I was lucky to work with a wonderful research group here at the University of Houston. I would also like to thank several group members who directly contributed to this project, notably Manjesh Kumar, Wei Qin, and Rishabh Jain. Without the support of the other members of this group, I would not have had the resilience to pursue this project.

I am grateful to my friends at the University of Houston for providing constant motivations and support during my stay in Houston. I want to dedicate this thesis to my family members. I owe everything to them. They have been the most prominent supporters in this endeavor.

In Situ Methods to Characterize Zeolite Growth by Nonclassical Pathway

An Abstract of

Dissertation

Presented to

the Faculty of the Department of Chemical and Biomolecular Engineering

University of Houston

In Partial Fulfillment

of the Requirements for the Degree

Doctor of Philosophy

in Chemical Engineering

by

Madhuresh K. Choudhary

August 2019

ABSTRACT

Zeolites are widely used in commercial processes spanning from ion exchange in detergents to catalysis in the (petro)chemical industry. Understanding the mechanisms of zeolite growth at a molecular level aids *a priori* selection of synthesis parameters to tailor their physicochemical properties. Despite significant effort in the past two decades to elucidate the mechanisms of nucleation and crystal growth, these pathways in zeolite synthesis are not well understood. This is due in large part to the inherent complexity of zeolite crystallization and the synthesis conditions (i.e., high pH, high temperature, etc.) that render *in situ* characterization challenging. Our group developed a way to carry out solvothermal *in situ* atomic force microscopy (AFM) wherein we can observe zeolite surfaces at near molecular resolution under realistic growth conditions. This dissertation focuses on *in situ* AFM studies of several industrially relevant zeolites (e.g., LTA, MFI).

Interest in understanding zeolite A (LTA) formation stems from its widespread use as a commercial molecular sieve; however, recent discoveries that zeolite A is an active catalyst for environmental applications and methanol to olefins reactions has placed this material in the spotlight. Using *in situ* AFM, we observe distinct growth regimes as a function of supersaturation and temperature. At high supersaturation and low temperature, we observe the three-dimensional assembly and structural evolution of gel-like islands on zeolite surfaces. These features, which derive from molecularly-dispersed solute, constitute a unique mode of growth among reported cases of nonclassical crystallization. Time-resolved AFM imaging also reveals that growth can occur by (nearly) oriented attachment, which is a rare phenomenon for zeolites, but is observed during crystallization by particle attachment (CPA) for other minerals.

A detailed analysis of zeolite A crystal growth at low supersaturation reveals a predominantly classical mechanism where the generation of new layers on <100> surfaces occurs via three distinct modes: spiral dislocations, 2-dimensional nuclei, and layers emanating from

protrusions (defects). Our findings indicate that the selection of silica source plays a vital role in the presence of amorphous deposits, which can become incorporated into advancing layers on zeolite A crystal surfaces. Moreover, *in situ* AFM measurements using growth solution with and without an organic structure-directing agent reveal that the latter induces the formation of gel-like islands, analogous to conditions of much higher supersaturation and lower synthesis temperature.

The presence of amorphous colloidal particles is ubiquitous in many zeolite syntheses, and has led to extensive efforts to understand the driving force(s) for their self-assembly and putative roles in processes of nucleation and growth. We use a combination of *in situ* scanning probe microscopy, particle dissolution measurements, and colloidal stability assays to elucidate the degree to which silica nanoparticles evolve in their structure during the early stages of silicalite-1 (siliceous analogue of the widely used ZSM-5 zeolite) synthesis. We show how changes in precursor structure are mediated by the presence of organics, and demonstrate how these changes lead to significant differences in precursor-crystal interactions that alter preferred modes of crystal growth. Our findings provide guidelines for selectively controlling silicalite-1 growth by particle attachment or monomer addition, thus allowing for the manipulation of anisotropic rates of crystallization. In doing so, we also address a longstanding question regarding what factors are at our disposal to switch from a nonclassical to classical mechanism.

Table of Contents

List of Figures

List of Tables

Chapter 1

Prior Work on Zeolite: Rational Design and Growth Mechanism

1.1. Introduction

Zeolites are aluminosilicate minerals and have been known for almost 250 years. The mineralogist Axel Fredrik Cronstedt, coined term “zeolite”, from the Greek word zéō, meaning "to boil" and líthos, meaning "stone" as he observed that upon heating the material (believed to be Stilbite) produced a large amount of steam from the absorbed water. There is a lot of interest in zeolite research due to its widespread use in ion exchange, gas separations, and catalysis; however, natural occurring zeolites are of limited use due to the presence of impurities. It was only the advent of synthetic zeolites in the 1950s that zeolites began to play a key role in commercial applications. The development of synthetic routes of zeolites A (LTA type) and X (FAU type) for their use as absorbents was the first breakthrough in zeolite commercialization[1]. One of the most significant events in zeolite science was the introduction of faujasite (FAU) as a fluid catalytic cracking (FCC) catalyst in 1962[2]. These new materials were not only more active than previously used amorphous silica, but the advent of FAU-based FCC catalysts also led to a significant increase in the production of gasoline[3] . It has been estimated that the cost of worldwide petroleum refining would be higher by at least $10 billion per year if synthetic zeolites were not available today[4]. After 1962, zeolite catalysts rapidly replaced existing catalysts in the field of petroleum refining and various processes in the petrochemical industry. The major processes where zeolites are used today are hydrocracking of petroleum distillates, octane enhancement by isomerization, and synthesis of ethylbenzene, to name a few[5,6]. Although catalysis is the most important application of zeolites, with estimates of its expected market share

being about 33.80 billion USD in 2022[7] , zeolite research is expanding with new opportunities in a broad range of applications with applications spanning energy to medicine[8-17].

Zeolites are crystalline microporous aluminosilicates and are composed of covalently bound TO_4 tetrahedral units. The T atom in the zeolite tetrahedra is either Si or Al with O atoms connecting adjacent T atoms. On the other hand, zeotypes are the structural analogs of zeolites with a broad range of heteroatoms at T sites (e.g. T = Ge, Ga, Sn, B, etc.) [18-20]. Prominent examples of zeotype families include silicoaluminophosphates (SAPOs) and aluminophosphates (AlPOs).

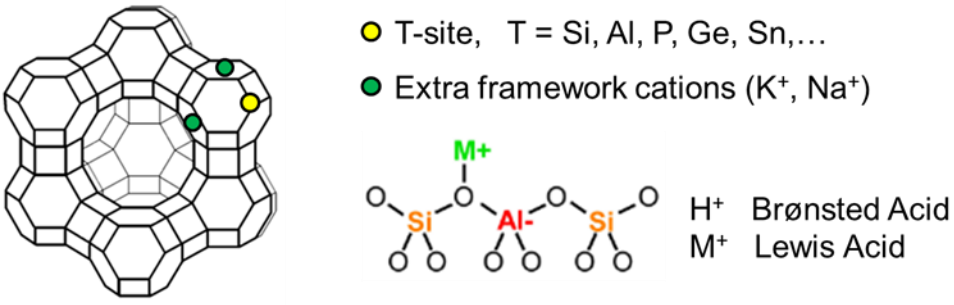

.

Figure 1.1: Faujasite zeolite framework depicting its cage and adjoining channels. T-sites are often occupied by Si and Al. The negative charge on Al is counterbalanced by extra-framework cations.

The tetrahedral units TO_4 are the primary building units of zeolites, and they combine to form over 30 periodically repeating secondary structural arrangements or secondary building units (SBUs). These SBUs are usually comprised of 8-12 membered rings resulting in small, medium, and large pores which can range in aperture from 3 to 10 Å[21-23]. These pores are interconnected in several different ways forming a network of pore channels. Depending on the connectivity of the pore channel, they can be divided as 1-dimensional (1D), 2D, and 3D, thereby forming intersecting or non-intersecting networks. The different network of channels results in over 235 different zeolite frameworks[24] each with unique arrangement of TO_4 units and is referred by three letter code by international Zeolite Association (IZA), such as FAU for faujasite-type zeolite, LTA for Linde type A zeolite, and so on.

The composition of aluminosilicate zeolites can vary over a wide range, from Si/Al = 1 to infinity. The lower limit of Si/Al = 1 of a zeolite framework[18] arises because of electrostatic repulsion between the negative charges on adjacent framework $Al(OH)^-_4$ species or Al-O-Al bond is not formed in usually zeolites (Löwenstein's rule) [25]. The amount of Al incorporated into the crystal lattice depends on the synthesis conditions and can be altered by post-synthetic modifications. A purely siliceous zeolite consists of all silicon T sites and has no charge in defect-free crystals (noting that defects, such as silanol vacancies and surface silanol groups, can lead to negative charge). The replacement of silicon T atoms by aluminum leads to a negative charge on the framework which has to be compensated by "extra-framework" cations (**Figure 1.1**). These cations can be alkali earth metals, transition state metals, or a proton, leading to Brønsted and/or Lewis acids sites in the zeolite framework[26]. The presence of these acids sites makes zeolites a unique class of catalysts with tunable acidity and whose selectivity and activity is enhanced by the well-defined pore channel. Hence, they are often considered to be catalytic micro-reactors (**Figure 1.2).** Furthermore, these extra framework cations are ion exchangeable leading to their widespread use in applications in ion exchange[27-32]. The amount of Al within the framework is a critical property. The hydrothermal stability and the hydrophobicity increases with the Si/Al ratio, while catalytic activity is also dependent on the Si/Al ratio.

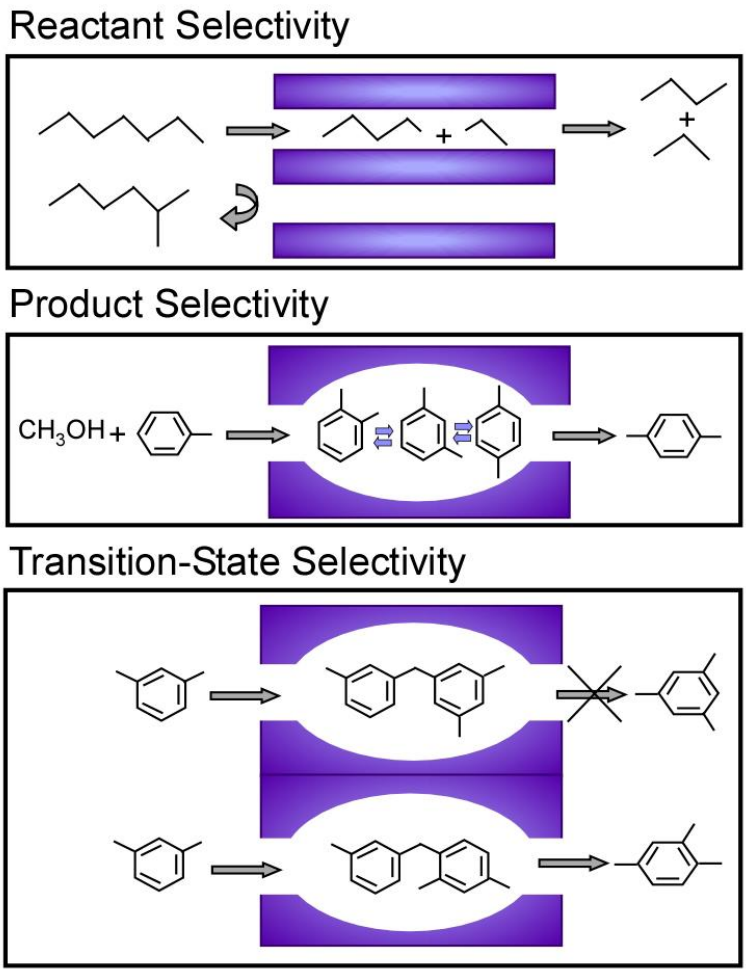

Figure 1.2: The shape selectivity effects during chemical reactions mediated by well-defined pore size and cage arrangements. Scheme has been adapted from previous work by Davis.[33]

1.2. Applications of zeolites

Zeolites are used commercially as catalysts and adsorbents owing to their unique properties such as (i) high surface area, (ii) well-defined pore size of molecular dimension, (iii) high adsorption capacity, (iv) their ability to partition reactants/products, (v) the possibility of modulating the electronic properties of active sites, (vi) high thermal stability, and (vii) the possibility for pre-activating the molecules in the pores by strong electric fields and molecular confinement [33,34]. In additions to applications in catalysis and adsorption (Figure 1.3), other novel applications (i.e., drug carriers, photonic devices) are being explored[18].

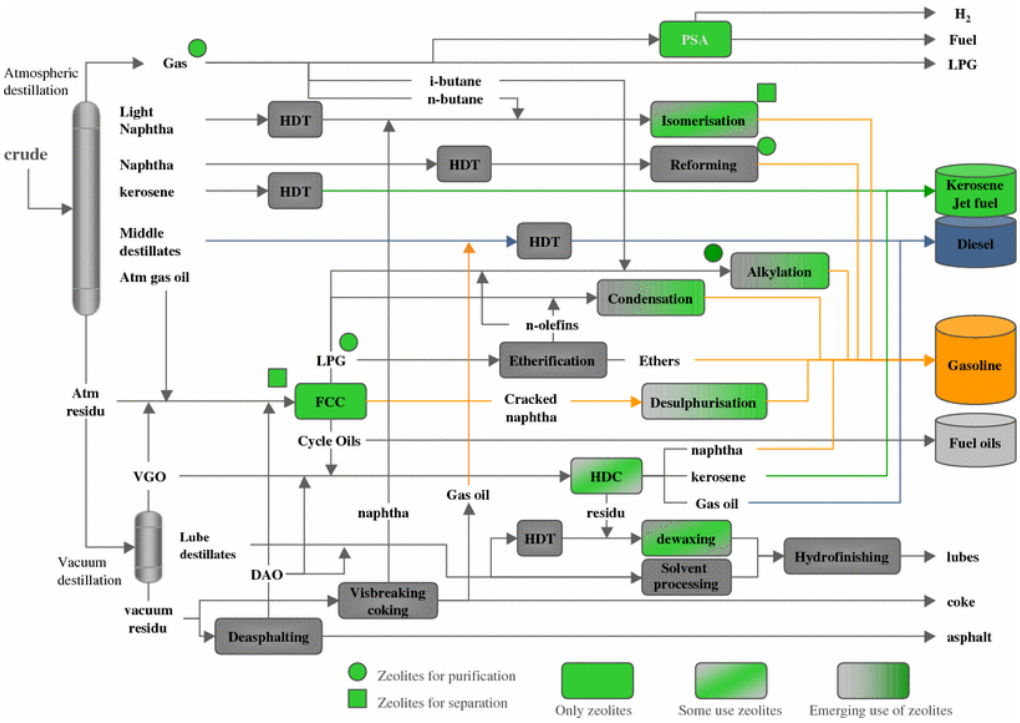

Figure 1.3: Some of the major operations found in modern refineries with current and emerging applications for zeolites [36]

1.2.1. Catalysis

Catalysis is the most important area of zeolite applications. Zeolites can mediate reactions through Brønsted acid sites, Lewis base sites, and bifunctional active sites (e.g., transition metal with an acid site that either act cooperatively or in tandem). The common applications of zeolites as catalysts are cracking, hydrocarbon isomerization, and hydrocarbon synthesis.

The reactions within the confined volume of zeolite pores can provide better control of selectivity of products. Fluid catalytic cracking is the largest and the oldest use of zeolite catalysts. The FCC units are the most important unit in refinery where most of the gasoline and diesel are produced from crude oil or it can be used to optimize the propylene production by changing operating conditions (with minor modification using catalyst additives)[2]. For instance, Faujasite (zeolite Y or USY) is the main FCC catalyst with ZSM-5 (MFI) additives to increase

the yield of propylene and butenes leading to a boost in gasoline octane[37-40]. In addition to its use as a FCC catalyst, zeolite Y is also used in hydrocracking, which enables the refinery to process a wide variety of feedstocks by converting vacuum gas oil (VGO) and heavier residue into mainly transportation fuels, i.e. converting low value products into higher value products. This also provides the refinery flexibility in operating based on crude quality and market/legislative requirements.

Zeolites are also widely used in selective catalytic reduction (SCR) due to increasing need to control of greenhouse gases (NOx, SOx) from various sources such as automobiles [41]. Strict environmental legislation has spurred efforts to develop new, and more effective, catalysts to reduce the NOx content in automobile exhaust streams. The discovery of Cu^{+} exchanged SSZ-13 has proven to be a good alternative and is used extensively in catalytic conversion of NO_x to N_2 [42-46]. Recently, high silica LTA has been found to have high thermal stability under NOx reaction conditions and is being explored for this application[47].

Fuel production from biomass is a rapidly expanding field to supplement the limited resource of fossil fuels [48-51]. There have been several efforts to explore the options of converting bio-feed stock to bio-fuel [50]. Given widespread success of zeolites in refining and the petrochemical industry, there is a growing interest in the use of zeolites for biomass processing[50]. Several biomass conversions studies have been reported using the unique chemistry of zeolites [52-54]; however, there are several obstacles before the successful commercialization of a zeolite catalyst for biomass conversion can be realized. These obstacles include unstable products, the low structural stability of zeolites in the reaction media and limited active site accessibility by large biomolecules [54].

The advent of shale gas as an energy source has a dramatic effect on the energy landscape and spurred research in conversion of smaller and saturated hydrocarbons into aromatics and olefins [55]. Zeolites and related materials (zeotypes) are being explored as potential candidates for

methanol-to-olefin (MTO) processes. To this end, the zeotype SAPO-34 (CHA type) is used in commercial MTO processes [55].

1.2.2. Absorbents

Zeolites can selectively adsorb molecules on the basis of their electrical charge and size. Hence, they are also called molecular sieves. The large surface area and large micropore volume make them excellent absorbents. Also, they have high (hydro)thermal stability, which makes them suitable for applications requiring multiple regenerations under relatively harsh environments. Hence, zeolites account for 85% for all inorganic absorbents [24]. They are also used as non-regenerative adsorbents for desiccants, NH_4^+ removal, promising hemostatic agent[56] and odor control[57]. Zeolites are used for bulk gas phase separation for N_2/O_2 and CO_2,CO from syngas [58]. They are also used for gas purification, such as absorbing NO_X and/or SO_2 from gas effluent. The effectiveness of microporous zeolites in these applications can be fine-tuned by varying the pore size or changing the distribution of cations within the pores [59].

1.2.3. Ion exchange

Cations within the zeolite pores can readily exchange with other cations in aqueous media. Hence, low silica zeolites such as zeolite A, are used extensively in ion exchange applications [60,61]. In fact, it is the most widely used application of zeolites by weight [1]. Zeolites are used in detergents and soaps for its water softening properties [28,32,33]; and zeolites can also be used to remove radioactive ions from water [62].

The economics of these applications and the zeolites selected for these applications depend on: (i) the performance of zeolites and (ii) the cost involved in zeolite synthesis. There exists structure-property-performance relationship which determines the overall performance of zeolites towards specific applications, which is described in more detail in the following section. For example, small crystals with reduced mass transport limitation has longer catalyst life time [63].

1.3. Structure-property and performance of zeolites

The demand for more efficient zeolites has spurred efforts to control their synthesis and resulting physicochemical properties. In this section, some of the important properties which affect the performance of zeolites and strategies used to tailor these properties of zeolites are discussed.

1.3.1. Acid site density

The amount of aluminum in the zeolite is an important property. It determines the number of active sites (i.e. total acidity) in catalytic processes. Also, the high aluminum content of zeolites, such as LTA and FAU, make them suitable for gas adsorption and ion exchange [34]. Moreover, the composition of zeolites (i.e. Si/Al ratio) has a significant impact on their hydrothermal stability as well as catalyst lifetime [64]. For example, low silica faujasite is not suitable as a catalyst for FCC reactions due to low thermal stability; however, the desilication of ultrastable Y (USY) by steaming or acid treatment affects the structural integrity of zeolite. Often high silica zeolites require the use of fluoride. Furthermore, siliceous zeolites are ideal for emerging applications in gas separations, sensors, and the next generation of low-k dielectric materials [65]. For these reasons, substantial effort has been directed into research and development to tailor the composition of zeolites [47,64,65].

1.3.2. Aluminum siting

The spatial distribution of acid sites in zeolites may differ in density with changes in bulk elemental composition (Si/Al ratio). Even at fixed bulk composition for a specific zeolite framework, the arrangement and distribution of framework Al atoms can lead to structural and catalytic diversity. The use of organic structure-directing agents (OSDAs) in zeolite synthesis have the potential to direct Al siting [66]. For example, the use of tetrapropylamonium (TPA) in

ZSM-5 (MFI) synthesis can place Al sites preferentially within 10-member ring(MR) channel intersections [67]. Conversely, Al is placed both in both the straight and sinusoidal channels of ZSM-5 synthesized in the presence of TPA and Na^+ [66], which serves as an inorganic structure-directing agent. The distribution of Al at different T sites of a given zeolite influences its catalytic activity, because reactive intermediates and transition states stabilization depends on the geometry of the localized confined environment [68]. The Al distribution at different T sites also influences the structural stability of a given zeolite [69]. Also, the proximity of Al atoms with the framework can affect catalyst activity and its structural stability [52,66]. Furthermore, the spatial distribution of acid sites affects the shape selectivity of product distribution [70]. Hence, approaches to tailor the spatial distribution of acid sites with specific channels or cages have been developed. Notable examples include the use of OSDAs [66,71] , whereas a more macroscopic control of Al distribution can be accomplished through the synthesis of core-shell structures [72] or so-called Si-zoned materials.

1.3.3. Diffusion path length

The micropores of zeolites affect the diffusion of molecules throughout their porous networks. In zeolites, the reaction is often limited by internal diffusion of molecules which affect the catalyst lifetime and product selectivity [73]. The diffusion path length of zeolites, in turn, depends on the catalyst size, morphology, and any mesoporosity that may be present in the zeolite. Conventional syntheses of zeolites often lead to materials with pore dimensions aligned along the longest dimension of the crystal, which generates a long diffusion path length. Hence, there is a considerable number of studies that are focused on controlling the morphology of zeolites [74-76]. Some notable examples include the use of zeolite growth modifiers (ZGMs) [74-76], novel OSDAs [77], and the control of synthesis conditions (e.g. pH, temperature, water content, and aging, among others) [78,79]. We have shown how ZGMs can be used to tailor the properties of several zeolite frameworks [74-76]. Similarly, it is widely reported in literature that the size of

zeolites can be reduced by using low temperature aging [78]. Many nanosized zeolites have been synthesized, as documented in a review by Mintova [79]. Finally, the internal diffusional path length can be controlled by generating hierarchal zeolites, which consist of additional mesoporosity in addition to the zeolite micropores that reduce mass transport limitations [80,81]. These hierarchal zeolites can be synthesized by either top down or bottom up approaches [73,82,83]. In first method, the additional mesoporosity is generated by post-synthetic treatment of zeolites [84], while the bottom up approach introduces mesoporosity during the synthesis [85]. Some notable examples of hierarchal zeolites were reported by Ryoo[77,86], Tsapatsis [87], and Garcia-Martinez [84]. The advantage of top down methods is that it is high facile however the Si/Al ratio and crystallinity is affected. While bottom up approach often required costly organic molecules (mostly OSDAs) which make the synthesis economically infeasible and also the removal OSDA leads to toxic gases and sometime framework collapses upon calcination.

1.4. Economics of zeolite synthesis

The chemicals used for zeolite syntheses include Si and Al sources. Often zeolite synthesis requires the use of organic molecules, either as OSDAs or modifiers, to tailor material properties and avoid the formation of impurities (e.g. polymorphs). The incorporation of these reagents can have a negative impact on the overall cost of zeolite synthesis. Often the removal of organics (post synthesis) leads to the generation of toxic gases, which require further mitigating measures that can further impact the overall economics of the process. As mentioned in previous sections, the synthesis of certain zeolites and post-synthesis treatments may require the use of fluoride ions, which is a safety concern, and hence fluoride-free syntheses are preferred. Thus, the overarching goal of zeolite synthesis optimization involves methods to eliminate OSDAs [88] and the selection of inexpensive chemicals [89]. Purity is another factor which is vital for zeolite synthesis. To this end, a seed-assisted synthesis approach has been used to avoid the formation of polymorphs and to reduce the synthesis time [90,91]. Improved heat exchange is another factor that

can lessen the time of crystallization. Indeed, Okubo and co-workers reported rapid hydrothermal treatment to produce zeolites using tubular reactor [92,93] . Other strategies reported are microwave assisted zeolite synthesis, which facilitates rapid crystallization [94]. The temperature used for zeolite synthesis is another important parameter that can affect the economics of commercial zeolite production as it impacts not only operational costs, but also equipment costs.

1.5. Zeolite growth mechanisms

Owing to the complexity of zeolite growth, the optimization of zeolite synthesis and its properties is difficult. The conventional synthesis of zeolite involves mixing of silica and alumina sources with a mineralizing agent such as NaOH or KOH in water. The mixture is hydrothermally treated for days to weeks at temperature from ranging from 35 to 200 °C [95]. The overall free energy change for a zeolite formation is typically small as the product and raw materials have a similar bond type[95,96]. Hence, zeolite formation is often kinetically controlled [95]. Moreover, zeolites are metastable species wherein a slight change in the kinetics or thermodynamic driving force can lead to different phases. This places greater emphasis on optimizing the synthesis conditions to promote the nucleation and growth of one phase over others. Despite significant effort over the last five decades from multiple research groups [95], the guidelines for selecting synthesis parameters *a priori* is lacking due to the presence of complex and diverse precursors involved in zeolite synthesis.

The crystallization of zeolite proceeds via two steps: (1) nucleation of particles of new zeolite phase and (2) further growth of zeolite crystals. During nucleation, the smallest entities characteristic of a crystalline zeolite are formed, upon which additional growth species attach as the crystal grow. Crystal growth is often described by sigmoidal curves defined by an induction period followed by an almost linear crystal growth rate. During nucleation and crystal growth, the attachment of solute is governed by the degree of supersaturation σ, which is defined as $\sigma = \frac{C}{C_e} - 1$, where C is the solute concentration and C_e is the solubility of the zeolite. Supersaturation is the

driving force behind the formation of a new phase and its growth. Interzeolite transformations are putatively governed by the free energy of the new phase, which is less than the free energy of the initial phase [97].

1.5.1. Nucleation

Crystallization is initiated by the nucleation of a new phase and further crystal growth occurs by the addition of solute. The early stage(s) of crystallization is crucial for the properties of the final crystal, such as the phase formed, its purity, and size (as determined by the number of nuclei generated in the growth solution). There have been numerous mechanistic studies of zeolite nucleation, both in industry and academia. Zeolite synthesis is usually carried out using a sol-gel mixture [98]. The mixing of Si and Al sources can lead to formation of a sol, which is clear solution containing colloidal particles. The mixture can also be a gel, which is a polymeric chain of aluminosilicates.

The molecular level understanding of solid state formation from the solution comprised of soluble species is not completely understood. Classical nucleation theory (CNT) is the common model to study the nucleation from the solution. It states that nucleation occurs via the formation of embryos of a new phase from the solution by the aggregation of solute at high supersaturation when the molecules come and arrange to form a cluster [99]. The free energy change determines the formation of nuclei and there are two opposing forces which determine whether they grow or they dissolve. The surface energy decreases while the bulk lattice energy increases with size. The surface contribution dominates until the critical size is reached. All the nuclei greater than the critical size grow whereas those less than the critical size dissolve. This phenomenon in solutions is called homogenous nucleation. The presence of foreign particles accelerates nucleation as it reduces the critical radius requirement. After nucleation, further growth occurs via the addition of solute to the growing crystal.

In zeolite syntheses, the events taking place are more multifaceted. The interface between the particle formed and solution is ill-defined as in the case of gel precursors where the transition from solution (or gel) to a solid phase occurs in multiple stages. In CNT, it is assumed that the nanosized particles to have similar properties as bulk materials[100], which may not be true. For example, small particles usually have much higher surface area to volume ratio. Hence, the properties of silica gels are in stark contrast to those of bulk materials, such as siliceous zeolite crystals or quartz. There is growing evidence that CNT is not applicable to zeolite nucleation. The process is more akin to the so-called two step mechanism observed for a wide range of materials[101,102]. Furthermore, the vast number of species and their size is a major obstacle in the understanding the zeolite nucleation which is further aggravated by the lack of suitable analytical techniques. In next section, studies related to soluble species in zeolite synthesis mixtures are discussed.

1.5.2. Soluble silicates in solution

Zeolite synthesis is usually carried out in alkaline solutions at a temperature ranging from 25 to 200 ºC with Si and Al concentrations in the range of 0.5 – 6.0 mol/L [103]. At these conditions, aluminum in the solution (in the absence of silicon) exists as $Al(OH)_4^-$ in basic media. Silica chemistry, however, is more complex. At low concentrations, silica can exist as a monomer, or silicic acid $Si(OH)_4$, but with increasing pH (>8) these neutral monomer species become deprotonated to various degrees. At high silica concentration, various oligomers have been observed using techniques such as ^{29}Si NMR[104]. The degree of connectivity of tetrahedral silicon atoms is often denoted as Q^n and one typically finds ^{29}Si NMR resonances corresponding to Q^0 (monomer, $T(OH)_4$), Q^1 (terminal), Q^2 (singly bridging,-O-T-O-), and Q^3 (corners of cage structures) centers. The formation of oligomers is favored by high Si concentration, low pH, and low temperature[105]. Some of the oligomers can be stabilized by cations, which are counterions to negatively charged silanol groups. For example, tetramethlammonium (TMA^+) is known to

promote the formation of double 4-membered rings (D4R) at high silica concentrations. Similarly tetraethylammonium (TEA^+) is reported to promote the formation double 3-membered ring (D3R) oligomers; however, even for conditions favorable to their formation, growth solutions are often comprised of different kinds of oligomers[106].

An important observation from ^{29}Si NMR measurements is that the formation of D4R species occurs slowly over many hours at room temperature in TMA-silicate solutions, which denotes the kinetic inertness of Q^3_n cage species [107]. It may be due to the absence of bound proton – notably, a Q^3_n cage is not expected to have protons attached, even under moderately alkaline conditions (pH>10) [108]. The stability of D4R species has also been confirmed by mass spectroscopy (MS) where D4R was found to reach isotopic equilibrium within hours, while TEA-silica oligomers (e.g. D3R) were found to reach equilibrium much faster[109] . It is uncertain whether the difference between two species is due to an inherent different in the stability of these oligomers or due to differences in the stabilization of these species by the cation. For instance, it is known that TMA^+ has much higher charge density, and hence it will prevent the hydrolysis much more effectively, than TEA^+.

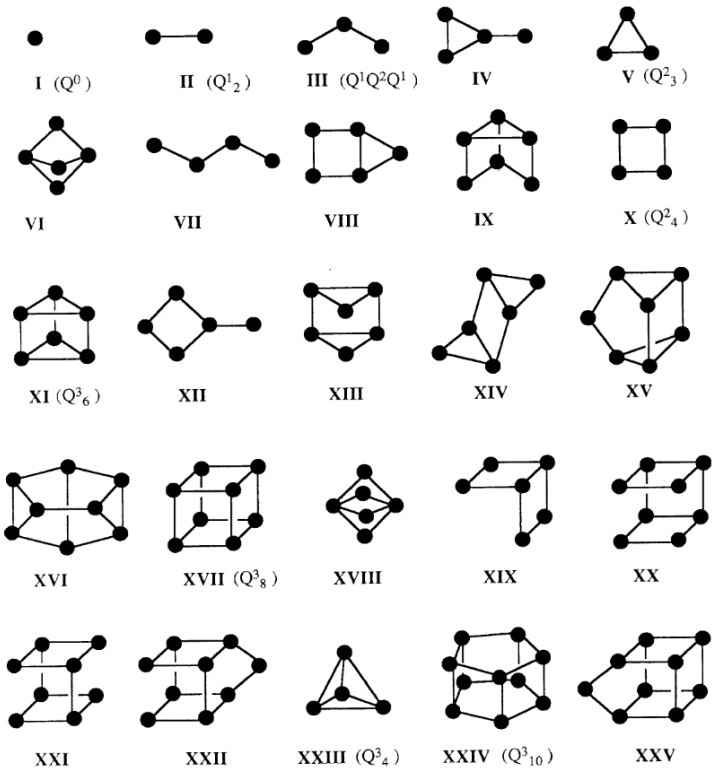

Figure 1.4: Various silicate oligomers detected in aqueous alkaline media by ^{29}Si NMR. The black filled circles represent Si atoms in tetrahedral sites surrounded by oxygen atoms; connecting lines represent shared oxygen atoms [110]

1.5.3. Soluble aluminosilicates in solution

It is expected that silicates will react rapidly with aluminates in an alkaline solution [110]. Using ^{27}Al NMR and ^{29}Si NMR, various aluminosilicate oligomers have been detected in alkaline media[110]. These oligomer species have also been detected by Raman [111], mass spectroscopy [109,112] and other spectroscopic techniques[110]. However, ^{29}Si NMR is a preferred method as it gives sharp, well-resolved peaks in contrast to broad peak from the quad polar ^{27}Al nucleus. One negative aspect is that ^{29}Si has low natural abundance and fairly long spin relaxation time in solutions, which requires long experiments and often enrichment. Various aluminosilicates have been identified using NMR (shown in **Figure 1.5**).

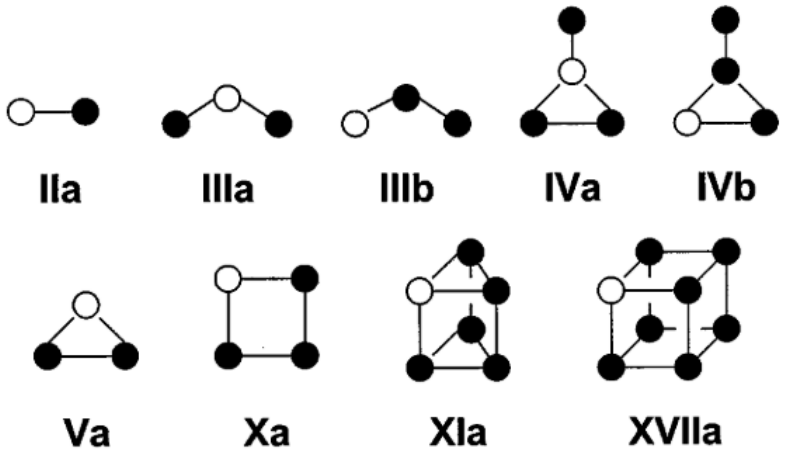

Figure 1.5: Various aqueous aluminosilicate oligomers for which NMR evidences have been reported[110]. Symbols are similar to those in **Figure 1.4,**with open circles indicating Al atoms at T sites surrounded by shared oxygens[110].

Chemical exchange between different species leads to broadening of peaks in NMR and affects identification of aqueous aluminosilicate species. Harris et al. [113] reported that the more highly connected Al (q^3, the aluminum counterpart of silica Q^3) in aqueous aluminosilicates are relatively inert kinetically, approaching equilibrium only over many hours in solutions prepared at room temperature. Furthermore, it has been concluded that small, acyclic aluminosilicate species are much more reactive than any silicate oligomers, and that ring or cage structures are particularly unreactive, whether or not they contain Al [110]. However, there are limited data available on the exchange rate of aluminosilicates. For instance, no information is available about the stability of the aluminosilicate D4R in solution, which has been postulated to be key precursor for zeolite A crystallization [114]. The stability of these species may affect whether they are involved as direct growth units in zeolite crystallization.

It has been inferred that the small aluminosilicate species are the active precursors in the hydrothermal crystallization of zeolites. Based on NMR analysis, it has postulated that larger aluminosilicate solutes may simply be a nutrient reservoir of small acyclic aluminosilicates [110]. One important implication of the stability of cyclic oligomers is that the critical radius during

zeolite crystallization by 2D nucleation is putatively small. Even for given growth mixture, a large number of variables can impact zeolite nucleation. Furthermore, zeolites are metastable materials that can undergo a series of transformations leading to structures that are more thermodynamically stable [95], and thus growth is largely kinetically controlled.

One of the pioneering studies of zeolite A nucleation is by Mintova et al. [115]. They studied the formation of zeolite A crystallization at room temperature in the presence of an OSDA (TMA) by means of high resolution transmission electron microscopy (HRTEM). Their HRTEM images revealed that the first crystallites were embedded in amorphous gel-like aggregates with each amorphous aggregates containing one nucleus which grew with the consumption of amorphous precursors. On the other hand, in a similar study with FAU type zeolite by the same group revealed an interesting observation[116]. The nucleation of faujasite was observed on the periphery of the amorphous gel. One important difference between the two studies was that the temperature. The study with faujasite was carried at 100 °C compared to room temperature for the study of LTA. In both of their experiments, measurements were carried out in the presence of an OSDA and both zeolites are low silica zeolites.

Another landmark study of zeolite nucleation is the room temperature study of silicalite-1 conducted over the course of a year to capture events of nucleation[117]. Silicalite-1 is a siliceous zeolite with a MFI framework and it serves as a model system for mechanistic studies of zeolite crystallization. The clear growth solutions used to prepare silicalite-1 consist of amorphous nanoparticles with dimensions of 1 to 6 nm[117] . Tsapatsis and coworkers used cryogenic transmission electron microscopy (cryo-TEM) to track the evolution of precursors during crystallization at room temperature [117]. With the increased synthesis time, the initially formed aggregates of nanoparticles became completely crystalline with ~5-nm protrusions on crystal exteriors which were commensurate with the size of initial nanoparticle precursors.

It is interesting to compare these studies with the nucleation of zeolite in the absence of OSDAs. Valtechev et al. [118] reported the OSDA-free synthesis of FAU zeolite at room

temperature. Their extensive investigation by HRTEM was coupled with dynamic light scattering (DLS), synchrotron X-ray diffraction (XRD), N_2 adsorption measurements, and chemical analysis. Their study suggested that the nucleation of FAU occurred inside the gel, within regions reported as "negative crystals" with liquid trapped in the gel phase.

1.6. Zeolite crystal growth

1.6.1. Classical growth

Classical crystal growth typically involves 2-dimensional (2D) nucleation of layers and their subsequent spreading by the addition of monomers [102]. Similar to the critical radius observed in homogeneous crystal nucleation, there exists a critical radius for 2D nucleation. If the size of the nucleus is less than its critical radius, the layer will dissolve, whereas layers with sizes larger than the critical radius most frequently lead to layer growth. As supersaturation increases, the critical radius decreases and becomes less than the size of the growth units resulting in kinetic roughening (i.e. a condition when the barriers for nucleation are low, and a single solute ion or molecule may serve as a nucleus).

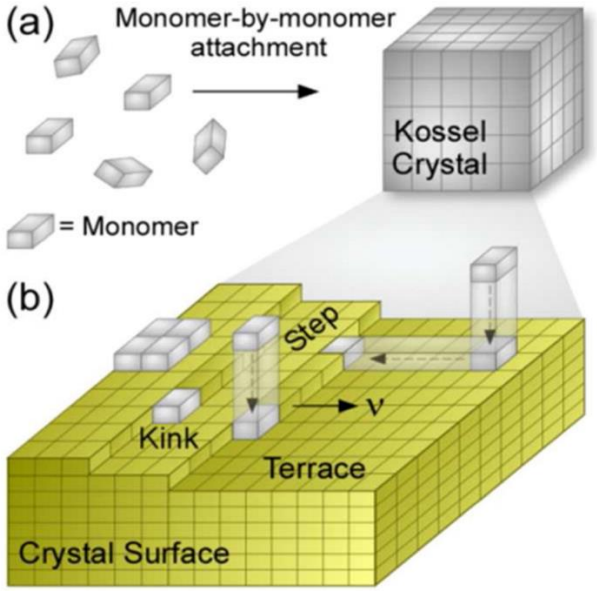

Figure 1.6: (A) Classical crystallization occurs through monomer-by-monomer attachment **(B)** Kossel crystal where monomers attach either by their direct incorporation or by their adsorption onto terraces followed by surface diffusion and incorporation [119]**.**

A Kossel crystal (Figure 1.6) is a model system that illustrates the three most typical sites on crystal faces for solute to attach: kinks, steps, and terraces [99]. Monomer attachment to a kink site is the most energetically favorable as it leads to the formation of three monomer–crystal bonds (compared to two bonds and a single bond for step and terraces). Depending upon the supersaturation, the attachment of monomer occurs at kinks, steps, and edges. The solute can only attach to kink sites at low supersaturation. Conversely, they attach to all the sites at high supersaturation, resulting in rapid 2D nucleation and rough growth. The distinct regimes of growth for classical mechanisms are broadly differentiated based on the relative supersaturation (Figure 1.7) [99].

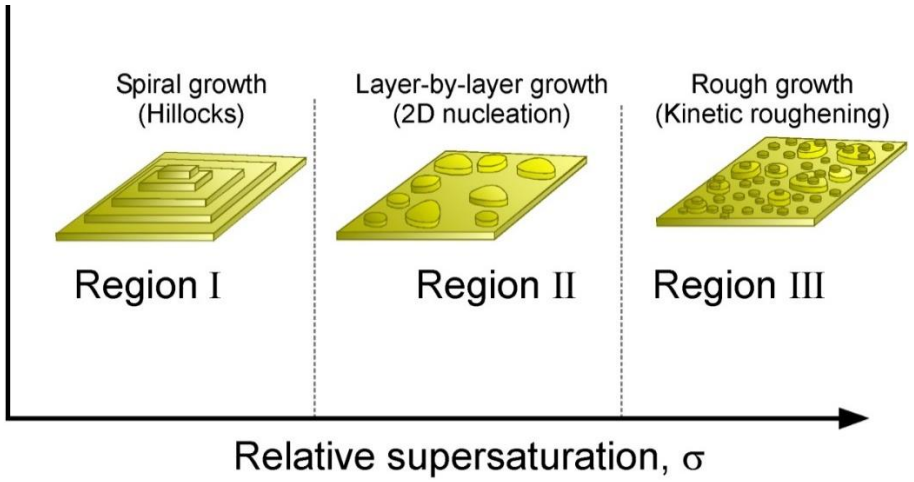

Figure 1.7: Scheme showing the different growth mechanisms of layer-by-layer growth on a crystal surface as a function of supersaturation.

On the other hand, as supersaturation decreases, the size of nuclei becomes large, and no nucleation happens. In these growth occurs via spiral growth resulting in the formation of growth hillocks emanating from a spiral dislocation source. This spiral growth usually occurs at low supersaturation. The spiral growth increase the growth rate as the addition of solutes on the steps does not decrease in the kinks site, and the growth rate continues forever. However, no all the hillocks are due to spiral dislocation as has been observed in zeolites and other crystals. They can be due to intergrowth or twin plane crystal. This twin plane crystal again helps in reducing the critical size requirement similar to heterogeneous nucleation.

1.6.2. Nonclassical growth

Crystal growth can occur via the attachment of a wide range of species (Figure 1.8) [120]. Often multiple pathways are at play throughout zeolite synthesis. The presence of unfinished layers on fully grown crystals often seems to suggest classical growth by monomers attachment in zeolite surfaces [121]; however, zeolite syntheses are carried out in a way that the silicon and aluminum sources do not dissolve completely leading to formation of a sol gel. The presence of particles during crystallization seems to suggest a nonclassical growth mechanism governed by particle attachment. The presence of amorphous precursors of varying structure, size and shape leads to a complicated mechanism of crystallization. In contrast to classical growth, the knowledge of nonclassical growth mechanism is limited due to the lack of suitable techniques to observe dynamics process *in situ* with sufficient spatiotemporal resolution[120].

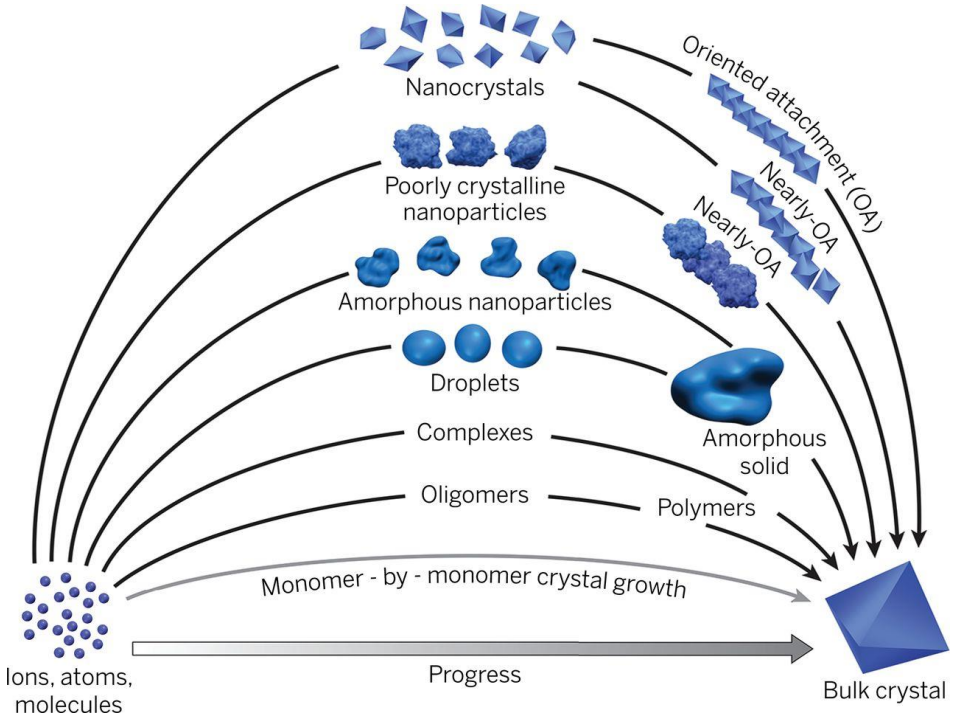

Figure 1.8: Scheme showing various pathways for crystallization[120]. Growth by monomer attachment is defined as classical while growth via other complex precursors is considered nonclassical pathways.

At low supersaturation, zeolites can grow classically by monomer addition[121]. At high concentrations, monomers can assemble into oligomers or larger particles, which may serve as growth precursors. At even higher amounts of nutrient, monomer or oligomers can form gels or liquid aggregates or can self-assemble to form primary particles. These particles can directly attach to crystal surface or can evolve in size and microstructure to attach to the crystal surface [121]. The kind of particle formed in the growth solution depends on the selection of Si and Al sources, the mineralizing agent, pH, and temperature. For example, when a Si source such as colloidal silica or fumed silica is added to alkaline solutions in the presence of alkali metal ions, these particles aggregate and fuse to form so-called worm-like particles (WLPs) [98]. These particles have been observed in various zeolite systems that include (but are not limited to) LTL [122], MFI [123],CHA [124], and LTA [125]. Despite their presence reported throughout synthesis of various zeolites, their role is not fully elucidated. There are two hypotheses regarding their role in zeolite crystal growth [119]: (1) They are a nutrient source that dissolve to produce molecular species, and/or (2) they directly attach to the crystal surface.

The choice of silica can have dramatic impact on the crystal growth mechanism. For example, when tetraethyl orthosilicate (TEOS) is used as silica source in the presence of OSDAs, they assemble into amorphous nanoparticles at sufficiently high silica concentration with physisorbed OSDA on their surfaces [126]. The exact microstructure of these nanoparticles is unknown, but they have been shown to evolve during zeolite nucleation [127]. Prior studies in our group have directly confirmed that these evolved particles attach to the crystal surface and undergo a disorder-to-order transition [128].

1.7. *In situ* studies of zeolite crystallization

The investigative work to understand zeolite growth mechanisms has been ongoing for the last 30 years [95]. Over the years, a variety of techniques have been used to study zeolite growth mechanisms. One way to study zeolite growth is by *ex situ* techniques where the growth mixtures

are quenched and particles are extracted from the growth medium and analyzed by batteries of techniques. However, the effects of sample preparation during quenching and extraction can limits the interpretation of data. Hence, *in situ* techniques are preferred. In this section, we will discuss some of the *in situ* techniques used to unravel zeolite growth.

1.7.1. Nuclear magnetic resonance spectroscopy

NMR spectroscopy can provide information of the atomic environment of framework elements in solids and in liquids. One of the advantages of NMR is that there is very little sample preparation required for analysis. Hence, it has been widely used in ex *situ* studies of zeolite synthesis. It can also provide detailed information of species present in the solution and to probe Si/Al chemistry. One of the limitations of NMR previously described is that Si has low natural abundance and also low sensitivity, which requires long experiment time. At high temperature, the sensitivity of NMR decreases, which is further aggravated by the rapid exchange between species to limits such analyses. *In situ* NMR can be carried out in two modes: (1) MAS (Magic Angle Spinning) mode to probe species in solids and (2) Liquid state mode to probe soluble species. One of first *in situ* NMR studies of zeolite A was carried out by Shi et al. [129]. In this study, ^{27}Al and ^{29}Si MAS NMR were used to track the species in solution and the solid phases. A parallel *in situ* X-ray diffraction study was used to investigate the crystallinity of the product. At the synthesis temperature, only monomers were observed in the solution phase. The concentration of dissolved Al monomers decreased during crystallization and it was concluded that the zeolite A growth occurs via solution mediated monomer addition.

In another study, *in situ* ^{27}Al NMR spectroscopy was used to measure the kinetics of zeolite A crystallization at 80 °C[130]. The changes of aluminum species present in the solid and solution phases during synthesis were monitored. From the gap in changes of alumina concentration, certain intensity curves of ^{27}Al NMR line from the solution phase, an 'autocatalytic nucleation' model of zeolite crystallization was inferred. Additionally, this study demonstrated

that *in situ* measurements do not require a specially constructed rotor as for ^{27}Al MAS NMR, which simplifies sample handling. Recently, the first *in situ* NMR study under hydrothermal conditions was reported for zeolite BEA [131]. The solution-based and solid-based growth was observed for two different synthesis procedures. The synthesis of silicalite-1 from clear solution is one of most studied zeolite crystallization systems. Liquid state ^{29}Si NMR of silicalite-1 has been used to monitor the oligomers present in solutions at room temperature [132]. The NMR peaks of the silica nanoparticles are broad in contrast to sharp peaks of oligomers[132]. Thus, ^{29}Si NMR can be used to monitor the connectivity of the silica nanoparticles during hydrothermal treatment. Due to the low natural abundance of silicon, the NMR experiments must be carried out in very high silicon concentration. Furthermore, the resolution of NMR peaks reduces at high temperature due to rapid exchange. Hence, most of the ^{29}Si NMR are carried out *ex situ* where the solution is cooled to room temperature after a set period of hydrothermal treatment. It has been concluded that the connectivity of silica nanoparticles increases upon heating [133], suggesting nanoparticles evolve in structure.

1.7.2. Dynamics light scattering

Dynamics light scattering (DLS) can provide information of the average size of particles in the solution. It has been used to monitor the crystal growth rate [134]. It can be also used to monitor the change in the growth precursor size. However, DLS only provides limited information about the size of the particle. Also, the application of DLS is limited to zeolite crystallization in clear solutions, which is a minor percentage of all zeolite growth media. It has been used for room temperature synthesis of zeolite A to monitor crystallization as a complement to other techniques, such as HRTEM [135].

1.7.3. Small-angle x-ray Scattering

Similar to DLS, small-angle x-ray scattering (SAXS) can also be used to estimate the size of smaller particle. Hence, SAXS is often used along with DLS and wide-angle x-ray scattering

(WAXS) to study zeolite growth. In addition to measurements of particle size, SAXS can be used to estimate the number density of particles. Hence, *in situ* SAXS/WAXS has been used to follow crystallization of silicalite-1 [132] and zeolite A [136]. These scattering techniques can provide information regarding the formation of particles, but they do not provide information about the chemical nature of particles. Small-angle neutron scattering (SANS) contrast measurements have been used to probe spatial distribution of OSDAs throughout precursors during silicalite-1 growth [137].

1.7.4. UV raman

Raman spectroscopy is a suitable to investigate species present in both solid and liquid phases. The use of *in situ* UV Raman was first reported by Li and coworkers for FAU growth [111]. A band at 575 cm^{-1} was observed in the solid, which decreased in intensity with crystallization time. The band was assigned to 4-ring species and was suggested to be a key precursor of zeolite X (FAU) synthesis. The same group later reported an *in situ* UV Raman study of zeolite A (LTA) crystallization where D4R species were reported to be a key precursor [114].

In addition to the aforementioned techniques, other *in situ* techniques, such as XRD [129] and calorimetry [138], have been used to probe zeolite crystallization. Recently, Kirschhock and coworkers [139] reported *in situ* electrochemical impedance spectroscopy to monitor the formation of nanoparticle and aggregates. One of the limitations of spectroscopy techniques is their inability to provide full spatiotemporal resolution that is required to fully elucidate the mechanism(s) of zeolite formation.

1.7.5. Atomic force microscopy

Atomic force microscopy (AFM) is a versatile and powerful microscopy technique to investigate sample surfaces at nanoscale resolution. It can not only provide three-dimensional topography of surfaces, but it can also provide information about the material properties with a high spatiotemporal resolution. AFM imaging requires minimal sample preparation, which makes

it a convenient tool to probe the surface at a molecular scale. Furthermore, it can be used in a variety of environments, including in air and in solution, which allows *in situ* investigation of crystal growth.

AFM is a type of scanning probe microscopy (SPM) that uses the interaction of a probe with a surface (**Figure 1.9**). AFM uses a flexible cantilever with a sharp tip to scan across the sample surface. As the tip approaches the sample, the attractive force between the surface and the tip causes the cantilever to bend towards the sample. However, the repulsive force dramatically increases as the cantilever is brought even closer to the surface. This leads to the cantilever to bend away from the sample surface.

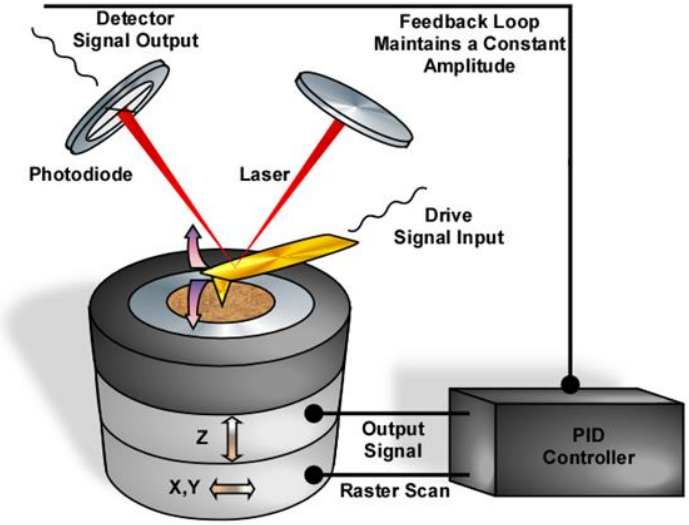

Figure 1.9: Diagram showing the basic operation of an AFM instrument. A cantilever with a sharp probe is used to track the surface. Laser based detection is used to monitor the deflection of tip to generate 3-D image of the surface.

The cantilever deflection is tracked using a laser where the incident beam is reflected off the flat top of the cantilever, and any change in cantilever deflection will result in changes in the direction of the reflected beam. A position-sensitive photodiode (PSPD) is then used to track these changes in deflection. As the AFM tip scans over an elevated surface feature, it results in a change in cantilever deflection and the subsequent shift in the direction of the reflected beam, which is registered by the PSPD. In contact mode imaging, the distance of the tip above the

surface is controlled by a feedback loop to maintain the constant deflection of the cantilever. A 3D image of the surface is generated from these movements of the probe in the z (vertical) direction as the probe raster across the surface in the x-y (lateral) plane.

Some of the disadvantages of contact mode imaging are the possibility of sample damage and decreased lateral resolution due to tip blunting depending upon the applied force. These obstacles can be overcome by operating in tapping mode (or AC mode). In tapping mode, the tip-sample forces are significantly reduced and thereby lessen sample damage during scanning. In this mode of operation, rather than measuring the static deflection of the tip, the cantilever is oscillating, and a similar laser beam deflection system is used to track the movement of the cantilever. The oscillation of the cantilever amplitude and phase are analyzed. Usually, the amplitude is used as a feedback signal for imaging sample surface. In other words, the amplitude is compared with a set point, and the difference is used to control the tip-sample distance, similar to contact mode. Moreover, the phase of the driver oscillation can be compared to that of cantilever oscillation, and the observed phase shift appears to reflect the various properties of the surface. The phase image is useful in identifying the surface feature that cannot be spotted in the height or amplitude image.

Another advantage of tapping mode is its extensive, linear operating range, which makes the vertical feedback system stable. Hence, tapping mode can be used to track the surface for an extended period during *in situ* crystal growth. This is more imperative during in *situ* zeolite growth studies where long imaging time is required for zeolite crystal growth at a high temperature. As the temperature of the solution is increased from the room temperature to synthesis temperature, it can take many hours to reach the thermal equilibrium resulting in unstable cantilever deflection. Hence, contact mode imaging tends to be unsteady while AC mode is comparatively more stable as the amplitude does not change with a minute change in temperature.

AFM has been used to probe the crystal surface of different materials, including biominerals (e.g. calcite), viruses, and proteins. With the introduction of the liquid cell, it has been extensively used for *in situ* studies of crystal growth. It has also been used to study the effect of modifiers [140], supersaturation, and impurities, among other factors.

AFM has also been to study the zeolite crystal growth; however, the vast majority are *ex situ* studies [129,141-144]. The first study in zeolites was reported by Weisenhorn et al. [145]. Anderson and coworkers have published a series of *ex situ* AFM studies, including analyses of zeolite Y showing evidence of classical layer growth [143]. Subsequent studies from the same group extended to other zeolites, such as silicalite-1 [141], zeolite A [142], and zeolite L [144]. Due to slow growth at room temperature and corrosive solutions, Anderson and coworkers were only able to report *in situ* measurements for limited cases, such as dissolution studies [146] or analyses of metal organic frameworks(MOFs) that grow at near ambient conditions [147]. The general conclusion of these AFM studies is the zeolite mainly grows via a classical pathway, which may be true at later stages of growth when solutions are depleted of precursors and the medium is at low supersaturation.

1.8. Thesis overview

Recently, our group developed a custom AFM solvothermal liquid cell for *in situ* measurements of zeolite growth. This AFM system can be carried out high temperature (30 – 80 °C) and crystal growth can be observed under realistic conditions of zeolite synthesis (including caustic solutions). It was previously observed using this AFM system that silicalite-1 grows via complex pathways involving the addition of both silica molecules and precursors [121]. This thesis expands upon these studies to more closely examine zeolite growth mechanisms over a variety of conditions, such as supersaturation and temperature, and in the presence of organic molecules (OSDAs and ZGMs) for different zeolite frameworks. Chapters 2 and 3 discuss the effect of supersaturation, temperature, and OSDA on the zeolite A crystallization under conditions leading to nonclassical and classical modes of growth, respectively.

One method to mediate zeolite growth is the use of organics as either zeolite growth modifiers or structure-directing agents. Given the multiple pathways of zeolite crystallization, the organics can affect growth by several ways. They can alter the speciation of different precursors (monomers, oligomers, nanoparticles, aggregates); and they can also affect nanoparticle evolution, or provide steric stabilization, that mediates the rate of particle attachment (i.e. nonclassical growth mechanisms). Another potential factor with the application of organics in zeolite synthesis is their chemical stability. In chapter 4, we explore the effect of D-Arginine, a zeolite growth modifier, on silicalite-1 crystallization. It is shown that the modifier decomposes *in situ* with the release of acid. A resulting reduction in solution pH provides a distinctive method to shift the growth from a classical mode by monomer addition to nonclassical growth by nanoparticle attachment.

Synthesis at low temperature is often dominated by nonclassical pathways where organics can mediate the rate of precursor evolution, which can lead to significant differences in precursor-crystal interactions that alter the preferred mode of crystal growth. Chapter 5 summarizes studies of various organics (both OSDAs and ZGMs) on the change in precursor structure and how disorder-to-order transitions can be used to selectively control precursor-crystal interactions in a manner that allows for the dominant mode of crystal growth to be shifted from a nonclassical to classical pathway.

Chapter 2

Transient Modes of Zeolite Surface Growth from 3D Gel-Like Islands to 2D Single Layers

2.1. Motivation

Identifying pathway(s) of crystallization is critical to understanding, and ultimately controlling, the formation of natural[148], synthetic[149], or biological[150] materials. It is increasingly evident that many crystalline materials exhibit nonclassical mechanisms involving the assembly and attachment of precursors that range in complexity from oligomers and liquid-like droplets to amorphous particles and small crystallites[151]. Examples include biominerals [152], metals[153], and metal oxides[154], as well as microporous zeolites that grow from diverse precursors[155] and by complex pathways involving monomer addition[156,157], particle attachment[158-160], and gel-to-crystal transformations[161,162]. Knowledge of zeolite crystallization is derived predominantly from ex situ studies that are insufficient to elucidate mechanism(s) of growth. For this study we focus on LTA (or zeolite A), which is a 3-dimensional small-pore (0.42 nm) zeolite. Conventional synthesis of LTA results in a high aluminum content (Si/Al = 1.0) that is ideal for adsorption and ion exchange[163], whereas high-silica LTA (Si/Al > 10) has garnered interest as a catalyst owing to recent findings[47] that Cu-exchanged LTA possesses unique properties for the selective catalytic reduction of NOx. Hypotheses of LTA crystallization derived from spectroscopy[164,165], microscopy[166,167], and molecular simulations[168,169] postulate diverse pathways that include gel transformations[170], precursor agglomeration and densification[171], and the attachment of composite building units (CBUs)[172,173]. Such broad disparity of pathways underscores the need to reconcile the mode(s) of LTA crystallization over a range of synthesis conditions.

Herein, we use atomic force microscopy (AFM) to track the dynamics of LTA (100) surface growth. The growth media used for this study are the supernatants of a reported synthesis mixture[88] after pre-heating for periodic times to generate a range of supersaturation with respect

to silica. *In situ* AFM measurements at two different temperatures (35 and 45°C) and variable supersaturation reveal multiple modes of growth that range from classical molecule-by-molecule addition to nonclassical pathways that, to our knowledge, have not been previously reported for zeolite crystallization. In this study, we show that time-resolved AFM imaging is able to capture the dynamics of these processes, thereby offering new insight into the mechanisms of LTA growth.

2.2. Result and discussion

2.2.1. Preparation of growth solutions with varying supersaturation

LTA crystals are prepared with Na^+ ions as inorganic structure-directing agents to facilitate the formation of a cubic lattice with tetrahedral sites that are occupied by Si and Al atoms supplied from colloidal silica and sodium aluminate, respectively. Growth solutions are comprised of amorphous precursors containing undissolved silica surrounded by a shell of alumina[174]. X-ray diffraction (**Figure 2.1A**) reveals the onset of nucleation within 3 h of heating at 65°C and the near completion of crystallization (**Figure 2.1B**) after approximately 4 h. Extraction and analysis of the supernatant after periodic heating times confirms that supersaturated solutions (**Figure 2.1C** and **Table A1**) have sufficient nutrient for the nucleation and growth of cubic LTA crystals (**Figure 2.2B** and **Figure A1**). Elemental analysis of the supernatant reveals a monotonic decrease in silicon concentration within the first 4 h of heating, followed by a gradual decrease to the equilibrium value after 24 h (solution S24 in **Figure 2.1C**).

Solutions S2 to S4 in **Figure 2.1C** are used as growth solutions for *in situ* measurements. A combination of small-angle X-ray scattering (**Figure 2.2A** and **Figure A2**) and dynamic light scattering show no trace of particulates in the supernatant, suggesting these clear solutions (**Figure A3**) are predominantly comprised of soluble monomers and/or small oligomers. Prior studies have shown that (alumino)silicate particles or sol gels in LTA growth solutions are sites for heterogeneous nucleation[170], while homogeneous nucleation has been observed in solutions

devoid of amorphous precursors[175]. The clear solutions used in this study differ from those of other zeolites, such as silicalite-1, which are predominantly suspensions of nanoparticles (1 – 6 nm)[176-178] that attach to crystal surfaces and undergo structural rearrangement to incorporate into the underlying crystal lattice[156]. As we report here, LTA crystallization occurs by an alternative mechanism.

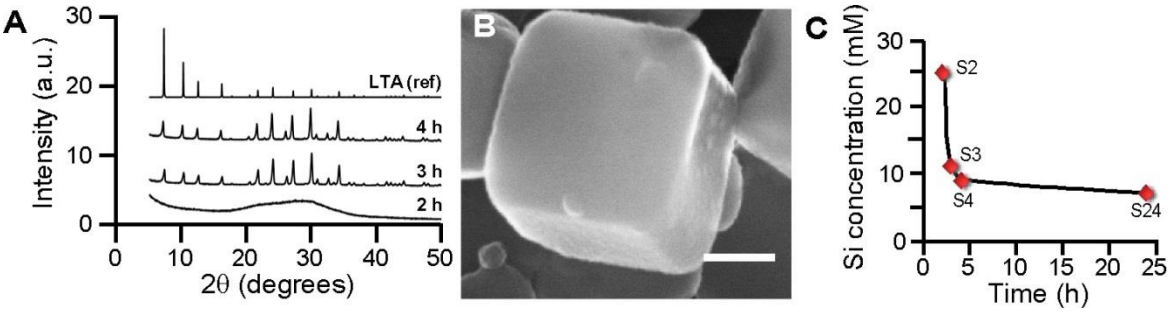

Figure 2.1: A. XRD patterns obtained after heating growth solutions at 65°C for various times. **B**. Electron micrograph of a LTA crystal after heating for 4 h. **C.** Silicon concentration in solution obtained at various times. All scale bars equal 200 nm

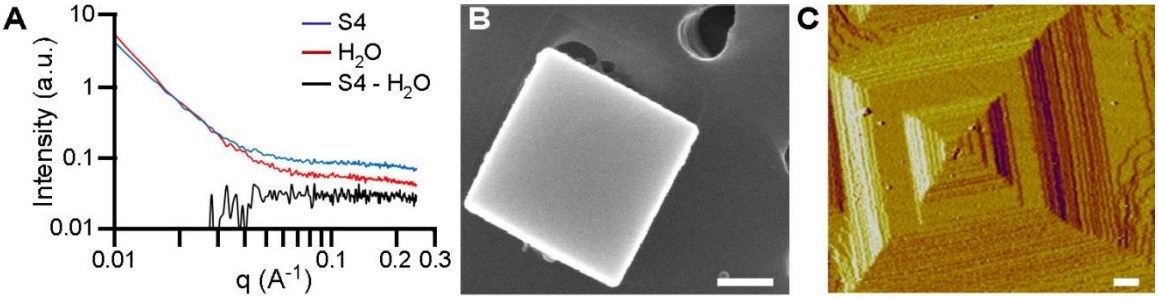

Figure 2.2: A. SAXS patterns of supernatant S4 and the background (water). **B.** Electron micrograph of a crystal prepared by heating supernatant S4 for 24 h at 45°C. **C.** AFM image of a LTA crystal surface. All scale bars equal 200 nm

2.2.2. AFM measurements at low temperature

Crystal substrates prepared for AFM (**Figure A4**) are laden with hillocks (**Figure 2.2C** and **Figure A4**) consisting of layers with step heights equal to the unit cell (**Figure A5**). The topography of LTA surfaces is similar to other zeolites extracted from their growth solutions at equilibrium (i.e., solubility). The appearance of unfinished layers suggests that growth occurs by layer advancement from the addition of monomers (or possibly small oligomers). Upon introduction of a highly supersaturated solution (S2) to an AFM liquid cell at room temperature,

there is no apparent change in surface topography. Once the cell is heated at 35°C, we observe the formation of islands (**Figure 2.3A**) that render faceted hillocks rough and individual layers less defined with time. Continuous imaging in tapping mode leads to a smoothening of crystal surfaces (**Figure 2.3B** and **Figure A6**) owing to the temporal reduction in island height (**Figure 2.3C).** An enlarged image (**Figure 2.3D**) clearly shows a *smooth* region (I in **Figure 2.3D**) corresponding to an original scanning area and the surrounding *rough* region (II in **Figure 2.3D**) outside of the previously imaged area. The rough region has a much broader distribution of surface feature heights than the former (**Figure 2.4A** and **Figure A7**).

Elemental analysis (**Table A2**) reveals that the amorphous islands contain more aluminum (Si/Al = 0.7). *Ex situ* studies of LTA crystal seeds grown in a S2 solution reveal a shift with increased heating time to the expected composition of LTA crystal surfaces (Si/Al = 1.1, **Table A2**) along with the reemergence of hillocks comprised of roughened steps (**Figure A8**). This suggests that growth occurs within the gel in close proximity to the crystal surface, thereby creating a growth front that advances normal to the gel-crystal interface. It is difficult to measure the rate of layer advancement by AFM owing to the absence of a constant baseline to accurately measure changes in height; however, bulk crystallization at 35°C confirms that LTA nucleates and grows into fully crystalline cubes under conditions that mimic the AFM liquid cell (**Figure A8**).

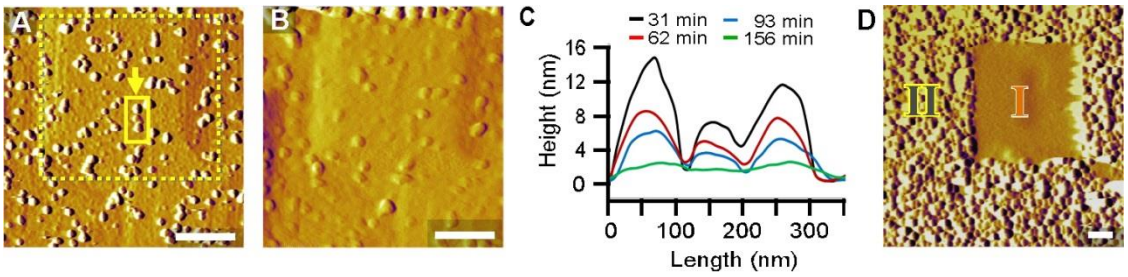

Figure 2.3: A and **B**. AFM images of a crystal surface at 35°C:**(A)** 30 min after reaching temperature and **(B)** after 3 h of imaging. (**C)** Time-resolved height profiles of the region. **(D)** Enlarged scan area showing (I) a *smooth* and (II) the *rough* region.

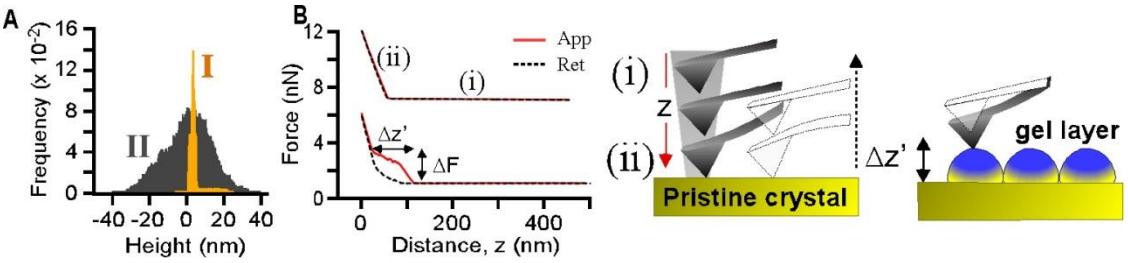

Figure 2.4: (A) Statistical analysis of feature heights in regions I and II . **(B)** CFM approach-retract curves as a function of distance *z* from substrates. Schematics depict an AFM tip far from the surface (i) and in contact with the surface (ii).

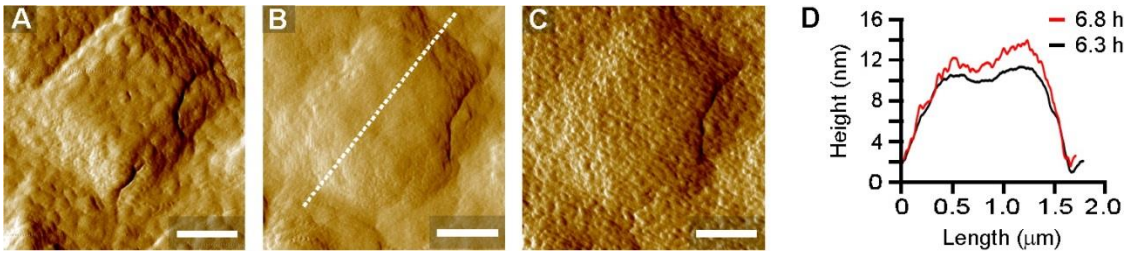

Figure 2.5:(A) 30 min after reaching the set point, **(B)** after 6.3 h of imaging, and **(C)** the same area after removing the AFM tip for 30 min and reimaging. **(D)**. Height profiles along the dashed line in image **B** for times 6.3 and 6.8 h Scale bars equal 500 nm

A reduction of island height with AFM tip rastering implies the removal of loosely-bound material from the crystal surface, which we attribute to a unique gel-like quality of the islands. Additional evidence is gleaned from chemical force microscopy (CFM) using a non-functionalized cantilever in S2 growth solution. CFM measurements prior to and after heating examine AFM tip interactions with pristine (crystalline) and gel layers, respectively (**Figure A9**). The approach curve for pristine surfaces is typical of most hard substrates, whereas the nonlinear profile on the gel layer (**Figure 2.4B**) is similar to those produced by elastic substrates (e.g., lipids)[179,180]. Nonlinear approach curves (**Figure A9E**) have an average breakpoint force ΔF of 1.8 ± 0.6 nN and an approach distance $\Delta z'$ of 52 ± 26 nm (**Figure A10**) that is commensurate with the height of surface features in AFM images (**Figure 2.4A**). Moreover, analysis of the retraction curves reveals a higher tip-substrate adhesion force on rough surfaces (**Figure A9F**) and a hysteresis of approach-retraction curves, consistent with an elastic response of gel layers. To our knowledge, this is the first observation of nonclassical crystal growth involving

molecularly-dispersed solute forming gel-like islands on crystal surfaces. The presence of gel-like islands are prevalent on LTA surfaces at 35°C. This is true even at reduced supersaturation (S3) where AFM tip-induced smoothening of crystal surfaces is observed (**Figure 2.5, A and B**, **Figure A11**). The latter is confirmed by removing the AFM tip from an area after continuous scanning and reengaging after a period of time (**Figure 2.5C**) to show the recovery to a roughened crystal interface (**Figure 2.5C** and **Figure A12**). One notable difference between gel-like islands formed from solutions of low (**Figure 2.5D**) and high (**Figure 2.4A**) supersaturation is larger feature sizes at the latter condition.

2.2.3. AFM measurements at higher temperature

AFM measurements at higher temperature (45°C) reveal crystal surfaces (**Figure 2.6A**) covered with smaller islands (ca. 6 nm, **Figure A13**). At these conditions, the temporal smoothening of surface features (**Figure 2.6, B – D**) is attributed to layer spreading. Indeed, there is a negligible difference in the topography of a continuously-imaged area (dashed box in **Figure 2.7A** and **Figure A14**) and its surrounding area, which suggests the islands are less gel-like at higher temperature, potentially due to the faster rate of crystallization. The image in **Figure 2.7A** shows a bimodal distribution of surface feature size owing to the presence of large islands (arrow in **Figure 2.7A**). Video 2 captures the generation of a large island, which occurs by the deposition of a particle from solution. These particles appear to be crystalline, suggesting their addition to the crystal surface involves (nearly) oriented attachment, similar to processes reported for iron oxide minerals [181]. Evidence of particle crystallinity is gathered from time-resolved AFM images that reveal the immediate growth of deposits with visible facets (**Figure 2.7, B and C**). Our findings indicate that the residence time of the growth solution in the AFM liquid cell (5 h) is sufficient for nucleation of nanocrystals. Reduced temperature increases the nucleation time well beyond the average liquid residence time in the AFM cell (**Figure A1**), which can explain why (nearly) oriented attachment is not observed during AFM measurements at 35°C.

AFM measurements at high temperature and low supersaturation (S4) reveal a different mode of growth: 2-dimensional (2D) layer nucleation and spreading. This mechanism is common in classical crystallization, but has never been observed *in situ* for zeolites. Other groups have inferred this mode of growth using *ex situ* microscopy images [142,182] of LTA surfaces removed from saturated solutions and from *in situ* dissolution studies [183] in undersaturated media; however, such approaches are incapable of fully resolving the mechanisms of layer nucleation and spreading. On the contrary, we report time-resolved images in **Figure 2.8** that were taken from Video 4 showing the dynamics of 2D growth. In these images, the original hillock is still discernable during growth, though the terraces are covered with newly generated layers as the steps advance across the surface (**Figure A15**). White arrows in high resolution images (**Figure 2.8A**, regions a1 to a3) depict steps that advance across the surface whereas yellow arrows indicate the generation of 2D nuclei.

Quantitative analysis of features over multiple crystal surfaces shows two distinct populations with average heights of 0.5 and 0.9 nm (**Figure 2.8B**). The exact molecular structure of these features cannot be established from AFM; however, it is interesting to point out that their heights are comparable to the sizes of double-4-member ring (*d4R*) and sodalite (*sod*) composite building units depicted in **Figure 2.8C**. Park et al.[184] proposed that high silica LTA crystallization occurs by the formation of *sod* cages around *lta* cages. Other groups have placed more emphasis on the role of *d4R* units in LTA crystallization[172,173]. Studies of LTA surface terminations by transmission electron microscopy[185] and energy minimization models[186] suggest the possibility of both CBUs as well as other configurations. It remains to be determined from our AFM data if layer generation occurs by the direct addition of CBUs or their concerted formation at the crystal interface via the assembly of molecular species.

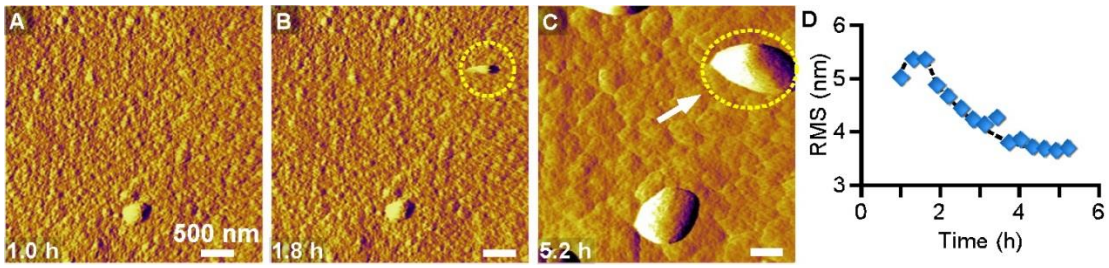

Figure 2.6:(A – C) Time-resolved AFM images showing the deposition of a particle from solution to the crystal surface **(D)**. Temporal change in the root mean square (RMS) roughness

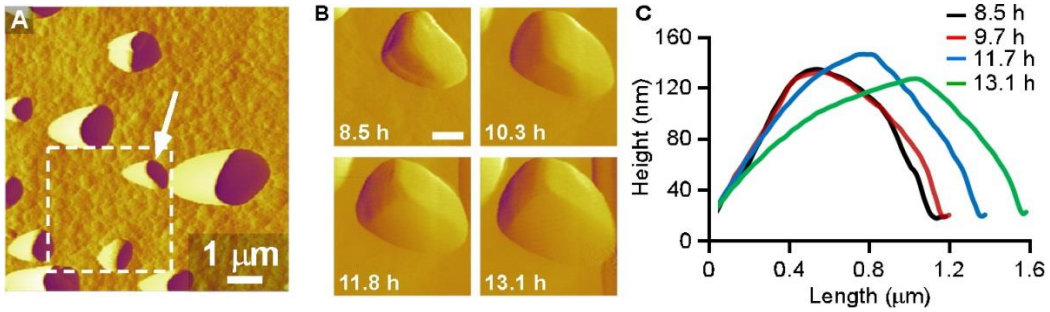

Figure 2.7:(A) Enlarged scan area that encompasses a region (dashed box) that was continuously imaged **(B)** Snapshots showing the growth of a island. **(C)** Graph showing the variation in height and length of a deposit with time. Scale bar equals 500 nm.

The comparison of newly formed nuclei and fully developed layers reveals that the latter have a much narrower distribution of step height (**Figure 2.8B**) with an average size of 1.2 nm, equal to the *lta* cage. As supersaturation is increased at high temperature, we observe a transition to a roughened interface (**Figure 2.9, A and B**) that grows by a mode resembling kinetic roughening in classical theories[187,188]. The micrograph in **Figure 2.9A** captures two neighboring hillocks that merge with increased imaging time as a result of in-plane layer advancement (**Figure 2.9C**). Analysis of out-of-plane growth is challenging due to the changing baseline. Indeed, the merging of adjacent hillocks gives the false appearance of decreasing height owing to the reduced interstitial region separating the hillocks.

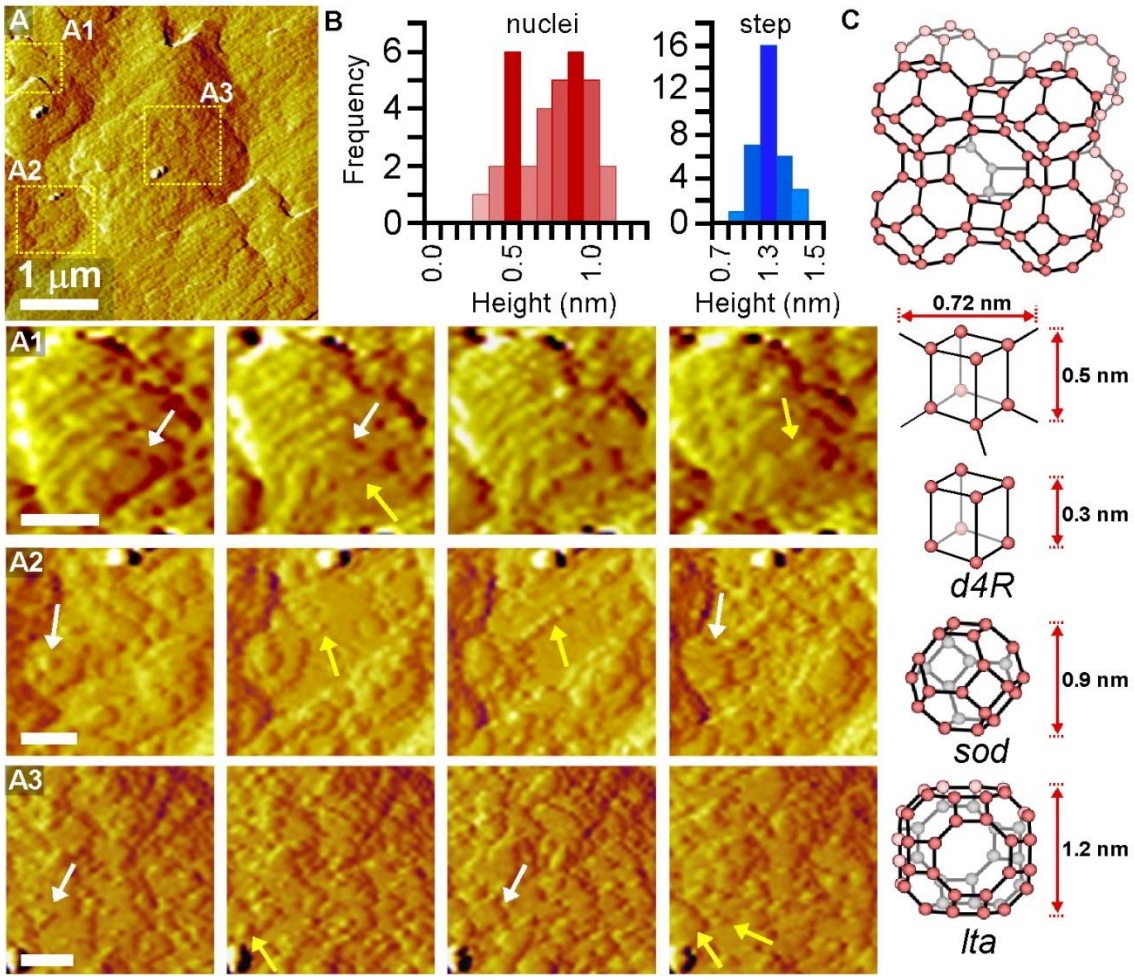

Figure 2.8:(A) AFM image of a crystal surface in solution S4. Time-elapsed images in areas A1-A3 (imaging time = 30 min). **(B)** Statistical analysis of nuclei and step heights **(C)**. LTA framework and CBUs. Scale bars equal 200 nm unless otherwise labelled.

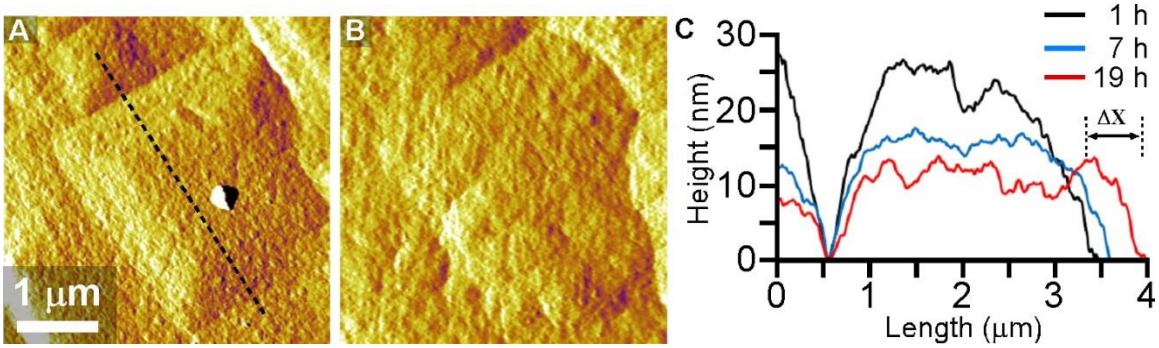

Figure 2.9:(A) and **(B)**. Time-resolved AFM images of a crystal surface growing in solution S3 **(A)** 1 h and **(B)** after 19 h of growth. **(C)** Temporal changes in the height profile along the dashed line in image A. Scale bars equal 200 nm unless otherwise labelled.

2.2.4. Diverse modes of LTA crystallization

Figure 2.10 depicts various pathways of LTA crystallization. Monomer-by-monomer addition is a classical pathway that falls within one of three modes of growth that depend upon supersaturation (**Figure A17**): spiral, layer-by-layer, and roughened growth[189]. Low supersaturation (near equilibrium) is reached at the end of zeolite synthesis where *ex situ* AFM images of zeolite surfaces are comprised of hillocks. Sacco and coworkers[167] previously showed the presence of spiral dislocations on the upper terrace of hillocks. Higher supersaturation results in layer-by-layer growth, which is marked by 2D generation and spreading of layers via the addition of monomers and/or oligomers. At high supersaturation, classical theories posit rough growth as a result of low energetic barriers for nucleation whereby solute can bind at all possible sites, allowing for the rapid formation of nuclei with critical sizes less than those required for layered growth. This phenomenon, commonly referred to as kinetic roughening, is observed for LTA growth at high temperature; however, the roughness observed at low temperature derives from a new type of surface feature that has not previously been reported. Notably, the formation of gel-like islands from molecularly-dispersed solute constitutes a unique mode of growth among reported cases of nonclassical crystallization. Measurements of LTA crystallization also reveal the first direct observation of zeolite growth by the (nearly) oriented attachment of crystals, which is an established nonclassical pathway in the formation of other types of minerals[151].

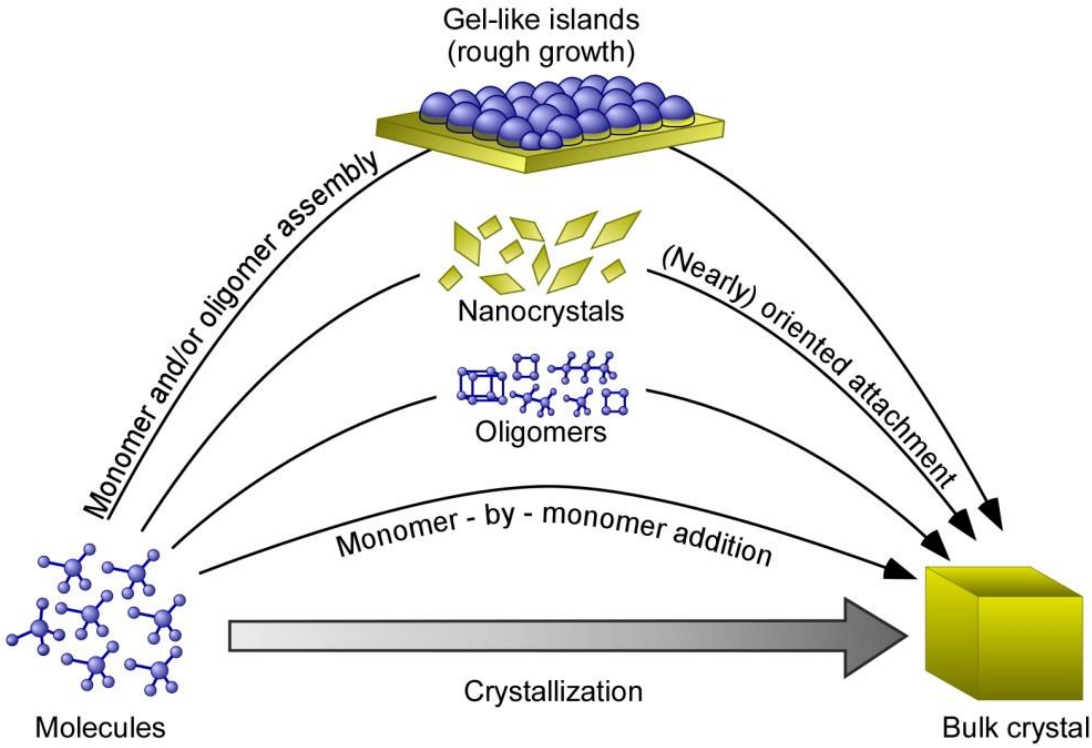

Figure 2.10: Illustrative renderings of crystal growth mechanisms for classical and nonclassical pathways.

These findings offer new insight into the complex processes of sol gel chemistry that are integral to zeolite formation and that are potentially applicable to other minerals that crystallize via similar routes. Elucidating the mechanism(s) of zeolite crystallization is challenging owing to the multitude of species that serve as putative growth units, as well as the lack of *in situ* techniques that are capable of resolving growth processes at sufficient spatiotemporal resolution. To this end, solvothermal AFM is a suitable tool for capturing time-resolved events of surface growth. Beyond identifying the modes of LTA growth, we have used these observations to establish that the choice of synthesis conditions governs distinct regimes of zeolite growth, and therefore, can be integral to rational design. Moreover, our findings reconcile disparate hypotheses of LTA growth wherein gel-to-crystal transitions have for many years been assumed to play a key role in zeolite crystallization. Given that the conditions selected for this study are

similar to a wide range of zeolite framework types, the pathways of crystal growth for LTA may prove to be representative of other related materials.

2.3. Material and methods

2.3.1. Chemicals for zeolite synthesis and growth experiments

The following chemicals were used as reagents: sodium hydroxide (98% pellets, MACRON Fine Chemicals), sodium aluminate ($Al_2O_3 \cdot Na_2O$ or $NaAlO_2$, 54.41% Al_2O_3 and 41.02% Na_2O, Alfa Aesar), Ludox AS-40 (40%, Sigma Aldrich), tetraethylorthosilicate (TEOS, 98%, Sigma Aldrich, St. Louis, MO), and triethanolamine (TEA, 100%, J.T. Baker). Deionized (DI) water was prepared using an Aqua Solutions RODI-C-12A purification system (18.2 MΩ). All reagents were used as received without further purification.

2.3.2. Synthesis of zeolite substrates for scanning probe microscopy

Cubic crystals of zeolite LTA were synthesized using a previously reported protocol [166]. The growth solution was prepared by mixing the required quantity of all components to yield a solution with molar composition 1.23 SiO_2: 1 Al_2O_3: 2.71 Na_2O: 5.5 TEA: 288 H_2O. To obtain a 15 g mixture of the growth solution, 0.28 g of NaOH was added to 11.80 g of DI water and mixed in a polypropylene (PP) container. Thereafter, 0.43 g of sodium aluminate was added to this mixture and stirred for 30 min to obtain a clear solution, followed by the addition of 1.89 g of TEA. To this mixture was added 0.60 g of TEOS. The solution was then aged at room temperature for 4 h while stirring. The PP container was heated in a Thermo-Fisher Precision Premium 3050 Series gravity oven at 85°C for 11 days and was quenched to room temperature. The precipitate was isolated using a 0.45 μm GHP filter (Pall Corporation) and washed multiple times with DI water.

2.3.3. Preparation of zeolite growth solutions

The growth solution for *in situ* atomic force microscopy (AFM) experiments was prepared from a 60 g mixture with molar composition 1 SiO_2: 0.87 Al_2O_3: 11.2 NaOH: 190.6 H_2O. In a PP container, 5.47 g of NaOH was added to 49.86 g of degassed DI water. Thereafter, 2.44 g of sodium aluminate was added and the resulting mixture was stirred for 30 min. To this solution was added 2.24 g of Ludox AS-40 and the mixture was left aging at room temperature for 24 h while stirring. The growth solution was heated in a Thermo-Fisher Precision Premium 3050 Series gravity oven at 65°C for various times and quenched in an ice bath. The precipitate was removed after centrifuging the solution at 13,000 rpm for 45 min in a Beckman Coulter Avanti J-E instrument. The supernatant was decanted and filtered twice, using a 25mm syringe filter fitted with a 0.45μm nylon membrane (VWR international). The resulting clear supernatant was used as a growth solution for *in situ* AFM measurements. The solutions (labelled in **Fig. 2.1c**) are referred to as S1, S2, S3, etc., where "S" refers to supernatant and the number represents the total hours of pre-heating at 65°C.

2.3.4. *In situ* atomic force microscopy

All AFM measurements were performed on an Asylum Research MFP-3D-SA instrument (Santa Barbara, CA) equipped with a custom-designed liquid sample cell for imaging under solvothermal conditions. A detailed description of the liquid cell is provided in a previous publication[156]. Cubic LTA crystals prepared as substrates for AFM were firmly placed on a 15-mm specimen disk (Ted Pella, Inc.) using quickset Loctite epoxy (Henkel Corporation) that was cured in an oven at 60°C for 1 h. The sample was then removed from the oven and cooled to room temperature in air. The sample was rinsed with DI water to remove loosely-bound crystals, and dried under inert Ar gas to remove dust. The sample was then placed in a closed AFM liquid cell (total volume ≈ 3 ml). AFM images were collected using a Cr/Au-coated silicon nitride cantilever (Olympus RC800PB) with a spring constant of 0.82 N m^{-1}. The LTA crystal substrate

was first scanned in air to locate a desired imaging area. The growth solution was then introduced into the AFM cell by a syringe and the sample was left to equilibrate with the solution at room temperature for ca. 30 min. The temperature was then ramped to a pre-determined set point at a rate of 1°C min^{-1}. Growth solution was continuously supplied to the liquid cell using a syringe pump (Razel Scientific Instruments, Model R100-E) at a rate of 0.9 cm^3 h^{-1}. Once the sample cell reached the set point temperature, the liquid flow rate was reduced to 0.6 cm^3 h^{-1}, which equates to an average residence time of 5 h. The sample cell was allowed to equilibrate for 0.5 to 1 h before imaging. AFM images were collected in tapping mode (to minimize tip-substrate contact) at a scan rate of 1.2 Hz and 256 lines per scan. Select areas were periodically imaged in contact mode when it was necessary to resolve large surface features.

2.3.5. Chemical force microscopy

CFM has proven to be a useful technique for measuring the unbinding force between AFM tips and sample interfaces [179,190]. AFM tips can be functionalized with an array of chemical moieties [191,192] or larger macromolecules (e.g., DNA or proteins) [193-199]. The information gleaned from these studies ranges from thermodynamics of tip-substrate bond breakage [200-204] to the dynamics of unraveling segments of macromolecules [198,205]. Recently, CFM has been used to investigate elastic substrates, such as lipids, surfactants, and thin films [180,206-210]. These studies have shown that the elastic-like character of substrates can yield nonlinear approach-retraction curves. We used the MFP-3D-SA instrument to measure the unbinding force between an AFM tip and LTA crystal surfaces. All measurements were carried out using a non-functionalized Cr-Au-coated silicon nitride cantilever (Olympus RC800PB) with a spring constant of 0.15 N m^{-1}. The cantilever was calibrated in air to determine the spring constant using an algorithm provided by the vendor. Growth solution S2 was introduced into the AFM liquid cell and was allowed to equilibrate for 2 h at room temperature. We first imaged as-synthesized LTA crystal surfaces in contact mode to locate regions for CFM measurements. Force curves at room temperature

correspond to pristine surfaces (see Supplementary Fig. 9). We selected a tip speed of 1 μm s^{-1} and trigger points of 2, 5 and 10 nN. A dwell time of 1 s was used for all measurements to promote tip-substrate interactions (note that the dwell time refers to a period when the tip is held in direct contact with the surface after engaging). We analyzed surface areas of 4 x 4 μm^2 to gather more than 250 data points for statistical analysis. After measuring pristine surfaces, the temperature was ramped to 35°C at a rate of 1°C min^{-1} while maintaining constant flow of growth solution at 0.9 cm^3 h^{-1}. Once reaching the set point, the flow of growth solution was reduced to 0.6 cm^3 h^{-1} and the system was equilibrated for 30 min. LTA crystal substrates were allowed to grow for an additional 4 h. The surface was imaged to confirm the presence of gel-like islands (i.e., rough surfaces). The temperature was then ramped down to room temperature and the AFM sample holder was removed and washed with DI water. The sample was again placed in the liquid cell with a new cantilever that was calibrated in air. Fresh growth solution (S2) was introduced into the liquid cell. After 2-h equilibration at room temperature, CFM measurements were performed as described above (see **Figure A9**).

2.3.6. Small-angle x-ray scattering (SAXS)

SAXS measurements were performed to check for the presence of (alumino)silicate nanoparticle precursors in the supernatant growth solutions used for *in situ* AFM studies. Clear growth solutions, prepared using the aforementioned protocol, were injected into a clean sample holder (1.5 mm quartz capillary cell). Scattering patterns were collected under vacuum at 25°C for 30 min using a Rigaku S-MAX3000 instrument (CuKα radiation λ = 1.54 Å; q = 0.008 – 0.24 $Å^{-1}$). Calibrations of the scattering vector *q* and beam center were performed on raw data using the SAXS gui software provided by Rigaku and a reference pattern from a AgBeh standard that was collected for 500 sec. A background (DI water) was subtracted from each sample. Normalized SAXS patterns were compared to those reported in previous studies of silicalite-1 precursors [126,159,160,211,212] to check for the presence of nanoparticles in LTA growth solutions.

2.3.7. Dynamic light scattering (DLS)

DLS was performed on a Brookhaven Instruments BI-200SM machine equipped with a TurboCorr Digital Correlator, a red HeNe laser diode (35 mW and 637 nm), and a decalin vat fitted with a filter to remove dust. Supernatant solutions (described previously) were used for particle size measurements. At least three measurements were performed per sample using a scattering angle of 90°. Autocorrelation functions were collected over 2 min and the data was evaluated using the method of cumulants to extract particle size assuming a refractive index of pure water and a viscosity that was measured using a calibrated CUC-25 Cannon Ubbelohde Viscometer (9721-K50, kinematic viscosity range 0.4−2.0 mm^2s^{-1}). In order to perform *in situ* DLS measurements, clear growth solutions were transferred to 20 ml disposable scintillation vials that were placed inside the decalin vat. Measurements were first taken at a temperature of 25°C, which was maintained using a Polyscience digital temperature controller. Thereafter, the temperature was ramped to 45°C at the rate of 1 °C min^{-1}. After reaching the set point temperature, measurements were taken periodically to track the average particle size. Time-elapsed measurements of growth solutions S1 and S2 are shown in **Figure A1**. Counts were too low for measurements of S3 and S4 growth solutions (even after 24 h of heating).

2.3.8. Scanning electron microscopy (SEM)

Scanning electron micrographs were obtained with a FEI 235 dual-beam (focused ion-beam) system operated at 15 kV and a 5 mm working distance. All SEM samples were coated with a thin carbon layer (ca. 20 nm) prior to imaging.

2.3.9. Energy-dispersive x-ray spectroscopy (EDX)

EDX analysis was performed using a JEOL JSM 6330F field emission SEM operated at 12 kV and 15 mm working distance.

2.3.10. X-ray photoelectron spectroscopy (XPS)

XPS spectra were collected from a Physical Electronics Model 5700 XPS instrument. A monochromatic $Al_{K\alpha}$ X-ray source (1486.6 eV) was used with the power at 350 W. All spectra were obtained once reaching a vacuum of 5×10^{-9} torr or better.

2.3.11. Powder x-ray diffraction (XRD)

Powder XRD patterns of as-synthesized zeolite samples were collected on a Siemens D5000 X-ray diffractometer using a Cu Kα source (40 kV, 30 mA). The LTA framework was confirmed using a reference pattern provided by the International Zeolite Association Structure Database [213].

Chapter 3

Multiple Pathways of Zeolite A Crystallization by Monomer Addition

3.1. Motivation

The demand for zeolite materials with preferred physicochemical properties has stimulated studies of zeolite growth mechanism to enable rational design of zeolite. Despite tremendous effort to elucidate the mechanisms of nucleation and crystal growth, these pathways in zeolite synthesis are not well understood due to inherent complexity of zeolite crystallization. Zeolite crystals are known to grow via complex pathways which can be classified as either classical pathway by monomer addition or nonclassical pathways by particle attachment wherein precursors range from oligomers to nanoparticles and amorphous phases. There is growing evidence that zeolite grows predominantly via nonclassical pathway by particle attachment. In a prior study, we used *in situ* atomic force microscopy (AFM) to show that silicalite-1 grows by a complex growth pathway involving the attachment of particles to crystal surfaces, as well as monomer addition[121]. Similarly, it has been previously discussed in Chapter 2 that zeolite A can also grow via nonclassical pathways. Furthermore, nonclassical growth by precursors attachment has been suggested for several framework types, such LTL [122], MFI [123], and CHA [124]. In many cases, it is postulated that growth occurs through the attachment of soluble small precursors that range from (alumino) silicate monomers/oligomers to composite building units (CBUs). On the other hand, zeolite crystallization towards the end of crystallization often involves classical growth via 2D nucleation and layer growth. Anderson and co-workers provided evidence of layer growth for faujasite (FAU) and other zeolites from *ex situ* AFM studies[141-144]. The classical growth by monomer addition can be exploited to tailor the crystal properties such as to reduce mass transport limitations in MFI zeolite[214]. Hence, the understanding of classical growth mechanism is central to the rational design of zeolite crystal.

Classical crystal growth via layer by layer mechanism typically involves 2-dimensional (2D) nucleation of new layers and their subsequent growth by the attachment of solutes to the advancing steps[99]. The new layer may grow or dissolve depending upon their radius **(Figure 3.1A)**, and the limit of which is defined as the critical radius (R_{crit}). The increase in supersaturation results in the reduction in the critical radius (R_{crit}). On the other hand, as supersaturation decreases, the size of critical radius becomes large, and consequently, further nucleation ceases. Under these conditions, crystallization can occurs via spiral growth which results in the formation of growth hillocks.. Similar to R_{crit}, there exists a critical length for spiral growth. The small segment of spiral below the critical length does not advances **(Figure 3.1B)**. When segment is greater than the critical length (L_{crit}), it advances. Similar to critical radius, L_{crit} reduces with the increase in supersaturation. At very high supersaturation, R_{crit} is less than the size of the growth units where a single solute ion or molecule may serve as a nucleus leading to rough crystal surface. Depending on the degree of supersaturation, classical growth can occur via spiral growth, 2D nucleation, or kinetic rough growth.

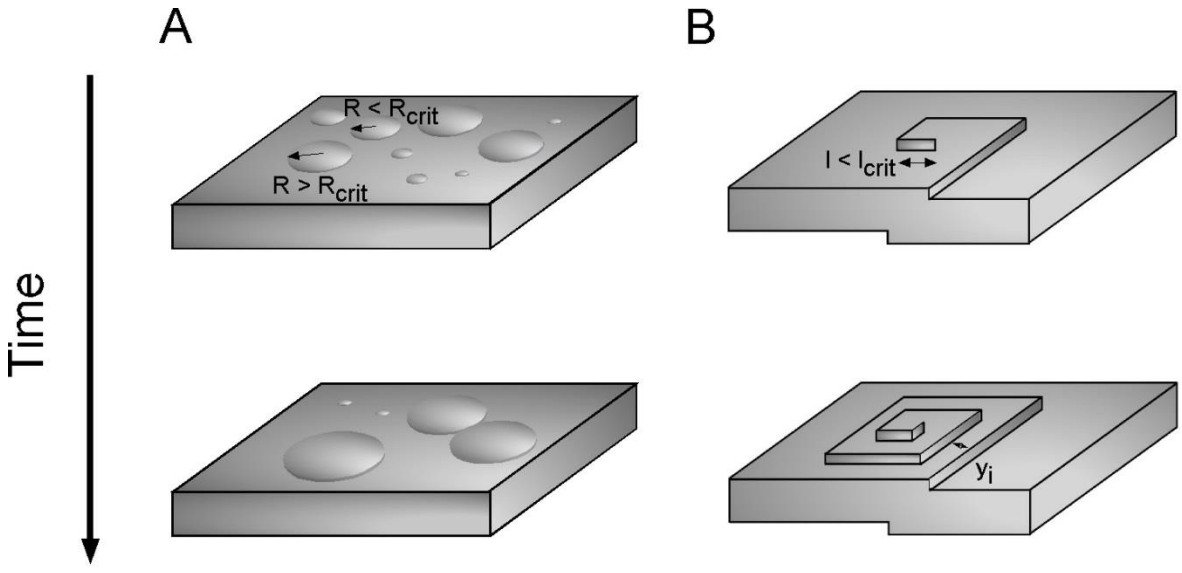

Figure 3.1: **(A)** Illustration of the critical radius of 2D nucleation. (B) Illustration of the critical length of spiral growth. (top scheme) the smallest step is below the critical length and is not moving. In (bottom) it has exceeded the critical length and begun to move

Given widespread commercial application of zeolite A and its rapid crystallization at low temperature, we have selected zeolite A as a model system to investigate the classical growth mechanism. Zeolite A was one of the first zeolite to synthesized and used commercially and has been extensively studied by various groups using a variety of techniques. One of the pioneering studies of zeolite A growth is by Mintova and coworkers, in which experiments were conducted at room temperature by means of high resolution transmission electron microscopy (HRTEM). [135] Their HRTEM study revealed that the nucleation occurs inside the amorphous gel-like aggregates, with each amorphous aggregates containing one nucleus which grew with the consumption of amorphous precursors. Studies by various other groups have postulated that zeolite A crystallizes via the attachment of composite building units (CBUs). For instance, Park et al. proposed that the high silica LTA growth occurs via the formation of *sod(sodalite)* cages around *lta* cages while other groups have suggested that D4R(double 4 rings) plays a role in the LTA growth[114,215]. And, the studies of zeolite A surface by transmission electron microscopy (TEM) indicate the terminal structure of zeolite A surface to be incomplete *sod* cages[185]. Furthermore, *ex-situ* AFM has also been extensively used to study zeolite A surface at nanoscale [142,146]. These studies indicated growth via classical growth via 2D nucleation and step propagation with a step height ~ 1.2 nm (i.e half unit cell). Sugiyama et al. observed step of 0.5 and 0.7 nm in addition to 1.2 nm steps , suggesting that D4R is a growth unit of zeolie A crystallization[216]. Along the same line, Anderson and coworkers have carried out extensive study of zeolite A surface using AFM and concluded that that D4R is the most stable surface termination[146]. In addition, Sacco and coworkers observed growth spirals and pyramids with the protrusions on the zeolite A surface in their study[217]. They postulated these protrusions are either a foreign particle or twin crystal at the apex of hillock, which promotes layer nucleation via twin-plane re-entrant corner mechanism. Most of these investigations were carried out *ex-situ* where crystal surface is analyzed after growth under ambient conditions. In our previous chapter, we carried out the *in*

situ zeolite A studies over a range of synthesis conditions and showed zeolite A grow via diverse pathway including 2D nucleation and layer propagation at low supersaturation.

In this chapter, we carry out in *situ* AFM measurements of zeolite A surface growth at low supersaturation to unravel the different modes of classical layer growth, and the specific role of surface protrusions in the formation of hillocks. Experiments are performed in the presence of an inorganic structure-directing agent, Na^+, as well as the commonly used OSDA for LTA crystallization, tetramethylammonium (TMA). The slow growth rate at low supersaturation allows us to carry out a detailed analysis of various growth dynamics occurring during the classical growth of zeolites. To this end, our findings are instrumental in deciphering the mechanism of zeolite growth by layer propagation.

3.2. Result and discussion

Here we used *in situ* AFM to monitor the growth of zeolite A <100> surfaces at 50 °C. Measurements of as made crystal substrates reveal the presence of two types of growth hillocks: (i) layers advancing from screw dislocations (**Figure 3.2B**) and (ii) layers emanating from protrusions at the apex of the hillock (**Figure 3.2C**). During *in situ* growth measurements we also observed the generation of 2D layers (**Figure 3.2D**) that are not evident on the surfaces of as made crystals, which is consistent with classical theories predicting growth by spiral dislocations at low supersaturation (i.e. during the final stage of zeolite synthesis prior to the extraction of crystals from the mother liquor). Growth solutions for AFM studies were prepared according to a previously reported method in chapter 2 wherein mixtures containing (alumino)silicate colloidal precursors and soluble species were heated for a period of time before extracting the supernatant by centrifugation and filtration. The resulting clear solutions contain no evidence of residual particulates, as confirmed by dynamic light scattering and small-angle X-ray scattering. Analysis of solutions by ^{27}Al NMR indicates only a single species, $Al(OH)_4^-$ monomer, without any detectable aluminosilicate oligomers.

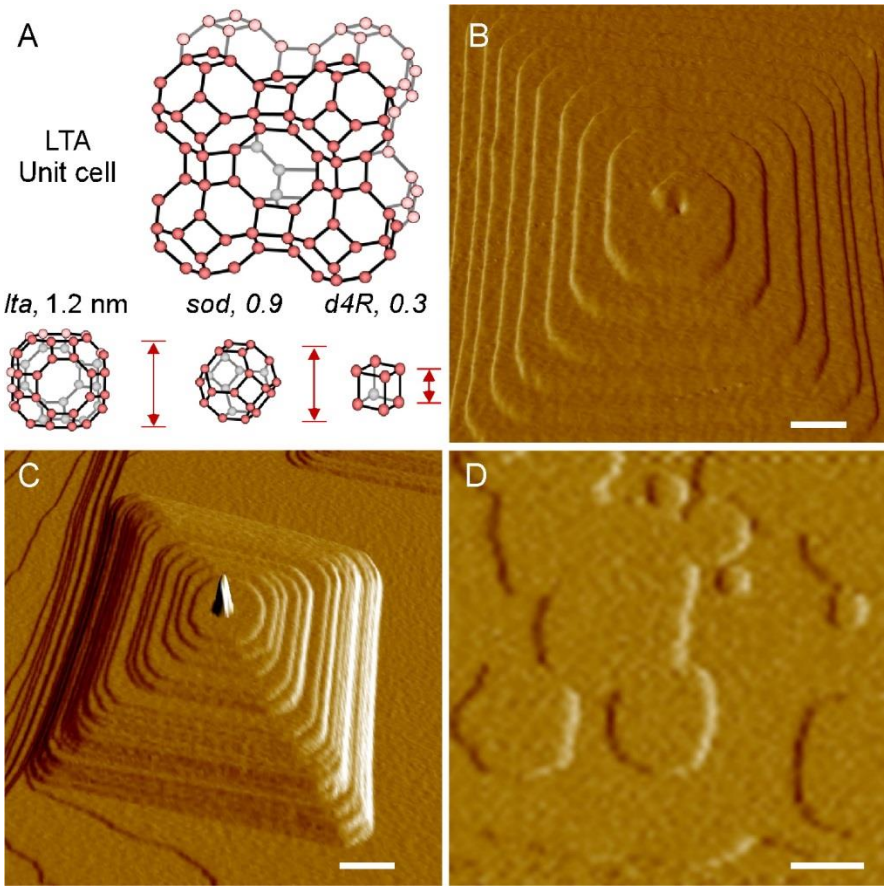

Figure 3.2: (A) Schematics of CBUs and LTA unit cell dimensions. AFM images reveal three types of layers on the crystal surface: **(B)** Hillocks formed by spiral growth; **(C)** Hillocks with a protrusion at their apex; and **(D)** 2-D layers that advance and merge.

We first focus on 2D generation and spreading, which was observed at a supersaturation of 0.6. This value was calculated from elemental analysis of the Si and Al molar compositions in growth solutions and the supernatant of a fully crystalline LTA synthesis mixture (**Table B1**). The latter is taken to be the approximate solubility of zeolite A at the particular temperature and pH of the growth conditions used in this study. It is uncommon to find supersaturation reported in studies of zeolite crystallization owing to the presence of multiple species (e.g., oligomers, gels, and colloidal particles); however, the solutions used in this study are predominantly comprised of monomers. It is important to emphasize that the reported supersaturations are considered to be approximate given that trace quantities of particulates or oligomers, below the threshold of

detection, may be present in these solutions. Assuming only the presence of monomeric species, the supersaturation (σ) was calculated using the following formula as

$$\sigma = \frac{[\mathrm{Al}][\mathrm{Si}]}{\mathrm{K_{sp}}} - 1. \qquad (1)$$

The solubility product, $K_{sp} = [Si]_e[Al]_e$, is estimated to be first-order in each component, which is consistent with the composition of the crystal (Si/Al = 1).

Time-elapsed AFM images of a <100> surface growth extracted from Movie S1 reveal 2D layer generation and spreading (**Figure 3.3A – D)**. During continuous imaging, a minor fraction of the layers dissolve (**Figure 3.3A**, III) while the majority of layers grow (**Figure 3.3A**, I and II) and eventually merge into a single layer. Statistical analysis of islands that dissolve (**Figure 3.3E**) and grow (**Figure 3.3F**) reveal a distribution of sizes. The critical radius of 2D nucleation is defined as the size at which a layer grows 50% of the time. The stochastic nature of nucleation leads to situations where layers with sizes less than R_{crit} can grow and those with sizes larger than R_{crit} can dissolve; thus, the determination of R_{crit} is the statistical average size of islands that tend to grow in size with time. Based on the relatively limited data from our study, island dissolution and growth are both observed within a similar range of radius = 15 – 30 nm, which provides an estimate of the critical nucleus size for zeolite A.

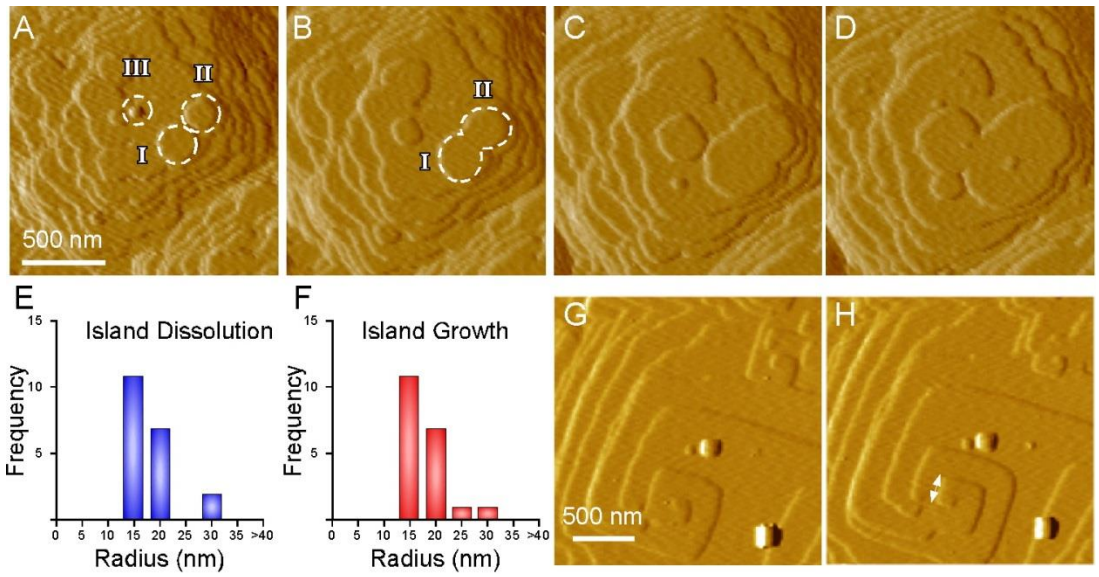

Figure 3.3: (**A-D**) Time-elapsed image showing 2D nucleation and layer propagation. (**E,F**) Statistical analysis of radius of 2D islands that dissolve and growth. (**G, H**) Time-elapsed images showing the birth of a new step segment from a screw dislocation.

For crystals that are grown classically, it is common that a reduction in supersaturation switches the predominant mode of layered growth from 2D nucleation/spreading to spiral dislocations. Time-elapsed AFM images of surface growth extracted from Movie S2 reveal the presence of screw dislocations (**Figure 3.3G and H)**. Analysis of sequential images for multiple dislocation centers shows that the first turn in the spiral occurs once reaching a critical length in the range of 25 – 40 nm

The third mode of growth observed from AFM measurements is that of layer generation from protrusions (**Figure 3.3D**). There are two different types of protrusions observed on zeolite A surfaces. The first type corresponds to larger features that are present on as made substrates (**Figure 3.4A**, I), which are almost always observed at the apex of hillocks. The second type corresponds to smaller features (**Figure 3.4A**, II) that only appear when imaging in growth solutions prepared with a colloidal silica source, which is evidence for the presence of a small quantity of particulates in the growth solution. For comparison, growth solutions prepared with an alternative silica source (e.g. sodium silicate) do not result in the formation of the second type of protrusions (**Figure 3.4B**). A similar effect was observed when the colloidal silica source was

first mixed with an alkaline solution to dissolve the silica particles prior to the addition of the aluminum source.

High resolution AFM images of type I protrusions (**Figure 3.4C**) reveal that these features are faceted. This observation suggests that the feature is crystalline, although its exact structure is unknown and difficult to identify by AFM or other techniques. It is possible that the cubic-like feature is an intergrowth of LTA, which has a cubic $P_{m\text{-}3m}$ space group. A prior study by Burchart et al. [218] has also shown that faujasite (FAU), which possesses a cubic $F_{d\text{-}3m}$ space group, is capable of growing epitaxially on the surfaces of zeolite A crystals. Syntheses of LTA and FAU are typically performed in Al- and Si-rich media, respectively [88]. Although *in situ* AFM measurements are performed in Al-rich growth solutions (Si/Al < 0.1), the protrusions are generated during the synthesis of substrates using growth solutions with Si/Al = 0.6 and an organic growth modifier, triethanolamine (TEA). The latter is known to sequester aluminates [218], and can potentially generate a pseudo Si-rich environment for FAU crystallization. This leads to greater uncertainty regarding the structure of type I protrusions.

The height of type I protrusions is nearly 3-4 times larger than those of type II (**Figure 3.4D**). During *in situ* growth of <100> surfaces, the height of type I features is approximately constant with few exceptions where the height can increase with imaging time. Type II features, which we attribute to undissolved colloidal silica, do not seem to impact the velocity of advancing layers. Time-resolved images of surface growth often show that layers advance through these features without their incorporation; however, there are examples, such as snapshots taken from Movie S3, showing that type II protrusions can be incorporated into advancing layers (**Figure 3.4E – G**). In this set of images, the protrusion highlighted by the dashed white circle in **Figure 3.4E** lies at the front of an advancing layer. Once the layer reaches the protrusion, it appears as though the entire feature is consumed within the advancing front (**Figure 3.4F**); however, the feature reemerges at a later time (**Figure 3.4G**), but with a height that is less than its original value (**Figure 3.4H**). More specifically, the original height of the

protrusion is nearly the same size as that of the layer, while the net difference in height once the layer has advanced past the protrusion is approximately one-half that of the step height. This suggests that only a fraction of the protrusion is occluded within the layer, which seems to indicate that the feature is partially raised from the surface during the process. This suggests that growth in the presence of type II protrusions leads to the occlusion of amorphous species within the crystal, thus leading to defects in LTA crystals prepared from colloidal silica sources. To our knowledge, these defects are not reported in literature.

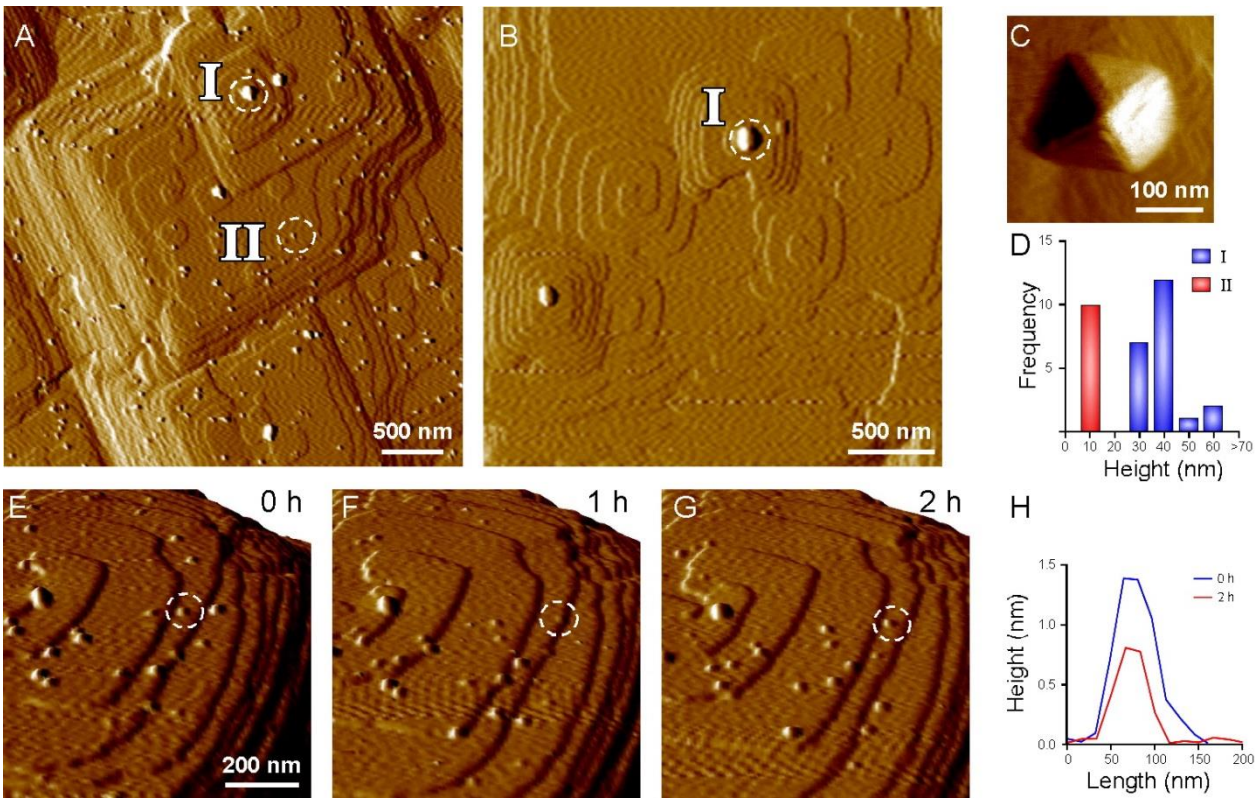

Figure 3.4: AFM images of crystal surfaces prepared with **(A)** colloidal silica and **(B)** sodium silicate. **(C)** High resolution image of feature I. **(D)** Statistical analysis of heights for features I and II. **(E-G**) Time-elapsed images showing layer advancement through feature II. **(H)** Height profile of the particles marked by white circles

Here we examine layer generation and spreading from type I protrusions in greater detail. For this study we selected a substrate (**Figure 3.5A**) that is representative of most samples where

protrusions are located at the apex of nearly all hillocks. Focusing on a single hillock with a protrusion located at the center of the upper terrace (**Figure 3.5B**), time-resolved images during *in situ* growth reveal the nucleation of a new layer on one side of the protrusion (**Figure 3.5C**). These new layers originate at a 45-degree angle and advance towards the nearest edge of the square hillock. This leads to an asymmetric growth front that wraps around, but is initially unable to encircle, the protrusion (**Figure 3.5D**). At a later time (**Figure 3.5E**), the growth is sufficient to generate a more symmetric layer, which has a geometry that is commensurate with the hillock. The square geometry of the new layer is achieved at later times owing to the initial rounded edges that grow more rapidly into (100) steps. This phenomenon is analogous to the recent study by Tsapatsis and coworkers[219] who reported the anisotropic growth of micron-sized silicalite-1 (MFI) nanosheets around silicalite-1 seed crystals.

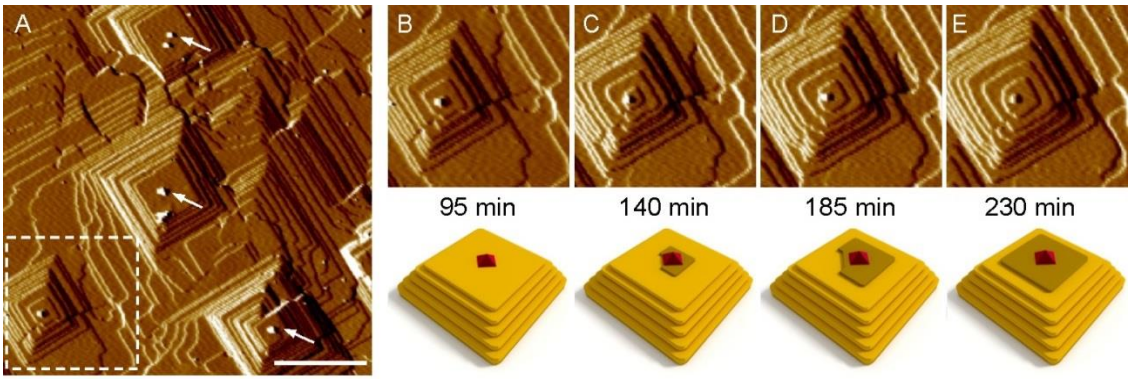

Figure 3.5: (A) AFM image showing multiple hillocks with deposits at the apex (arrows). **(B-E)** Time-elapsed images of the region in panel A showing a new layer emanating from the edge of the deposit with schematics depicting the different stages of growth.

Comparison of step velocities advancing from the three different sources of layer nucleation (**Figure 3.3B – D**) reveals that the kinetics are similar within error (**Figure 3.6**), with the rate of 2D advancement being slightly higher. This indicates that the rate of in-plane growth is comparable.

Given that 2D nucleation is observed at higher supersaturation, a direct comparison with the other two cases measured at lower supersaturation is not reasonable. If we then compare the two different types of hillocks generated from dislocations and protrusions, we observe that the latter results in much higher growth rates normal to the surface.

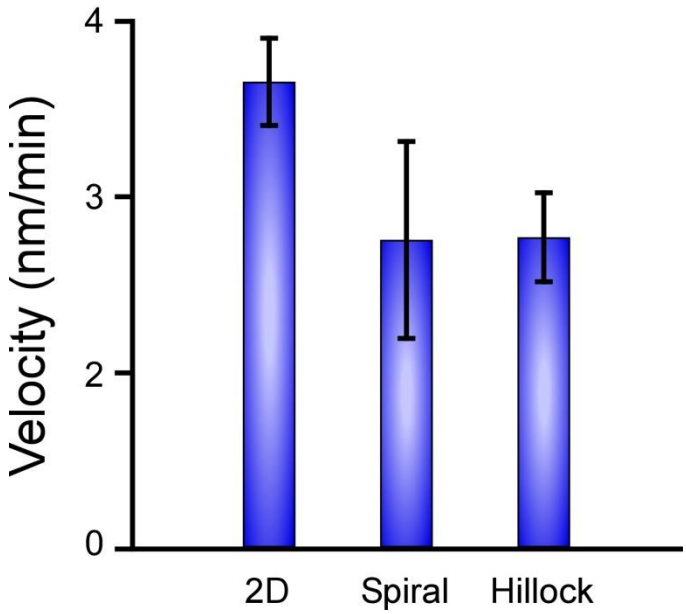

Figure 3.6: Comparison of <100> step velocities of layer advancement during *in situ* measurements at 50 °C. The steps correspond to 2D layers (**Figure 3.3A**), spiral dislocations (**Figure 3.3G**), and hillocks emanating from deposits (**Figure 3.5A**).

Liquid phase NMR spectroscopy can be used to obtain information concerning chemical species present as well as their relative concentrations. One of the advantages of liquid NMR is that it requires almost no sample preparation and can be carried out under *in-situ* conditions. Hence, NMR spectroscopy was utilized to characterize the aluminosilicates species present in the growth solution. Our growth solution is dilute in silicon; hence we carried out liquid ^{27}Al NMR (**Figure 3.7A**). We observe only monomers of aluminum ($Al(OH)_4^-$) at room temperature. Further NMR analysis was carried out at a higher temperature to ascertain if oligomers are formed at the higher temperature. No additional peaks were detected during the experiment. However, there was a reduction in peak area upon heating. To verify whether the decrease in peak area is due to oligomer formation or due to reduction in the sensitivity of NMR with temperature, we carried

out a controlled experiment with sodium aluminate solution which is reported to contain only monomer. The comparison of peak areas (**Figure 3.7B**)of two solutions suggests that the reduction in peak area is due to a reduction in the sensitivity of NMR with increasing temperature. Another viable reason for the absence of oligomer peaks can be the rapid exchange between different species in the presence of Na^+, leading to peak broadening and merging with baseline. We carried out an experiment with a solution in which Na^+ was replaced entirely with TMA^+ to diminish the exchange rate. No oligomers were detected in NMR analysis of TMA^+ solution((**Figure B3**), further suggesting the growth solution consist of predominantly monomer of Al and Si. This is consistent with the previous report of the Yokoyama et al. that at the high alkalinity, the solution consists of monomers [220]. Also, it is known that Al cannot form bond with Al monomer in alkaline solution as per Lowenstein's rule and while low Si concentration imply, the alkaline solution of Si will only consist of monomer. Moreover, the pH of the solution is >14, which is higher than pK_a^2 of $Si(OH)_4$, leading to -2 charge on silica monomers. This further lessens the reaction between Si and Al monomers.

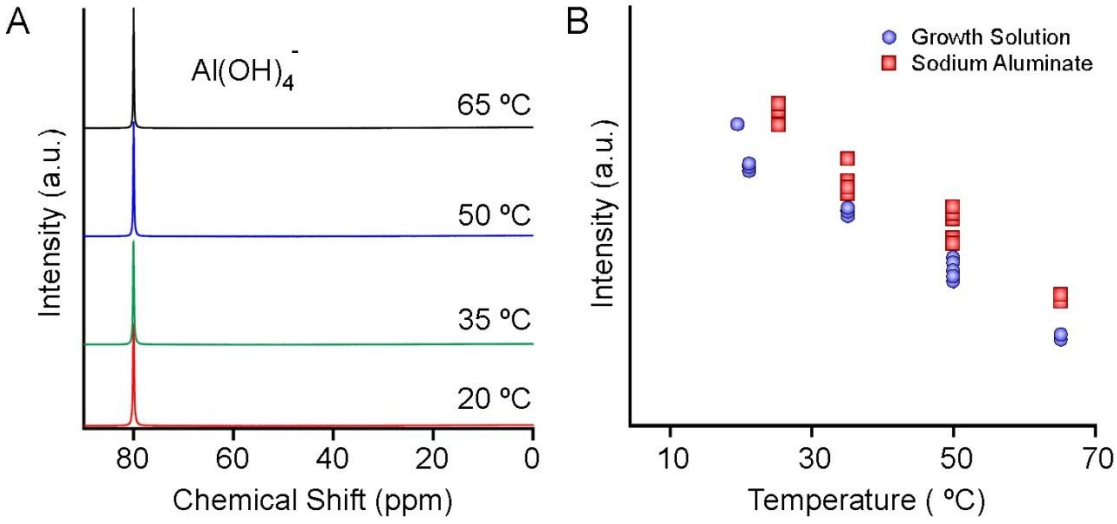

Figure 3.7: (A) Liquid ^{27}Al NMR spectrum of growth solutions at various temperatures. **(B)** Comparison of monomer (δ = 80 ppm) peak areas for the growth solutions in (A) along with solutions prepared with only sodium aluminate.

An important implication of the NMR study is that the growth solutions can be prepared by mixing the alkaline solutions of Al and Si since these solutions will have Si and Al monomers. It should be noted that the growth solution in this study was prepared using the previously reported procedure in chapter 2 that is the clear solution was obtained by removing the particles from the opaque LTA growth mixture. Based on the result of the NMR analysis and elemental analysis of the growth solution, we attempted to prepare an AFM growth solution by adding Si and Al sources. The AFM study with this growth solution suggests there is no difference between the solution made via two methods: (1) Solution prepared by removing particles from opaque LTA growth mixture (2) Solution prepared by mixing Al and Si in composition estimated from the ICP analysis of the solution made from method 1. We also experimented to see the effect of aging, pretreatment and silica sources which can point out the difference in speciation. The AFM experiment and NMR experiment does not show any impact of these parameters. However, we observe the deposition of Ludox particles when Ludox AS-40 was added into a sodium aluminate solution, and the growth rate was slower. These results further support our conclusion that the growth solutions contain primarily monomers and layer growth of LTA occurs via direct attachment of monomers.

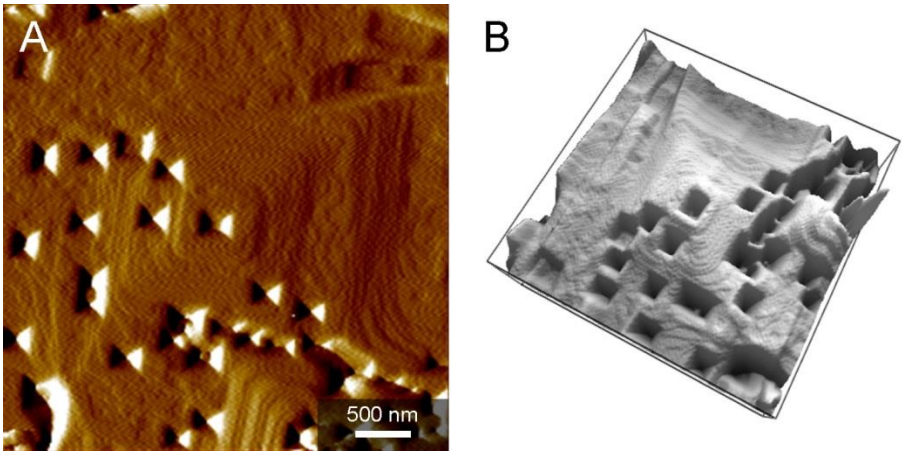

Figure 3.8: (A) AFM mode image taken from a series of continuous images showing the dissolution of zeolite A with steps retreating and the generation of square base pyramid shaped etch pits. **(B)** Corresponding 3-D height mode of the same surface.

For the experiment at very low supersaturation, we did not observe any growth, suggesting that the solution is at equilibrium with LTA crystal. The growth solution is deficient in Si i.e. Si/Al <0.1. The ICP analysis suggests Si = 7mM that is consistent with value previously reported ([Si] = [Al] =5-10 mM) for LTA under similar condition (NaOH=3 M and 50-65 °C). However, our growth solution contains a much higher amount of aluminum. To ascertain the solubility of LTA, we carry experiment with growth solution Si=Al=7 mM, and we observe dissolution with the formation of square-shaped etch pits at the center of the hillock and also at other locations (**Figure 3.8**). We also observe dissolution by step retreat. Anderson et al.[146] estimated the value of 0.002-0.2 nm/min from their dissolution studies at room temperature. Additionally, they reported a reduction in step height from 1.2 nm to 0.9 nm during dissolution. However, our AFM experiment does not suggest any change in height. The step height was 1.2 nm (**Figure B4**)for most of the layers, and the similar value was observed for single layer etch pits.

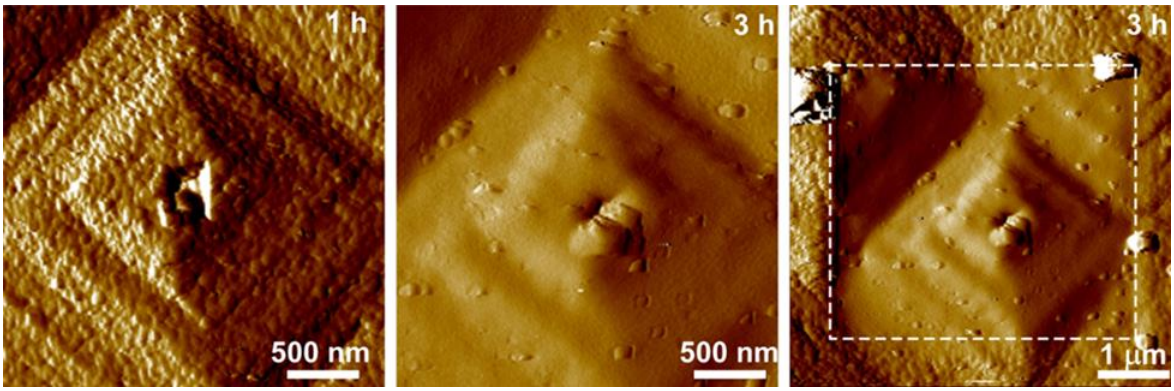

Figure 3.9: Zeolite A growth in the presence of TMA^+. **(A and B)** Time-elapsed images show growth via gel-like islands, and the progressive smoothening of the surface **(C)** Increased scan size shows the area of continuous imaging (white dashed box).

We also studied the effect of TMA^+ on the growth of LTA. TMA^+ is the most commonly OSDA used for the synthesis of LTA and has been used to synthesize nanosized LTA[136,221] and high silica LTA[221]. In order to observe the effect of TMA^+, we prepared a growth solution by replacing NaOH with TMAOH keeping the total $[OH^-]$ constant. AFM experiment at $[TMA+]/[OH^-]=0.5$, we observe the nonclassical mode of growth by gel-like particle attachment

even at high temperature while we encountered this kind of growth at a lower temperature in the presence of Na^+. This can be attributed to the previous report[106] of stabilization of the oligomers by TMA^+ and preventing their hydrolysis which is also consistent with the slow exchange of oligomers in a TMA-aluminosilicates solution, observed by NMR spectroscopy while the addition of Na^+ leads to faster exchange.

The nucleation of a crystal and a 2D layer is governed by the formation and dissolution of nuclei. Due to the stabilization effect of TMA^+, we expect the critical radius will decrease, thereby, promoting nucleation. However, the dissolution rate will also reduce; thus, we expect the crystallization rate will decrease as well. Hence at high concentration of TMA^+, it is possible that the rate of growth units' attachment on the crystal surface reduces. But, at the same time, their dissolution decreases by a more significant amount, thereby leading to a rapid formation of nuclei but with slower crystallization rate. This decrease in the crystallization rate might leads to the formation of gel-like particles, and a similar phenomenon can be happen at a lower temperature in the presence of Na^+. This hypothesis is consistent with the fact that the nucleation rate is favored by lower temperature while the crystallization rate promoted at a higher temperature. If this hypothesis is correct, we would expect the kinetic roughening at lower supersaturation in the presence of TMA^+. So, further studies are underway to confirm this hypothesis.

We have shown in chapter 2 that LTA grows via diverse pathways that depend upon the supersaturation and temperature of the growth solution. In this study, we have focused on the classical growth regime at lower supersaturation and have found different modes of growth: hillock growth, spiral growth, and, 2D nucleation and layer growth. The LTA crystal substrate is mainly comprised of hillocks with protrusions at the center. We have elucidated the role of these protrusions in zeolite growth using *in situ* AFM experiments. The analysis of growth solution suggests that growth occurs by the addition of monomers. We have also reported the effect of silica sources and sequence of addition of alumina and silica sources. Finally, experiments with TMA show non-classical growth even at higher temperature due to the stabilization effect of

TMA. These results elucidate the complex sol-gel chemistry of zeolite A and will assist in the rational design of zeolites.

3.3. Material and methods

3.3.1. Chemicals for zeolite synthesis and growth experiments

The following chemicals were used as reagents: sodium hydroxide (98% pellets, MACRON Fine Chemicals), sodium aluminate (Al2O3·Na2O or NaAlO2, 54.41% Al2O3 and 41.02% Na2O, Alfa Aesar), Ludox AS-40 (40%, Sigma Aldrich), tetraethylorthosilicate (TEOS, 98%, Sigma Aldrich, St. Louis, MO), Sodium silicate (Na_2SiO_3, 29%, J.T. Baker) and triethanolamine (TEA, 100%, J.T. Baker). Deionized (DI) water was made using an Aqua Solutions RODI-C-12A purification system (18.2 MΩ). All reagents were used as received without further purification.

3.3.2. Synthesis of zeolite substrates for scanning probe microscopy

Large cubic crystals of zeolite LTA were synthesized using a previously reported protocol [166]. The growth solution was prepared by mixing the chemicals in 125 ml polypropylene (PP) container to yield a solution with molar composition 1.23 SiO_2: 1 Al_2O_3: 2.71 Na_2O: 5.5 TEA: 288 H_2O. The solution was then aged at room temperature for 4 h while stirring. The PP container was heated in a Thermo-Fisher Precision Premium 3050 Series gravity oven at 85°C for 14 days and was quenched to room temperature. The zeolite crystals were recovered using a 1 μm GHP filter (Pall Corporation) and washed multiple times with DI water.

3.3.3. Preparation of zeolite growth solutions

The growth solution for in situ atomic force microscopy (AFM) experiments was prepared from a 90 g mixture with molar composition 1 SiO_2: 0.87 Al_2O_3: 11.2 NaOH: 190.6 H_2O. In a PP container, NaOH was added to degassed DI water with subsequent addition of

sodium aluminate. The silica source, Ludox AS-40 was added to the resulting solution after 30 min of stirring and the mixture was left aging at room temperature for 48 h while stirring. The growth solution was heated in a Thermo-Fisher Precision Premium 3050 Series gravity oven at 65°C for various times and quenched in an ice bath. The precipitate was removed after centrifuging the solution twice at 13,000 rpm for 45 min in a Beckman Coulter Avanti J-E instrument. The supernatant was decanted and filtered twice, using a 25mm syringe filter fitted with a 0.20μm nylon membrane (VWR international). The resulting clear supernatant was used as a growth solution for in situ AFM measurements.

3.3.4. *In situ* atomic force microscopy

Large LTA crystals were firmly placed on a 15-mm specimen disk (Ted Pella, Inc.) using quickset Loctite epoxy (Henkel Corporation) that was cured in an oven at 65°C for 12 h. The sample was then removed from the oven and cooled to room temperature in air. The sample was rinsed with DI water to remove loosely-bound crystals, and dried with N_2 gas. All AFM measurements were performed on an Asylum Research MFP-3D-SA instrument (Santa Barbara, CA) equipped with a custom liquid sample cell.[156] The sample was then placed in a closed AFM liquid cell. AFM images were collected using an uncoated silicon nitride cantilever (Olympus TR800PSA) with a spring constant of 0.60 N m^{-1}. The LTA crystal substrate was first scanned in air to locate a desired imaging area. The growth solution was then introduced into the AFM cell by a syringe and the sample was left to equilibrate with the solution at room temperature for ca. 30 min. The temperature was then ramped to a 50 °C at a rate of 1°C min^{-1}. Growth solution was continuously supplied to the liquid cell using a syringe pump (Razel Scientific Instruments, Model R100-E) at a rate of 1.2 cm^3 h^{-1}. The sample cell was allowed to equilibrate for 1 h before imaging in tapping mode at a scan rate of 1.2 Hz and 256 lines per scan.

3.3.5. Liquid Nuclear magnetic resonance spectroscopy

All ^{27}Al NMR were performed on a JOEL ECA-600 NMR spectrometer operating at 600 MHz with 10 wt% deuterated water added to the solution for frequency lock. NMR measurements were carried out room temperature as well as high temperature. The temperature was ramped at pre-determined temperature at the rate of 1°C min^{-1}. The solution was allowed to equilibrate for 10 min before collecting spectrum.

Chapter 4

Molecular Modifiers Suppress Nonclassical Pathways of Zeolite Crystallization

4.1. Motivation

The unique physicochemical properties of zeolites are ideal for industrial applications in ion-exchange,[222] selective separations,[223,224] and catalysis.[225-231] The vast majority of zeolites are aluminosilicates with approximately 20 framework types used in commercial processes relative to more than 235 known structures. Only a small fraction of zeolites have been prepared as purely siliceous crystals, which have more limited applications than their aluminosilicate analogues, but have traditionally been used as model systems to elucidate the mechanisms of zeolite crystallization.[134,232-240] Moreover, the propensity for an all-silica zeolite synthesis to yield controllable, monodisperse crystal sizes has permitted systematic studies of diffusion in their confined pores.[241-245] Despite significant efforts over the past 30 years to understand the mechanism(s) of zeolite crystallization, there are many unanswered questions owing to their complexity.

One of the many motives for understanding zeolite crystallization is the potential for using this knowledge to tailor their properties – notably the preparation of ultrasmall crystallites. Different strategies have been implemented to generate nanosized zeolites.[246] To a limited extent, the modification of zeolite size and morphology can be accomplished through the judicious selection of synthesis conditions, such as molar composition[247] and temperature.[248,249] Examples include the work of Mintova and coworkers[249] who applied a low temperature aging method to maintain highly uniform precursor particles and ultimately achieved ultrasmall FAU-type zeolites. Alternative approaches include the design of organic structure-directing agents (OSDAs), such as those introduced by Ryoo and coworkers,[250] to synthesize nanosheets (ca. 2nm thick) and other 2-dimensional zeolites.[251-253] Similar methods have been used by Tsapatsis and

coworkers[254] to produce self-pillared zeolite nanosheets of unit cell thickness, and by Okubo and coworkers[255] to prepare hierarchical zeolites with sequential intergrowths.

We previously demonstrated an approach to tailor the anisotropic growth rates of zeolites using zeolite growth modifiers (ZGMs).[256-260] Growth modifiers are molecules or macromolecules that either interact with specific facets of zeolite crystals or associate with amorphous precursors to mediate the kinetics of nucleation and growth, thereby altering crystal morphology and/or size.[119] Modifiers that bind to specific crystal surfaces inhibit the attachment of growth units, thereby reducing the growth rate normal to the surface. This mechanism is illustrated in **Scheme 4.1** for zeolite MFI, which exhibits a coffin-like habit. ZGMs that preferentially bind to the {101} and {010} surfaces result in increased or decreased crystal thickness in the [010] direction (*b* direction), respectively. To date, this approach has been successfully demonstrated by our group and others for numerous zeolite frameworks, such as MFI (silicalite-1),[257,260,261] LTL (zeolite L),[256,259,262] CHA (SSZ-13, SAPO-34),[258,263] FAU (zeolite Y),[264] MWW (MCM-22),[265] IWR (ECNU-20),[266] AEL (SAPO-11),[267] and MTW (ZSM-12)[268]. Inspiration for this approach derives from natural and biological systems where organic-inorganic interactions are of paramount importance for the regulation (inhibition or promotion) of crystal growth.[269-283]

Silicalite-1 is the purely siliceous form of ZSM-5, which is one of the most commonly used zeolites in commercial applications, and has been a prototype for mechanistic studies of zeolite crystallization. Silicalite-1 and ZSM-5 both have an MFI framework with 3-dimensional pores consisting of interconnecting straight and sinusoidal channels oriented along the [010] and [100] directions, respectively. The straight channels present the least tortuous path for internal diffusion; therefore, for applications in catalysis it is desirable to selectively reduce the [010] thickness of MFI crystals. We previously identified modifiers, such as tributylphosphine oxide (TBPO), that preferentially interact with the silicalite-1 (010) surface.[260] Likewise, we reported that the amino acid D-arginine (D-Arg) increases the [010] thickness, which was attributed to its binding specificity to silicalite-1 {101} surfaces.[260] This conclusion was derived from

experimental observations using a combination of bulk crystallization and *ex situ* atomic force microscopy measurements. The latter showed a larger population of step bunches on the (010) basal surface, which seemed to indicate a preferential binding to step sites on layers advancing across the (010) surface, consistent with scanning electron micrographs indicating an increased crystal thickness.

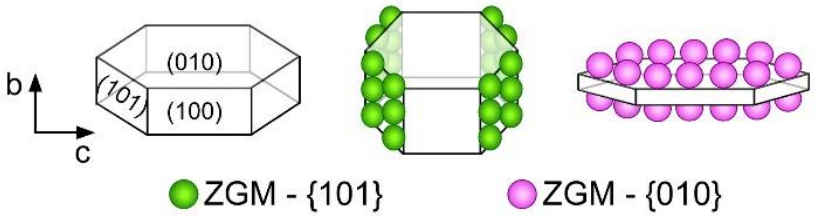

Scheme 4.1: Idealized effects of modifiers on MFI-type zeolite

In this study, we explore the mechanism for D-Arg modification of silicalite-1 crystallization and show that its mode of action is more complex than previously reported. Here, we selected two growth solutions with distinct populations of precursors. Using a combination of experiments and modeling, we assess modifier-zeolite interactions and their effect on the size and morphology of silicalite-1 crystals. Our findings indicate that D-Arg is chemically unstable during synthesis and decomposes to a new product that is the active component in growth modification. We also show that there is a marked reduction in growth solution alkalinity that accompanies D-Arg decomposition, which appears to shift the predominant growth unit involved in silicalite-1 crystallization. The latter effect is responsible for increased [010] thickness, whereas the preferential binding of modifier to zeolite surfaces is deemed to be less influential.

4.2. Result and discussion

4.2.1. Chemical decomposition of D-Arg

A potential outcome of employing organics in zeolite synthesis as either structure-directing agents or modifiers is their propensity to chemically decompose in alkaline media at high temperature (i.e. typical conditions of zeolite synthesis). This is particularly true for an

amino acid, such as D-Arg, which is susceptible to hydrolysis. To test the stability of D-Arg, an alkaline solution containing 3 wt% D-Arg was heated at 160°C for 3 days and the resulting organic(s) were isolated and analyzed by mass spectroscopy (**Figure C1**) and ^{13}C NMR (**Figures C2 and C3**). These analyses confirmed that D-Arg undergoes a chemical decomposition to (R)-ornithine-lactam (R-OL). The proposed decomposition reaction is shown in **Figure 4.1** where the first step (the hydrolysis of D-Arg) leads to the generation of urea as a byproduct. Although urea reportedly acts as a modifier of zeolite MFI growth [284,285], it can undergo hydrolysis under typical synthesis conditions to form ammonia and carbonic acid. A detailed kinetic study of urea decomposition by Sahu et al.[286] revealed that at 160°C there is ca. 65% loss within one hour. To test the long-term thermal stability of urea, we performed a similar study where urea was heated in alkaline solution at 160°C for periodic times and then analyzed by ^{13}C NMR to reveal complete decomposition within 8 h (**Figure C4)**. An identical study was performed on the second intermediate, D-ornithine, which fully decomposes to R-OL with similar hydrothermal treatment (**Figure C5**). Under the alkaline conditions of zeolite synthesis, the final product of decomposition, R-OL, is neutral, i.e., the pH of the growth solution lies between the two dissociation constants (pKa) of ornithine-lactam, 7.8 for the primary amine group and 16.0 for the amide group.[7,287]

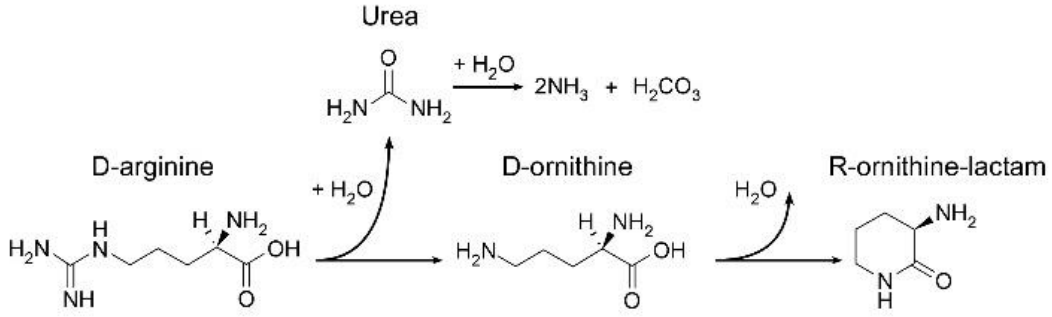

Figure 4.1: Putative decomposition of D-arginine (D-Arg) during hydrothermal treatment in alkaline media (pH > 11). The final product, (R)-ornithine-lactam (R-OL), retains the chirality of the original amino acid.

In a previous study[260] we reported that D-Arg preferentially binds to silicalite-1 {101} surfaces and increases crystal thickness along the *b*-direction. Prior experiments used small quantities of modifier (0.3% D-Arg) and a dilute silica concentration with an equimolar ratio of SiO_2 and TPAOH, which we refer to as solution S(I). Here, we performed syntheses over a much broader range of D-Arg concentration (0 – 7 wt%, **Figure 4.2A**). We observed that silicalite-1 crystals synthesized from solution S(I) exhibit an elongated hexagonal platelet morphology with an average *c/b* aspect ratio of 15 (**Figure 4.2B**). Similar to what was reported previously[260], the presence of D-Arg in small quantities increases the crystal thickness (**Figure 4.2C**); however, bulk crystallization assays reveal an unexpected trend in crystal morphology whereby the relative thickness increases with modifier addition at low D-Arg concentrations, reaches a maximum at ca. 1 wt% D-Arg, and then monotonically decreases with further increase in D-Arg concentration. At the most concentrated D-Arg condition assessed in this study (7 wt%) we observe thinner crystals (**Figure 4.2E**) than those prepared in the absence of modifier (**Figure 4.2B,** control).

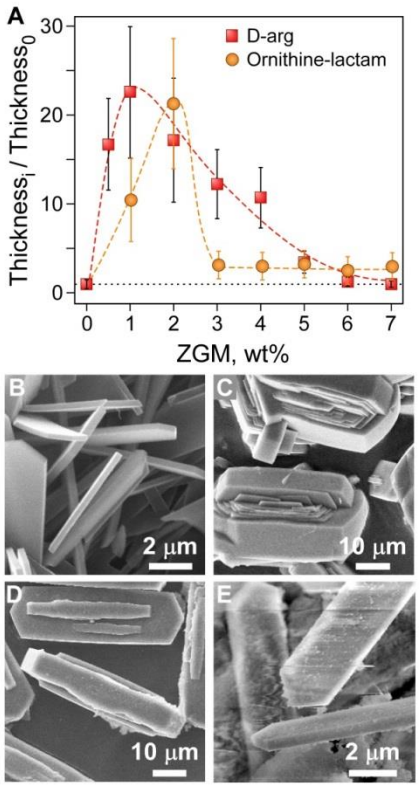

Figure 4.2: (A) Ratio of the crystal thickness in the presence of D-Arg or R/S-OL relative to the crystal thickness of the control, as a function of modifier content **(B – E)** SEM of crystals prepared with **(B)** control **(C)** 1 wt%, **(D)** 3 wt%, and **(E)** 7 wt% D-Arg.

In order to validate that the effect of silicalite-1 habit modification is due to R-OL (the byproduct of D-Arg decomposition), we replaced D-Arg with an equivalent concentration of R/S-OL (racemic mixture). As shown in **Figure 4.2A**, R/S-OL has the same effect on silicalite-1 crystal size. There is a slight difference in the relative thickness of silicalite-1 crystals, which we attribute to the chirality of OL (as discussed in Section 4.2.3). Evidence for the decomposition of D-Arg to R-OL is also gleaned from the change in pH during hydrothermal treatment. The pH of the growth mixture during room temperature aging is constant, irrespective of D-Arg concentration (**Figure 4.3**, open blue squares), which indicates that D-Arg is stable under these conditions. The constant pH is expected due to D-Arg being zwitterionic where the dissociation of the carboxylic acid is offset by the protonation of the amidinium group (pKa = 3.1 and 12.5, respectively). The measured pH after hydrothermal treatment (**Figure 4.3**, closed blue squares) reveals that there is a monotonic decrease in alkalinity with increasing D-Arg content. This is

consistent with the release of carbonic acid (H_2CO_3) during the chemical decomposition of D-Arg (**Figure 4.1**). The plateau in solution pH around 10.2 is likely a buffering effect given that the pH roughly coincides with the range of silanol dissociation constants reported for silicates (i.e., soluble species, amorphous precursors, and zeolite crystals).[288]

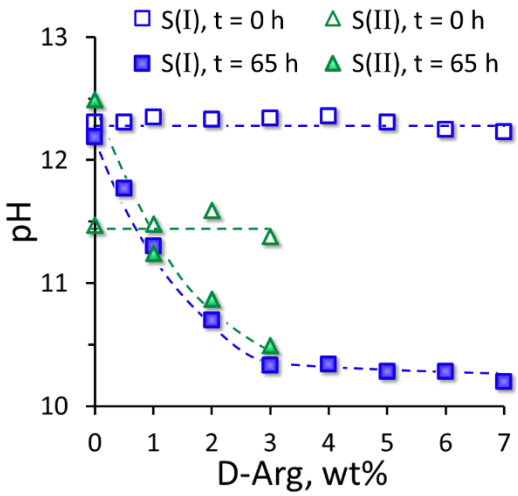

Figure 4.3: Changes in the pH of silicalite-1 growth solutions S(I) and S(II) prior to (pH_i, open symbols) and after (pH_o, solid symbols) hydrothermal treatment as a function of D-Arg. weight percent.

4.2.2. Hypothesis of growth modification.

Here we propose a mechanism for the trend in **Figure 4.2A** based on a putative shift in the predominant mode of crystallization from a classical route involving the addition of soluble species to a nonclassical pathway governed by the addition of amorphous nanoparticles. Silicalite-1 has been shown to grow via complex pathways involving both monomer/oligomer species and amorphous silica nanoparticles.[156] Prior studies [288-290] have shown that nanoparticle self-assembly occurs at a silica concentration, referred to as the *critical aggregation concentration* (CAC), with an approximate molar ratio SiO_2:OH^- = 1. Silicalite-1 growth mixtures are prepared using tetraethylorthosilicate (TEOS) as a silica source and tetrapropylammonium (TPA^+) as the structure-directing agent. The hydrolysis of TEOS leads to the assembly of amorphous nanoparticles at silica concentrations exceeding the CAC. This is

depicted in **Figure 4.4A** where region I refers to solutions containing soluble species (monomer and oligomers) and region II refers to solutions containing metastable silica nanoparticles in pseudo-equilibrium with soluble species. The dashed line dividing these regions is the CAC.

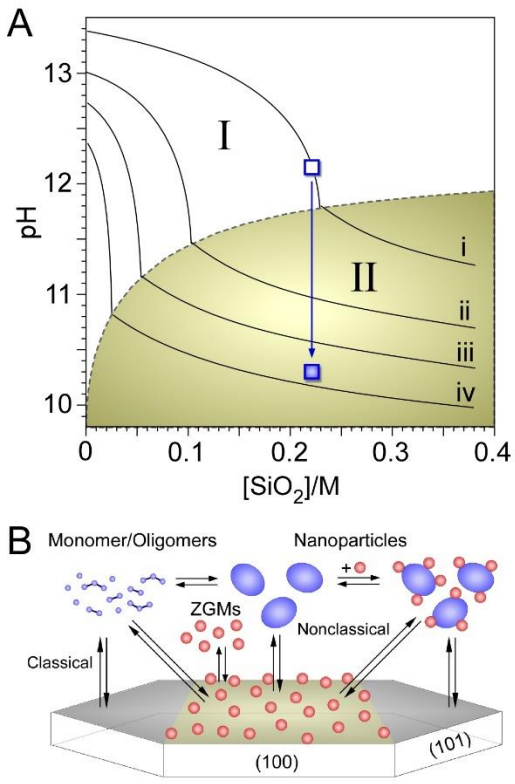

Figure 4.4: (A) Silica phase diagram for silicalite-1 synthesis[290]. The solid lines are reported for TEOS addition to mixtures containing molar ratios x TPAOH:H_2O with x=(i) 40 (ii)18 (iii) 9 and (iv)4. **(B)** Schematic of classical and nonclassical growth pathways

Growth mixture S(I) lies within region I of the phase diagram (**Figure 4.4A**, open blue square). A sufficient quantity of D-Arg added to S(I), followed by its decomposition to R-OL, reduces the pH and shifts the growth mixture to region II (**Figure 4.4A**, solid blue square). This suggests that crystallization in the absence of modifier occurs predominantly by molecule addition (classical pathway), whereas crystallization in the presence of modifier occurs by a nonclassical pathway that involves the addition of nanoparticle precursors, as illustrated in **Figure 4.4B**. We surmise that the increased thickness of silicalite-1 crystals at low D-Arg content (≤1 wt% in **Figure 4.2A**) is due to an inherent change in the growth pathway. This is seemingly consistent with the finding of Shete et al.,[291] who showed that the ability to shift the predominant

pathway of silicalite-1 growth to a classical route leads to enhanced growth in the *a*- and *c*-directions with reduced growth in the *b*-direction (note that this was not accomplished by altering silica concentration or pH, but rather by exchanging TPA^+ with tetraethylammonium, TEA^+). A shift from classical to nonclassical growth can explain the trend in **Figure 4.2A** at low modifier concentration where nanoparticle addition leads to enhanced growth in the [010] direction; however, as the concentration of modifier increases, there is a monotonic reduction in crystal thickness indicating a reduced rate of growth normal to the basal (010) surface.

We previously reported that a low concentration of D-Arg (0.3 wt%) increases crystal thickness via its preferential binding to silicalite-1 {101} surfaces; however, in view of the current findings, it is now evident that this effect is attributed to the switch from region I to II in the phase diagram based on changes in solution alkalinity. It should be noted that the CAC line in **Figure 4.4A** is based on room temperature measurements and is considered approximate. At higher temperature it is likely that there is a shift in the division between the two regions. Indeed, the 0.3 wt% D-Arg result seems to suggest that the crossover from region I to II occurs at higher pH than indicated in the phase diagram. To further test this observation, we performed two experiments where the pH of the growth solution S(I) was lowered. We first replaced D-Arg with urea using a molar equivalent of 0.3 wt% D-Arg and observed the expected pH reduction due to its thermal decomposition, which increased the thickness of silicalite-1 crystals (**Figure 4.5A**).

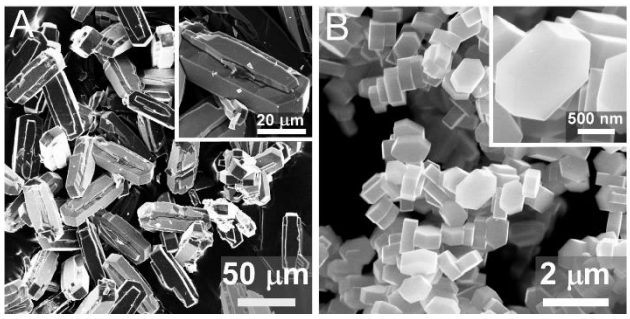

Figure 4.5: Modified S(I) growth solutions to assess the effects of urea decomposition and lower TPAOH content. SEM images show crystals prepared with **(A)** addition of 1 wt% urea to solution S(I) and **(B)** a solution with reduced TPAOH content

In a second test we reduced the quantity of TPAOH to lower the pH of the growth solution to 10.7 (in the absence of modifier) and observed a net reduction in crystal size (**Figure 4.5B**). It is evident that a reduced pH increases the number of silicalite-1 nuclei. Moreover, the crystals exhibit larger b/c aspect ratios than the control (**Figure 4.2B**), indicating that a switch from region I to II in the phase diagram enhances the rate of silicalite-1 growth in the b-direction. The stark differences in crystal habit between **Figure 4.5B** and those in **Figures 4.2C and 4.5A** indicate that D-Arg and the products of its thermal decomposition (e.g. urea and R-OL) inhibit nucleation in region II, leading to a reduced population of crystals with larger size.

The trend in **Figure 4.2A** at higher D-Arg concentration corresponding to a reduction in silicalite-1 crystal thickness would seem to indicate a preferential interaction of the modifier R-OL with the MFI (010) surface; however, an alternative explanation is that R-OL impedes the attachment of nanoparticles to silicalite-1 surfaces. The multiple routes of growth (and growth inhibition) are illustrated in **Figure 4.4B** where crystallization in the absence of modifier can occur by molecule addition, the attachment of nanoparticles, or combinations thereof. In the presence of R-OL, a putative reduction in nanoparticle attachment is consistent with bulk crystallization assays indicating a slower rate of growth in the [010] direction. To assess the hypothesis that preferential interactions between modifier and zeolite surfaces leads to the reduction in [010] thickness, we investigated the interaction of R-OL with different silicalite-1 surfaces using USMD simulations to compute the adsorption free energy profile $F(z)$. As shown in **Figure 4.6**, the function $F(z)$ is approximately constant for $z > 0.5\,\mathrm{nm}$ for each surface, indicating that the interactions between R-OL and silicalite-1 are short ranged and negligible beyond this distance. Near the surface, however, $F(z)$ exhibits a global minimum at the characteristic distance ($z = z_{\mathrm{min}}$) where R-OL interacts most strongly and binds to silicalite-1. The absence of a maximum in $F(z)$ larger than $k_{\mathrm{B}}T$ at intermediate distances reveals that the binding process is essentially barrierless, as is typical for small molecules.[292,293] Adsorption of R-OL into the pores of silicalite-1, by contrast, is inhibited by a large barrier ($> 10\ k_{\mathrm{B}}T$) observed

at $z <$ 0.2 nm for each surface. The presence of these barriers is consistent with the observation that R-OL does not diffuse into the pores of silicalite-1 during long (> 100 ns) unbiased MD simulations and the hypothesis that R-OL influences growth by a surface adsorption mechanism.

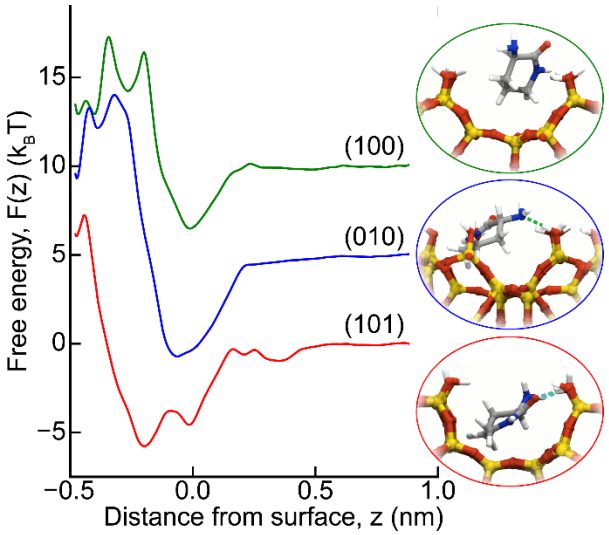

Figure 4.6: Free energy as a function of the R-OL center-of-mass distance from the (100), (010), and (101) surfaces of silicalite-1 computed using USMD. In each case, the z=0 plane is defined as the positions of the protons on the surface silanol groups.

The adsorption free energy for R-OL interactions with silicalite-1 was computed using the relation $\Delta A^{ads} = F(z_{\min}) - F(z \to \infty)$, yielding values of $\Delta A^{ads}_{(100)} \approx -3.5 \pm 0.5\, k_B T$, $\Delta A^{ads}_{(010)} \approx -5.7 \pm 0.5\, k_B T$, and $\Delta A^{ads}_{(101)} \approx -5.7 \pm 0.5\, k_B T$ for the (100), (010) and (101) surfaces, respectively. The small magnitudes of the ΔA^{ads} values indicate that R-OL adsorption is reversible on each surface, in accord with our previous experiments showing a negligible mass of modifiers on extracted solids after post-synthesis washing.[258,259] Analysis of the simulation trajectories reveals that R-OL binding is driven by adsorption into hydrophobic pockets on the surface created by partially formed pores (representative images are shown in **Figure 4.6**). In each case, R-OL adsorbs with the hydrophobic region of its aromatic carbon ring is inside a pocket such that its hydrophilic amine and carboxyl functional groups are left exposed to form hydrogen bonds with surface silanol (SiO^- and SiOH) groups and water molecules near the interface. Deep pockets on the (101) facet (**Figure C7**) formed by the major sinusoidal channels

oriented along the [100] axis of silicalite-1 provide favorable adsorption sites for R-OL. The accessible pockets on the (100) and (010) surfaces are relatively shallow by comparison. The narrow width of the pockets on the (010) surface, however, enhances confinement and facilitates stronger interactions between the functional groups of R-OL and the surface silanols of silicalite-1. Thus, the adsorption free energies for the (010) and (101) surfaces are comparable and more favorable than for the (100) surface. This finding is consistent with the experimental observation that R-OL (the product of D-Arg decomposition) reduces the [010] thickness of silicalite-1; however, it cannot fully rationalize the insensitivity of [001] length to the presence of R-OL

In order to provide additional evidence for the effect of R-OL, we examined a growth mixture with increased silica concentration. To this end, we selected a molar ratio of 157 SiO_2:47 TPAOH, referred to as solution S(II), which has a silica concentration three times higher than the CAC, thus placing this composition well within region II of the phase diagram. This indicates that the majority of silica species are in the form of nanoparticle precursors (with sizes of ca. 1-6 nm). Silicalite-1 crystals synthesized in S(II) without modifier are relatively homogenous in size (**Figure 4.7A**) with dimensions that are smaller than the crystals prepared in S(I) (**Figure 4.2B**). When evaluating changes in silicalite-1 morphology, we define the length and thickness of crystals using dimensions in the *c*- and *b*-directions, respectively. We observed that 3 wt% R-OL reduces the thickness (*b*-direction) of silicalite-1 by a factor of two (**Figure 4.7B**). Examination over a broader range of modifier concentration (**Figure 4.7C**) revealed a monotonic reduction in crystal thickness with increasing R-OL content, while the crystal length is relatively constant. This seems to indicate a preferential binding of modifier to the basal (010) surface, which is only partially consistent with USMD simulations that predict equal binding affinity for the (010) and (101) surfaces. This seems to suggest that [010] size reduction is not attributed to a preferential binding of R-OL to the basal surface, but rather an inherent ability of the modifier to impede the attachment of nanoparticles to zeolite interfaces.

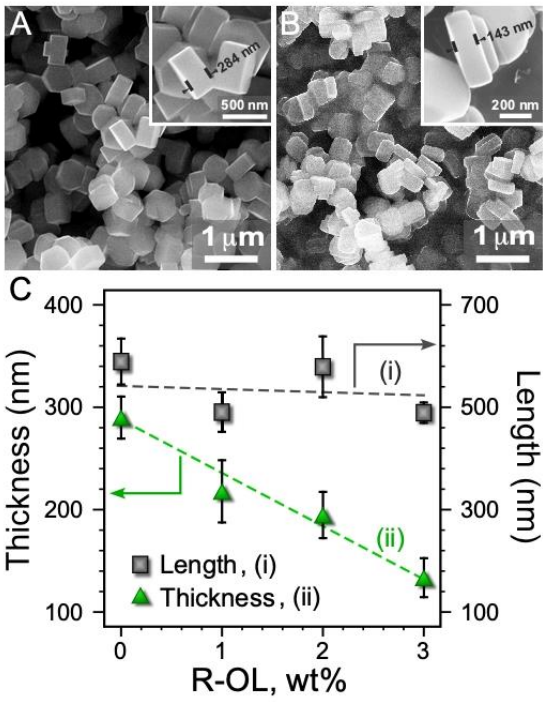

Figure 4.7: SEM images of crystals prepared **(A)** in the absence of modifier and **(B)** with 3 wt% R-OL **(C)** Changes in silicalite-1 [001] length and [010] thickness as a function of increasing modifier weight percent

The high silica concentration of solution S(II) exhibits lower pH owing to the dissociation of additional silanol groups. Measurements of pH during room temperature aging (**Figure 4.3**, open triangles) reveal that D-Arg, which is stable under these conditions, does not alter the alkalinity of solution S(II), analogous to measurements of S(I). During hydrothermal treatment there is an increase in S(II) solution pH in the absence of modifier that is attributed to the evolution of silica nanoparticles. Notably, it has been shown that nanoparticle precursors evolve in both size and microstructure with prolonged aging time and/or hydrothermal treatment.[137] This process occurs by Ostwald ripening wherein a population of nanoparticles grows at the expense of others that dissolve. During growth, there is a progressive (albeit not well understood) change in microstructure from an initially amorphous material to one that is more structured, but still lacks long-range order. During this process, silica condensation reduces the number of silanol groups, which increases solution pH. Interestingly, hydrothermal treatment of solutions S(I) and S(II) results in nearly identical pH. The same is true during the addition of

modifier, where the generation of R-OL and concomitant decrease in solution pH are identical for both growth solutions. This confirms that the mode of R-OL action on silicalite-1 growth is not attributed to differences in alkalinity.

We compared the temporal change in solution pH (**Figure 4.8A**) with powder X-ray diffraction (XRD) patterns of extracted solids at periodic times of silicalite-1 crystallization to determine if D-Arg decomposition occurs prior to nucleation. In the absence of modifier, the pH of solution S(II) increases with heating time and reaches a plateau within 4 h, whereas the pH of solution S(I) is relatively unchanged. In the presence of 3 wt% D-Arg, the pH of solution S(I) rapidly decreases from 12.3 to a steady value of 10.5 within 4 h of heating, which signals the completion of D-Arg decomposition to R-OL. For solution S(II), the presence of D-Arg resulted in an initial increase in pH ($t < 1$ h), followed by a decrease to a value that coincides with that of solution S(I). Powder XRD patterns of extracted solids (**Figure 4.8B**) reveal that the onset of Bragg peaks around 24 h of heating, which indicates that D-Arg decomposition occurs during the early stages of the induction period, well before nucleation. Conversely, *ex situ* analysis of powder XRD patterns of extracted solids from solution S(II) reveal Bragg peaks at 4 h of heating (**Figure C9**), which indicates that nucleation occurs prior to the complete decomposition of D-Arg. As such, we cannot preclude the potential involvement of D-Arg and other organics (i.e. the products of D-Arg thermal decomposition) during the early stages of silicalite-1 crystallization.

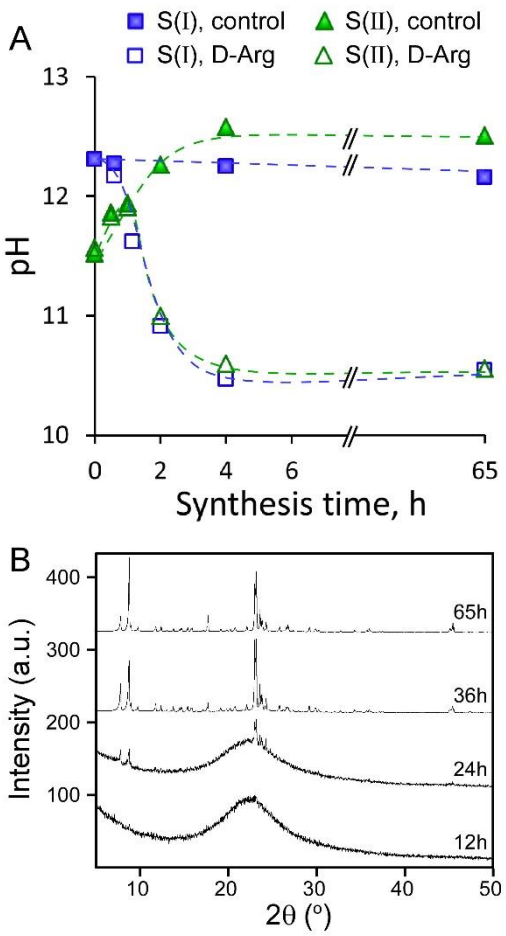

Figure 4.8: (A) *Ex situ* measurements of growth solution pH as a function of hydrothermal treatment time in the absence of D-Arg and in the presence of 3 wt% D-Arg **(B)** Powder XRD patterns of extracted solids from S(I) growth

We also investigated whether the incorporation of aluminum in the synthesis (leading to the formation of ZSM-5) would alter the effect of R-OL on zeolite crystallization. Using a S(II)'growth solution composition that was modified to include aluminum (Si/Al = 50), we observed a monotonic reduction in the relative thickness of ZSM-5 crystals with increasing D-Arg concentration (Figure C9). Interestingly, the change in crystal morphology is due to an increased [001] length of crystals, whereas the [010] thickness remained relatively unchanged by the presence of R-OL. This trend is opposite the one observed for silicalite-1 (**Figure 4.7C**), although the net result for both cases is qualitatively consistent in that R-OL leads to a reduction in the [010]/[001] ratio of MFI crystals. It is evident that additional experiments are required to

fully understand the impact of Al on MFI zeolite growth mechanisms in the absence and presence of modifiers. Moreover, it remains to be determined whether the introduction of R-OL alters zeolite nucleation or if the effect is solely attributed to changes in the anisotropic rates of crystal growth. In the next section, we discuss in more detail the potential impact of modifiers on zeolite nucleation.

4.2.3. Impact of modifier chirality.

Examples in prior literature have shown that enantiomers of a particular modifier can have markedly different effects on crystal growth, which can be attributed to changes in molecular recognition for binding to the surfaces of crystals and/or precursors.[294,295] The decomposition of D-Arg generates a single enantiomer, R-OL. Comparison of silicalite-1 growth in solutions containing R-OL and a racemic mixture, R/S-OL, reveals nearly identical trends (**Figure 4.2A**); however, the exact percentage of each enantiomer in the racemic mixture (obtained and used as received from the vendor) is unknown. To assess the potential differences in modifier chirality on silicalite-1 crystallization, we performed a synthesis with solution S(I) using 1 wt% of the enantiomer S-OL. Scanning electron micrographs reveal that crystals grown in the presence of R-OL (**Figure 4.2C**) and R/S-OL (**Figure 4.9A**) exhibit almost identical size and morphology; however, synthesis with S-OL (**Figure 4.9B**) results in an approximate order of magnitude reduction in crystal size (with a more uniform size distribution) and fewer defects associated with the presence of intergrowths on basal (010) surfaces.

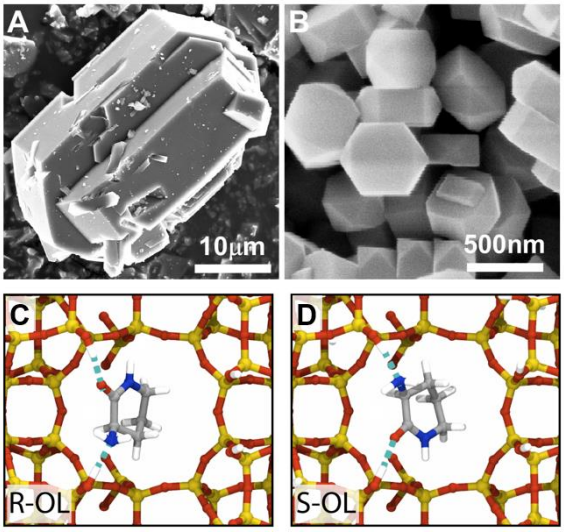

Figure 4.9: SEM images of silicalite-1 crystals prepared in solution S(I) with **(A)** 1 wt% R/S-OL and **(B)** 1 wt% S-OL. **(C and D)** Binding configurations for (C) R-OL and (D) S-OL on the (101) surface of silicalite-1 identified in USMD simulations.

To rationalize the effects of modifier chirality, USMD simulations were performed to characterize the interactions between S-OL and idealized surfaces of silicalite-1. The adsorption free energy profiles $F(z)$ for S-OL were found to be statistically indistinguishable from those calculated for R-OL, yielding binding energies similar to those reported in **Figure 4.6**. Moreover, inspection of the simulation trajectories suggests that the dominant binding configurations of the two enantiomers are energetically indistinguishable due to underlying symmetries of the silicalite-1 surfaces. This fact was confirmed by using energy minimization to characterize the binding conformation of the enantiomers *in vacuo*. On the (101) surface, for example, it was observed that R-OL and S-OL both favor conformations in which their aromatic ring resides in the primary surface pocket and their amine and carboxyl groups are each hydrogen bonded to a nearby silanol (**Figure 4.9C and D**). Despite the differences in chirality, the binding configurations for R-OL and S-OL are energetically similar due to the pocket's symmetry. Similar results were observed for the other surface of silicalite-1.

Experimental and modeling results indicate that the changes in crystal morphology cannot be explained by differences in the adsorption of R-OL and S-OL to the surfaces of silicalite-1 crystals. Previous investigations of other molecules have shown that interactions

between the adsorbate and extra-framework cations can result in enantioselective behavior in achiral zeolites.[296,297] It is possible that similar interactions, or the presence of surface defects that are expected during growth, which are not accounted for in the models examined here, could cause differences in adsorption of R-OL and S-OL and hence modifier chirality effects observed in experiment. However, it is more probable that S-OL impacts zeolite nucleation, which is consistent with the observed increase in crystal number density with a concomitant reduction in average crystal size (similar to the effects of reduced solution pH in the absence of modifiers; **Figure 4.5B**). The exact mechanism for this process is unknown and difficult to extract from *ex situ* measurements, but may involve interactions between S-OL and amorphous precursors that are distinctly different than those of R-OL.

4.2.4. Conclusions

In summary, we have identified a system that uniquely provides a way to direct the pathways of silicalite-1 growth. The decomposition of arginine and resulting reduction in solution pH acts as a switch that changes the predominant growth species. Few examples exist where the pathways of zeolite crystallization can be selectively shifted to classical modes governed by the addition of soluble species. The presence of multiple precursors in silicalite-1 growth solutions (i.e. monomer, oligomers, nanoparticles) renders it difficult to determine how modifiers impact processes of nucleation and crystal growth. Our findings seem to suggest that ornithine-lactam impedes the attachment of amorphous nanoparticles, thereby suppressing nonclassical pathways of crystallization.

Molecular dynamics simulations revealed unexpectedly low binding energies between modifiers and zeolite surfaces. These results seem to suggest that traditional viewpoints of crystal growth modifiers acting through preferential interactions with crystal surfaces are not solely responsible for their effects on zeolite formation. Indeed, we posit alternative modes of action involving modifier-precursor interactions that impede (or significantly slow) the rate of precursor

attachment to crystal surfaces. Molecular modeling of these interactions are difficult owing to the unknown microstructure of silica nanoparticles, and the fact that these species evolve with synthesis time. We hypothesize that there are distinct differences in the surface structures of silica precursors and silicalite-1 given the ability of S-OL to impact nucleation, which has been shown to occur through the aggregation of nanoparticles. Conversely, R-OL has a seemingly more pronounced effect on zeolite growth.

Collectively, these studies highlight the complexity of elucidating the role of modifiers in zeolite synthesis. It is evident that the judicious selection of modifiers can be a facile and highly efficient method of tailoring crystal size and morphology. Indeed, subtle changes in the functional groups and/or stereochemistry of modifiers can markedly change the nature of their mode(s) of action. To this end, continued studies are required to gain a more fundamental understanding of molecular modification in zeolite crystallization.

4.3. Material and methods

The following reagents were used for the preparation of zeolite growth solutions: tetrapropylammonium hydroxide (TPAOH, 40%, Alfa Aesar), tetraethylorthosilicate (TEOS, 98%, Sigma-Aldrich), and aluminum sulfate hydrate ($Al_2(SO_4)_3 \cdot 18H_2O$, 98%, Sigma-Aldrich). The following reagents were used as zeolite growth modifiers: D-arginine (D-Arg, 98% TLC, Sigma-Aldrich), (S)-3-aminopiperidine-2-one((S)-ornithine-lactam, Sigma-Aldrich), urea (EMD Chemicals Inc.), and 3-aminopiperidin-2-one(racemic ornithine-lactam, AK Scientific, Inc.). D-ornithine (Sigma-Aldrich) was used for thermal stability tests. Deionized (DI) water was produced with an Aqua Solutions RODI-C-12A purification system (18.2 MΩ). All reagents were used as received without further purification.

4.3.1. Materials

Silicalite-1 crystals were synthesized from two different clear growth solutions with molar compositions of 40 SiO_2:40 TPAOH:9420 H_2O:160 EtOH and 157 SiO_2:47 TPAOH:9420 H_2O:628 EtOH. These are referred to as growth solutions S(I) and S(II), respectively. The organic structure-directing agent TPAOH was added to DI water followed by the addition of the silica source, TEOS. The mixtures were aged at room temperature for two hours under continuous stirring. The ZGM of choice was added to the solution after aging, followed by an additional 10 min of stirring. The growth solution was then placed in a Teflon-lined stainless steel acid digestion bomb (Parr Instruments) and heated at 160°C under autogenous pressure for 65 h. For the synthesis of ZSM-5, we used a growth mixture with a molar composition of 157 SiO_2:1.57 Al_2O_3:47 TPAOH:9420 H_2O:628 EtOH:3 H_2SO_4. The protocol for ZSM-5 was identical to that of silicalite-1 with aluminum sulfate added after TPAOH. The pH of growth mixtures was measured with a Thermo Scientific Orion 3-Star pH meter and an Orion Ross Ultra electrode. The pH meter was calibrated with standardized pH 7, 10, and 12 buffer solutions (Orion).

4.3.2. Zeolite crystallization

Crystals were isolated from the supernatant by three cycles of centrifugation at 13,000 rpm for 45 min and washings with DI water. The solid phase was dried in air prior to characterization. Powder X-ray diffraction (XRD) patterns were collected on a Rigaku diffractometer using Cu Kα radiation (40kV, 40 mA). Scanning electron microscopy (SEM) was conducted at the Methodist Hospital Research Institute in the Department of Nanomedicine SEM Core using a Nova NanoSEM 230 instrument with ultrahigh resolution FESEM (operated at 15 kV and a 5-mm working distance).

4.3.3. Materials characterization

Crystals were isolated from the supernatant by three cycles of centrifugation at 13,000 rpm for 45 min and washings with DI water. The solid phase was dried in air prior to characterization. Powder X-ray diffraction (XRD) patterns were collected on a Rigaku diffractometer using Cu Kα radiation (40kV, 40 mA). Scanning electron microscopy (SEM) was conducted at the Methodist Hospital Research Institute in the Department of Nanomedicine SEM Core using a Nova NanoSEM 230 instrument with ultrahigh resolution FESEM (operated at 15 kV and a 5-mm working distance).

4.3.4. D-arginine decomposition.

A NaOH solution (pH 12.3) was made by mixing NaOH pellets with DI water. To this solution was added D-Arg and the mixture was heated at 160°C for 3 days. The solution was analyzed by high-resolution mass spectroscopy using an Orbitrap MS equipped with a TriVersa NanoMate nano-electrospray source to obtain the molecular weight information for the dissolved species in the mixtures. The resulting species were collected by air drying for carbon nuclear magnetic resonance (^{13}C NMR) measurements. All ^{13}C NMR were performed on a JOELECA-600 NMR spectrometer operating at 600 MHz in deuterated dimethyl sulfoxide (DMSO-d_6). The ^{13}C chemical shift was referenced to the DMSO-d_6 resonance at 39.5 ppm. The ^{13}C-NMR spectrum of R/S-ornithine-lactam(OL) in deuterated DMSO was used to confirm the product of D-Arg thermal decomposition. The stability of urea and D-ornithine was tested by heating a NaOH solution (pH 12.3) containing 3 wt% of urea or D-ornithine at 160 °C for 0 to 8 h. Deuterated DMSO (10 wt%) was added to each sample before NMR analysis.

4.3.5. Molecular modeling.

Umbrella sampling[298,299] molecular dynamics (USMD) simulations were conducted with GROMACS 4.6.7[300] to study the adsorption of modifiers on (010), (100) and (101) surfaces of

silicalite-1. Atoms in the silicalite-1 framework were described using the clay force field (ClayFF) of Cygan et al.,[301] and the SPC/E model[302] was used for water. The modifiers, R- and S-orinithine-lactum (R-OL and S-OL, respectively), were modeled using the generalized AMBER force field (GAFF),[303,304] with partial atomic charges derived using the RED III web server.[305] Standard Lorentz-Berthelot combining rules were used to specify potential parameters for unlike atoms. All interactions were truncated using a cutoff of 1.2 nm, and the particle mesh Ewald (PME) method was used to treat long-range electrostatics. Parameters for the PME method were chosen to ensure a relative error of less than 10^{-4} in the computed energy.

The silicalite-1 framework was modeled using crystallographic data (atomic positions and lattice parameters) from the International Zeolite Association database. The periodic unit cell of silicalite-1 was replicated to create a $3 \times 3 \times 3$ supercell. Model surfaces were created by cleaving the supercell along different crystallographic planes. The size of the simulation box was subsequently increased in the normal direction to expose the cleaving plane and create a region of vacuum approximately 8 nm in height above the surface. The cleaving planes were chosen to minimize the number of exposed SiO^- groups on each surface, creating terminations consistent with those observed in high-resolution transmission electron micrographs of ultra-thin silicalite-1 crystals by Tsapatsis and co-workers.[306] The alkaline conditions of the silicalite-1 growth solution were mimicked by randomly protonating under-coordinated surface oxygens to achieve an areal density of ~0.7 SiO^- per nm^2, in accord with estimates obtained by Emami et al.[307] from analyzing titration data for siliceous materials. Following the method reported by Kroutil et al.[308], excess surface charge was neutralized by distributing a counter charge over atoms in the bulk framework.

USMD simulations were conducted to compute the adsorption free energy profile (potential of mean force) $F(z)$, where z is the vertical distance between the zeolite surface and the center of mass of the sorbate. Initial configurations for the USMD simulations were prepared

by inserting a molecule (modifier) in the vacuum space above each surface and then solvating this region with SPC/E water. Solvation was followed by energy minimization using the steepest decent algorithm to remove pair-wise forces larger than 10 kJ mol^{-1} nm^{-1}. The system was subsequently equilibrated at ambient temperature and pressure for 5 ns in the NP_zT ensemble using the leapfrog algorithm with a 1 fs time step to integrate the equations of motion. Temperature was maintained using a Bussi-Parinello velocity rescaling thermostat[309] with a 0.2 ps time constant. A Parrinello-Rahman barostat[310] with a relaxation time of 1 ps was applied to the major axis (*z*-axis) of the simulation cell to impose a constant pressure (stress) in the direction normal to the zeolite surface. The equilibrated system was used to initialize USMD simulations in the *NVT* ensemble, with the *z*-dimension of the simulation cell fixed to the average value calculated from the last 2 ns of the NP_zT simulation. Independent USMD simulations were conducted in 50 windows along *z*. Sampling in each window was performed by applying a harmonic umbrella restraint along *z* with a spring constant of 2000 kJ mol^{-1} nm^{-2} using the PLUMED 2.2.1[311] plugin for GROMACS. The USMD simulations were run for 12 ns. Data from the last 5 ns in each window were analyzed using a Bayesian reformulation of the weighted histogram analysis method (BayesWHAM[312]) to obtain an unbiased estimate of $F(z)$ and the associated statistical uncertainties.

Chapter 5

Regulating Nonclassical Pathways of Silicalite-1 Crystallization through Controlled Evolution of Amorphous Precursors

5.1. Motivation

The widespread use of zeolites in commercial processes such as ion-exchange [313], adsorption [314], and catalysis [35,49,229,315] has stimulated efforts to optimize their physicochemical properties. Different strategies have been used to control zeolite crystallization, which include the design of sophisticated organic structure-directing agents (OSDAs) [316-322] and the judicious selection of synthesis conditions[249], such as growth solution composition and/or supersaturation.[120,323,324] The lack of fundamental understandings of zeolite crystal growth mechanisms is a significant obstacle for the *a priori* selection of synthesis conditions. This is due to in large part to the inherent complexity of zeolite crystallization from solutions comprised of multiple species, which renders the identification of growth units challenging. For instance, the presence of monomers, small oligomers, and amorphous nanoparticles allows for growth by a classical pathway (i.e. monomer-by-monomer addition) and/or nonclassical pathways involving gel [115,325] or solid-state transformations [252], the attachment of oligomers and larger precursors[323,326-329], or combinations thereof.[120]

In this study we focus on the siliceous zeolite silicalite-1 to better understand how organics influence the mode(s) of crystallization. Silicalite-1 and its aluminosilicate isostructure ZSM-5 both have a MFI framework consisting of 3-dimensional pores. ZSM-5 is one of the most widely used zeolites in commercial applications,[330] whereas silicalite-1 is commonly used as a model system for mechanistic studies of zeolite growth.[134,232,331-334] It is well established that silicalite-1 growth solutions are sols comprised of uniform silica nanoparticles (1 – 6 nm). These precursors are solvated amorphous silicates with OSDA molecules physisorbed on the exterior surfaces, thus forming core-shell structures **(Scheme 5.1**).[126,335] Upon heating, nanoparticles

evolve in both size and microstructure, but still lack long-range order.[127,137] It has been hypothesized that the degree to which nanoparticles structurally evolve leads to differences in their kinetic rates of attachment to silicalite-1 surfaces (k_i, **Scheme 5.1**).[127] In a previous study, we used *in situ* atomic force microscopy (AFM) to show that silicalite-1 growth occurs by a combination of classical and nonclassical pathways.[156] In a recent study by Shete et al.[336] it was shown that changes in the OSDA can suppress nonclassical growth by inhibiting nanoparticle attachment to yield desirable changes in crystal size and shape. These findings qualitatively agree with previous studies by our group showing that organic additives, referred to as zeolite growth modifiers (ZGMs), can hinder particle attachment with a similar effect on the anisotropic rates of zeolite crystallization.[328,337]

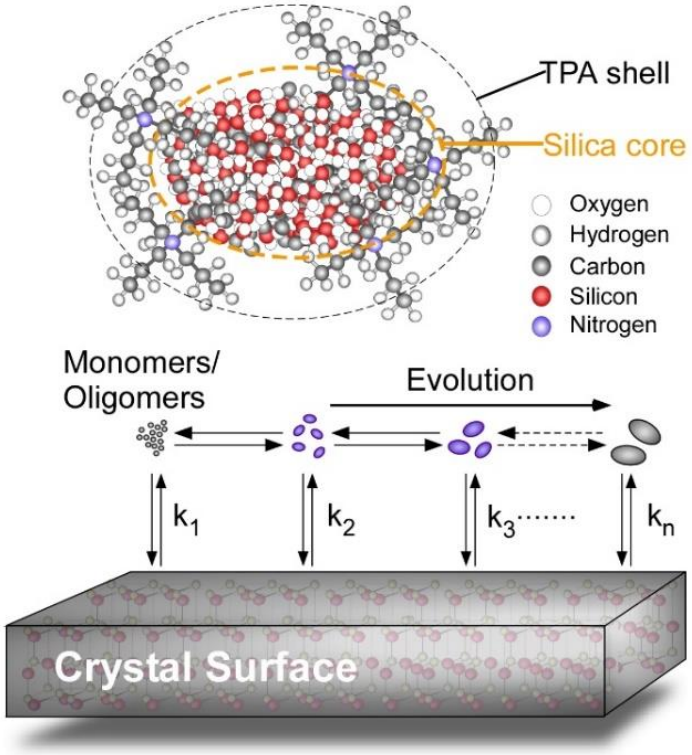

Scheme 5.1: (top) Idealized core-shell structure of as-synthesized nanoparticles with a shell of TPA molecules and a core of hydrated amorphous silica. (bottom) Putative pathways of silicalite-1 crystallization illustrating growth by monomer or oligomer addition

Herein we use a combination of experimental techniques to assess the degree to which nanoparticle structure influences nonclassical pathways. To this end, we investigate the impact of

various organic additives (OSDAs and ZGMs) on the extent of precursor evolution, and the degree to which structural changes influence precursor-precursor and precursor-crystal interactions. This study underlies a growing interest in zeolite synthesis with broad efforts to characterize growth species (i.e. soluble silicates and particulates) and elucidate their impact,[119,257] in combination with organics[119], on zeolite crystal growth. Using methods to assess the evolution of silica nanoparticles, we show that a switch from growth by particle attachment to one involving classical monomer addition is achieved by restricting the disorder-to-order transition of precursors during the early stages of synthesis.

5.2. Result and discussion

Here we use *in situ* atomic force microscopy (AFM) to monitor silicalite-1 (010) surface growth in the presence of various tetraalkylammonium (TAA) cations and tributylphosphine oxide (TBPO), a known zeolite growth modifier.[74,260] The most common TAA cation employed in silicalite-1 (MFI) synthesis is tetrapropylammonium (TPA), which functions as an OSDA. It has been shown that silicalite-1 can be prepared in the presence of either tetraethylamonium (TEA) when using crystalline MFI seeds[338] or tetrabutylammonium (TBA) that often leads to the formation of silicalite-2 (MEL) impurity.[338] To our knowledge, it is not possible to synthesize silicalite-1 using tetramethylammonium (TMA) as an OSDA.

In this study, we monitored silicalite-1 surfaces exposed to growth solutions of molar composition $48SiO_2$: 33TAA: $9500H_2O$: $192C_2H_5OH$ prepared with each of the four TAA molecules (**Figure 5.1**). Silicalite-1 crystals used as substrates for AFM studies are comprised of layers with step heights equal to 1 nm (**Figure D1**), one-half the unit cell of the MFI framework ($b/2$ = 0.99 nm). Exposing the substrate surface to growth solutions at 60 °C for 1 h reveals little change in topography when TAA = TMA (**Figure 5.1A**), TEA (**Figures 5.1C and D2**), and TBA **(Figures 5.1G and D3**); however, surfaces in contact with TPA-containing solutions (**Figures**

5.1E and D4) result in an incomplete coverage of attached silica nanoparticles. After 17 h of AFM imaging at discrete time intervals, we observe that TMA has little effect on the surface topography (**Figure 5.1B**) and the solution containing TEA (**Figure 5.1D**) results in few attached nanoparticles to the silicalite-1 surface (i.e. the original layers on the substrate are clearly visible). In solutions containing TPA and TBA, the original layers are indiscernible owing to a high coverage of attached nanoparticles (**Figure 5.1F and H**, respectively). These time-resolved studies indicate that TAA molecules can be grouped into two general categories: those that inhibit nanoparticle attachment (TMA and TEA) and those that enable attachment (TPA and TBA).

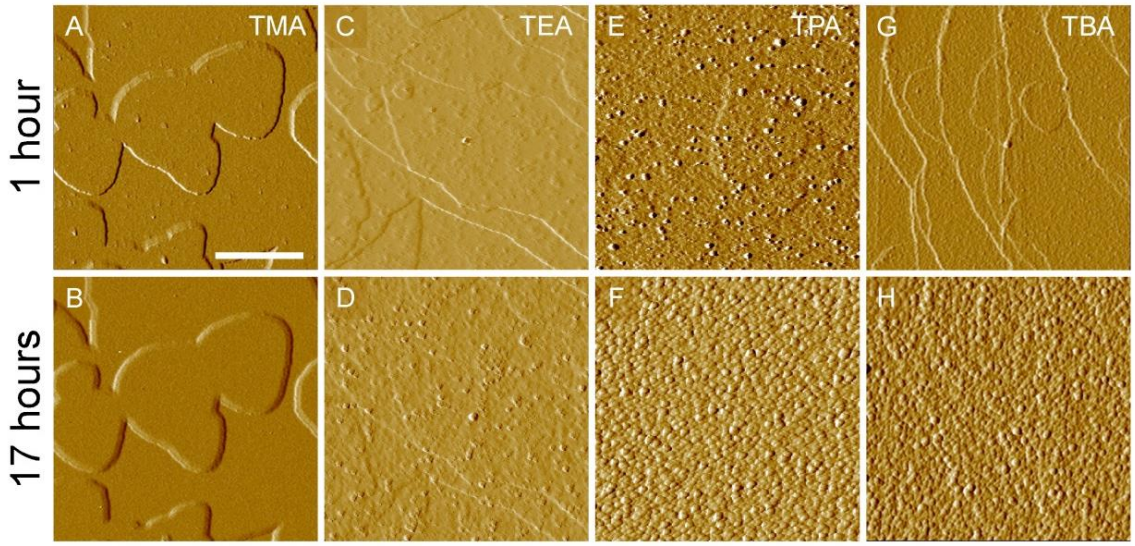

Figure 5.1: Time-resolved AFM images of silicalite-1 surfaces Measurements were performed in growth solutions with the following TAA molecules: **(A and B)** TMA, (**C and D)** TEA, **(E and F)** TPA, and **(G and H)** TBA. The scale bar equals 500 nm.

Prior calorimetry[128] and NMR studies[339] have shown that TPA is unique among TAA molecules. For instance, the enthalpy of formation for as-synthesized TPA-silica nanoparticles is ca. 20 kJ/mol SiO_2 compared to values of ca. 5 kJ/mol SiO_2 for other TAA molecules.[340] This is qualitatively consistent with our observation that TPA-nanoparticles are distinct in AFM measurements via their ability to readily attach to crystalline substrates (**Figure 5.1E**); however, at later stages of growth, once the surface has a nearly complete coverage of precursor particles, the rate of nanoparticle attachment significantly decreases. This is evident in Movie S1 that

shows the dynamics of silicalite-1 (010) surface growth during continuous *in situ* AFM imaging. We hypothesize that the observed switch between rapid and slow addition of precursors to silicalite-1 surfaces is attributed to the disorder-to-order transition of nanoparticles (post-attachment) that is necessary for the incorporation of amorphous precursors into the underlying crystal surface. This implies that the barriers for nanoparticle attachment to silicalite-1 (a crystalline interface) are less than its attachment to another nanoparticles (amorphous interfaces). This hypothesis agrees with the observed colloidal stability of precursors wherein prior studies have shown that isolated nanoparticles are observed throughout silicalite-1 crystallization, while relatively few nanoparticle aggregates are detected.[137] The latter have been identified as sites for nucleation,[127,341] which is consistent with nanoparticle aggregation being a rare event. Tsapatsis and coworkers[127] have postulated that evolved particles more readily attach to crystalline surfaces, which they demonstrated with TPA-nanoparticles and a mica substrate. This suggests that evolved nanoparticles, which possess a higher degree of order, more favorably attach to silicalite-1 surfaces (i.e. $k_n >> k_2$ in **Scheme 5.1**).

The fundamental basis for nanoparticle stability is not well understood. Colloidal models such as DLVO theory are incapable of predicting particle stability on the basis of surface charge.[134] Thus, non-DLVO forces (e.g. solvation or steric stability) likely play critical roles. For instance, TAA molecules form an exterior shell (Scheme 1) that can impart steric stabilization, but this alone has been shown to be insufficient to fully rationalize the stability of as-synthesized nanoparticles. Notably, substitution of TAA molecules with less bulky ions such as Na^+ lead to stable nanoparticles at room temperature,[342] whereas we observe that TAA molecules do hinder nanoparticle aggregation at higher temperatures. Another aspect of silica nanoparticles that is difficult to resolve is their microstructure and changes thereof during synthesis. Precursors are amorphous by X-ray diffraction, although variations in local order have been detected by spectroscopy (e.g. FTIR and NMR).[343] Electron microscopy, while able to detect amorphous-to-crystalline transitions in nanoparticle aggregates,[127,341] lacks the resolution to provide molecular

level details of precursor microstructure. Indirect methods, however, have been used to monitor changes in precursor structure. These approaches leverage the fact that silicates spanning from amorphous silica and zeolites to quartz exhibit sufficiently large differences in their rates (and enthalpies) of dissolution (**Figure D5**). Rimer et al. showed that as-synthesized silica nanoparticles have a rate of dissolution that lies between amorphous silica and silicalite-1; and that over the course of precursor evolution there is a monotonic reduction in the rate of dissolution towards that of silicalite-1. This observed shift in the rate of dissolution can be correlated to a disorder-to-order transition, although fully-evolved nanoparticles still lack long-range order.

Using dissolution assays as a surrogate to ascertain the net change in precursor microstructure, we quantified the kinetic rate of silica nanoparticle dissolution using small-angle X-ray scattering (SAXS) to track the temporal reduction in particle size. For these studies we used a more concentrated growth solution with higher nanoparticle number density. Excess TAAOH was added prior to the start of the experiment to increase solution pH, thereby initiating nanoparticle dissolution (**Figure D6**). Time-resolved SAXS patterns (**Figures 5.2A**) show a monotonic reduction in the scattering intensity at room temperature. The average size of nanoparticles was extracted from SAXS data using a previously reported protocol.[257] This procedure was repeated for all TAA molecules using growth solutions aged at room temperature (0 h) and those heated at 60 °C for 5 h to assess the difference between as-synthesized and evolved nanoparticles, respectively.

We observe several trends in the dissolution rates (**Figure 5.2B**) for various TAA ions. First, the dissolution rate of as-synthesized nanoparticles decreases with reduced TAA alkyl chain length in the following order: TBA >> TPA > TEA > TMA. Prior studies of silica dissolution in MOH solutions (where M = Na^+ or K^+) have demonstrated that the kinetics are significantly impacted by the selection of the alkali metal;[71] therefore, we anticipate that the TAA shell surrounding silica nanoparticles has a distinct effect on the rate of dissolution depending on the

length of its alkyl group, which can account for the differences among as-synthesized samples in **Figure 5.2B**.

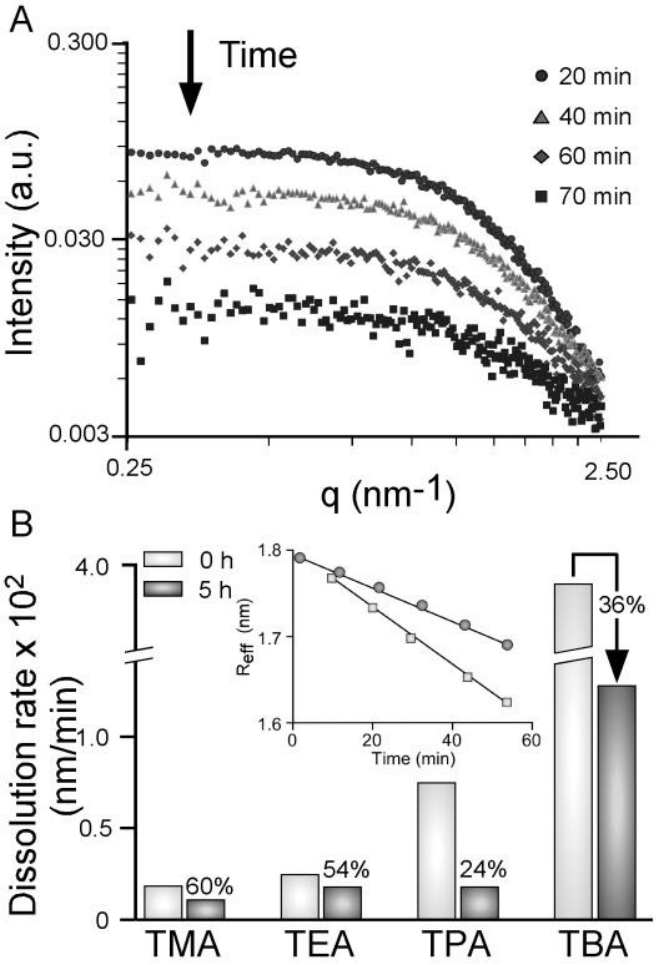

Figure 5.2: (**A**) Time-resolved SAXS patterns of as-synthesized TPA-nanoparticles dissolved at 25 °C. **(B)** Dissolution rate of as-synthesized (0 h) and evolved (5 h at 60 °C) TAA-nanoparticles. The percentage change in dissolution rate is denoted for each sample

We also observed a reduction in the rate of silica dissolution for all evolved TAA-nanoparticles (**Figure 5.2B**), which indicates a change in nanoparticle microstructure. Interestingly, the percent reduction in the rate of dissolution (0 h vs. 5 h) differs among the TAA molecules, which implies that the organics impact the degree to which nanoparticles evolve. By normalizing the dissolution rates for each TAA (i.e. dividing the rate of the evolved sample by its corresponding as-synthesized sample), we assessed the degree to which TAA molecules impact nanoparticle evolution. There is an apparent demarcation between data sets around 50% reduction

in the rate of dissolution whereby TAA molecules that inhibit nanoparticle attachment to silicalite-1 surfaces (TMA and TEA) result in<50% reduction in silica nanoparticle dissolution rate. This suggests that TAA-nanoparticles evolving to a lesser extent (i.e. those that retain a more amorphous-like quality) are less likely to attach to silicalite-1 surfaces. Conversely, TAA molecules (TPA and TBA) that exhibit a more significant reduction in the rate of dissolution (>50%) have a greater tendency to attach to silicalite-1 surfaces. This is consistent with the hypothesis that more ordered (or structurally-evolved) nanoparticles have lower energetic barriers for their attachment to crystalline interfaces.

To further explore the effect of TAA molecules on silica nanoparticle evolution, we performed a colloidal stability assay to characterize nanoparticle-nanoparticle interactions. Based on prior observations that evolved nanoparticles exhibit a greater propensity to attach to a crystalline interface, we posit that the colloidal stability of silica nanoparticles progressively decreases with increased microstructural evolution. To test this hypothesis, we performed critical coagulation concentration (CCC) experiments wherein the ionic strength of silicalite-1 growth solutions was increased by the addition of NaCl. In these studies, Na^+ cations screen the electrostatic repulsion between negatively-charged silica nanoparticles, thus leading to their coagulation at a threshold salt concentration. Unlike traditional CCC experiments that observe nearly instantaneous coagulation of colloidal particles upon the introduction of salt, our experiments reveal a kinetic effect where the onset of coagulation occurs after an induction period that decreases with increasing salt concentration. The induction period also varies among TAA molecules, which likely reflects different timescales needed for alkali ions to displace adsorbed TAA cations on nanoparticle surfaces. Coagulation was monitored using UV-Vis to track the temporal change in absorbance of growth solutions. As shown in **Figure 5.3A**, there is a sigmoidal increase in UV-Vis absorbance after the addition of NaCl. The increase in absorbance is indicative of growth by nanoparticle coagulation that ceases once the solution becomes a gel (indicated by the plateau in absorbance). At low salt concentration (0.5 M NaCl), there is no

detectable absorbance until ca. 100 min; however, high salt concentrations (e.g. 0.8 M NaCl) result in a nearly instantaneous increase in absorbance. With increasing salt concentration for a given TAA molecule, we observe distinct trends in the induction period (**Figure D7A**), the rate at which the absorbance increases approximately linearly with time (**Figure D8**), and the final plateau in absorbance at longer times (**Figure D8**). When comparing growth solutions containing different TAA molecules, we use a fixed salt concentration (0.53 M NaCl) and estimate the onset of coagulation by extrapolating the linear increase in absorbance to the baseline, referred to as the *coagulation time* (**Figure 5.3B**).

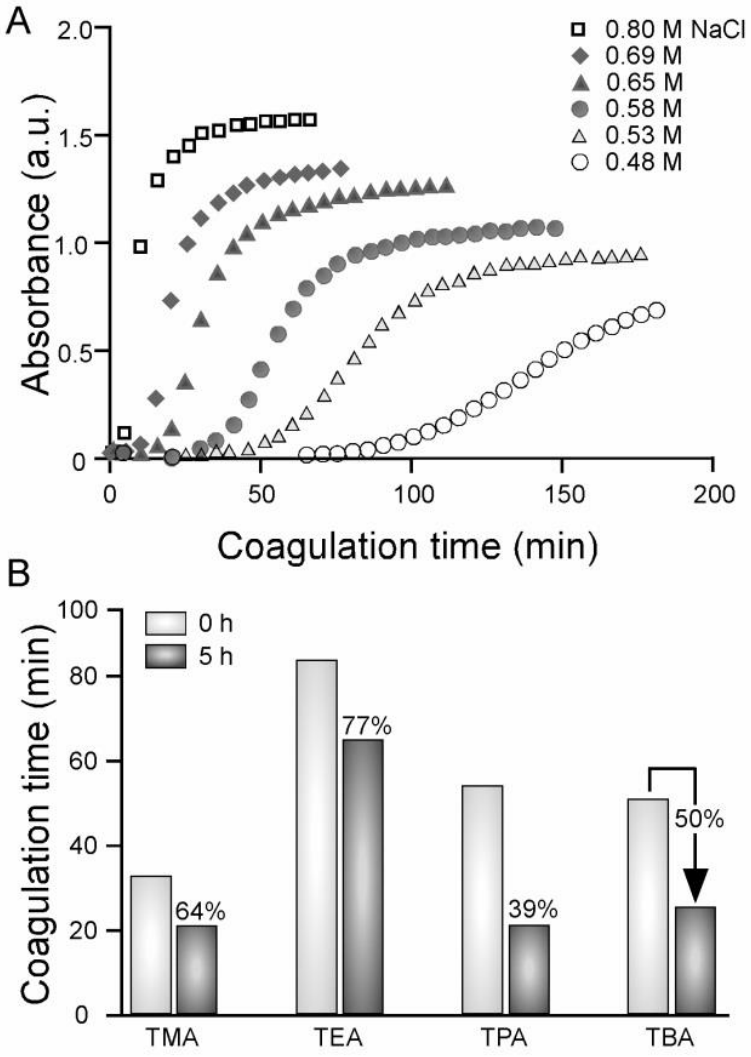

Figure 5.3: (A) UV-Vis absorbance measurements of TPA-nanoparticle suspensions with different amounts of NaCl added to the growth solution. **(B)** Coagulation times for growth solutions as-synthesized and evolved TAA-nanoparticles

Unlike trends in dissolution rates, the coagulation times for as-synthesized silica nanoparticles do not exhibit a clear trend with respect to TAA size (i.e. TEA >> TPA ≈ TBA > TMA). We hypothesize that these differences are attributed to at least two effects that cannot be easily discerned from CCC measurements: differences in the coverage of TAA molecules on nanoparticles surfaces and/or the energetic barriers for Na^+ ions to displace TAA cations. One consistent trend is that all evolved samples exhibit a reduced coagulation time, which agrees with data in **Figure 5.2B** indicating a reduction in nanoparticle stability with increased structural

evolution. For each TAA-nanoparticle growth solution, the coagulation time monotonically decreases with increased heating time (**Figure D7B**). Similar to dissolution studies, we compared the difference in coagulation time between evolved particles (5 h heating) and their corresponding as-synthesized particles (0 h). Interestingly, colloidal stability assays also reveal an apparent 50% demarcation where TAA molecules that lead to less than 50% reduction in coagulation time (TMA and TEA) inhibit nanoparticle attachment to silicalite-1 surfaces, while TAA molecules (TPA and TBA) that exhibit larger reductions in coagulation time enable nanoparticle attachment. To our knowledge, this is the first demonstration that colloidal stability assays can be used as a proxy for dissolution studies to assess the relative extent of precursor evolution.

Our findings suggest that the transition between a classical pathway (molecule attachment) and a nonclassical pathway (nanoparticle attachment) of silicalite-1 growth is governed by the degree to which silica precursors evolve. We previously posited that a similar switch between these two modes of growth is achieved using ZGMs. For example, we showed that organics such as TBPO (**Figure 5.4A**, inset) can alter the anisotropic growth of silicalite-1 crystals, leading to reduced thickness along the [010] direction.[260] We proposed a mechanism of steric hindrance wherein TBPO preferentially adsorbs on (010) surfaces and hinders the attachment of TPA-nanoparticles. This is consistent with *in situ* AFM measurements (**Figure D10**) that show a reduction in the root mean square (RMS) roughness of silicalite-1 (010) surfaces with increasing TBPO concentration (**Figure 5.4A**). In the absence of modifier, the increased RMS roughness with time is attributed to a progressive accumulation of TPA-nanoparticles on the crystal surface, which creates a roughened interface (**Figure 5.1**). In the presence of TBPO, there is a reduction in the magnitude of RMS roughness as well as a reduced slope of roughness versus time. While this is consistent with the hypothesis that TBPO blocks nanoparticle attachment to silicalite-1 surfaces, we also observe that the ZGM hinders precursor evolution. Notably, the dissolution rate (**Figure 5.4B**) and coagulation time (**Figure 5.4C**) are both reduced by approximately 50%, which corresponds to the apparent boundary identified in

Figures 5.2 and 5.3 demarcating growth by nanoparticle attachment. The fact that TBPO-nanoparticles lie at the boundary explains why we observe a reduction in nanoparticle attachment, but not complete inhibition. Therefore, it appears that the mechanism for ZGM action is related to its ability to slow the rate of precursor evolution. While we cannot fully rule out the previously proposed mechanism of steric hindrance, recent studies by Rimer and collaborators[337] have shown that the binding energy of several ZGMs on silicalite-1 surfaces is weaker than expected. Therefore, the extent to which ZGM adsorption on zeolite surfaces influences nanoparticle attachment remains elusive.

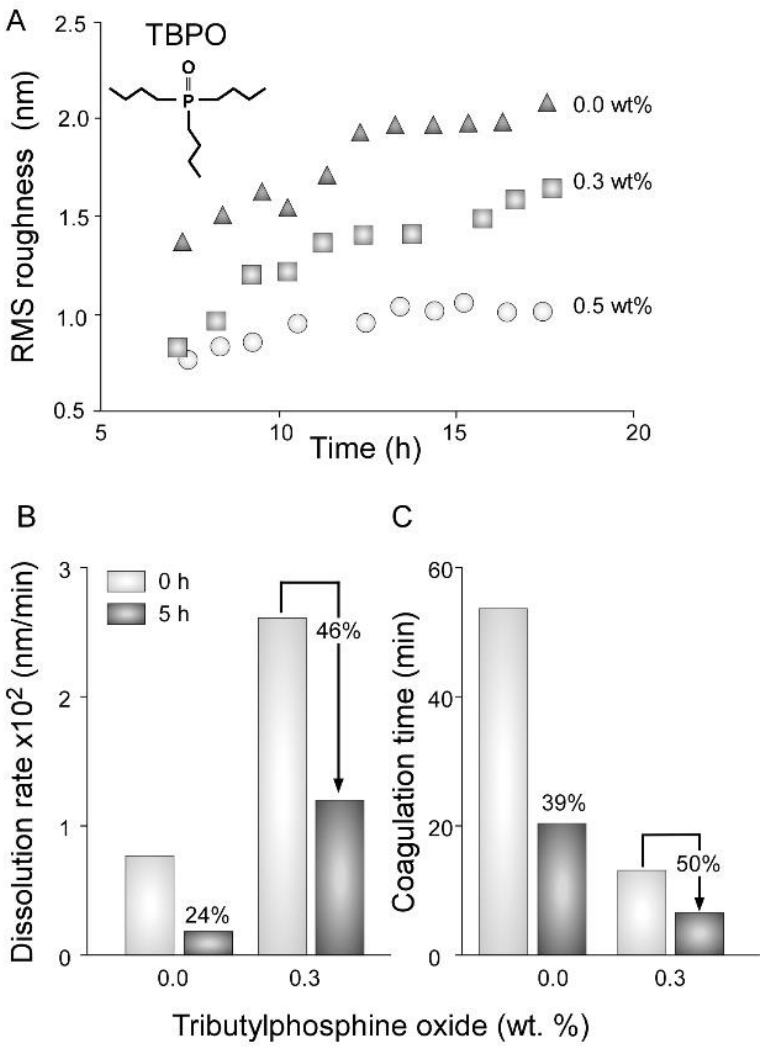

Figure 5.4: (A) Temporal change in the roughness of a silicalite-1 surface area. Comparison of the **(B)** dissolution rate and **(C)** coagulation time of as-synthesized and evolved TPA-nanoparticles. The number on each bar denotes the percentage reduction

In summary, we provide evidence showing how organic structure-directing agents and modifiers mediate pathways of silicalite-1 crystallization. Prior studies have demonstrated that the ability of organics to switch the predominant mode of silicalite-1 growth from a nonclassical to classical mechanism has practical advantages for reducing growth along the b-direction, thus leading to thinner crystals that improve their performance, for example, as silicalite-1 membranes or ZSM-5 catalysts, owing to reduced internal diffusion limitations along straight channels

oriented in the [010] direction.[86] In this study, we show that the ability to alter silica nanoparticle evolution is a critical factor in the regulation of silicalite-1 growth pathways. It is evident from our findings that the crystallization of silicalite-1 via monomer addition can be achieved by preserving the amorphous nature of as-synthesized precursors. A significant challenge that remains is the ability to resolve structural features of silica nanoparticles at mesoscopic length scales, which is not yet possible using conventional microscopy, diffraction, or spectroscopy techniques. Here we present two alternative methods of characterization – dissolution and colloidal stability – that can be used as indirect methods of assessing the relative change in nanoparticle microstructure, thus serving as approximate descriptors for predicting the predominant mode(s) of silicalite-1 crystallization.

5.3. Material and methods

5.3.1. Preparation of zeolite substrates

Large silicalite-1 crystals (ca. 25 μm) were synthesized using a previously reported protocol[121] from a growth solution containing the molar ratio $40SiO_2$: 40TPAOH: $9500H_2O$: $160C_2H_5OH$. The following reagents were used for the preparation of the growth solutions: tetrapropylammonium hydroxide (TPAOH, 40%, Alfa Aesar) and tetraethylorthosilicate (TEOS, 98%, Sigma-Aldrich). Deionized (DI) water was produced with an Aqua Solutions RODI-C-12A purification system (18.2 MΩ). All reagents were used as received without further purification

The organic structure-directing agent TPA was added to deionized water followed by dropwise addition of the silica source, TEOS. The mixture was stirred at room temperature for 2 h, and was then placed in a Teflon-lined stainless steel acid digestion bomb (Parr Instruments) and heated at 160°C under autogenous pressure in a ThermoFisher Precision Premium 3050 Series gravity oven without stirring or rotation. After heating for 65 h, the solution was quenched to room temperature and the crystals were isolated using a 1-μm GHP filter (Pall Corporation)

and washed multiple times with DI water. These crystals served as substrates for all atomic force microscopy (AFM) experiments.

5.3.2. Preparation of growth solutions

The growth solutions used for *in situ* AFM experiments were prepared as 60 g mixtures with molar compositions of $48SiO_2$: 33TAAOH: $9500H_2O$: 192 C_2H_5OH (where TAA = tetraalkylammonium). The following reagents were used as TAA molecules: tetramethylammonium hydroxide (TMAOH, 25% Sigma Aldrich), tetraethylammonium hydroxide (TEAOH, 35% Sigma Aldrich), TPAOH (same as above), and tetrabutylammonium hydroxide (TBAOH, 40% Sigma Aldrich). Each TAAOH reagent was added to de-gassed DI water followed by dropwise addition of TEOS. The mixtures were stirred at room temperature overnight. The solutions were filtered twice, using a 25-mm syringe filter fitted with a 0.45-μm nylon membrane (VWR International) before injection into the AFM closed cell.

5.3.3. Atomic force microscopy

All *in situ* AFM measurements were performed on an Asylum Research Cypher ES instrument (Santa Barbara, CA) equipped with a liquid sample cell for imaging at high temperatures. Silicalite-1 substrates were firmly placed on 15-mm specimen disks (Ted Pella, Inc.) with their basal (010) surfaces normal to the plane of imaging using quickset Loctite epoxy (Henkel Corporation) that was cured in an oven at 50 °C for 24 h. The sample was then removed from the oven and cooled to ambient temperature in air. The sample was rinsed with DI water and dried under inert Ar gas to remove loosely bound crystals. The sample was then placed in a closed AFM liquid cell holder. AFM images were collected using a Cr/Au-coated silicon nitride cantilever (Olympus RC800PB with a spring constant of 0.80 N m^{-1}). The substrate was first scanned in air to locate a desired imaging area. AFM images were collected in tapping mode to minimize tip–substrate contact at a scan rate of 2 Hz and 256 lines per scan.

After locating areas on the silicalite-1 substrate for *in situ* AFM measurements, the growth solution was introduced into the liquid cell using a syringe pump (Razel Scientific Instruments, Model R100-E) at a flow rate of 1.2 cm^3 h^{-1}. The sample was left to equilibrate in the solution at room temperature for ca. 30 min prior to imaging. The temperature of the AFM liquid cell was then increased to a predetermined set point at rate of 1°C /min^{-1}. AFM images were collected in tapping mode at time intervals of 1 h. In order to rule out potential tip interference, we compared random areas on the substrate and measured the root mean square (RMS) roughness among the different sampling areas (see **Figure D11**).

We tracked the temporal change surface roughness of the (010) surface of silicalite-1 crystals during *in situ* AFM measurements to compare the rate of nanoparticle attachment. The RMS roughness was calculated using the height image data for 500 x 500 nm^2 area. We measured RMS roughness values (Figure 4A) using three AFM images for each time point.

5.3.4. Dissolution and colloidal stability assays

Growth solutions were prepared with a higher number density of silica nanoparticles (relative to solutions used for AFM studies) by preparing mixtures with molar composition $40SiO_2$: 9TAAOH: $9500H_2O$: 192 C_2H_5OH (using the aforementioned protocol). The solutions were stirred overnight and filtered with a 0.45-μm nylon membrane (VWR International) prior to analysis. We denote solutions aged at room temperature as containing "as-synthesized" nanoparticles. Thermal treatment of these solutions was carried out by placing 10 mL of solution in a sealed propylene tube at 60°C in a water bath (Julabo ED version 2). Individual samples were removed at various times and quenched in an ice bath. These samples are referred to as "evolved" nanoparticles.

Dissolution assays were performed using *in situ* small-angle X-ray scattering (SAXS) to monitor the temporal reduction in silica nanoparticle size. The dissolution of silica nanoparticles was induced by increasing pH via the addition of excess TAAOH to the solutions while stirring in

an ice bath. The adjusted TAAOH concentration for these measurements was 0.3 M. To monitor the temporal change in nanoparticle size, the solutions were injected into a clean SAXS sample holder (1.5-mm quartz capillary cell) and scattering patterns were collected under vacuum at 25 °C for every 10 min using a Rigaku S-MAX3000 instrument (CuKα radiation $\lambda = 1.54$ Å; $q = 0.008$–0.24 Å^{-1}). Calibrations of the scattering vector q and beam center were performed on raw data using the SAXS gui software provided by Rigaku and a reference pattern from a AgBeh standard that was collected for 500 s. A background measurement (pure DI water) was subtracted from each sample. The SasView software was used to fit SAXS patterns. Using an established method reported by Lobo, Vlachos, and Rimer, an oblate ellipsoid form factor, P(q), was used to model SAXS patterns and estimate the radii for the a-axis, R_a, and b-axis, R_b, of the ellipsoid as

$$P_E(q,R,\varepsilon) = \int_0^{\pi/2} \left(\frac{3\cdot[\sin(qr(R,\varepsilon,\alpha)) - qr(R,\varepsilon,\alpha)cos(qr(R,\varepsilon,\alpha))]}{(qr(R,\varepsilon,\alpha))^2} \right)^2 \sin\alpha d\alpha. \quad \text{(S1)}$$

The solutions used for this study were sufficiently dilute to disregard the structure factor when fitting SAXS patterns (i.e. S(q) ≈1). In this study, we used an effective sphere radius, R_{eff}, obtained from the ellipsoidal volume as a measure of the average of particle size as

$$R_{eff} = (R_a \times {R_b}^2)^{\frac{1}{3}}. \quad \text{(S2)}$$

Colloidal stability assays were performed using a conventional critical coagulation concentration (CCC) analysis wherein sodium chloride salt was added to TAA-nanoparticle solutions. A stock solution of 5.4 M sodium chloride (NaCl, Alfa Aesar, 99.0%) was prepared by dissolving the salt in DI water. An aliquot (1 mL) of TAA-nanoparticle solution was placed in a plastic cuvette (3 mL). To this cuvette was added the salt solution by micropipette to give the

desired molarity. The temporal change in UV-Vis absorbance was measured in a Beckman Coulter DU 800 spectrophotometer at a wavelength of 500 nm at intervals of 5-10 min. The coagulation times were obtained by extrapolating the curves within the time period of linear increase in absorbance to the approximate baseline.

Chapter 6

Summary and future outlook

There has been considerable interest in zeolite synthesis with an overarching aim to improve the overall economics of zeolite-based processes. However, zeolite synthesis is more of an art rather than science despite the significant efforts by various research groups over the last several decades. There exists a substantial gap in our knowledge of zeolite crystallization, which occurs via complex pathways involving a range of precursors. This is further aggravated by a lack of suitable techniques to probe growth *in situ* with sufficient spatiotemporal resolution. Recently, Lupulescu et al. reported first *in situ* AFM measurements of zeolite growth under realistic synthesis conditions [121]. The objective of this thesis was to use this novel technique to advance our molecular level understanding of zeolite crystallization. We have selected silicalite-1 and zeolites A in this study with the goals to (i) identify the growth species and (ii) understand how major synthesis parameters affect their respective roles in nucleation and growth. We expect the result of this study would further our understanding of zeolite growth mechanisms and ultimately enable us to select synthesis conditions *a priori* to tailor the physicochemical properties (such as size, morphology, and Si/Al ratio) of zeolites.

In chapter 1, we probed zeolite A crystallization using *in situ* AFM and studied the effects of various synthesis parameters. The AFM study showed that zeolite A grows via diverse pathways. At low temperature, the growth occurs via the generation of 3D gel-like islands, which constitutes a novel nonclassical pathway. At high temperature and high supersaturation, nonclassical growth by oriented attachment of nanocrystals was observed. A decrease in supersaturation resulted in a switch in growth to 2D nucleation and layer propagation. Prior to these studies, the modes of growth have been inferred from *ex situ* analyses; however, with the advent of solvothermal AFM, these processes can be observed *in situ*. Furthermore, the study of

2D island nucleation on zeolite surfaces reveals the putative role of the composite building units in the zeolite A crystal growth.

In chapter 2, we extended these AFM studies of zeolite A crystal growth to low supersaturation. The surface of crystal substrates used for these measurements are laden with hillocks containing protrusions at their apex. The role of this protrusion in the formation of new layers is unknown; however, they are highly proficient at generating new layers, thereby leading to faster rates of growth in the direction normal to the interface. Our AFM studies at low supersaturation show that the protrusions promote 2D nucleation. Chemical analysis by NMR reveals that the growth solutions are predominantly comprised of monomeric species, and thus crystal growth occurs via monomer addition (in contrast to reported hypotheses in literature of the role of oligomers and composite building units). Moreover, our studies indicate that TMAOH, a common additive in zeolite A crystallization, promotes nonclassical growth via the generation of gel-like islands under the conditions where classical growth occurs in the absence of organics (using only NaOH). In summary, our study of zeolite A shows that its growth occurs via multiple pathways which can be controlled by conditions such as temperature, supersaturation, and organic additives. These methods to control the pathways of zeolite growth can also be leveraged to tune the final properties of the crystal.

Organic additives are often used in zeolite synthesis to optimize the physiochemical properties of final products. Our group has pioneered the use of zeolite growth modifiers (ZGMs) to tailor the shape and size of crystals and demonstrated their efficacy in syntheses of various frameworks. However, there still is a lack of understanding regarding their mode(s) of action. Often classical models of modifier-crystal interactions are invoked to explain their effect on crystal habit. Nonetheless, recent studies have shown that ZGMs affect zeolite growth in diverse ways [257,328]. Depending on synthesis conditions, they can either promote nucleation or have no apparent impact [257]. A critical parameter in the use of organics in zeolite synthesis is their thermal chemical stability during the reaction conditions. In chapter 4, we examined the mechanisms by

which a modifier alters the growth of silicalite-1 at high temperature. The modifier, D-arginine, decomposes at high temperature, resulting in decreased pH, shifting the growth from classical to nonclassical growth. Hence, this study showed that a modifier can also affect the supersaturation of the growth solution, thereby altering zeolite crystal growth. This new finding provides us with a unique tool to control the properties of zeolite crystals.

At low temperature, silicalite-1 crystallization proceeds by a predominantly nonclassical pathway. In chapter 5, we studied the effect of modifiers at low temperature and provided evidence of how organics can mediate nanoparticle precursor evolution and colloidal stability. Furthermore, we showed that the change in precursor microstructure is critical factor governing their attachment to crystal surfaces. Given the lack of analytical tools to probe the microstructure of the nanoparticle, we also reported a new method to assay the relative extent of precursor evolution.

One of the pervasive questions surrounding zeolite growth mechanisms has been the identity of active growth precursors with associated challenges to distinguish them from spectator species. *In situ* AFM studies of zeolite are critical to address these questions as they often provide direct evidence of the role of growth precursors, which can further enhance our understanding of zeolite growth. My research in this dissertation has provided an improved foundation for understanding zeolite crystallization, and in doing so has helped the ongoing endeavor to develop models which can be used to select synthesis conditions *a priori* in order to tailor the physicochemical properties of zeolites with some degree of predictability.

References

1 Weitkamp, J. Zeolites and catalysis. *Solid State Ionics* **131**, 175-188, doi:https://doi.org/10.1016/S0167-2738(00)00632-9 (2000).

2 Vogt, E. & Weckhuysen, B. Fluid catalytic cracking: recent developments on the grand old lady of zeolite catalysis. *Chem. Soc. Rev.* **44**, 7342-7370 (2015).

3 Venuto, P. B. & Habib Jr, E. T. Fluid catalytic cracking with zeolite catalysts. (1979).

4 Naber, J., Jong, K., Stork, W. & Kuipers, H. Zeolites and Related Microporous Materials: State of the Art 1994. *Stud. Surf. Sci. Catal.* **84**, 2197 (1994).

5 Dwyer, F. G. Catalysis of Organic Reactions. *Chemical Industries* **5**, 39 (1981).

6 Scherzer, J. & Gruia, A. J. *Hydrocracking science and technology*. (Crc Press, 1996).

7 https://www.grandviewresearch.com/industry-analysis/zeolites-market (2019).

8 Daramola, M. O., Aransiola, E. F. & Ojumu, T. V. Potential Applications of Zeolite Membranes in Reaction Coupling Separation Processes. *Materials* **5**, 2101-2136, doi:10.3390/ma5112101 (2012).

9 Cejka, J., Corma, A. & Zones, S. *Zeolites and catalysis: synthesis, reactions and applications*. (John Wiley & Sons, 2010).

10 Larsen, S. C. Nanocrystalline zeolites and zeolite structures: synthesis, characterization, and applications. *J. Phys. Chem. C* **111**, 18464-18474 (2007).

11 Moliner, M., Martínez, C. & Corma, A. Multipore zeolites: synthesis and catalytic applications. *Angew. Chem. Int. Ed.* **54**, 3560-3579 (2015).

12 Øye, G., Sjöblom, J. & Stöcker, M. Synthesis, characterization and potential applications of new materials in the mesoporous range. *Adv. Colloid Interface Sci.* **89**, 439-466 (2001).

13 Pina, M., Mallada, R., Arruebo, M., Urbiztondo, M., Navascués, N. d., De La Iglesia, O. & Santamaria, J. Zeolite films and membranes. Emerging applications. *Microporous Mesoporous Mater.* **144**, 19-27 (2011).

14 Ramesh, K. & Reddy, D. D. in *Advances in agronomy* Vol. 113 219-241 (Elsevier, 2011).

15 Tao, Y., Kanoh, H., Abrams, L. & Kaneko, K. Mesopore-modified zeolites: preparation, characterization, and applications. *Chem. Rev. (Washington, DC, U. S.)* **106**, 896-910 (2006).

16 Walcarius, A. Zeolite- modified electrodes: Analytical applications and prospects. *Electroanalysis* **8**, 971-986 (1996).

17 Yilmaz, B. & Müller, U. Catalytic applications of zeolites in chemical industry. *Top. Catal.* **52**, 888-895 (2009).

18 Auerbach, S. M., Carrado, K. A. & Dutta, P. K. *Handbook of zeolite science and technology*. (CRC press, 2003).

19 Kärger, J., Vasenkov, S. & Auerbach, S. M. in *Handbook of Zeolite Science and Technology* 458-560 (CRC Press, 2003).

20 Szostak, R. *Handbook of molecular sieves: structures*. (Springer Science & Business Media, 1992).

21 Davis, M. E. The Quest for Extra- Large Pore, Crystalline Molecular Sieves. *Chemistry–A European Journal* **3**, 1745-1750 (1997).

22 Wulfers, M. J., Teketel, S., Ipek, B. & Lobo, R. F. Conversion of methane to methanol on copper-containing small-pore zeolites and zeotypes. *Chem. Commun.* **51**, 4447-4450 (2015).

23 Zielinski, P., Van Neste, A., Akolekar, D. & Kaliaguine, S. Effect of high-energy ball milling on the structural stability, surface and catalytic properties of small-, medium-and large-pore zeolites. *Microporous Materials* **5**, 123-133 (1995).

24 https://www.kmizeolite.com/wp-content/uploads/2016/12/Hogg_Zeolites-Absorbents-Adsorbents-3.pdf

25 Fletcher, R. E., Ling, S. & Slater, B. Violations of Löwenstein's rule in zeolites. *Chemical Science* **8**, 7483-7491, doi:10.1039/c7sc02531a (2017).

26 Verdoliva, V., Saviano, M. & De Luca, S. Zeolites as Acid/Basic Solid Catalysts: Recent Synthetic Developments. *Catalysts* **9**, 248 (2019).

27 Basaldella, E. I., Vázquez, P. G., Iucolano, F. & Caputo, D. Chromium removal from water using LTA zeolites: effect of pH. *J. Colloid Interface Sci.* **313**, 574-578 (2007).

28 Yangxin, Y., Jin, Z. & Bayly, A. E. Development of surfactants and builders in detergent formulations. *Chin. J. Chem. Eng.* **16**, 517-527 (2008).

29 Guan, G., Kusakabe, K. & Morooka, S. Gas permeation properties of ion-exchanged LTA-type zeolite membranes. *Sep. Sci. Technol.* **36**, 2233-2245 (2001).

30 Palomino, M., Corma, A., Rey, F. & Valencia, S. New Insights on CO2− Methane separation using LTA zeolites with different Si/Al ratios and a first comparison with MOFs. *Langmuir* **26**, 1910-1917 (2009).

31 Beyaz Kayiran, S. & Lamari Darkrim, F. Synthesis and ionic exchanges of zeolites for gas adsorption. *Surface and Interface Analysis: An International Journal devoted to the development and application of techniques for the analysis of surfaces, interfaces and thin films* **34**, 100-104 (2002).

32 Karge, H. G. & Weitkamp, J. *Zeolites as catalysts, sorbents and detergent builders: applications and innovations*. Vol. 46 (Elsevier, 1989).

33 Davis, M. E. Zeolites and molecular sieves: not just ordinary catalysts. *Ind. Eng. Chem. Res.* **30**, 1675-1683 (1991).

34 Corma, A. State of the art and future challenges of zeolites as catalysts. *J. Catal.* **216**, 298-312 (2003).

35 Primo, A. & Garcia, H. Zeolites as catalysts in oil refining. *Chem. Soc. Rev.* **43**, 7548-7561, doi:10.1039/c3cs60394f (2014).

36 Vermeiren, W. & Gilson, J.-P. J. T. i. C. Impact of zeolites on the petroleum and petrochemical industry. **52**, 1131-1161 (2009).

37 Corma, A., Melo, F., Sauvanaud, L. & Ortega, F. Different process schemes for converting light straight run and fluid catalytic cracking naphthas in a FCC unit for maximum propylene production. *Appl. Catal., A* **265**, 195-206 (2004).

38 Jermy, B., Siddiqui, M., Aitani, A., Saeed, M. & Al-Khattaf, S. Utilization of ZSM-5/MCM-41 composite as FCC catalyst additive for enhancing propylene yield from VGO cracking. *J. Porous Mater.* **19**, 499-509 (2012).

39 Liu, H., Zhao, H., Gao, X. & Ma, J. A novel FCC catalyst synthesized via in situ overgrowth of NaY zeolite on kaolin microspheres for maximizing propylene yield. *Catal. Today* **125**, 163-168 (2007).

40 Wang, G., Xu, C. & Gao, J. Study of cracking FCC naphtha in a secondary riser of the FCC unit for maximum propylene production. *Fuel Process. Technol.* **89**, 864-873 (2008).

41 Gounder, R. & Moini, A. Automotive NO x abatement using zeolite-based technologies. *Reaction Chemistry & Engineering* (2019).

42 Bates, S. A., Verma, A. A., Paolucci, C., Parekh, A. A., Anggara, T., Yezerets, A., Schneider, W. F., Miller, J. T., Delgass, W. N. & Ribeiro, F. H. Identification of the active Cu site in standard selective catalytic reduction with ammonia on Cu-SSZ-13. *J. Catal.* **312**, 87-97, doi:10.1016/j.jcat.2014.01.004 (2014).

43 Deka, U., Lezcano-Gonzalez, I., Weckhuysen, B. M. & Beale, A. M. Local Environment and Nature of Cu Active Sites in Zeolite-Based Catalysts for the Selective Catalytic Reduction of NOx. *Acs Catalysis* **3**, 413-427, doi:10.1021/cs300794s (2013).

44 Davidova, M., Nachtigallova, D., Nachtigall, P. & Sauer, J. Nature of the Cu+-NO bond in the gas phase and at different types of Cu+ sites in zeolite catalysts. *J. Phys. Chem. B* **108**, 13674-13682, doi:10.1021/jp0478007 (2004).

45 Bulanek, R., Drobna, H., Nachtigall, P., Rubes, M. & Bludsky, O. On the site-specificity of polycarbonyl complexes in Cu/zeolites: combined experimental and DFT study. *Phys. Chem. Chem. Phys.* **8**, 5535-5542, doi:10.1039/b613805e (2006).

46 Beale, A. M., Gao, F., Lezcano-Gonzalez, I., Peden, C. H. F. & Szanyi, J. Recent advances in automotive catalysis for NOx emission control by small-pore microporous materials. *Chem. Soc. Rev.* **44**, 7371-7405, doi:10.1039/c5cs00108k (2015).

47 Ryu, T., Ahn, N. H., Seo, S., Cho, J., Kim, H., Jo, D., Park, G. T., Kim, P. S., Kim, C. H., Bruce, E. L., Wright, P. A., Nam, I.-S. & Hong, S. B. Fully Copper-Exchanged High-Silica LTA Zeolites as Unrivaled Hydrothermally Stable NH3-SCR Catalysts. *Angewandte Chemie International Edition* **56**, 3256-3260, doi:10.1002/anie.201610547 (2017).

48 Bulushev, D. A. & Ross, J. R. Catalysis for conversion of biomass to fuels via pyrolysis and gasification: a review. *Catal. Today* **171**, 1-13 (2011).

49 Jae, J., Tompsett, G. A., Foster, A. J., Hammond, K. D., Auerbach, S. M., Lobo, R. F. & Huber, G. W. Investigation into the shape selectivity of zeolite catalysts for biomass conversion. *J. Catal.* **279**, 257-268 (2011).

50 Perego, C. & Bosetti, A. Biomass to fuels: The role of zeolite and mesoporous materials. *Microporous Mesoporous Mater.* **144**, 28-39 (2011).

51 Taarning, E., Osmundsen, C. M., Yang, X., Voss, B., Andersen, S. I. & Christensen, C. H. Zeolite-catalyzed biomass conversion to fuels and chemicals. *Energy & Environmental Science* **4**, 793-804 (2011).

52 Hu, X. & Gholizadeh, M. Biomass pyrolysis: A review of the process development and challenges from initial researches up to the commercialisation stage. *Journal of Energy Chemistry* **39**, 109-143, doi:https://doi.org/10.1016/j.jechem.2019.01.024 (2019).

53 Pattiya, A., Titiloye, J. O. & Bridgwater, A. V. Fast pyrolysis of cassava rhizome in the presence of catalysts. *J. Anal. Appl. Pyrolysis* **81**, 72-79, doi:https://doi.org/10.1016/j.jaap.2007.09.002 (2008).

54 Zhou, C.-H., Xia, X., Lin, C.-X., Tong, D.-S. & Beltramini, J. Catalytic conversion of lignocellulosic biomass to fine chemicals and fuels. *Chem. Soc. Rev.* **40**, 5588-5617, doi:10.1039/c1cs15124j (2011).

55 Liang, T., Chen, J., Qin, Z., Li, J., Wang, P., Wang, S., Wang, G., Dong, M., Fan, W. & Wang, J. Conversion of Methanol to Olefins over H-ZSM-5 Zeolite: Reaction Pathway Is Related to the Framework Aluminum Siting. *Acs Catalysis* **6**, 7311-7325, doi:10.1021/acscatal.6b01771 (2016).

56 Li, J., Cao, W., Lv, X.-x., Jiang, L., Li, Y.-j., Li, W.-z., Chen, S.-z. & Li, X.-y. Zeolite-based hemostat QuikClot releases calcium into blood and promotes blood coagulation in vitro. *Acta Pharmacol. Sin.* **34**, 367-372, doi:10.1038/aps.2012.159 (2013).

57 Cai, L., Koziel, J. A., Liang, Y., Nguyen, A. T. & Xin, H. Evaluation of zeolite for control of odorants emissions from simulated poultry manure storage. *J. Environ. Qual.* **36**, 184-193 (2007).

58 Sethia, G., Somani, R. S. & Chand Bajaj, H. Adsorption of carbon monoxide, methane and nitrogen on alkaline earth metal ion exchanged zeolite-X: structure, cation position and adsorption relationship. *RSC Adv.* **5**, 12773-12781, doi:10.1039/c4ra11511b (2015).

59 Cheung, O. & Hedin, N. Zeolites and related sorbents with narrow pores for CO 2 separation from flue gas. *RSC Adv.* **4**, 14480-14494 (2014).

60 Ćurković, L., Cerjan-Stefanović, Š. & Filipan, T. Metal ion exchange by natural and modified zeolites. *Water Res.* **31**, 1379-1382 (1997).

61 Sherry, H. S. The ion-exchange properties of zeolites. I. Univalent ion exchange in synthetic faujasite. *J. Phys. Chem.* **70**, 1158-1168 (1966).

62 Borai, E., Harjula, R. & Paajanen, A. Efficient removal of cesium from low-level radioactive liquid waste using natural and impregnated zeolite minerals. *J. Hazard. Mater.* **172**, 416-422 (2009).

63 Yang, G., Wei, Y., Xu, S., Chen, J., Li, J., Liu, Z., Yu, J. & Xu, R. Nanosize-Enhanced Lifetime of SAPO-34 Catalysts in Methanol-to-Olefin Reactions. *J. Phys. Chem. C* **117**, 8214-8222, doi:10.1021/jp312857p (2013).

64 Oleksiak, M. D., Muraoka, K., Hsieh, M.-F., Conato, M. T., Shimojima, A., Okubo, T., Chaikittisilp, W. & Rimer, J. D. Organic-Free Synthesis of a Highly Siliceous Faujasite Zeolite with Spatially Biased Q4(nAl) Si Speciation. *Angew. Chem. Int. Ed.* **56**, 13366-13371, doi:10.1002/anie.201702672 (2017).

65 Vattipalli, V., Paracha, A. M., Hu, W., Chen, H. & Fan, W. Broadening the Scope for Fluoride-Free Synthesis of Siliceous Zeolites. *Angew. Chem. Int. Ed.* **57**, 3607-3611, doi:10.1002/anie.201712684 (2018).

66 Di Iorio, J. R. & Gounder, R. Controlling the Isolation and Pairing of Aluminum in Chabazite Zeolites Using Mixtures of Organic and Inorganic Structure-Directing Agents. *Chem. Mater.* **28**, 2236-2247, doi:10.1021/acs.chemmater.6b00181 (2016).

67 Yokoi, T., Mochizuki, H., Namba, S., Kondo, J. N. & Tatsumi, T. Control of the Al distribution in the framework of ZSM-5 zeolite and its evaluation by solid-state NMR technique and catalytic properties. *J. Phys. Chem. C* **119**, 15303-15315 (2015).

68 Gounder, R. & Iglesia, E. The catalytic diversity of zeolites: confinement and solvation effects within voids of molecular dimensions. *Chem. Commun.* **49**, 3491-3509 (2013).

69 Vjunov, A., Fulton, J. L., Camaioni, D. M., Hu, J. Z., Burton, S. D., Arslan, I. & Lercher, J. A. Impact of aqueous medium on zeolite framework integrity. *Chem. Mater.* **27**, 3533-3545 (2015).

70 Zhu, Q., Kondo, J. N., Ohnuma, R., Kubota, Y., Yamaguchi, M. & Tatsumi, T. The study of methanol-to-olefin over proton type aluminosilicate CHA zeolites. *Microporous Mesoporous Mater.* **112**, 153-161 (2008).

71 Chawla, A., Li, R., Jain, R., Clark, R. J., Sutjianto, J. G., Palmer, J. C. & Rimer, J. D. Cooperative effects of inorganic and organic structure-directing agents in ZSM-5 crystallization. *Molecular Systems Design & Engineering* **3**, 159-170 (2018).

72 Ghorbanpour, A., Gumidyala, A., Grabow, L. C., Crossley, S. P. & Rimer, J. D. Epitaxial Growth of ZSM-5@Silicalite-1: A Core–Shell Zeolite Designed with Passivated Surface Acidity. *ACS Nano* **9**, 4006-4016, doi:10.1021/acsnano.5b01308 (2015).

73 Rimer, J. D., Chawla, A. & Le, T. T. Crystal Engineering for Catalysis. *Annual review of chemical and biomolecular engineering* **9**, 283-309 (2018).

74 Lupulescu, A. I., Kumar, M. & Rimer, J. D. A Facile Strategy To Design Zeolite L Crystals with Tunable Morphology and Surface Architecture. *J. Am. Chem. Soc.* **135**, 6608-6617, doi:10.1021/ja4015277 (2013).

75 Lupulescu, A. I. & Rimer, J. D. Tailoring Silicalite- 1 Crystal Morphology with Molecular Modifiers. *Angew. Chem. Int. Ed.* **51**, 3345-3349 (2012).

76 Rimer, J., Kumar, M., Li, R., Lupulescu, A. & Oleksiak, M. Tailoring the physicochemical properties of zeolite catalysts. *Catal. Sci. Technol.* **4**, 3762-3771 (2014).

77 Na, K., Choi, M., Park, W., Sakamoto, Y., Terasaki, O. & Ryoo, R. Pillared MFI Zeolite Nanosheets of a Single-Unit-Cell Thickness. *J. Am. Chem. Soc.* **132**, 4169-4177, doi:10.1021/ja908382n (2010).

78 Awala, H., Gilson, J.-P., Retoux, R., Boullay, P., Goupil, J.-M., Valtchev, V. & Mintova, S. Template-free nanosized faujasite-type zeolites. *Nat. Mater.* **14**, 447 (2015).

79 Mintova, S., Gilson, J.-P. & Valtchev, V. Advances in nanosized zeolites. *Nanoscale* **5**, 6693-6703 (2013).

80 Möller, K., Yilmaz, B., Jacubinas, R. M., Müller, U. & Bein, T. One-step synthesis of hierarchical zeolite beta via network formation of uniform nanocrystals. *J. Am. Chem. Soc.* **133**, 5284-5295 (2011).

81 Verboekend, D. & Pérez-Ramírez, J. Design of hierarchical zeolite catalysts by desilication. *Catal. Sci. Technol.* **1**, 879-890 (2011).

82 Pérez- Ramírez, J., Verboekend, D., Bonilla, A. & Abelló, S. Zeolite catalysts with tunable hierarchy factor by pore- growth moderators. *Adv. Funct. Mater.* **19**, 3972-3979 (2009).

83 Yu, L., Huang, S., Miao, S., Chen, F., Zhang, S., Liu, Z., Xie, S. & Xu, L. A Facile Top-Down Protocol for Postsynthesis Modification of Hierarchical Aluminum- Rich MFI Zeolites. *Chemistry–A European Journal* **21**, 1048-1054 (2015).

84 García-Martínez, J., Johnson, M., Valla, J., Li, K. & Ying, J. Y. Mesostructured zeolite Y—high hydrothermal stability and superior FCC catalytic performance. *Catal. Sci. Technol.* **2**, 987-994 (2012).

85 Li, K., Valla, J. & Garcia- Martinez, J. Realizing the commercial potential of hierarchical zeolites: new opportunities in catalytic cracking. *ChemCatChem* **6**, 46-66 (2014).

86 Choi, M., Na, K., Kim, J., Sakamoto, Y., Terasaki, O. & Ryoo, R. Stable single-unit-cell nanosheets of zeolite MFI as active and long-lived catalysts. *Nature* **461**, 828, doi:10.1038/nature08493 (2009).

87 Fan, W., Snyder, M. A., Kumar, S., Lee, P.-S., Yoo, W. C., McCormick, A. V., Penn, R. L., Stein, A. & Tsapatsis, M. Hierarchical nanofabrication of microporous crystals with ordered mesoporosity. *Nat. Mater.* **7**, 984 (2008).

88 Maldonado, M., Oleksiak, M. D., Chinta, S. & Rimer, J. D. Controlling crystal polymorphism in organic-free synthesis of Na-zeolites. *J. Am. Chem. Soc.* **135**, 2641-2652 (2013).

89 Chandrasekhar, S., Satyanarayana, K., Pramada, P., Raghavan, P. & Gupta, T. Review processing, properties and applications of reactive silica from rice husk—an overview. *J. Mater. Sci.* **38**, 3159-3168 (2003).

90 Edelman, R. D., Kudalkar, D. V., Ong, T., Warzywoda, J. & Thompson, R. W. Crystallization phenomena in seeded zeolite syntheses. *Zeolites* **9**, 496-502 (1989).

91 Lassinantti, M., Hedlund, J. & Sterte, J. Faujasite-type films synthesized by seeding. *Microporous Mesoporous Mater.* **38**, 25-34 (2000).

92 Liu, Z., Zhu, J., Wakihara, T. & Okubo, T. Ultrafast synthesis of zeolites: breakthrough, progress and perspective. *Inorganic Chemistry Frontiers* **6**, 14-31 (2019).

93 Liu, Z., Okabe, K., Anand, C., Yonezawa, Y., Zhu, J., Yamada, H., Endo, A., Yanaba, Y., Yoshikawa, T. & Ohara, K. Continuous flow synthesis of ZSM-5 zeolite on the order of seconds. *Proceedings of the National Academy of Sciences* **113**, 14267-14271 (2016).

94 Querol, X., Alastuey, A., López-Soler, A., Plana, F., Andrés, J. M., Juan, R., Ferrer, P. & Ruiz, C. R. A fast method for recycling fly ash: microwave-assisted zeolite synthesis. *Environ. Sci. Technol.* **31**, 2527-2533 (1997).

95 Cundy, C. S. & Cox, P. A. The hydrothermal synthesis of zeolites: Precursors, intermediates and reaction mechanism. *Microporous Mesoporous Mater.* **82**, 1-78 (2005).

96 Piccione, P. M., Laberty, C., Yang, S., Camblor, M. A., Navrotsky, A. & Davis, M. E. Thermochemistry of pure-silica zeolites. *J. Phys. Chem. B* **104**, 10001-10011 (2000).

97 Rimer, J. D. & Tsapatsis, M. Nucleation of open framework materials: Navigating the voids. *MRS Bulletin* **41**, 393-398 (2016).

98 Li, R., Chawla, A., Linares, N., Sutjianto, J. G., Chapman, K. W., Martínez, J. G. & Rimer, J. D. Diverse Physical States of Amorphous Precursors in Zeolite Synthesis. *Ind. Eng. Chem. Res.* **57**, 8460-8471 (2018).

99 De Yoreo, J. J. & Vekilov, P. G. Principles of crystal nucleation and growth. *Rev. Mineral. Geochem.* **54**, 57-93 (2003).

100 Lim, I. H., Schrader, W. & Schüth, F. The formation of zeolites from solution–Analysis by mass spectrometry. *Microporous Mesoporous Mater.* **166**, 20-36 (2013).

101 Vekilov, P. G. Dense liquid precursor for the nucleation of ordered solid phases from solution. *Cryst. Growth Des.* **4**, 671-685 (2004).

102 De Yoreo, J. J., Gilbert, P. U., Sommerdijk, N. A., Penn, R. L., Whitelam, S., Joester, D., Zhang, H., Rimer, J. D., Navrotsky, A. & Banfield, J. F. Crystallization by particle attachment in synthetic, biogenic, and geologic environments. *Science* **349**, aaa6760 (2015).

103 Xu, R., Pang, W., Yu, J., Huo, Q. & Chen, J. *Chemistry of zeolites and related porous materials: synthesis and structure*. (John Wiley & Sons, 2009).

104 Cho, H., Felmy, A. R., Craciun, R., Keenum, J. P., Shah, N. & Dixon, D. A. Solution State Structure Determination of Silicate Oligomers by 29Si NMR Spectroscopy and Molecular Modeling. *J. Am. Chem. Soc.* **128**, 2324-2335, doi:10.1021/ja0559202 (2006).

105 Belton, D. J., Deschaume, O. & Perry, C. C. An overview of the fundamentals of the chemistry of silica with relevance to biosilicification and technological advances. *The FEBS journal* **279**, 1710-1720 (2012).

106 Kinrade, S. D. & Swaddle, T. W. J. I. C. Silicon-29 NMR studies of aqueous silicate solutions. 1. Chemical shifts and equilibria. **27**, 4253-4259 (1988).

107 Kinrade, S. D., Knight, C. T. G., Pole, D. L. & Syvitski, R. T. Silicon-29 NMR Studies of Tetraalkylammonium Silicate Solutions. 1. Equilibria, 29Si Chemical Shifts, and 29Si Relaxation. *Inorg. Chem.* **37**, 4272-4277, doi:10.1021/ic971629e (1998).

108 Swaddle, T. W., Salerno, J. & Tregloan, P. A. Aqueous aluminates, silicates, and aluminosilicates. *Chem. Soc. Rev.* **23**, 319-325 (1994).

109 Pelster, S. A., Weimann, B., Schaack, B. B., Schrader, W. & Schüth, F. Dynamics of silicate species in solution studied by mass spectrometry with isotopically labeled compounds. *Angew. Chem. Int. Ed.* **46**, 6674-6677 (2007).

110 Swaddle, T. W. Silicate complexes of aluminum (III) in aqueous systems. *Coord. Chem. Rev.* **219**, 665-686 (2001).

111 Xiong, G., Yu, Y., Feng, Z.-c., Xin, Q., Xiao, F.-S. & Li, C. UV Raman spectroscopic study on the synthesis mechanism of zeolite X. *Microporous Mesoporous Mater.* **42**, 317-323, doi:https://doi.org/10.1016/S1387-1811(00)00340-1 (2001).

112 Pelster, S. A., Kalamajka, R., Schrader, W. & Schüth, F. Monitoring the nucleation of zeolites by mass spectrometry. *Angew. Chem. Int. Ed.* **46**, 2299-2302 (2007).

113 Harris, R. K., Samadi-Maybodi, A. & Smith, W. The incorporation of aluminum into silicate ions in alkaline aqueous solutions, studied by aluminum-27 n.m.r. *Zeolites* **19**, 147-155, doi:https://doi.org/10.1016/S0144-2449(97)00060-2 (1997).

114 Ren, L., Li, C., Fan, F., Guo, Q., Liang, D., Feng, Z., Li, C., Li, S. & Xiao, F. S. UV–Raman and NMR spectroscopic studies on the crystallization of zeolite A and a new synthetic route. *Chemistry–A European Journal* **17**, 6162-6169 (2011).

115 Mintova, S., Olson, N. H., Valtchev, V. & Bein, T. Mechanism of Zeolite A Nanocrystal Growth from Colloids at Room Temperature. *Science* **283**, 958-960, doi:10.1126/science.283.5404.958 %J Science (1999).

116 Mintova, S., Olson, N. H. & Bein, T. Electron microscopy reveals the nucleation mechanism of zeolite Y from precursor colloids. *Angew. Chem. Int. Ed.* **38**, 3201-3204 (1999).

117 Davis, T. M., Drews, T. O., Ramanan, H., He, C., Dong, J., Schnablegger, H., Katsoulakis, M. A., Kokkoli, E., McCormick, A. V. & Penn, R. L. Mechanistic principles of nanoparticle evolution to zeolite crystals. *Nat. Mater.* **5**, 400 (2006).

118 Valtchev, V. P. & Bozhilov, K. N. Transmission electron microscopy study of the formation of FAU-type zeolite at room temperature. *J. Phys. Chem. B* **108**, 15587-15598 (2004).

119 Olafson, K. N., Li, R., Alamani, B. G. & Rimer, J. D. Engineering Crystal Modifiers: Bridging Classical and Nonclassical Crystallization. *Chem. Mater.* **28**, 8453-8465, doi:10.1021/acs.chemmater.6b03550 (2016).

120 De Yoreo, J. J., Gilbert, P. U. P. A., Sommerdijk, N. A. J. M., Penn, R. L., Whitelam, S., Joester, D., Zhang, H., Rimer, J. D., Navrotsky, A., Banfield, J. F., Wallace, A. F., Michel, F. M., Meldrum, F. C., Cölfen, H. & Dove, P. M. Crystallization by particle attachment in synthetic, biogenic, and geologic environments. *Science* **349**, aaa6760, doi:10.1126/science.aaa6760 (2015).

121 Lupulescu, A. I. & Rimer, J. D. In Situ Imaging of Silicalite-1 Surface Growth Reveals the Mechanism of Crystallization. **344**, 729-732, doi:10.1126/science.1250984 %J Science (2014).

122 Kumar, M., Li, R. & Rimer, J. D. Assembly and evolution of amorphous precursors in zeolite L crystallization. *Chem. Mater.* **28**, 1714-1727 (2016).

123 Fan, W., Duan, R.-G., Yokoi, T., Wu, P., Kubota, Y. & Tatsumi, T. Synthesis, crystallization mechanism, and catalytic properties of titanium-rich TS-1 free of extraframework titanium species. *J. Am. Chem. Soc.* **130**, 10150-10164 (2008).

124 Kumar, M., Luo, H., Román-Leshkov, Y. & Rimer, J. D. SSZ-13 crystallization by particle attachment and deterministic pathways to crystal size control. *J. Am. Chem. Soc.* **137**, 13007-13017 (2015).

125 Greer, H., Wheatley, P. S., Ashbrook, S. E., Morris, R. E. & Zhou, W. Early stage reversed crystal growth of zeolite A and its phase transformation to sodalite. *J. Am. Chem. Soc.* **131**, 17986-17992 (2009).

126 Fedeyko, J. M., Rimer, J. D., Lobo, R. F. & Vlachos, D. G. Spontaneous formation of silica nanoparticles in basic solutions of small tetraalkylammonium cations. *J. Phys. Chem. B* **108**, 12271-12275, doi:10.1021/jp047623+ (2004).

127 Davis, T. M., Drews, T. O., Ramanan, H., He, C., Dong, J., Schnablegger, H., Katsoulakis, M. A., Kokkoli, E., McCormick, A. V., Penn, R. L. & Tsapatsis, M. Mechanistic principles of nanoparticle evolution to zeolite crystals. *Nat. Mater.* **5**, 400-408, doi:10.1038/nmat1636 (2006).

128 Rimer, J. D., Trofymluk, O., Navrotsky, A., Lobo, R. F. & Vlachos, D. G. Kinetic and Thermodynamic Studies of Silica Nanoparticle Dissolution. *Chem. Mater.* **19**, 4189-4197, doi:10.1021/cm070708d (2007).

129 Shi, J., Anderson, M. W. & Carr, S. W. Direct observation of zeolite A synthesis by in situ solid-state NMR. *Chem. Mater.* **8**, 369-375 (1996).

130 Miladinović, Z. P., Zakrzewska, J., Kovačević, B. T. & Miladinović, J. M. In situ 27Al NMR kinetic investigation of zeolite A crystallization. *Microporous Mesoporous Mater.* **195**, 131-142, doi:https://doi.org/10.1016/j.micromeso.2014.04.022 (2014).

131 Ivanova, I. I., Kolyagin, Y. G., Kasyanov, I. A., Yakimov, A. V., Bok, T. O. & Zarubin, D. N. Time-Resolved In Situ MAS NMR Monitoring of the Nucleation and Growth of Zeolite BEA Catalysts under Hydrothermal Conditions. *Angew. Chem. Int. Ed.* **56**, 15344-15347, doi:10.1002/anie.201709039 (2017).

132 Aerts, A., Follens, L. R., Haouas, M., Caremans, T. P., Delsuc, M.-A., Loppinet, B., Vermant, J., Goderis, B., Taulelle, F. & Martens, J. A. Combined NMR, SAXS, and DLS study of concentrated clear solutions used in silicalite-1 zeolite synthesis. *Chem. Mater.* **19**, 3448-3454 (2007).

133 Aerts, A., Haouas, M., Caremans, T. P., Follens, L. R. A., van Erp, T. S., Taulelle, F., Vermant, J., Martens, J. A. & Kirschhock, C. E. A. Investigation of the Mechanism of Colloidal Silicalite-1 Crystallization by Using DLS, SAXS, and 29Si NMR Spectroscopy. *Chemistry – A European Journal* **16**, 2764-2774, doi:10.1002/chem.200901688 (2010).

134 Nikolakis, V., Kokkoli, E., Tirrell, M., Tsapatsis, M. & Vlachos, D. G. Zeolite Growth by Addition of Subcolloidal Particles: Modeling and Experimental Validation. *Chem. Mater*. **12**, 845-853, doi:10.1021/cm990653i (2000).

135 Mintova, S., Olson, N. H., Valtchev, V. & Bein, T. Mechanism of Zeolite A Nanocrystal Growth from Colloids at Room Temperature. **283**, 958-960, doi:10.1126/science.283.5404.958 %J Science (1999).

136 Fan, W., Ogura, M., Sankar, G. & Okubo, T. In situ Small-Angle and Wide-Angle X-ray Scattering Investigation on Nucleation and Crystal Growth of Nanosized Zeolite A. *Chem. Mater.* **19**, 1906-1917, doi:10.1021/cm062827j (2007).

137 Rimer, J. D., Vlachos, D. G. & Lobo, R. F. Evolution of Self-Assembled Silica−Tetrapropylammonium Nanoparticles at Elevated Temperatures. *J. Phys. Chem. B* **109**, 12762-12771, doi:10.1021/jp052045y (2005).

138 Savitz, S., Siperstein, F., Gorte, R. J. & Myers, A. L. Calorimetric Study of Adsorption of Alkanes in High-Silica Zeolites. *J. Phys. Chem. B* **102**, 6865-6872, doi:10.1021/jp981836f (1998).

139 Brabants, G., Lieben, S., Breynaert, E., Reichel, E., Taulelle, F., Martens, J., Jakoby, B. & Kirschhock, C. Monitoring early zeolite formation via in situ electrochemical impedance spectroscopy. *Chem. Commun.* **52**, 5478-5481 (2016).

140 Chung, J., Granja, I., Taylor, M. G., Mpourmpakis, G., Asplin, J. R. & Rimer, J. D. Molecular modifiers reveal a mechanism of pathological crystal growth inhibition. *Nature* **536**, 446 (2016).

141 Agger, J. R., Hanif, N., Cundy, C. S., Wade, A. P., Dennison, S., Rawlinson, P. A. & Anderson, M. W. Silicalite Crystal Growth Investigated by Atomic Force Microscopy. *J. Am. Chem. Soc.* **125**, 830-839, doi:10.1021/ja020899f (2003).

142 Agger, J. R., Pervaiz, N., Cheetham, A. K. & Anderson, M. W. Crystallization in zeolite A studied by atomic force microscopy. *J. Am. Chem. Soc.* **120**, 10754-10759, doi:10.1021/ja981665s (1998).

143 Anderson, M. W., Agger, J. R., Thornton, J. T. & Forsyth, N. Crystal Growth in Zeolite Y Revealed by Atomic Force Microscopy. *Angewandte Chemie International Edition in English* **35**, 1210-1213, doi:10.1002/anie.199612101 (1996).

144 Brent, R. & Anderson, M. W. in *Stud. Surf. Sci. Catal.* Vol. 174 (eds Antoine Gédéon, Pascale Massiani, & Florence Babonneau) 909-912 (Elsevier, 2008).

145 Scandella, L., Kruse, N. & Prins, R. Imaging of zeolite surface structures by atomic force microscopy. *Surf. Sci.* **281**, L331-L334, doi:https://doi.org/10.1016/0039-6028(93)90631-S (1993).

146 Itzel Meza, L., Anderson, M. W., Slater, B. & Agger, J. R. In situ atomic force microscopy of zeolite A dissolution. *Phys. Chem. Chem. Phys.* **10**, 5066-5076, doi:10.1039/b804857f (2008).

147 Cubillas, P., Etherington, K., Anderson, M. W. & Attfield, M. P. Crystal growth of MOF-5 using secondary building units studied by in situ atomic force microscopy. *CrystEngComm* **16**, 9834-9841 (2014).

148 Habraken, W., Tao, J. H., Brylka, L. J., Friedrich, H., Bertinetti, L., Schenk, A. S., Verch, A., Dmitrovic, V., Bomans, P. H. H., Frederik, P. M., Laven, J., van der Schoot, P., Aichmayer, B., de With, G., DeYoreo, J. J. & Sommerdijk, N. Ion-association complexes unite classical and non-classical theories for the biomimetic nucleation of calcium phosphate. *Nature Communications* **4**, doi:10.1038/ncomms2490 (2013).

149 Zhang, L., Roling, L. T., Wang, X., Vara, M., Chi, M., Liu, J., Choi, S.-I., Park, J., Herron, J. A., Xie, Z., Mavrikakis, M. & Xia, Y. Platinum-based nanocages with subnanometer-thick walls and well-defined, controllable facets. *Science* **349**, 412-416, doi:10.1126/science.aab0801 (2015).

150 Zheng, J. P., Birktoft, J. J., Chen, Y., Wang, T., Sha, R. J., Constantinou, P. E., Ginell, S. L., Mao, C. D. & Seeman, N. C. From molecular to macroscopic via the rational design of a self-assembled 3D DNA crystal. *Nature* **461**, 74-77, doi:10.1038/nature08274 (2009).

151 De Yoreo, J. J., Gilbert, P. U. P. A., Sommerdijk, N. A. J. M., Penn, R. L., Whitelam, S., Joester, D., Zhang, H., Rimer, J. D., Navrotsky, A., Banfield, J. F., Wallace, A. F., Michel, F. M., Meldrum, F. C., Cölfen, H. & Dove, P. M. Crystallization by particle attachment in synthetic, biogenic, and geologic environments. *Science* **349**, doi:10.1126/science.aaa6760 (2015).

152 Nielsen, M. H., Aloni, S. & De Yoreo, J. J. In situ TEM imaging of CaCO3 nucleation reveals coexistence of direct and indirect pathways. *Science* **345**, 1158-1162, doi:10.1126/science.1254051 (2014).

153 Liao, H. G., Cui, L. K., Whitelam, S. & Zheng, H. M. Real-Time Imaging of Pt3Fe Nanorod Growth in Solution. *Science* **336**, 1011-1014, doi:10.1126/science.1219185 (2012).

154 Banfield, J. F., Welch, S. A., Zhang, H. Z., Ebert, T. T. & Penn, R. L. Aggregation-based crystal growth and microstructure development in natural iron oxyhydroxide biomineralization products. *Science* **289**, 751-754, doi:10.1126/science.289.5480.751 (2000).

155 Aerts, A., Kirschhock, C. E. & Martens, J. A. Methods for in situ spectroscopic probing of the synthesis of a zeolite. *Chem Soc Rev* **39**, 4626-4642, doi:10.1039/b919704b (2010).

156 Lupulescu, A. I. & Rimer, J. D. In Situ Imaging of Silicalite-1 Surface Growth Reveals the Mechanism of Crystallization. *Science* **344**, 729-732, doi:10.1126/science.1250984 (2014).

157 Shete, M., Kumar, M., Kim, D. H., Rangnekar, N., Xu, D. D., Topuz, B., Agrawal, K. V., Karapetrova, E., Stottrup, B., Al-Thabaiti, S., Basahel, S., Narasimharao, K., Rimer, J. D. & Tsapatsis, M. Nanoscale Control of Homoepitaxial Growth on a Two-Dimensional Zeolite. *Angew. Chem.-Int. Edit.* **56**, 535-539, doi:10.1002/anie.201607063 (2017).

158 Kumar, M., Luo, H., Roman-Leshkov, Y. & Rimer, J. D. SSZ-13 crystallization by particle attachment and deterministic pathways to crystal size control. *J. Am. Chem. Soc.* **137**, 13007-13017, doi:10.1021/jacs.5b07477 (2015).

159 Davis, T. M., Drews, T. O., Ramanan, H., He, C., Dong, J., Schnablegger, H., Katsoulakis, M. A., Kokkoli, E., McCormick, A. V., Penn, R. L. & Tsapatsis, M. Mechanistic principles of nanoparticle evolution to zeolite crystals. *Nat Mater* **5**, 400-408, doi:10.1038/nmat1636 (2006).

160 Kumar, S., Davis, T. M., Ramanan, H., Penn, R. L. & Tsapatsis, M. Aggregative growth of silicalite-1. *Journal of Physical Chemistry B* **111**, 3398-3403, doi:10.1021/jp0677445 (2007).

161 Mintova, S., Olson, N. H. & Bein, T. Electron microscopy reveals the nucleation mechanism of zeolite Y from precursor colloids. *Angew Chem Int Ed Engl* **38**, 3201-3204 (1999).

162 Ren, N., Subotic, B., Bronic, J., Tang, Y., Sikiric, M. D., Misic, T., Svetlicic, V., Bosnar, S. & Jelic, T. A. Unusual Pathway of Crystallization of Zeolite ZSM-5 in a Heterogeneous System: Phenomenology and Starting Considerations. *Chem. Mat.* **24**, 1726-1737, doi:10.1021/cm203194v (2012).

163 Corma, A., Rey, F., Rius, J., Sabater, M. J. & Valencia, S. Supramolecular self-assembled molecules as organic directing agent for synthesis of zeolites. *Nature* **431**, 287-290 (2004).

164 Smaihi, M., Barida, O. & Valtchev, V. Investigation of the crystallization stages of LTA-type zeolite by complementary characterization techniqnes. *Eur J Inorg Chem*, 4370-4377, doi:10.1002/ejic.200300154 (2003).

165 Fan, W., Meneau, F., Bras, W., Ogura, M., Sankar, G. & Okubo, T. Effects of silicon sources on the formation of nanosized LTA: An in situ small angle X-ray scattering and wide angle X-ray scattering study. *Microporous Mesoporous Mat.* **101**, 134-141, doi:10.1016/j.micromeso.2006.10.007 (2007).

166 Sugiyama, S., Yamamoto, S., Matsuoka, O., Nozoye, H., Yu, J., Zhu, G., Qiu, S. & Terasaki, I. AFM observation of double 4-rings on zeolite LTA crystals surface. *Micropor. Mesopor. Mater.* **28**, 1-7, doi:10.1016/s1387-1811(98)00271-6 (1999).

167 Dumrul, S., Bazzana, S., Warzywoda, J., Biederman, R. R. & Sacco, A. Imaging of crystal growth-induced fine surface features in zeolite A by atomic force microscopy. *Microporous Mesoporous Mat.* **54**, 79-88, doi:10.1016/s1387-1811(02)00354-2 (2002).

168 Yang, C. S., Mora-Fonz, J. M. & Catlow, C. R. A. Modeling the nucleation of zeolite A. *J. Phys. Chem. C* **117**, 24796-24803, doi:10.1021/jp4050034 (2013).

169 Van Speybroeck, V., Hemelsoet, K., Joos, L., Waroquier, M., Bell, R. G. & Catlow, C. R. A. Advances in theory and their application within the field of zeolite chemistry. *Chemical Society Reviews* **44**, 7044-7111, doi:10.1039/c5cs00029g (2015).

170 Mintova, S., Olson, N. H., Valtchev, V. & Bein, T. Mechanism of zeolite A nanocrystal growth from colloids at room temperature. *Science* **283**, 958-960 (1999).

171 Valtchev, V. P. & Bozhilov, K. N. Evidences for zeolite nucleation at the solid-liquid interface of gel cavities. *J. Am. Chem. Soc.* **127**, 16171-16177, doi:10.1021/ja0546267 (2005).

172 Ren, L., Li, C., Fan, F., Guo, Q., Liang, D., Feng, Z., Li, S. & Xiao, F. S. UV-Raman and NMR spectroscopic studies on the crystallization of zeolite A and a new synthetic route. *Chemistry* **17**, 6162-6169, doi:10.1002/chem.201100098 (2011).

173 Xiao, Y. C., Sheng, N., Chu, Y. Y., Wang, Y. Q., Wu, Q. M., Liu, X. L., Deng, F., Meng, X. J. & Feng, Z. C. Mechanism on solvent-free crystallization of NaA zeolite. *Microporous Mesoporous Mat.* **237**, 201-209, doi:10.1016/j.micromeso.2016.09.029 (2017).

174 Oleksiak, M. D., Soltis, J. A., Conato, M. T., Penn, R. L. & Rimer, J. D. Nucleation of FAU and LTA zeolites from heterogeneous aluminosilicate precursors. *Chem. Mat.* **28**, 4906-4916, doi:10.1021/acs.chemmater.6b01000 (2016).

175 Fan, W., O'Brien, M., Ogura, M., Sanchez-Sanchez, M., Martin, C., Meneau, F., Kurumada, K., Sankar, G. & Okubo, T. In situ observation of homogeneous nucleation of nanosized zeolite A. *Phys. Chem. Chem. Phys.* **8**, 1335-1339, doi:10.1039/b510963a (2006).

176 Kragten, D. D., Fedeyko, J. M., Sawant, K. R., Rimer, J. D., Vlachos, D. G., Lobo, R. F. & Tsapatsis, M. Structure of the silica phase extracted from silica/(TPA)OH solutions containing nanoparticles. *J. Phys. Chem. B* **107**, 10006-10016, doi:10.1021/jp035110h (2003).

177 de Moor, P., Beelen, T. P. M., Komanschek, B. U., Diat, O. & van Santen, R. A. In situ investigation of Si-TPA-MFI crystallization using (ultra-) small- and wide-angle X-ray scattering. *Journal of Physical Chemistry B* **101**, 11077-11086, doi:10.1021/jp9724784 (1997).

178 Watson, J. N., Iton, L. E. & White, J. W. In situ observation of the growth of silicalite nuclei by small-angle X-ray and neutron scattering. *Chemical Communications*, 2767-2768, doi:10.1039/cc9960002767 (1996).

179 Butt, H. J., Cappella, B. & Kappl, M. Force measurements with the atomic force microscope: Technique, interpretation and applications. *Surf. Sci. Rep.* **59**, 1-152, doi:10.1016/j.surfrep.2005.08.003 (2005).

180 Pera, I., Stark, R., Kappl, M., Butt, H. J. & Benfenati, F. Using the atomic force microscope to study the interaction between two solid supported lipid bilayers and the influence of synapsin I. *Biophysical Journal* **87**, 2446-2455, doi:10.1529/biophysj.104.044214 (2004).

181 Li, D. S., Nielsen, M. H., Lee, J. R. I., Frandsen, C., Banfield, J. F. & De Yoreo, J. J. Direction-Specific Interactions Control Crystal Growth by Oriented Attachment. *Science* **336**, 1014-1018, doi:10.1126/science.1219643 (2012).

182 Cubillas, P., Stevens, S. M., Blake, N., Umemura, A., Chong, C. B., Terasaki, O. & Anderson, M. W. AFM and HRSEM invesitigation of zeolite A crystal growth. Part 1: In the absence of organic additives. *J. Phys. Chem. C* **115**, 12567-12574, doi:10.1021/jp2032862 (2011).

183 Itzel Meza, L., Anderson, M. W., Slater, B. & Agger, J. R. In situ atomic force microscopy of zeolite A dissolution. *Phys. Chem. Chem. Phys.* **10**, 5066-5076, doi:10.1039/b804857f (2008).

184 Park, M. B., Lee, Y., Zheng, A. M., Xiao, F. S., Nicholas, C. P., Lewis, G. J. & Hong, S. B. Formation pathway for LTA zeolite crystals synthesized via a charge density mismatch approach. *J. Am. Chem. Soc.* **135**, 2248-2255, doi:10.1021/ja309831e (2013).

185 Wakihara, T., Sasaki, Y., Kato, H., Ikuhara, Y. & Okubo, T. Investigation of the surface structure of zeolite A. *Phys. Chem. Chem. Phys.* **7**, 3416-3418 (2005).

186 Slater, B., Titiloye, J. O., Higgins, F. M. & Parker, S. C. Atomistic simulation of zeolite surfaces. *Curr. Opin. Solid State Mat. Sci.* **5**, 417-424, doi:10.1016/s1359-0286(01)00039-0 (2001).

187 Cuppen, H. M., Meekes, H., van Enckevort, W. J. P., Vissers, G. W. M. & Vlieg, E. Kinetic roughening of Kossel and non-Kossel steps. *Surf Sci* **569**, 33-46, doi:10.1016/j.susc.2004.07.010 (2004).

188 Halpinhealy, T. & Zhang, Y. C. Kinetic roughening phenomena, stochastic growth directed polymers and all that - aspects of multidisciplinary statistical-mechanics. *Physics Reports-Review Section of Physics Letters* **254**, 215-415, doi:10.1016/0370-1573(94)00087-j (1995).

189 Tilbury, C. J. & Doherty, M. F. Modeling Layered Crystal Growth at Increasing Supersaturation by Connecting Growth Regimes. *Aiche J.* **63**, 1338-1352, doi:10.1002/aic.15617 (2017).

190 Noy, A., Vezenov, D. V. & Lieber, C. M. Chemical force microscopy. *Annu. Rev. Mater. Sci.* **27**, 381-421, doi:10.1146/annurev.matsci.27.1.381 (1997).

191 Frisbie, C. D., Rozsnyai, L. F., Noy, A., Wrighton, M. S. & Lieber, C. M. Functional-group imaging by chemical force microscopy. *Science* **265**, 2071-2074, doi:10.1126/science.265.5181.2071 (1994).

192 Noy, A. Chemical force microscopy of chemical and biological interactions. *Surf. Interface Anal.* **38**, 1429-1441, doi:10.1002/sia.2374 (2006).

193 Rief, M., Gautel, M., Oesterhelt, F., Fernandez, J. M. & Gaub, H. E. Reversible unfolding of individual titin immunoglobulin domains by AFM. *Science* **276**, 1109-1112, doi:10.1126/science.276.5315.1109 (1997).

194 Bao, G. & Suresh, S. Cell and molecular mechanics of biological materials. *Nat. Mater.* **2**, 715-725, doi:10.1038/nmat1001 (2003).

195 Strunz, T., Oroszlan, K., Schafer, R. & Guntherodt, H. J. Dynamic force spectroscopy of single DNA molecules. *Proc. Natl. Acad. Sci. U. S. A.* **96**, 11277-11282, doi:10.1073/pnas.96.20.11277 (1999).

196 Evans, E. Probing the relation between force - Lifetime - and chemistry in single molecular bonds. *Annu. Rev. Biophys. Biomolec. Struct.* **30**, 105-128, doi:10.1146/annurev.biophys.30.1.105 (2001).

197 Carrion-Vazquez, M., Oberhauser, A. F., Fowler, S. B., Marszalek, P. E., Broedel, S. E., Clarke, J. & Fernandez, J. M. Mechanical and chemical unfolding of a single protein: A comparison. *Proc. Natl. Acad. Sci. U. S. A.* **96**, 3694-3699, doi:10.1073/pnas.96.7.3694 (1999).

198 del Rio, A., Perez-Jimenez, R., Liu, R., Roca-Cusachs, P., Fernandez, J. M. & Sheetz, M. P. Stretching Single Talin Rod Molecules Activates Vinculin Binding. *Science* **323**, 638-641, doi:10.1126/science.1162912 (2009).

199 Wong, S. S., Joselevich, E., Woolley, A. T., Cheung, C. L. & Lieber, C. M. Covalently functionalized nanotubes as nanometre-sized probes in chemistry and biology. *Nature* **394**, 52-55 (1998).

200 Noy, A. & Friddle, R. W. Practical single molecule force spectroscopy: How to determine fundamental thermodynamic parameters of intermolecular bonds with an atomic force microscope. *Methods* **60**, 142-150, doi:10.1016/j.ymeth.2013.03.014 (2013).

201 Friddle, R. W., Noy, A. & De Yoreo, J. J. Interpreting the widespread nonlinear force spectra of intermolecular bonds. *Proc. Natl. Acad. Sci. U. S. A.* **109**, 13573-13578, doi:10.1073/pnas.1202946109 (2012).

202 Friddle, R. W., Battle, K., Trubetskoy, V., Tao, J. H., Salter, E. A., Moradian-Oldak, J., De Yoreo, J. J. & Wierzbicki, A. Single-molecule determination of the face-specific adsorption of amelogenin's C-terminus on Hydroxyapatite. *Angew. Chem.-Int. Edit.* **50**, 7541-7545, doi:10.1002/anie.201100181 (2011).

203 Noy, A., Zepeda, S., Orme, C. A., Yeh, Y. & De Yoreo, J. J. Entropic barriers in nanoscale adhesion studied by variable temperature chemical force microscopy. *J. Am. Chem. Soc.* **125**, 1356-1362, doi:10.1021/ja026865p (2003).

204 Friddle, R. W., Podsiadlo, P., Artyukhin, A. B. & Noy, A. Near-equilibrium chemical force microscopy. *J. Phys. Chem. C* **112**, 4986-4990, doi:10.1021/jp7095967 (2008).

205 Rief, M., Fernandez, J. M. & Gaub, H. E. Elastically coupled two-level systems as a model for biopolymer extensibility. *Phys. Rev. Lett.* **81**, 4764-4767, doi:10.1103/PhysRevLett.81.4764 (1998).

206 Garcia-Manyes, S. & Sanz, F. Nanomechanics of lipid bilayers by force spectroscopy with AFM: A perspective. *Biochim. Biophys. Acta-Biomembr.* **1798**, 741-749, doi:10.1016/j.bbamem.2009.12.019 (2010).

207 Garcia-Manyes, S., Redondo-Morata, L., Oncins, G. & Sanz, F. Nanomechanics of Lipid Bilayers: Heads or Tails? *J. Am. Chem. Soc.* **132**, 12874-12886, doi:10.1021/ja1002185 (2010).

208 Ong, Y. L., Razatos, A., Georgiou, G. & Sharma, M. M. Adhesion forces between E-coli bacteria and biomaterial surfaces. *Langmuir* **15**, 2719-2725, doi:10.1021/la981104e (1999).

209 Manne, S., Cleveland, J. P., Gaub, H. E., Stucky, G. D. & Hansma, P. K. Direct visualization of surfactant hemimicelles by force microscopy of the electrical double layer. *Langmuir* **10**, 4409-4413, doi:10.1021/la00024a003 (1994).

210 Johnson, S. B., Drummond, C. J., Scales, P. J. & Nishimura, S. Comparison of techniques for measuring the electrical double -layer properties of surfaces in aqueous-solution-Hexadecyltrimethylammonium bromide self-assembly structures as a model system. *Langmuir* **11**, 2367-2375, doi:10.1021/la00007a009 (1995).

211 Rimer, J. D., Vlachos, D. G. & Lobo, R. F. Evolution of self-assembled silica-tetrapropylammonium nanoparticles at elevated temperatures. *J. Phys. Chem. B* **109**, 12762-12771, doi:10.1021/jp052045y (2005).

212 Aerts, A., Follens, L. R. A., Haouas, M., Caremans, T. P., Delsuc, M. A., Loppinet, B., Vermant, J., Goderis, B., Taulelle, F., Martens, J. A. & Kirschhock, C. E. A. Combined NMR, SAXS, and DLS study of concentrated clear solutions used in silicalite-1 zeolite synthesis. *Chem. Mat.* **19**, 3448-3454, doi:10.1021/cm070693j (2007).

213 International Zeolite Association, http://www.iza-structure.org/.

214 Shete, M., Kumar, M., Kim, D., Rangnekar, N., Xu, D., Topuz, B., Agrawal, K. V., Karapetrova, E., Stottrup, B., Al-Thabaiti, S., Basahel, S., Narasimharao, K., Rimer, J. D. & Tsapatsis, M. Nanoscale Control of Homoepitaxial Growth on a Two-Dimensional Zeolite. **56**, 535-539, doi:10.1002/anie.201607063 (2017).

215 Park, M. B., Lee, Y., Zheng, A., Xiao, F.-S., Nicholas, C. P., Lewis, G. J. & Hong, S. B. Formation pathway for LTA zeolite crystals synthesized via a charge density mismatch approach. *J. Am. Chem. Soc.* **135**, 2248-2255 (2012).

216 Sugiyama, S., Yamamoto, S., Matsuoka, O., Nozoye, H., Yu, J., Zhu, G., Qiu, S. & Terasaki, O. AFM observation of double 4-rings on zeolite LTA crystals surface. *Microporous Mesoporous Mater.* **28**, 1-7, doi:https://doi.org/10.1016/S1387-1811(98)00271-6 (1999).

217 Dumrul, S., Bazzana, S., Warzywoda, J., Biederman, R. R. & Sacco Jr, A. Imaging of crystal growth-induced fine surface features in zeolite A by atomic force microscopy. *Microporous Mesoporous Mater.* **54**, 79-88 (2002).

218 de Vos Burchart, E., Jansen, J. & Van Bekkum, H. Ordered overgrowth of zeolite X onto crystals of zeolite A. *Zeolites* **9**, 432-435 (1989).

219 Jeon, M. Y., Kim, D., Kumar, P., Lee, P. S., Rangnekar, N., Bai, P., Shete, M., Elyassi, B., Lee, H. S. & Narasimharao, K. Ultra-selective high-flux membranes from directly synthesized zeolite nanosheets. *Nature* **543**, 690 (2017).

220 Yokoyama, T., Yamanaka, C. & Tarutani, T. *Formation of silicato complexes of aluminium in aqueous solution*.

221 Dusselier, M. & Davis, M. E. Small-Pore Zeolites: Synthesis and Catalysis. *Chem. Rev. (Washington, DC, U. S.)* **118**, 5265-5329, doi:10.1021/acs.chemrev.7b00738 (2018).

222 Erdem, E., Karapinar, N. & Donat, R. The Removal of Heavy Metal Cations by Natural Zeolites. *Journal of Colloid and Interface Science* **280**, 309-314, doi:https://doi.org/10.1016/j.jcis.2004.08.028 (2004).

223 Wang, Q., Luo, J., Zhong, Z. & Borgna, A. CO_2 Capture by Solid Adsorbents and Their Applications: Current Status and New Trends. *Energy & Environmental Science* **4**, 42-55, doi:10.1039/c0ee00064g (2011).

224 Bereciartua, P. J., Cantín, Á., Corma, A., Jordá, J. L., Palomino, M., Rey, F., Valencia, S., Corcoran, E. W., Kortunov, P., Ravikovitch, P. I., Burton, A., Yoon, C., Wang, Y., Paur, C., Guzman, J., Bishop, A. R. & Casty, G. L. Control of Zeolite Framework Flexibility and Pore Topology for Separation of Ethane and Ethylene. *Science* **358**, 1068-1071, doi:10.1126/science.aao0092 (2017).

225 Martínez, C. & Corma, A. Inorganic Molecular Sieves: Preparation, Modification and Industrial Application in Catalytic Processes. *Coordination Chemistry Reviews* **255**, 1558-1580 (2011).

226 Jae, J., Tompsett, G. A., Foster, A. J., Hammond, K. D., Auerbach, S. M., Lobo, R. F. & Huber, G. W. Investigation into the Shape Selectivity of Zeolite Catalysts for Biomass Conversion. *Journal of Catalysis* **279**, 257-268 (2011).

227 Williams, C. L., Chang, C.-C., Do, P., Nikbin, N., Caratzoulas, S., Vlachos, D. G., Lobo, R. F., Fan, W. & Dauenhauer, P. J. Cycloaddition of Biomass-Derived Furans for Catalytic Production of Renewable p-Xylene. *ACS Catalysis* **2**, 935-939, doi:10.1021/cs300011a (2012).

228 Roy, S. & Baiker, A. NO_x Storage−Reduction Catalysis: From Mechanism and Materials Properties to Storage−Reduction Performance. *Chemical Reviews* **109**, 4054-4091, doi:10.1021/cr800496f (2009).

229 Olsbye, U., Svelle, S., Bjørgen, M., Beato, P., Janssens, T. V. W., Joensen, F., Bordiga, S. & Lillerud, K. P. Conversion of Methanol to Hydrocarbons: How Zeolite Cavity and

Pore Size Controls Product Selectivity. *Angew. Chem. Int. Ed.* **51**, 5810-5831, doi:10.1002/anie.201103657 (2012).

230 Ilias, S. & Bhan, A. Mechanism of the Catalytic Conversion of Methanol to Hydrocarbons. *ACS Catalysis* **3**, 18-31, doi:10.1021/cs3006583 (2013).

231 Yarulina, I., Chowdhury, A. D., Meirer, F., Weckhuysen, B. M. & Gascon, J. Recent Trends and Fundamental Insights in the Methanol-to-Hydrocarbons Process. *Nature Catalysis* **1**, 398-411, doi:10.1038/s41929-018-0078-5 (2018).

232 de Moor, P.-P. E. A., Beelen, T. P. M., Komanschek, B. U., Diat, O. & van Santen, R. A. In Situ Investigation of Si-TPA-MFI Crystallization Using (Ultra-) Small- and Wide-Angle X-ray Scattering. *J. Phys. Chem. B* **101**, 11077-11086, doi:10.1021/jp9724784 (1997).

233 de Moor, P.-P. E. A., Beelen, T. P. M., Komanschek, B. U. & van Santen, R. A. Nanometer Scale Precursors in the Crystallization of Si-TPA-MFI. *Microporous and Mesoporous Materials* **21**, 263-269, doi:https://doi.org/10.1016/S1387-1811(98)00008-0 (1998).

234 de Moor, P.-P. E. A., Beelen, T. P. M., van Santen, R. A., Beck, L. W. & Davis, M. E. Si-MFI Crystallization Using a “Dimer” and “Trimer” of TPA Studied with Small-Angle X-Ray Scattering. *The Journal of Physical Chemistry B* **104**, 7600-7611, doi:10.1021/jp0006476 (2000).

235 de Moor, P.-P. E. A., Beelen, T. P. M., van Santen, R. A., Tsuji, K. & Davis, M. E. SAXS and USAXS Investigation on Nanometer-Scaled Precursors in Organic-Mediated Zeolite Crystallization from Gelating Systems. *Chemistry of Materials* **11**, 36-43, doi:10.1021/cm9807079 (1999).

236 Schoeman, B. J. Analysis of the Nucleation and Growth of TPA-Silicalite-1 at Elevated Temperatures with the Emphasis on Colloidal Stability. *Microporous and Mesoporous Materials* **22**, 9-22, doi:https://doi.org/10.1016/S1387-1811(98)00080-8 (1998).

237 Schoeman, B. J. & Regev, O. A Study of the Initial Stage in the Crystallization of TPA-Silicalite-1. *Zeolites* **17**, 447-456, doi:https://doi.org/10.1016/S0144-2449(96)00038-3 (1996).

238 Watson, J. N., Brown, A. S., Iton, L. E. & White, J. W. Detection of TPA-Silicalite Precursors Nucleated during the Room Temperature Aging of a Clear Homogeneous Synthesis Solution. *Journal of the Chemical Society, Faraday Transactions* **94**, 2181-2186, doi:10.1039/a801924j (1998).

239 Watson, J. N., Iton, L. E., Keir, R. I., Thomas, J. C., Dowling, T. L. & White, J. W. TPA−Silicalite Crystallization from Homogeneous Solution: Kinetics and Mechanism of Nucleation and Growth. *The Journal of Physical Chemistry B* **101**, 10094-10104, doi:10.1021/jp971531l (1997).

240 Watson, J. N., Iton, L. E. & White, J. W. In Situ Observation of the Growth of Silicalite Nuclei by Small-Angle X-Ray and Neutron Scattering. *Chemical Communications* **0**, 2767-2768, doi:10.1039/cc9960002767 (1996).

241 Chang, C.-C., Teixeira, A. R., Li, C., Dauenhauer, P. J. & Fan, W. Enhanced Molecular Transport in Hierarchical Silicalite-1. *Langmuir* **29**, 13943-13950, doi:10.1021/la403706r (2013).

242 Qi, X., Vattipalli, V., Dauenhauer, P. J. & Fan, W. Silica Nanoparticle Mass Transfer Fins for MFI Composite Materials. *Chemistry of Materials* **30**, 2353-2361, doi:10.1021/acs.chemmater.7b05400 (2018).

243 Teixeira, A. R., Chang, C.-C., Coogan, T., Kendall, R., Fan, W. & Dauenhauer, P. J. Dominance of Surface Barriers in Molecular Transport through Silicalite-1. *The Journal of Physical Chemistry C* **117**, 25545-25555, doi:10.1021/jp4089595 (2013).

244 Teixeira, A. R., Qi, X., Conner, W. C., Mountziaris, T. J., Fan, W. & Dauenhauer, P. J. 2D Surface Structures in Small Zeolite MFI Crystals. *Chemistry of Materials* **27**, 4650-4660, doi:10.1021/acs.chemmater.5b01046 (2015).

245 Vattipalli, V., Qi, X., Dauenhauer, P. J. & Fan, W. Long Walks in Hierarchical Porous Materials due to Combined Surface and Configurational Diffusion. *Chemistry of Materials* **28**, 7852-7863, doi:10.1021/acs.chemmater.6b03308 (2016).

246 Valtchev, V. & Tosheva, L. Porous Nanosized Particles: Preparation, Properties, and Applications. *Chemical Reviews* **113**, 6734-6760, doi:10.1021/cr300439k (2013).

247 Bosnar, S., Bronić, J., Brlek, Đ. & Subotić, B. Chemically Controlled Particulate Properties of Zeolites: Towards the Face-Less Particles of Zeolite A. 2. Influence of Aluminosilicate Batch Concentration and Alkalinity of the Reaction Mixture (Hydrogel) on the Size and Shape of Zeolite A Crystals. *Microporous and Mesoporous Materials* **142**, 389-397, doi:http://dx.doi.org/10.1016/j.micromeso.2010.12.027 (2011).

248 Iwasaki, A., Hirata, M., Kudo, I. & Sano, T. Behavior of the (010) Face of Silicalite Crystal. *Zeolites* **16**, 35-41, doi:http://dx.doi.org/10.1016/0144-2449(95)00102-6 (1996).

249 Awala, H., Gilson, J.-P., Retoux, R., Boullay, P., Goupil, J.-M., Valtchev, V. & Mintova, S. Template-free nanosized faujasite-type zeolites. *Nat. Mater.* **14**, 447, doi:10.1038/nmat4173

https://www.nature.com/articles/nmat4173#supplementary-information (2015).

250 Choi, M., Na, K., Kim, J., Sakamoto, Y., Terasaki, O. & Ryoo, R. Stable Single-Unit-Cell Nanosheets of Zeolite MFI as Active and Long-Lived Catalysts. *Nature* **461**, 246-249, (2009).

251 Dhainaut, J., Daou, T. J., Bidal, Y., Bats, N., Harbuzaru, B., Lapisardi, G., Chaumeil, H., Defoin, A., Rouleau, L. & Patarin, J. One-Pot Structural Conversion of Magadiite into MFI Zeolite Nanosheets Using Mononitrogen Surfactants as Structure and Shape-Directing Agents. *Crystengcomm* **15**, 3009-3015, doi:10.1039/c3ce40118a (2013).

252 Roth, W. J., Nachtigall, P., Morris, R. E. & Čejka, J. Two-Dimensional Zeolites: Current Status and Perspectives. *Chem. Rev. (Washington, DC, U. S.)* **114**, 4807-4837, doi:10.1021/cr400600f (2014).

253 Seo, Y., Lee, S., Jo, C. & Ryoo, R. Microporous Aluminophosphate Nanosheets and Their Nanomorphic Zeolite Analogues Tailored by Hierarchical Structure-Directing Amines. *Journal of the American Chemical Society* **135**, 8806-8809, doi:10.1021/ja403580j (2013).

254 Zhang, X., Liu, D., Xu, D., Asahina, S., Cychosz, K. A., Agrawal, K. V., Al Wahedi, Y., Bhan, A., Al Hashimi, S., Terasaki, O., Thommes, M. & Tsapatsis, M. Synthesis of Self-Pillared Zeolite Nanosheets by Repetitive Branching. *Science* **336**, 1684-1687, doi:10.1126/science.1221111 (2012).

255 Watcharop, C., Yuki, S., R., M. R., Tatsuya, S., Keisuke, S., Keiji, I., Atsushi, S. & Tatsuya, O. Formation of Hierarchically Organized Zeolites by Sequential Intergrowth. *Angewandte Chemie International Edition* **52**, 3355-3359, doi:doi:10.1002/anie.201209638 (2013).

256 Li, R., Smolyakova, A., Maayan, G. & Rimer, J. D. Designed Peptoids as Tunable Modifiers of Zeolite Crystallization. *Chemistry of Materials* **29**, 9536-9546, doi:10.1021/acs.chemmater.7b03798 (2017).

257 Lupulescu, A. I., Qin, W. & Rimer, J. D. Tuning Zeolite Precursor Interactions by Switching the Valence of Polyamine Modifiers. *Langmuir* **32**, 11888-11898, doi:10.1021/acs.langmuir.6b03212 (2016).

258 Kumar, M., Luo, H., Román-Leshkov, Y. & Rimer, J. D. SSZ-13 Crystallization by Particle Attachment and Deterministic Pathways to Crystal Size Control. *J Am Chem Soc* **137**, 13007-13017 (2015).

259 Lupulescu, A. I., Kumar, M. & Rimer, J. D. A Facile Strategy To Design Zeolite L Crystals with Tunable Morphology and Surface Architecture. *J Am Chem Soc* **135**, 6608-6617, doi:10.1021/ja4015277 (2013).

260 Lupulescu, A. I. & Rimer, J. D. Tailoring Silicalite-1 Crystal Morphology with Molecular Modifiers. *Angewandte Chemie International Edition* **51**, 3345-3349, doi:10.1002/anie.201107725 (2012).

261 Zhang, Q., Chen, G., Wang, Y., Chen, M., Guo, G., Shi, J., Luo, J. & Yu, J. High-Quality Single-Crystalline MFI-Type Nanozeolites: A Facile Synthetic Strategy and MTP Catalytic Studies. *Chemistry of Materials* **30**, 2750-2758, doi:10.1021/acs.chemmater.8b00527 (2018).

262 Das, R., Ghosh, S. & Kanti Naskar, M. Effect of Secondary and Tertiary Alkylamines for the Synthesis of Zeolite L. *Materials Letters* **143**, 94-97, doi:https://doi.org/10.1016/j.matlet.2014.12.076 (2015).

263 Zheng, J., Zhang, W., Liu, Z., Huo, Q., Zhu, K., Zhou, X. & Yuan, W. Unraveling the Non-Classic Crystallization of SAPO-34 in a Dry Gel System Towards Controlling Meso-Structure with the Assistance of Growth Inhibitor: Growth Mechanism, Hierarchical Structure Control and Catalytic Properties. *Microporous and Mesoporous Materials* **225**, 74-87, doi:https://doi.org/10.1016/j.micromeso.2015.12.007 (2016).

264 Chen, Z., Chen, C., Zhang, J., Zheng, G., Wang, Y., Dong, L., Qian, W., Bai, S. & Hong, M. Zeolite Y Microspheres with Perpendicular Mesochannels and Metal@Y Heterostructures for Catalytic and SERS Applications. *Journal of Materials Chemistry A* **6**, 6273-6281, doi:10.1039/c7ta10444h (2018).

265 Gallego, E. M., Paris, C., Sanchez, C., Moliner, M. & Corma, A. Nanosized MCM-22 Zeolite Using Simple Non-Surfactant Organic Growth Modifiers: Synthesis and Catalytic Application. *Chemical Communications* **54**, 9989-9992, doi:10.1039/c8cc05356a (2018).

266 Zhang, L., Chen, Y., Jiang, J.-G., Xu, L., Guo, W., Xu, H., Wen, X.-D. & Wu, P. Facile Synthesis of ECNU-20 (IWR) Hollow Sphere Zeolite Composed of Aggregated Nanosheets. *Dalton Transactions* **46**, 15641-15645, doi:10.1039/c7dt03420b (2017).

267 Jin, D., Liu, Z., Zheng, J., Hua, W., Chen, J., Zhu, K. & Zhou, X. Nonclassical from-Shell-to-Core Growth of Hierarchically Organized SAPO-11 with Enhanced Catalytic Performance in Hydroisomerization of n-Heptane. *RSC Advances* **6**, 32523-32533, doi:10.1039/c6ra03039d (2016).

268 Jegatheeswaran, S., Cheng, C.-M. & Cheng, C.-H. Effects of Adding Alcohols on ZSM-12 Synthesis. *Microporous and Mesoporous Materials* **201**, 24-34, doi:https://doi.org/10.1016/j.micromeso.2014.09.008 (2015).

269 Chung, J., Granja, I., Taylor, M. G., Mpourmpakis, G., Asplin, J. R. & Rimer, J. D. Molecular Modifiers Reveal a Mechanism of Pathological Crystal Growth Inhibition. *Nature* **536**, 446-450, doi:10.1038/nature19062 (2016).

270 Rimer, J. D., An, Z., Zhu, Z., Lee, M. H., Goldfarb, D. S., Wesson, J. A. & Ward, M. D. Crystal Growth Inhibitors for the Prevention of Cystine Kidney Stones Through Molecular Design. *Science* **330**, 337-341, doi:10.1126/science.1191968 (2010).

271 J.-S., J. & F., S. D. Biomimetic Silica Formation: Effect of Block Copolypeptide Chemistry and Solution Conditions on Silica Nanostructure. *Advanced Materials* **19**, 2951-2956, doi:doi:10.1002/adma.200602813 (2007).

272 Meldrum, F. C. & Cölfen, H. Controlling Mineral Morphologies and Structures in Biological and Synthetic Systems. *Chemical Reviews* **108**, 4332-4432, doi:10.1021/cr8002856 (2008).

273 Evans, J. S. "Tuning in" to Mollusk Shell Nacre- and Prismatic-Associated Protein Terminal Sequences. Implications for Biomineralization and the Construction of High

Performance Inorganic−Organic Composites. *Chemical Reviews* **108**, 4455-4462, doi:10.1021/cr078251e (2008).

274 Graether, S. P., Kuiper, M. J., Gagné, S. M., Walker, V. K., Jia, Z., Sykes, B. D. & Davies, P. L. β-Helix Structure and Ice-Binding Properties of a Hyperactive Antifreeze Protein from an Insect. *Nature* **406**, 325-328, doi:10.1038/35018610 (2000).

275 Doxey, A. C., Yaish, M. W., Griffith, M. & McConkey, B. J. Ordered Surface Carbons Distinguish Antifreeze Proteins and Their Ice-Binding Regions. *Nature Biotechnology* **24**, 852-855, doi:10.1038/nbt1224 (2006).

276 Dickerson, M. B., Sandhage, K. H. & Naik, R. R. Protein- and Peptide-Directed Syntheses of Inorganic Materials. *Chemical Reviews* **108**, 4935-4978, doi:10.1021/cr8002328 (2008).

277 Cha, J. N., Stucky, G. D., Morse, D. E. & Deming, T. J. Biomimetic Synthesis of Ordered Silica Structures Mediated by Block Copolypeptides. *Nature* **403**, 289-292 (2000).

278 Rodríguez, F., Glawe, D. D., Naik, R. R., Hallinan, K. P. & Stone, M. O. Study of the Chemical and Physical Influences upon in Vitro Peptide-Mediated Silica Formation. *Biomacromolecules* **5**, 261-265, doi:10.1021/bm034232c (2004).

279 Mavredaki, E., Neville, A. & Sorbie, K. S. Initial Stages of Barium Sulfate Formation at Surfaces in the Presence of Inhibitors. *Crystal Growth & Design* **11**, 4751-4758, doi:10.1021/cg101584f (2011).

280 Sriram, R., Ha, K. J., Pankaj, K., Sahar, F. & D., R. J. A High-Throughput Assay for Screening Modifiers of Calcium Oxalate Crystallization. *Aiche Journal* **62**, 3538-3546, doi:doi:10.1002/aic.15390 (2016).

281 Hudait, A., Odendahl, N., Qiu, Y., Paesani, F. & Molinero, V. Ice-Nucleating and Antifreeze Proteins Recognize Ice through a Diversity of Anchored Clathrate and Ice-like

Motifs. *Journal of the American Chemical Society* **140**, 4905-4912, doi:10.1021/jacs.8b01246 (2018).

282 Mochizuki, K. & Molinero, V. Antifreeze Glycoproteins Bind Reversibly to Ice via Hydrophobic Groups. *Journal of the American Chemical Society* **140**, 4803-4811, doi:10.1021/jacs.7b13630 (2018).

283 Graham, B., Fayter, A. E. R., Houston, J. E., Evans, R. C. & Gibson, M. I. Facially Amphipathic Glycopolymers Inhibit Ice Recrystallization. *Journal of the American Chemical Society* **140**, 5682-5685, doi:10.1021/jacs.8b02066 (2018).

284 Liu, Y., Zhou, X., Pang, X., Jin, Y., Meng, X., Zheng, X., Gao, X. & Xiao, F.-S. Improved para-Xylene Selectivity in meta-Xylene Isomerization Over ZSM-5 Crystals with Relatively Long b-Axis Length. *ChemCatChem* **5**, 1517-1523, doi:10.1002/cctc.201200691 (2013).

285 Shan, Z., Wang, H., Meng, X., Liu, S., Wang, L., Wang, C., Li, F., Lewis, J. P. & Xiao, F.-S. Designed synthesis of TS-1 crystals with controllable b-oriented length. *Chemical Communications* **47**, 1048-1050, doi:10.1039/c0cc03613g (2011).

286 Sahu, J. N., Mahalik, K., Patwardhan, A. V. & Meikap, B. C. Equilibrium and Kinetic Studies on the Hydrolysis of Urea for Ammonia Generation in a Semibatch Reactor. *Industrial & Engineering Chemistry Research* **47**, 4689-4696, doi:10.1021/ie800481z (2008).

287 Oberholzer, V. G. & Briddon, A. 3-Amino-2-Piperidone in the Urine of Patients with Hyperornithinemia. *Clinica Chimica Acta* **87**, 411-415, doi:https://doi.org/10.1016/0009-8981(78)90186-9 (1978).

288 Rimer, J. D., Lobo, R. F. & Vlachos, D. G. Physical Basis for the Formation and Stability of Silica Nanoparticles in Basic Solutions of Monovalent Cations. *Langmuir* **21**, 8960-8971, doi:10.1021/la0511384 (2005).

289 Fedeyko, J. M., Rimer, J. D., Lobo, R. F. & Vlachos, D. G. Spontaneous Formation of Silica Nanoparticles in Basic Solutions of Small Tetraalkylammonium Cations. *The Journal of Physical Chemistry B* **108**, 12271-12275, doi:10.1021/jp047623+ (2004).

290 Rimer, J. D., Fedeyko, J. M., Vlachos, D. G. & Lobo, R. F. Silica Self-Assembly and Synthesis of Microporous and Mesoporous Silicates. *Chemistry – A European Journal* **12**, 2926-2934, doi:10.1002/chem.200500684 (2006).

291 Meera, S., Manjesh, K., Donghun, K., Neel, R., Dandan, X., Berna, T., Varoon, A. K., Evguenia, K., Benjamin, S., Shaeel, A.-T., Sulaiman, B., Katabathini, N., D., R. J. & Michael, T. Nanoscale Control of Homoepitaxial Growth on a Two-Dimensional Zeolite. *Angewandte Chemie International Edition* **56**, 535-539, doi:doi:10.1002/anie.201607063 (2017).

292 Sprenger, K. G., Prakash, A., Drobny, G. & Pfaendtner, J. Investigating the Role of Phosphorylation in the Binding of Silaffin Peptide R5 to Silica with Molecular Dynamics Simulations. *Langmuir* **34**, 1199-1207, doi:10.1021/acs.langmuir.7b02868 (2018).

293 Emami, F. S., Puddu, V., Berry, R. J., Varshney, V., Patwardhan, S. V., Perry, C. C. & Heinz, H. Prediction of Specific Biomolecule Adsorption on Silica Surfaces as a Function of pH and Particle Size. *Chemistry of Materials* **26**, 5725-5734, doi:10.1021/cm5026987 (2014).

294 Chung, J., Taylor, M. G., Granja, I., Asplin, J. R., Mpourmpakis, G. & Rimer, J. D. Factors Differentiating the Effectiveness of Polyprotic Acids as Inhibitors of Calcium Oxalate Crystallization in Kidney Stone Disease. *Crystal Growth & Design* **18**, 5617-5627, doi:10.1021/acs.cgd.8b00945 (2018).

295 Nealon, G. L., Brown, D. H., Jones, F., Parkinson, G. & Ogden, M. I. An Azobenzene-Based Photoswitchable Crystal Growth Modifier. *Crystengcomm* **19**, 1286-1293, doi:10.1039/c6ce02514e (2017).

296 van Erp, T. S., Caremans, T. P., Dubbeldam, D., Martin-Calvo, A., Calero, S. & Martens, J. A. Enantioselective Adsorption in Achiral Zeolites. *Angew Chem Int Ed Engl* **49**, 3010-3013, doi:10.1002/anie.200906083 (2010).

297 Martin-Calvo, A., Calero, S., Martens, J. A. & van Erp, T. S. Enantiomeric Adsorption of Lactic Acid Mixtures in Achiral Zeolites. *The Journal of Physical Chemistry C* **118**, 14991-14997, doi:10.1021/jp504497t (2014).

298 Torrie, G. M. & Valleau, J. P. Nonphysical Sampling Distributions in Monte Carlo Free-Energy Estimation: Umbrella Sampling. *Journal of Computational Physics* **23**, 187-199, doi:https://doi.org/10.1016/0021-9991(77)90121-8 (1977).

299 Palmer, J. C. & Debenedetti, P. G. Recent Advances in Molecular Simulation: A Chemical Engineering Perspective. *AIChE Journal* **61**, 370-383, doi:10.1002/aic.14706 (2014).

300 Hess, B., Kutzner, C., van der Spoel, D. & Lindahl, E. GROMACS 4: Algorithms for Highly Efficient, Load-Balanced, and Scalable Molecular Simulation. *J Chem Theory Comput* **4**, 435-447, doi:10.1021/ct700301q (2008).

301 Cygan, R. T., Liang, J.-J. & Kalinichev, A. G. Molecular Models of Hydroxide, Oxyhydroxide, and Clay Phases and the Development of a General Force Field. *The Journal of Physical Chemistry B* **108**, 1255-1266, doi:10.1021/jp0363287 (2004).

302 Berendsen, H. J. C., Grigera, J. R. & Straatsma, T. P. The Missing Term in Effective Pair Potentials. *The Journal of Physical Chemistry* **91**, 6269-6271, doi:10.1021/j100308a038 (1987).

303 Cornell, W. D., Cieplak, P., Bayly, C. I., Gould, I. R., Merz, K. M., Ferguson, D. M., Spellmeyer, D. C., Fox, T., Caldwell, J. W. & Kollman, P. A. A Second Generation Force Field for the Simulation of Proteins, Nucleic Acids, and Organic Molecules. *Journal of the American Chemical Society* **117**, 5179-5197, doi:10.1021/ja00124a002 (1995).

304 Wang, J., Wolf, R. M., Caldwell, J. W., Kollman, P. A. & Case, D. A. Development and Testing of a General Amber Force Field. *J Comput Chem* **25**, 1157-1174, doi:10.1002/jcc.20035 (2004).

305 Vanquelef, E., Simon, S., Marquant, G., Garcia, E., Klimerak, G., Delepine, J. C., Cieplak, P. & Dupradeau, F. Y. R.E.D. Server: A Web Service for Deriving RESP and ESP Charges and Building Force Field Libraries for New Molecules and Molecular Fragments. *Nucleic Acids Res* **39**, W511-W517, doi:10.1093/nar/gkr288 (2011).

306 Díaz, I., Kokkoli, E., Terasaki, O. & Tsapatsis, M. Surface Structure of Zeolite (MFI) Crystals. *Chemistry of Materials* **16**, 5226-5232, doi:10.1021/cm0488534 (2004).

307 Emami, F. S., Puddu, V., Berry, R. J., Varshney, V., Patwardhan, S. V., Perry, C. C. & Heinz, H. Force Field and a Surface Model Database for Silica to Simulate Interfacial Properties in Atomic Resolution. *Chemistry of Materials* **26**, 2647-2658, doi:10.1021/cm500365c (2014).

308 Kroutil, O., Chval, Z., Skelton, A. A. & Předota, M. Computer Simulations of Quartz (101)–Water Interface over a Range of pH Values. *The Journal of Physical Chemistry C* **119**, 9274-9286, doi:10.1021/acs.jpcc.5b00096 (2015).

309 Bussi, G., Donadio, D. & Parrinello, M. Canonical Sampling through Velocity Rescaling. *The Journal of Chemical Physics* **126**, 014101, doi:10.1063/1.2408420 (2007).

310 Parrinello, M. & Rahman, A. Polymorphic Transitions in Single Crystals: A New Molecular Dynamics Method. *Journal of Applied Physics* **52**, 7182-7190, doi:10.1063/1.328693 (1981).

311 Tribello, G. A., Bonomi, M., Branduardi, D., Camilloni, C. & Bussi, G. PLUMED 2: New Feathers for an Old Bird. *Computer Physics Communications* **185**, 604-613, doi:https://doi.org/10.1016/j.cpc.2013.09.018 (2014).

312 Ferguson, A. L. BayesWHAM: A Bayesian Approach for Free Energy Estimation, Reweighting, and Uncertainty Quantification in the Weighted Histogram Analysis Method. *J Comput Chem* **38**, 1583-1605, doi:10.1002/jcc.24800 (2017).

313 Wang, S. & Peng, Y. Natural zeolites as effective adsorbents in water and wastewater treatment. *Chem. Eng. J. (Lausanne)* **156**, 11-24, doi:https://doi.org/10.1016/j.cej.2009.10.029 (2010).

314 Su, F. & Lu, C. CO2 capture from gas stream by zeolite 13X using a dual-column temperature/vacuum swing adsorption. *Energy & Environmental Science* **5**, 9021-9027, doi:10.1039/c2ee22647b (2012).

315 Weckhuysen, B. M. & Yu, J. Recent advances in zeolite chemistry and catalysis. *Chem. Soc. Rev.* **44**, 7022-7024, doi:10.1039/c5cs90100f (2015).

316 Li, C., Paris, C., Martínez-Triguero, J., Boronat, M., Moliner, M. & Corma, A. Synthesis of reaction adapted zeolites as methanol-to-olefins catalysts with mimics of reaction intermediates as organic structure- directing agents. *Nature Catalysis* **1**, 547-554, doi:10.1038/s41929-018-0104-7 (2018).

317 Gallego, E. M., Portilla, M. T., Paris, C., León-Escamilla, A., Boronat, M., Moliner, M. & Corma, A. "Ab initio" synthesis of zeolites for preestablished catalytic reactions. *Science* **355**, 1051-1054, doi:10.1126/science.aal0121 (2017).

318 Bonilla, G., Díaz, I., Tsapatsis, M., Jeong, H.-K., Lee, Y. & Vlachos, D. G. Zeolite (MFI) Crystal Morphology Control Using Organic Structure-Directing Agents. *Chemistry of Materials* **16**, 5697-5705, doi:10.1021/cm048854w (2004).

319 Davis, T. M., Liu, A. T., Lew, C. M., Xie, D., Benin, A. I., Elomari, S., Zones, S. I. & Deem, M. W. Computationally Guided Synthesis of SSZ-52: A Zeolite for Engine Exhaust Clean-up. *Chemistry of Materials* **28**, 708-711, doi:10.1021/acs.chemmater.5b04578 (2016).

320 Brand, S. K., Schmidt, J. E., Deem, M. W., Daeyaert, F., Ma, Y. H., Terasaki, O., Orazov, M. & Davis, M. E. Enantiomerically enriched, polycrystalline molecular sieves. *Proc. Natl. Acad. Sci. U. S. A.* **114**, 5101-5106, doi:10.1073/pnas.1704638114 (2017).

321 Turrina, A., Garcia, R., Watts, A. E., Greer, H. F., Bradley, J., Zhou, W. Z., Cox, P. A., Shannon, M. D., Mayoral, A., Casci, J. L. & Wright, P. A. STA-20: An ABC-6 Zeotype Structure Prepared by Co-Templating and Solved via a Hypothetical Structure Database and STEM-ADF Imaging. *Chemistry of Materials* **29**, 2180-2190, doi:10.1021/acs.chemmater.6b04892 (2017).

322 Jo, C., Jung, J., Shin, H. S., Kim, J. & Ryoo, R. Capping with Multivalent Surfactants for Zeolite Nanocrystal Synthesis. *Angew. Chem.-Int. Edit.* **52**, 10014-10017, doi:10.1002/anie.201303088 (2013).

323 Kumar, M., Choudhary, M. K. & Rimer, J. D. Transient modes of zeolite surface growth from 3D gel-like islands to 2D single layers. *Nat. Commun.* **9**, 2129, doi:10.1038/s41467-018-04296-4 (2018).

324 Liu, Y., Li, Y. & Yang, W. Fabrication of Highly b-Oriented MFI Film with Molecular Sieving Properties by Controlled In-Plane Secondary Growth. *J. Am. Chem. Soc.* **132**, 1768-1769, doi:10.1021/ja909888v (2010).

325 Valtchev, V. P. & Bozhilov, K. N. Evidences for Zeolite Nucleation at the Solid−Liquid Interface of Gel Cavities. *J. Am. Chem. Soc.* **127**, 16171-16177, doi:10.1021/ja0546267 (2005).

326 Ren, N., Bosnar, S., Bronić, J., Dutour Sikirić, M., Mišić, T., Svetličić, V., Mao, J.-J., Antonić Jelić, T., Hadžija, M. & Subotić, B. Role of Subcolloidal (Nanosized) Precursor Species in the Early Stage of the Crystallization of Zeolites in Heterogeneous Systems. *Langmuir* **30**, 8570-8579, doi:10.1021/la5012296 (2014).

327 Ren, N., Subotić, B., Bronić, J., Tang, Y., Dutour Sikirić, M., Mišić, T., Svetličić, V., Bosnar, S. & Antonić Jelić, T. Unusual Pathway of Crystallization of Zeolite ZSM-5 in a

Heterogeneous System: Phenomenology and Starting Considerations. *Chem. Mater.* **24**, 1726-1737, doi:10.1021/cm203194v (2012).

328 Kumar, M., Luo, H., Román-Leshkov, Y. & Rimer, J. D. SSZ-13 Crystallization by Particle Attachment and Deterministic Pathways to Crystal Size Control. *Journal of the American Chemical Society* **137**, 13007-13017, doi:10.1021/jacs.5b07477 (2015).

329 Kumar, S., Davis, T. M., Ramanan, H., Penn, R. L. & Tsapatsis, M. Aggregative Growth of Silicalite-1. *J. Phys. Chem. B* **111**, 3398-3403, doi:10.1021/jp0677445 (2007).

330 Corma, A. Inorganic Solid Acids and Their Use in Acid-Catalyzed Hydrocarbon Reactions. *Chem. Rev. (Washington, DC, U. S.)* **95**, 559-614, doi:10.1021/cr00035a006 (1995).

331 Schoeman, B. J. Analysis of the nucleation and growth of TPA-silicalite-1 at elevated temperatures with the emphasis on colloidal stability1Dedicated to Professor Lovat V.C. Rees in recognition and appreciation of his lifelong devotion to zeolite science and his outstanding achievements in this field.1. *Microporous Mesoporous Mater.* **22**, 9-22, doi:https://doi.org/10.1016/S1387-1811(98)00080-8 (1998).

332 Cheng, C.-H. & Shantz, D. F. Silicalite-1 Growth from Clear Solution: Effect of the Structure-Directing Agent on Growth Kinetics. *J. Phys. Chem. B* **109**, 13912-13920, doi:10.1021/jp050733b (2005).

333 Yang, S. & Navrotsky, A. Early-Stage Reactions in Synthesis of TPA−Silicalite-1: Studies by in Situ Calorimetry, SAXS, and pH Measurements. *Chem. Mater.* **16**, 3682-3687, doi:10.1021/cm035272q (2004).

334 Houssin, C. J. Y., Kirschhock, C. E. A., Magusin, P., Mojet, B. L., Grobet, P. J., Jacobs, P. A., Martens, J. A. & van Santen, R. A. Combined in situ Si-29 NMR and small-angle X-ray scattering study of precursors in MFI zeolite formation from silicic acid in TPAOH solutions. *Phys. Chem. Chem. Phys.* **5**, 3518-3524 (2003).

335 Bosnar, S., Antonić Jelić, T., Bronić, J., Dutour Sikirić, M., Šegota, S., Čadež, V., Smrečki, V., Palčić, A. & Subotić, B. Deep Insights into the Processes Occurring during Early Stages of the Formation and Room-Temperature Evolution of the Core (Amorphous SiO2)@Shell (Organocations) Nanoparticles. *The Journal of Physical Chemistry C* **122**, 9441-9454, doi:10.1021/acs.jpcc.8b00024 (2018).

336 Shete, M., Kumar, M., Kim, D., Rangnekar, N., Xu, D., Topuz, B., Agrawal, K. V., Karapetrova, E., Stottrup, B., Al-Thabaiti, S., Basahel, S., Narasimharao, K., Rimer, J. D. & Tsapatsis, M. Nanoscale Control of Homoepitaxial Growth on a Two-Dimensional Zeolite. *Angewandte Chemie International Edition* **56**, 535-539, doi:10.1002/anie.201607063 (2017).

337 Qin, W., Agarwal, A., Choudhary, M. K., Palmer, J. C. & Rimer, J. D. Molecular Modifiers Suppress Nonclassical Pathways of Zeolite Crystallization. *Chem. Mater.* **31**, 3228-3238, doi:10.1021/acs.chemmater.9b00066 (2019).

338 Tuel, A., Ben Taărit, Y. & Naccache, C. Characterization of TS-1 synthesized using mixtures of tetrabutyl and tetraethyl ammonium hydroxides. *Zeolites* **13**, 454-461, doi:https://doi.org/10.1016/0144-2449(93)90120-R (1993).

339 Li, X. & Shantz, D. F. PFG NMR Investigations of Tetraalkylammonium−Silica Mixtures. *J. Phys. Chem. C* **114**, 8449-8458, doi:10.1021/jp101006f (2010).

340 Rimer, J. D., Trofymluk, O., Lobo, R. F., Navrotsky, A. & Vlachos, D. G. Thermodynamics of Silica Nanoparticle Self-Assembly in Basic Solutions of Monovalent Cations. *J. Phys. Chem. C* **112**, 14754-14761, doi:10.1021/jp802902x (2008).

341 Kumar, S., Wang, Z., Penn, R. L. & Tsapatsis, M. A Structural Resolution Cryo-TEM Study of the Early Stages of MFI Growth. *J. Am. Chem. Soc.* **130**, 17284-17286, doi:10.1021/ja8063167 (2008).

342 Rimer, J. D., Kragten, D. D., Tsapatsis, M., Lobo, R. & Vlachos, D. in *Stud. Surf. Sci. Catal.* Vol. 154 (eds E. van Steen, I. M. Claeys, & L. H. Callanan) 317-324 (Elsevier, 2004).

343 Aerts, A., Kirschhock, C. E. A. & Martens, J. A. Methods for in situ spectroscopic probing of the synthesis of a zeolite. *Chem. Soc. Rev.* **39**, 4626-4642, doi:10.1039/B919704B (2010).

344 De Yoreo, J. J. & Vekilov, P. G. in *Biomineralization* Vol. 54 *Reviews in Mineralogy & Geochemistry* (eds P. M. Dove, J. J. DeYoreo, & S. Weiner) 57-93 (Mineralogical Soc America, 2003).

345 Penn, R. L. & Banfield, J. F. Imperfect oriented attachment: Dislocation generation in defect-free nanocrystals. *Science* **281**, 969-971, doi:10.1126/science.281.5379.969 (1998).

346 Chung, J., Granja, I., Taylor, M. G., Mpourmpakis, G., Asplin, J. R. & Rimer, J. D. Molecular modifiers reveal a mechanism of pathological crystal growth inhibition. *Nature* **536**, 446-450, doi:10.1038/nature19062 (2016).

347 Teng, H. H., Dove, P. M. & De Yoreo, J. J. Kinetics of calcite growth: Surface processes and relationships to macroscopic rate laws. *Geochim. Cosmochim. Acta* **64**, 2255-2266, doi:10.1016/s0016-7037(00)00341-0 (2000).

348 Rimer, J. D., An, Z., Zhu, Z., Lee, M. H., Goldfarb, D. S., Wesson, J. A. & Ward, M. D. Crystal growth inhibitors for the prevention of L-Cystine kidney stones through molecular design. *Science* **330**, 337-341, doi:10.1126/science.1191968 (2010).

349 Reviakine, I., Georgiou, D. K. & Vekilov, P. G. Capillarity effects on crystallization kinetics: Insulin. *J. Am. Chem. Soc.* **125**, 11684-11693, doi:10.1021/ja030194t (2003).

350 Vekilov, P. G. What determines the rate of growth of crystals from solution? *Cryst. Growth Des.* **7**, 2796-2810, doi:10.1021/cg070427i (2007).

351 Markov, I. V. Crystal Growth for Beginners. *World Scientific* **2nd Edition** (1995).

352 Lovette, M. A. & Doherty, M. F. Predictive Modeling of Supersaturation-Dependent Crystal Shapes. *Cryst. Growth Des.* **12**, 656-669, doi:10.1021/cg200855p (2012).

353 Evans, J. W., Thiel, P. A. & Bartelt, M. C. Morphological evolution during epitaxial thin film growth: Formation of 2D islands and 3D mounds. *Surf. Sci. Rep.* **61**, 1-128, doi:10.1016/j.surfrep.2005.08.004 (2006).

354 De Yoreo, J. J., Land, T. A. & Dair, B. Growth morphology of vicinal hillocks on the {101} face of KH_2PO_4: From step-flow to layer-by-layer growth. *Phys. Rev. Lett.* **73**, 838-841 (1994).

355 Heringdorf, F., Reuter, M. C. & Tromp, R. M. Growth dynamics of pentacene thin films. *Nature* **412**, 517-520, doi:10.1038/35087532 (2001).

356 Tersoff, J., Van der Gon, A. D. & Tromp, R. Critical island size for layer-by-layer growth. *Phys. Rev. Lett.* **72**, 266 (1994).

357 Liu, X. Y., Vanhoof, P. & Bennema, P. Surface roughening of normal alkane crystals: solvent dependent critical behavior *Phys. Rev. Lett.* **71**, 109-112, doi:10.1103/PhysRevLett.71.109 (1993).

358 Liu, X. Y. & Bennema, P. Foreign body induced kinetic roughening: Kinetics and observations. *J. Chem. Phys.* **115**, 4268-4274, doi:10.1063/1.1391256 (2001).

359 Sleutel, M., Maes, D., Wyns, L. & Willaert, R. Kinetic roughening of glucose isomerase crystals. *Cryst. Growth Des.* **8**, 4409-4414, doi:10.1021/cg701220t (2008).

360 Gorti, S., Forsythe, E. L. & Pusey, M. L. Kinetic roughening and energetics of tetragonal lysozyme crystal growth. *Cryst. Growth Des.* **4**, 691-699, doi:10.1021/cg034164d (2004).

361 Gorti, S., Forsythe, E. L. & Pusey, M. L. Growth modes and energetics of (101) face lysozyme crystal growth. *Cryst. Growth Des.* **5**, 473-482, doi:10.1021/cg049733b (2005).

362 Jetten, L., Human, H. J., Bennema, P. & Vandereerden, J. P. On the observations of the roughening transition of organic crystals, growing from solution. *J. Cryst. Growth.* **68**, 503-516, doi:10.1016/0022-0248(84)90457-3 (1984).

363 Liu, X. Y. & Bennema, P. Observations on the roughening transition and the influence on morphology of crystals. *J. Cryst. Growth.* **139**, 179-189, doi:10.1016/0022-0248(94)90043-4 (1994).

364 Bennema, P. Morphology of crystals determined by alpha factors, roughening temperature, F faces and connected nets. *J. Phys. D-Appl. Phys.* **26**, B1-B6, doi:10.1088/0022-3727/26/8b/001 (1993).

365 Cuppen, H. M., Meekes, H., van Enckevort, W. J. P., Vlieg, E. & Knops, H. J. F. Nonequilibrium free energy and kinetic roughening of steps on the Kossel(001) surface. *Phys Rev B* **69**, doi:10.1103/PhysRevB.69.245404 (2004).

366 Halpinhealy, T. & Zhang, Y. C. Kinetic roughening phenomena, stochastic growth directed polymers and all that. Aspects of multidisciplinary statistical mechanics. *Phys. Rep.-Rev. Sec. Phys. Lett.* **254**, 215-415, doi:10.1016/0370-1573(94)00087-j (1995).

367 Cuppen, H. M., Meekes, H., van Enckevort, W. J. P. & Vlieg, E. Kink incorporation and step propagation in a non-Kossel model. *Surf Sci* **571**, 41-62, doi:10.1016/j.susc.2004.08.002 (2004).

368 Majaniemi, S., AlaNissila, T. & Krug, J. Kinetic roughening of surfaces: Derivation, solution, and application of linear growth equations. *Phys Rev B* **53**, 8071-8082, doi:10.1103/PhysRevB.53.8071 (1996).

369 Salditt, T. & Spohn, H. Kinetic roughening of a terrace ledge. *Phys. Rev. E* **47**, 3524-3531, doi:10.1103/PhysRevE.47.3524 (1993).

370 Jeong, H. C. & Williams, E. D. Steps on surfaces: experiment and theory. *Surf. Sci. Rep.* **34**, 171-294, doi:10.1016/s0167-5729(98)00010-7 (1999).

371 Spinner, M. A., Watkins, R. W. & Goldbeckwood, G. Simulation of growth and surface roughening of polymer single crystals. *J. Chem. Soc.-Faraday Trans.* **91**, 2587-2592, doi:10.1039/ft9959102587 (1995).

372 Burton, W. K., Cabrera, N. & Frank, F. C. *The growth of crystals and the equilibrium structure of their surfaces*. Vol. 243 (1951).

373 Elwenspoek, M. & Vandereerden, J. P. Kinetic roughening and step free energy in the solid-on-solid model and on naphthalene crystals. *J. Phys. A-Math. Gen.* **20**, 669-678, doi:10.1088/0305-4470/20/3/029 (1987).

Appendix A

Chapter 2 Supplementary Information

Note A1. Classical theories of crystal growth.

Mechanisms of crystallization tend to involve the nucleation and spreading of layers via monomer-by-monomer addition. This mode of growth has been confirmed for numerous crystals[344]. There are various physicochemical parameters, such as supersaturation and temperature, which directly impact growth pathway(s). Supplementary Fig. 17 shows three distinct regimes of growth that are broadly differentiated on the basis of the relative supersaturation σ,

$$\sigma = \frac{C}{C_o} - 1 \qquad (1)$$

$$\Delta\mu = kTln(1+\sigma) \equiv kT\sigma \qquad (2)$$

where k is the Boltzmann constant, T is temperature, $\Delta\mu$ is the change in chemical potential per molecule, C is the solute concentration, and C_o is the equilibrium concentration (or solubility).

At low σ (**Figure A17**, Region I), surfaces grow by the direct addition of solute to defect sites (e.g., screw dislocations[345]), resulting in the formation of hillocks. AFM has proven to be a useful technique for capturing the presence and growth of such features on the surfaces of inorganic[346,347] and organic crystals[348-350]. The growth of a crystal surface follows different dynamics depending on the limitations of solute addition. The Damköhler number (*D*a) is often used to differentiate the rate limiting steps. For instance, when Da << 1 the growth rate is limited by surface integration, and when Da >>1 the growth rate it is limited by bulk transport. In the

kinetic regime, the normal growth rate R of a surface[347,351] exhibits a parabolic relationship with σ as

$$R = C''\sigma^2. \quad (3)$$

The rate constant C" is a function of several parameters,

$$C'' = \frac{nkT}{19\chi a}\,\beta_{st} C_0 \upsilon_c \quad (4)$$

where a is the step height, β_{st} is the kinetic coefficient of step growth, υ_c is the volume of a single building unit, and n is the number of dislocations. The parameter χ is given by

$$\chi = (1 + \frac{D_s}{\lambda_s \beta_{st}})^{-1} \quad (5)$$

where λ_s is the mean distance covered by adatoms during their lifetime, and D_s is the surface diffusion coefficient.

At higher supersaturation (**Figure A17**, Region II), the rate of 2D nucleation becomes sufficiently high to compete with spiral growth, and there is a crossover to the regime where crystallization occurs by 2D layer nucleation and spreading[352]. This mode of growth has been observed for a wide range of materials that include metals[353], inorganics[354], and organics[355]. Nuclei can form on defect free terraces and generate a new layer that advances by monomer addition to steps sites (e.g., kinks). The rate of 2D nucleation determines the mode of growth. At low nucleation rate, the layer extends across the entire crystal surface prior to a new nucleation event. This phenomenon, which is typically referred to as monolayer growth, is more pronounced on small crystal faces at low supersaturation. In this regime, the nucleation rate varies

exponentially with supersaturation while the rate of step growth follows a linear trend. Conversely, the formation of new nuclei before the completion of the underlying layer gives rise to multilayer growth[356]. This regime can be subdivided into two categories depending on the growth area and nucleating area. If the growth area is larger than the nucleating area, the layer emanating from a sparse population of nucleating centers will start merging, and the growth rate of the crystal surface is dominated by the step velocity. However, if the rate of nucleation is high enough that steps merge quickly due to a large population of nuclei, it is referred to as the polynuclear regime. Our observations suggest that LTA surfaces exhibit multilayer growth, $R_{2D,ML,}$ via a birth and spread model as

$$R_{2D,ML} = \omega(\Delta\mu)^{5/6} \exp(-\frac{\Delta G_c}{3kT}) \ . \quad (6)$$

The term ΔG_c (α $1/\Delta\mu$) is the free energy barrier for 2D nucleation. The constant ω is expressed as

$$\omega = [\frac{K_1}{\sqrt{\sigma}}(\beta_{st} C_0 v_c)^2]^{1/3} . \quad (7)$$

Where K_1 is a pre-exponential term for 2D nucleation in solution.

As the supersaturation increases further, classical theory posits a transition from smooth (layered) to rough growth. This phenomenon, which is commonly referred to as kinetic roughening, has been observed for various crystalline materials. The transition from smooth to rough growth can be controlled by supersaturation and/or temperature[357-361]. During kinetic roughening, there is a loss of faceting on crystal surfaces owing to rounded step edges, which can have a concomitant effect on the bulk morphology of crystals[362-364]. Based on the Gibbs-Thompson inverse correlation between a critical radius and supersaturation, the size of a nucleus

in this regime is generally smaller than the critical nucleus size for 2D generation of islands at higher supersaturation. This is attributed to a negligible energetic barrier[365] for solute attachment to crystal surfaces, which renders molecules (i.e., monomers) or small clusters thereof as viable nuclei. Under conditions when barriers to monomer addition are small, there is a high density of nuclei on the surface wherein the average distance between layers is small (e.g., interatomic distances). This, in turn, leads to highly rough surfaces when monomers can attach at all possible binding sites on crystal surfaces.

Various theoretical models[366-369] based on either known or estimated thermodynamic parameters[370,371] have been used to modify the original growth models of Burton, Cabrera, and Frank[372] to account for kinetic roughening. Measurements of crystal growth in the kinetic roughening regime (**Figure A17**, Region III) reveal that the normal growth rate of crystal surfaces varies linearly with increasing supersaturation[373], expressed as

$$R_{KR} \sim \mathrm{C}_{KR} C_o \sigma \qquad (8)$$

where C_{KR} is the kinetic rate constant for kinetic roughening (labelled "*KR*"). In our study, we show a unique form of roughening at low temperature owing to the formation of gel-like islands. Our findings indicate that it is possible for 3D nucleation to occur in a cohesive region when there is partial wetting of the surface by solute. This regime requires higher supersaturation than that of 2D nucleation. The fact that we observe gel-like islands in LTA surface growth at sufficiently high σ suggests a transition from an adhesive region (2D nucleation) to a cohesive region (3D nucleation).

Note A2. Statistical analysis of feature heights in AFM images.

Histograms of feature heights in AFM images were generated using the Igor Pro software provided by the vendor. The software plots the height distribution of individual pixels on AFM height images against the baseline of an average height, which is used as a scaling parameter. Standard deviations were calculated from Gaussian fits to each distribution of feature height. We used the image analysis tool to obtain Gaussian fits to our data. Negative values of height can occur due to scaling.

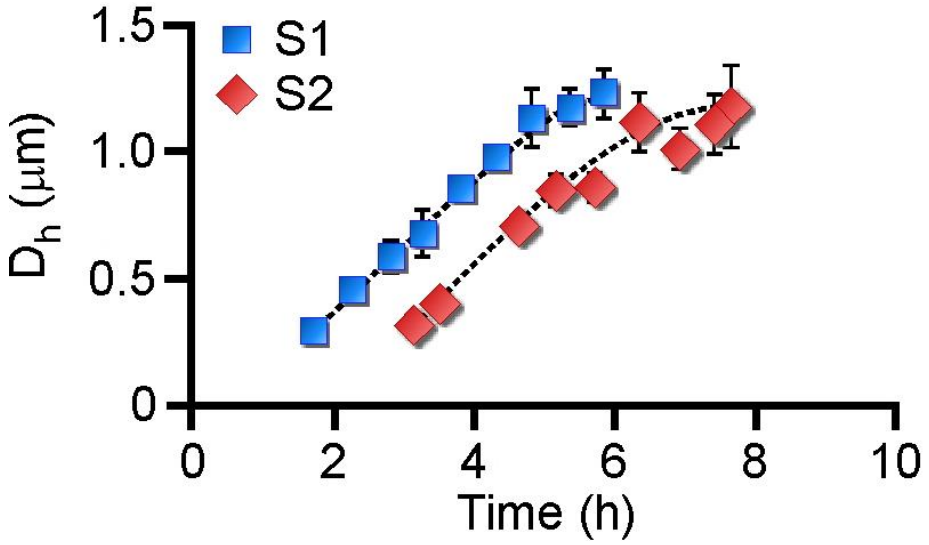

Figure A1: Time-elapsed particle evolution. *In situ* DLS measurements of supernatant solutions S1 (blue squares) and S2 (red diamonds) heated at 45°C as a function of time. Solutions at initial times do not contain any detectable particles, consistent with SAXS measurements in figure **2.2A**.

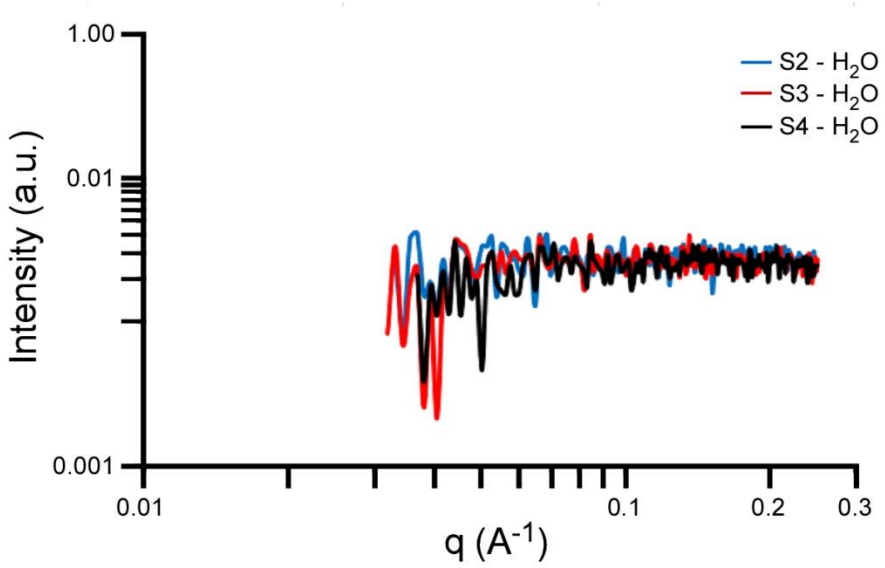

Figure A2: Determination of particle in growth solution: Small-angle X-ray scattering patterns of supernatant solutions S2 (blue), S3 (red), and S4 (black) with subtracted background patterns (water).

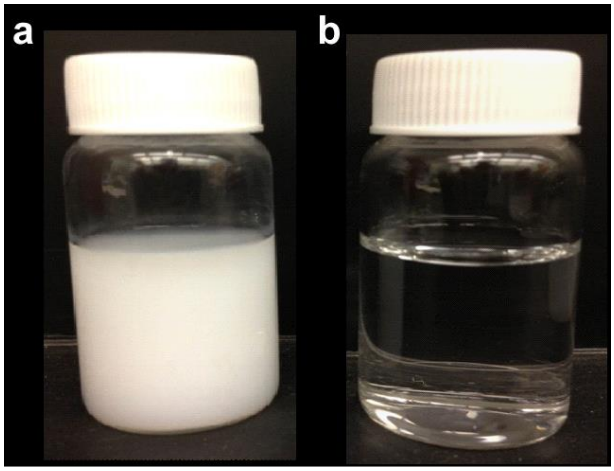

Figure A3: Growth solution before and after filtration:(a) Growth solutions prepared for *in situ* AFM measurements prior to filtration are opaque. **(b)** The same growth solution after centrifugation at 13,000 rpm for 45 min and then filtering twice.

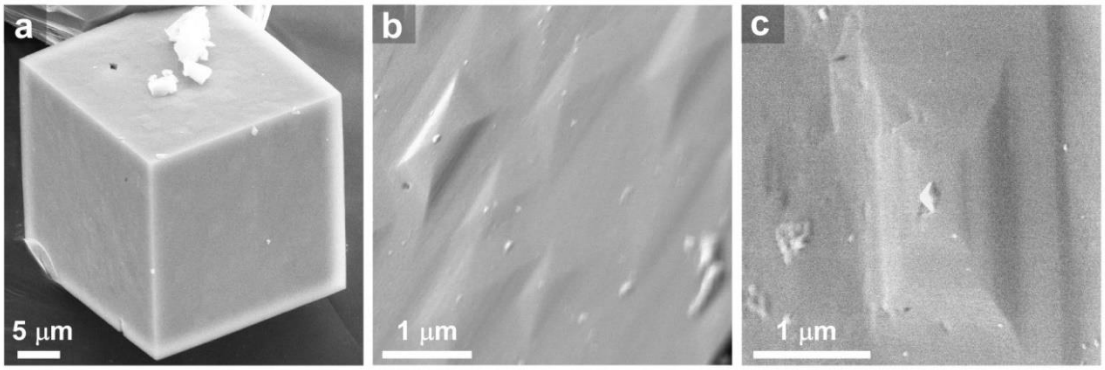

Figure A4: Zeolite A seed crystal: (a) Scanning electron micrograph of a representative LTA crystal used as a substrate for *in situ* AFM measurements. **(b and c)** Corresponding high resolution SEM images of crystal surfaces showing the presence of hillocks.

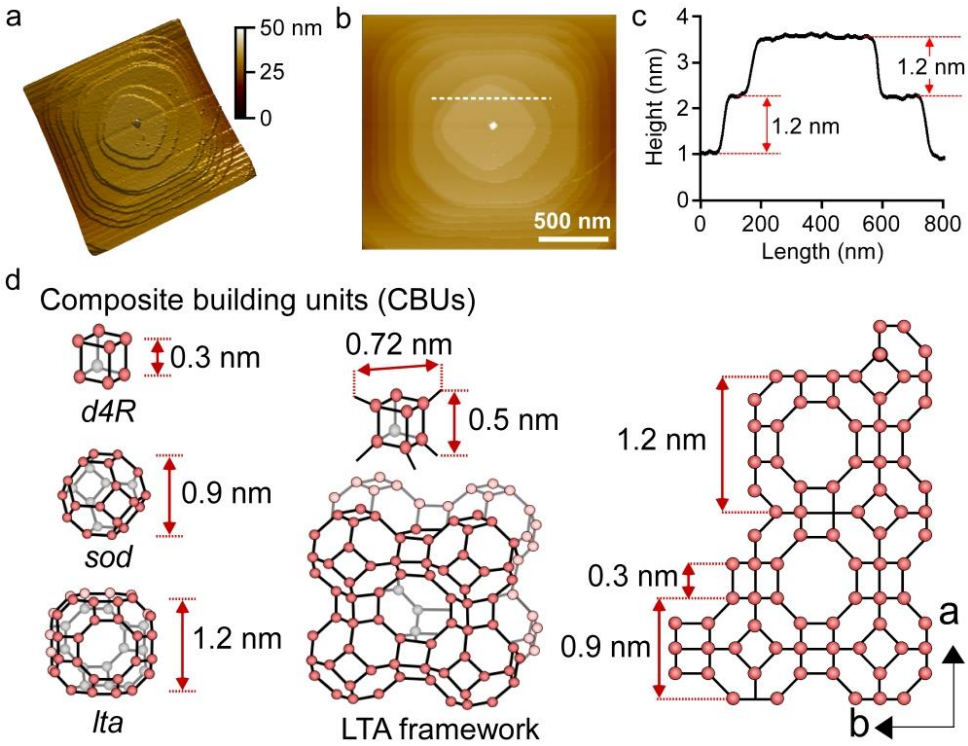

Figure A5: Surface architecture of substrate LTA crystal:(a and b) A 3D and 2D height mode scan of a hillock on the surface of a LTA crystal. **(c)** Height profile along the dashed white line labeled in image B. (**d)** Schematics of composite building units (CBUs)

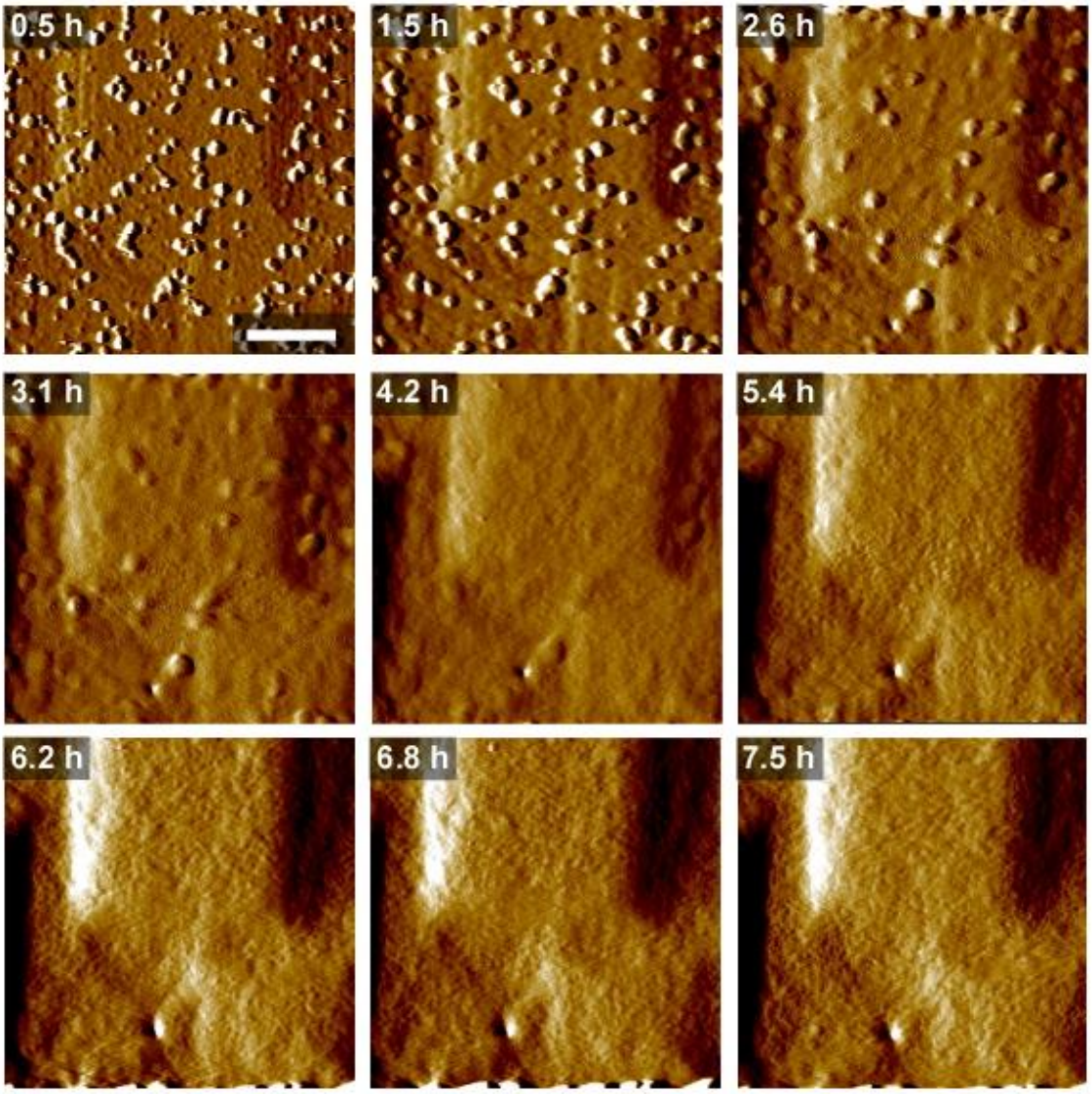

Figure A6: Surface evolution at low temperature and high saturation: Time-resolved AFM amplitude mode images of LTA surface growth at 35°C in growth solution S2.

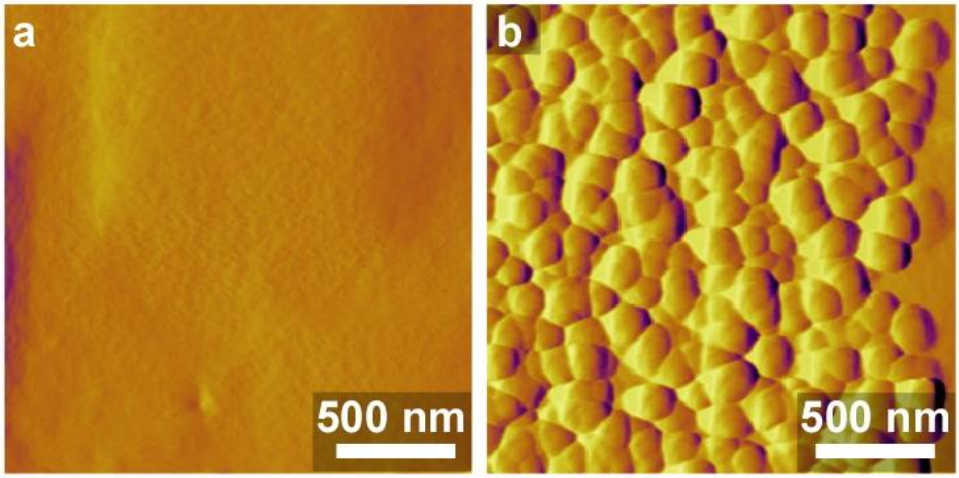

Figure A7: Image depicting tip effect:.(a). High resolution AFM amplitude mode image of the smooth area (region I) in figure **2.3D** with its corresponding narrow height distribution in **figure 2.3A**. b. High resolution amplitude mode image of the rough area in **figure 2.3D**

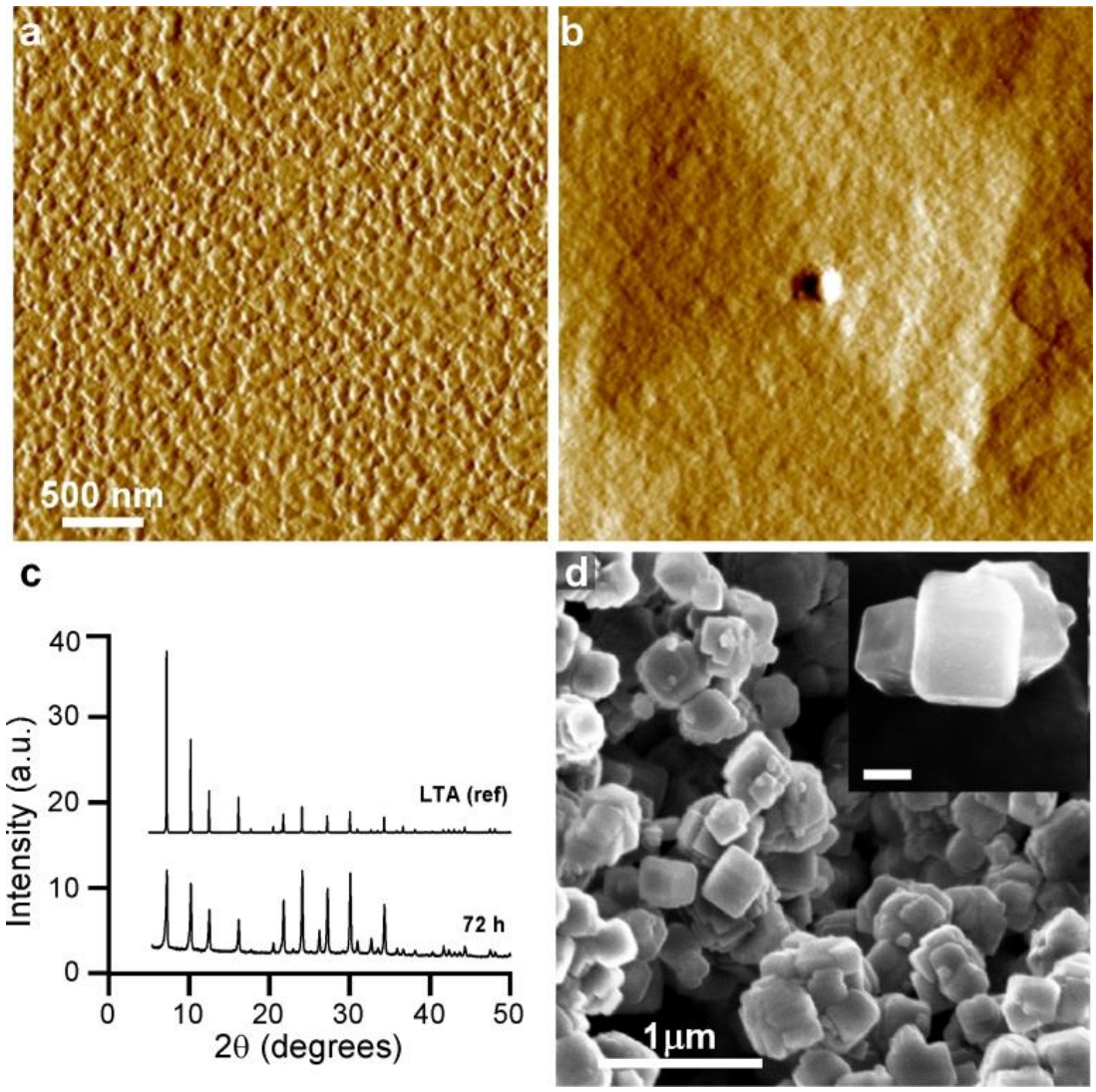

Figure A8: LTA crystallization at 35°C. (a and b) AFM images of the LTA samples used for XPS analysis after (a) 2 h and (b) 12 h of heating**. (c)** Powder XRD pattern of the product from a LTA growth mixture after 72 h heating. (**d)** SEM of LTA crystals

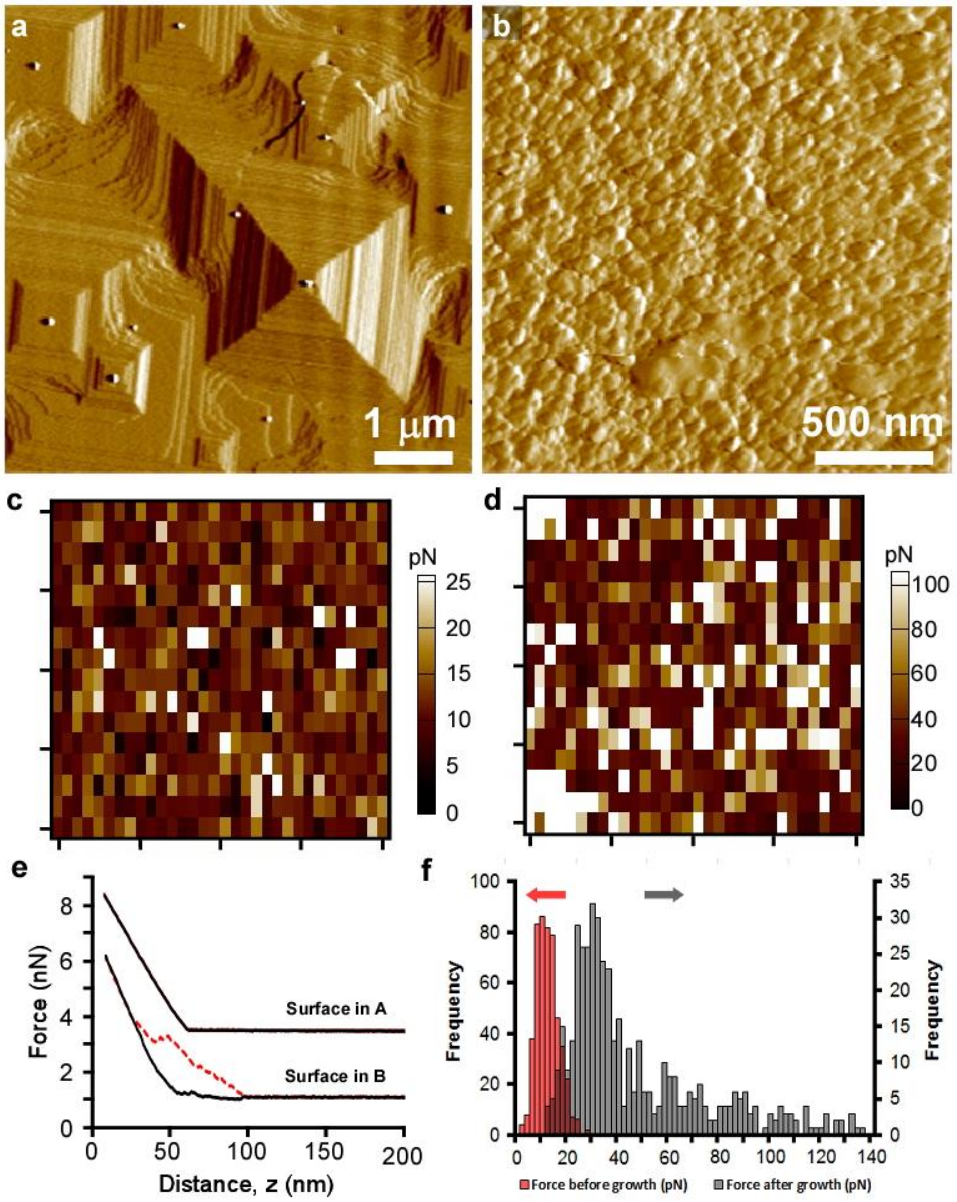

Figure A9: Chemical force microscopy before and after growth: (**a and b)** AFM mode images of a LTA crystal surface (A) before and (B) after growth,. **(c and d)** Discretized force measurements for sample areas corresponding to images A and B. (**e)** Representative approach-retract profiles from CFM analysis (**f)** Histograms of the unbinding force

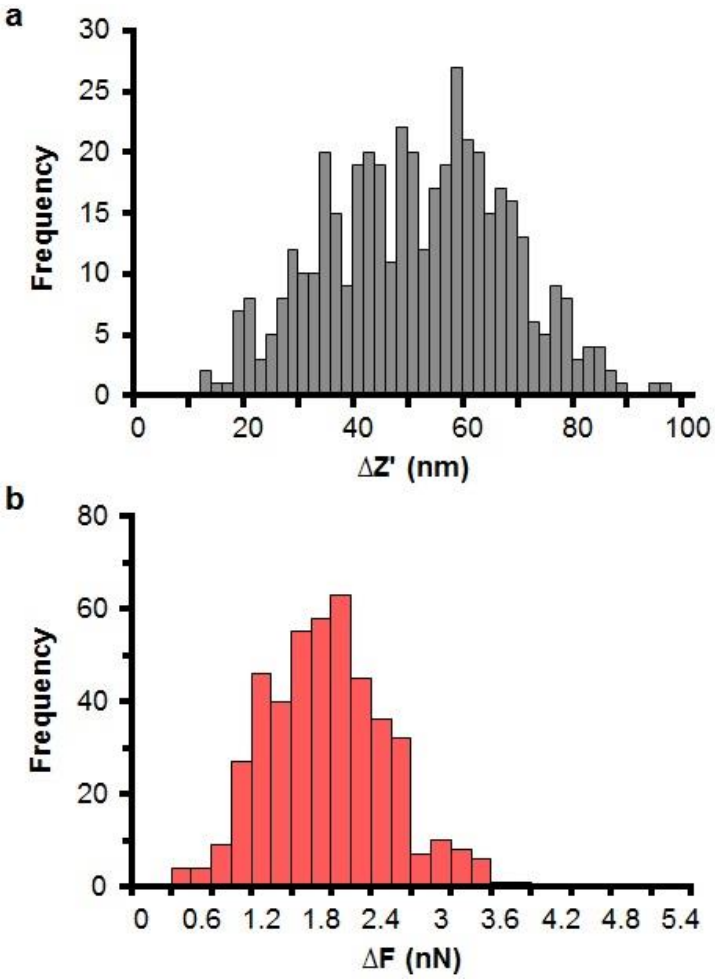

Figure A10: Hysteresis analysis between approach and retraction curve. (a). Distribution of approach distances $\Delta z'$ for CFM measurements of rough LTA surfaces (**b)** The corresponding distribution of breakpoint forces ΔF for the nonlinear approach curve.

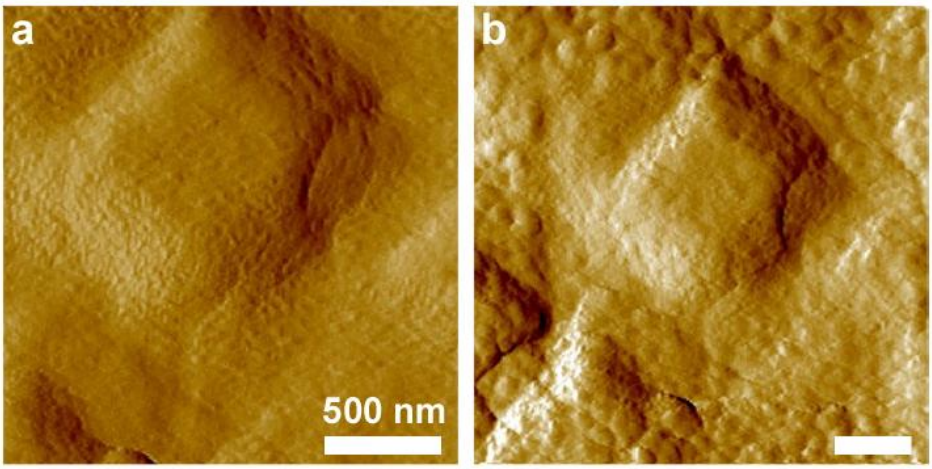

Figure A11: Tip effect at intermediate saturation and low temperature: a. Time-resolved AFM image showing an area after continuous scanning in growth solution S3 at 35°C. **b.** An enlarged scan area with the smooth region a surrounded by rough areas.

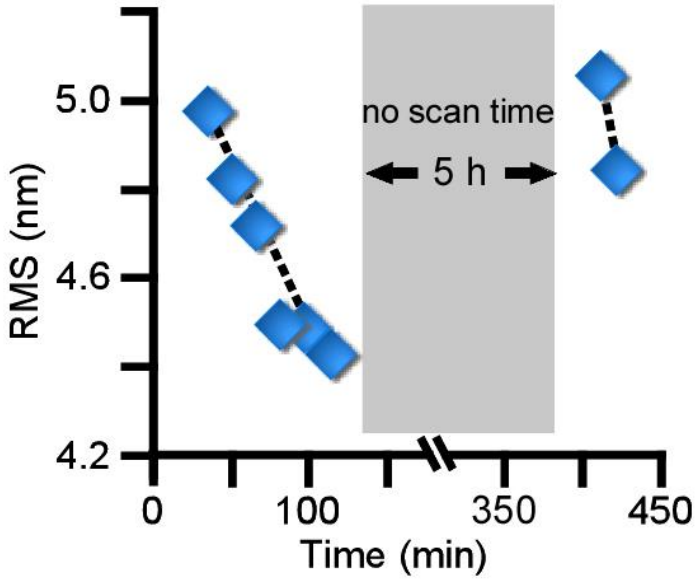

Figure A12: Evolution of surface roughness. Changes in the root mean squared roughness of a LTA crystal surface as a function of time for a crystal substrate grown in solution S3.

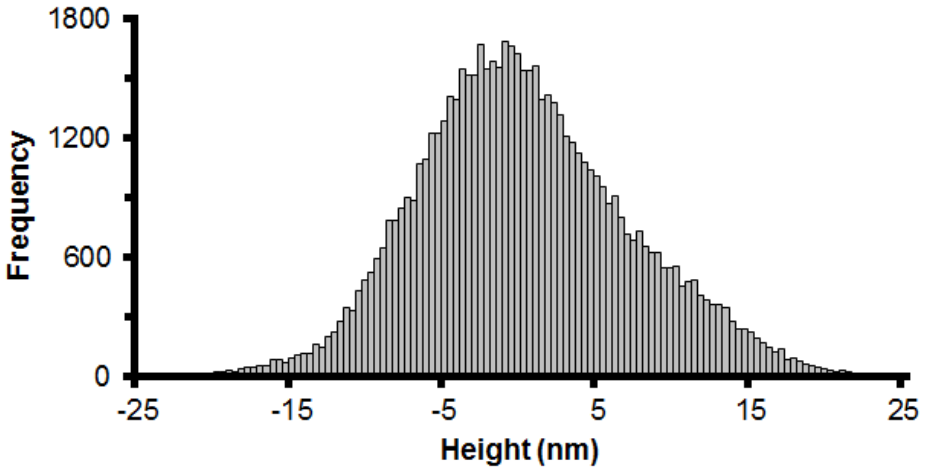

Figure A13: Height histogram of nanoparticle deposits. Height distribution of islands on the LTA crystal surface shown in figure 1.3a. The substrate was heated in growth solution S2 for 1 h at 45°C prior to analysis.

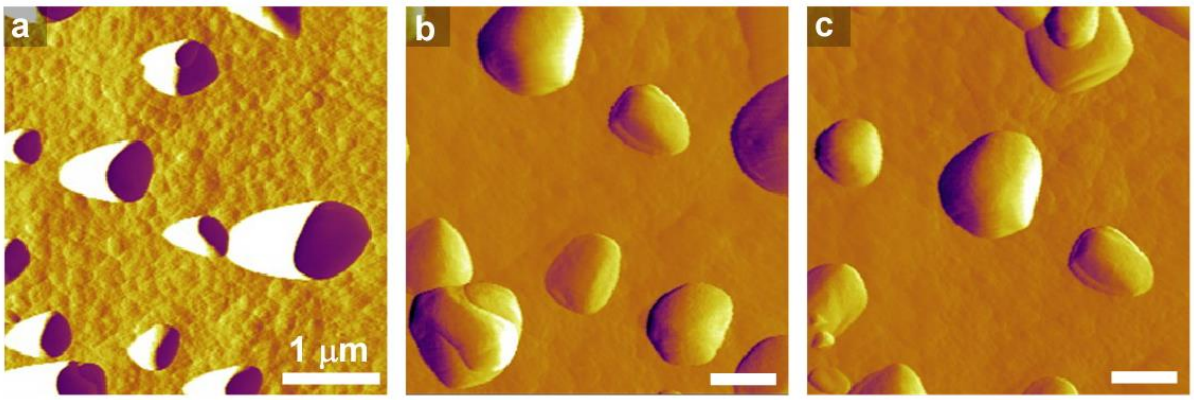

Figure A14: AFM images at high temperature .(a) AFM of the same area shown in figure 1.3e. (**b and c)** AFM images taken in contact mode. Comparison of surfaces before and after continuous imaging show no visible signs of AFM tip effects.

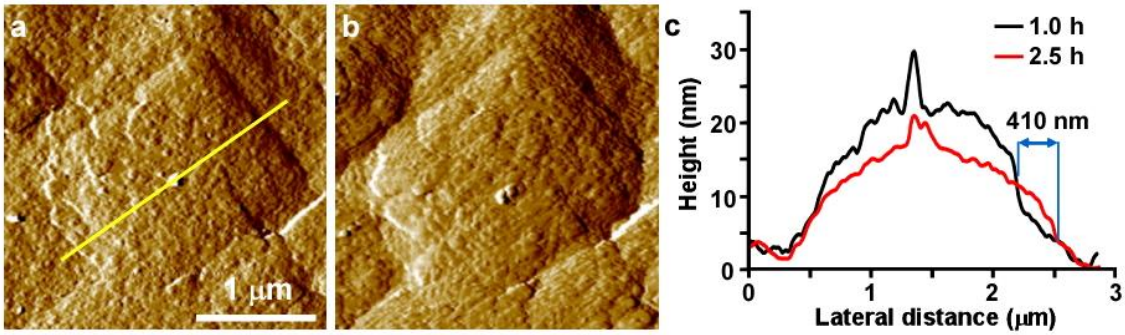

Figure A15: **Growth of hillocks. a and b.** AFM images of a crystal surface after **(a)** 1 h and **(b)** 2.5 h of imaging at 45°C in growth solution S4. **(c)** Height profiles along the yellow line in image a reveal an increase in the length of the hillock (Δx = 410 nm).

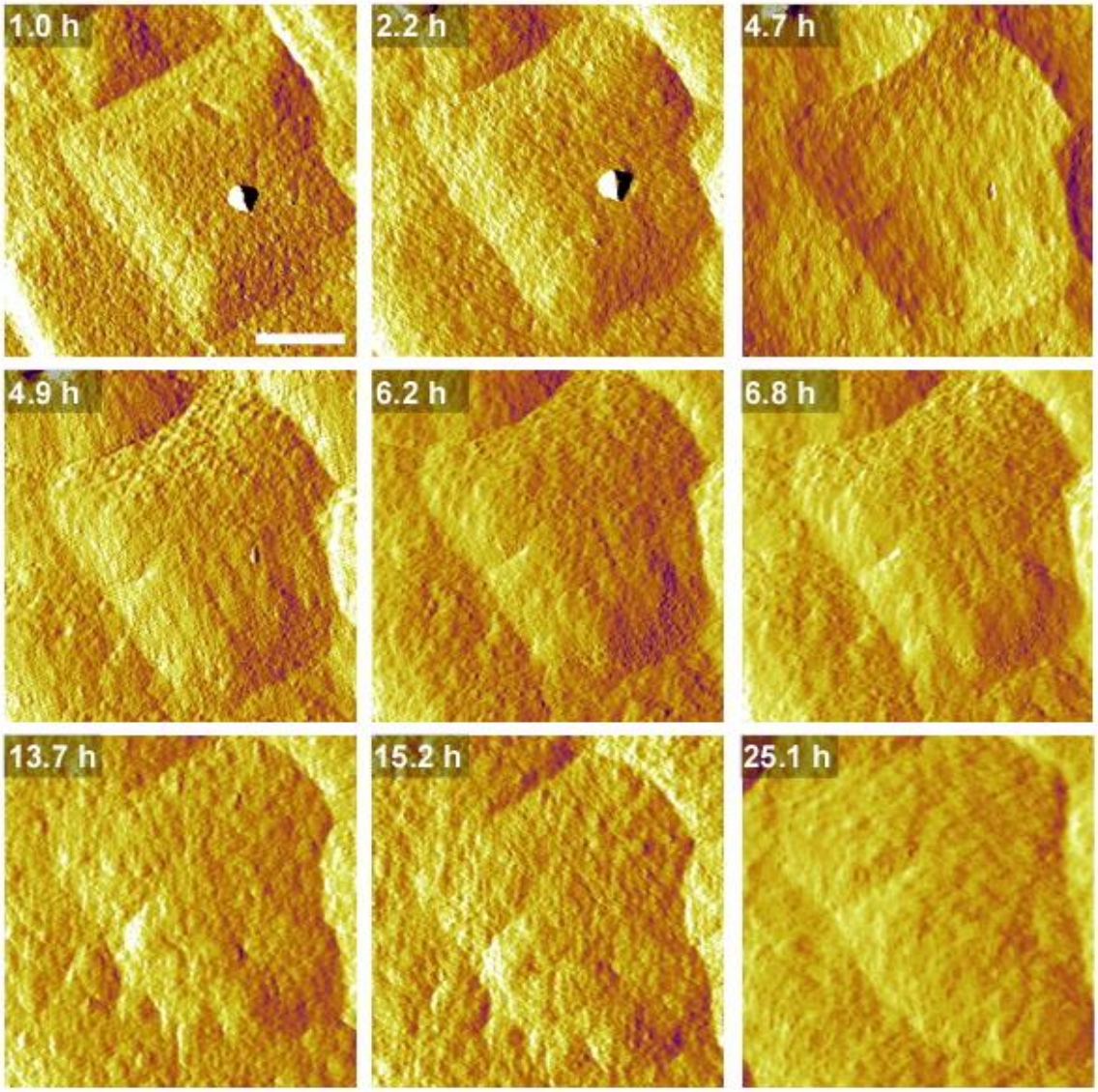

Figure A16: Evolution of crystal surface at high temperature and moderate supersaturation. Time-resolved AFM images of a crystal surface grown in solution S3 at 45°C.

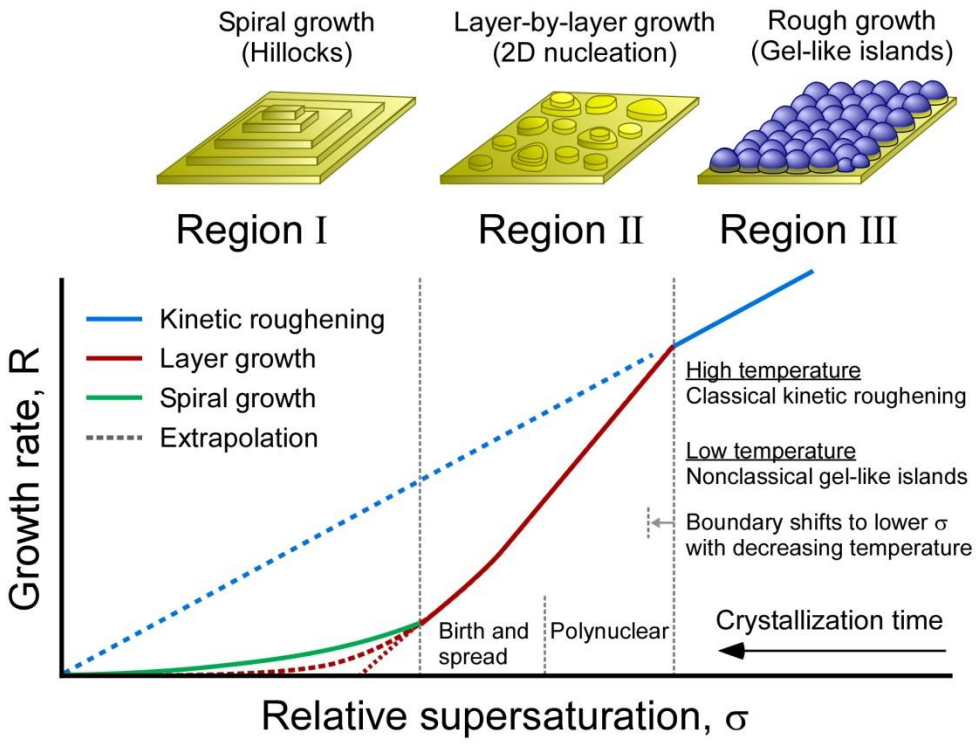

Figure A17: Growth regimes with supersaturation. Illustrative renderings of crystal growth mechanisms as a function of the relative supersaturation σ. (bottom) Growth rate dependency on σ (solid lines) for each regime according to the classical theories

Table A1: Elemental analysis of growth solutions using ICP-OES.

Solution	Concentration (M) [a], [b]			pH
	Si	Al	Na	
S2	0.025	0.292	2.81	13.7
S3	0.011	0.228	2.96	13.7
S4	0.009	0.218	2.90	13.7
S24 [c]	0.007	0.204	2.96	13.7

[a] Obtained by ICP-OES analysis (Intertek-Whitehouse)

[b] The water content changes by less than 0.1 wt%

[c] Approximate solubility of zeolite A; note that the supersaturation of zeolite growth solutions is difficult to define[182] owing to the presence of various oligomeric species and amorphous precursors

Table A2: Elemental analysis (Si/Al ratio) of crystals before and during an intermediate stage of growth.

Sample / Growth Conditions	Si/Al Ratio [b]	
	EDX	XPS
LTA crystals	1.0	1.1
Ex situ growth (S2, 45 °C, 2 h) [a]	1.0	0.9
Ex situ growth (S2, 35 °C, 2 h) [a]	1.0	0.7
Ex situ growth (S2, 35 °C, 12 h) [a]	1.0	1.1

[a] LTA crystals (ca. 10 mg) were suspended in a S2 growth solutions (ca. 3 g) that was heated to the set point temperature. Samples were removed either after 2 h of heating (i.e., intermediate stage of growth) or after 12 h of heating (i.e., complete growth).

[b] Energy dispersive X-ray spectroscopy (EDX) data is an estimate of the bulk (overall) crystal composition while X-ray photoelectron spectroscopy (XPS) is a surface-sensitive technique that estimates the composition of exterior regions of the particle.

Appendix B

Chapter 3 Supplementary Information

Table B1: Elemental analysis of growth solutions using ICP-OES.

Solution	Concentration (M)[a]			σ[c]
	Si	Al	Na	
S_2D	0.03	0.24	3.03	2.7
S_Spiral	0.01	0.24	2.97	0.6
S_eq[b]	0.007	0.246	3.15	0.0

[a] Obtained by ICP-OES analysis (Intertek-Whitehouse)
[b] Approximate solubility of zeolite A
[c] Supersaturation (σ) $= \frac{[Al][Si]}{[Al]_{eq}[Si]_{eq}} - 1$

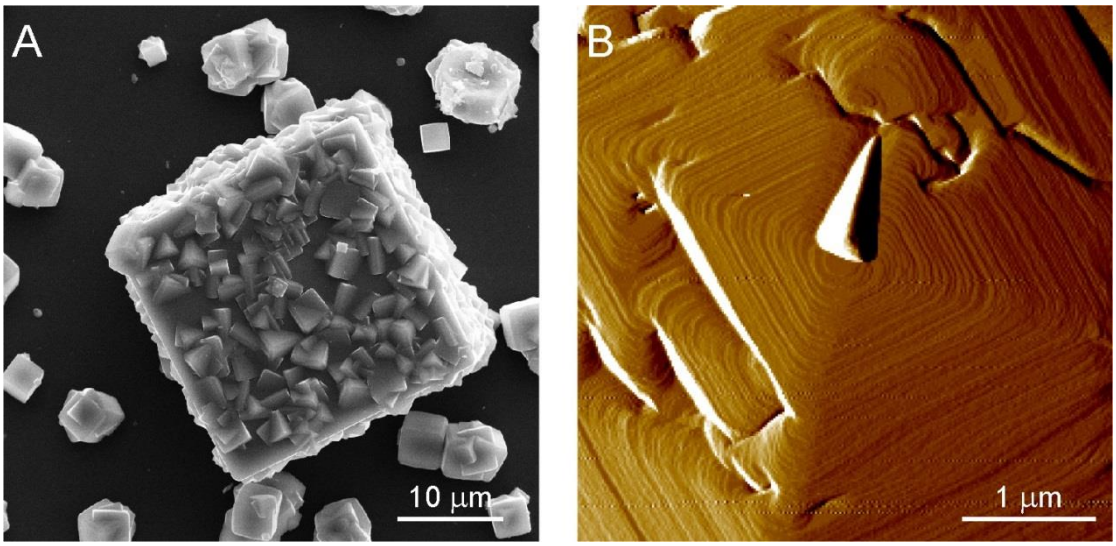

Figure B1: (A) Scanning electron micrograph of a representative LTA crystal after *in situ* AFM experiment at high supersaturation depicting oriented attachment. **(B)** AFM micrograph showing protrusions

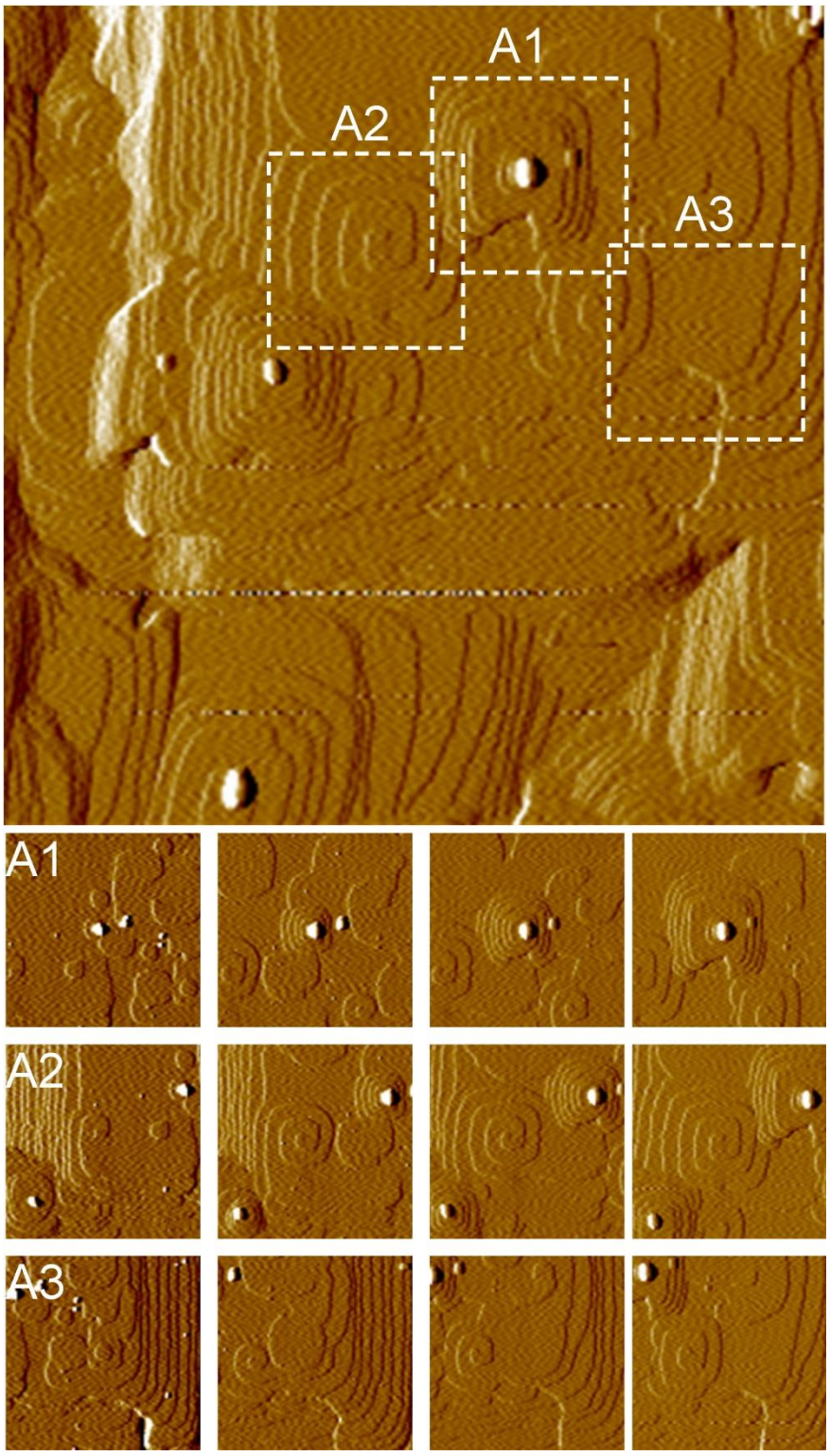

Figure B2: AFM amplitude mode image of a crystal surface in solution in S2 (low supersaturation). High resolution images of selected areas A1, A2, and A3 highlight the dynamics of surface growth (total imaging time = 3.5 h).

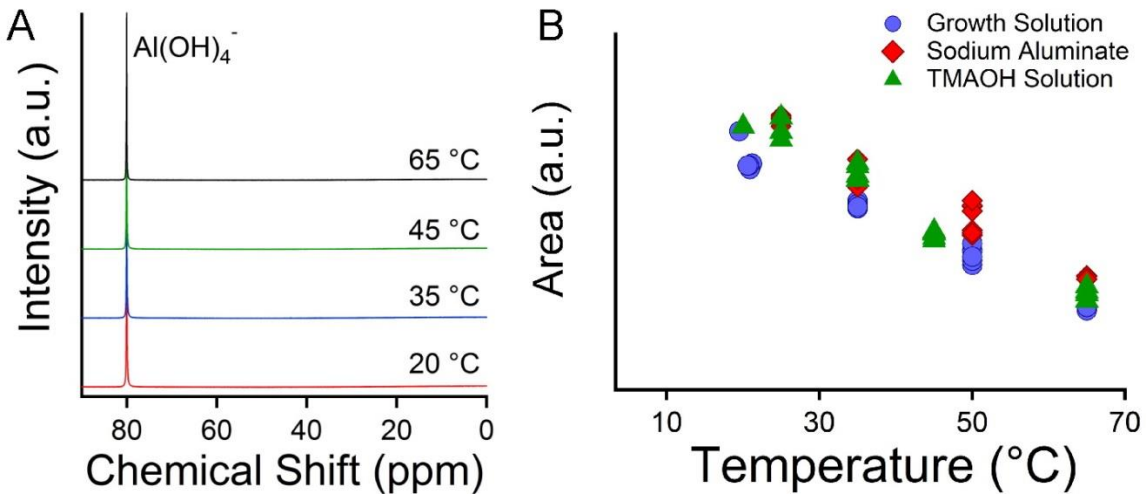

Figure B3:(A) Liquid ^{27}Al NMR spectrum of growth solutions at various temperatures **(B)** Comparison of monomer (δ = 80 ppm) peak areas for the growth solutions in (A) along with solutions prepared with only sodium aluminate.

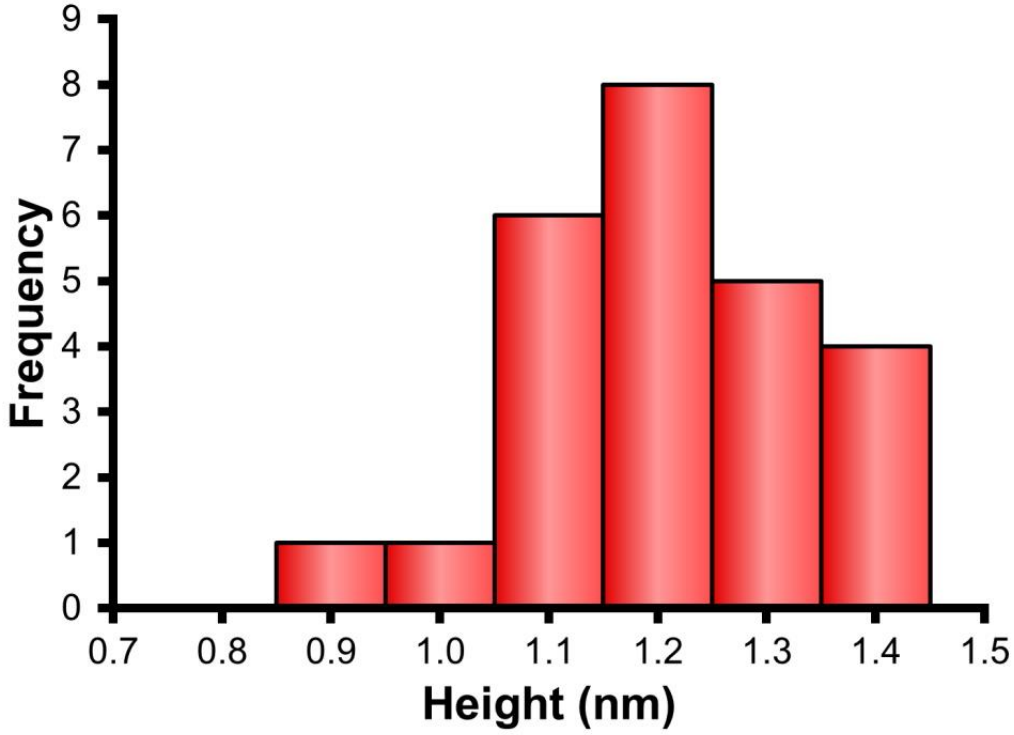

Figure B4: Statistical analysis of height of steps during dissolution process

Appendix C

Chapter 4 Supplementary Information

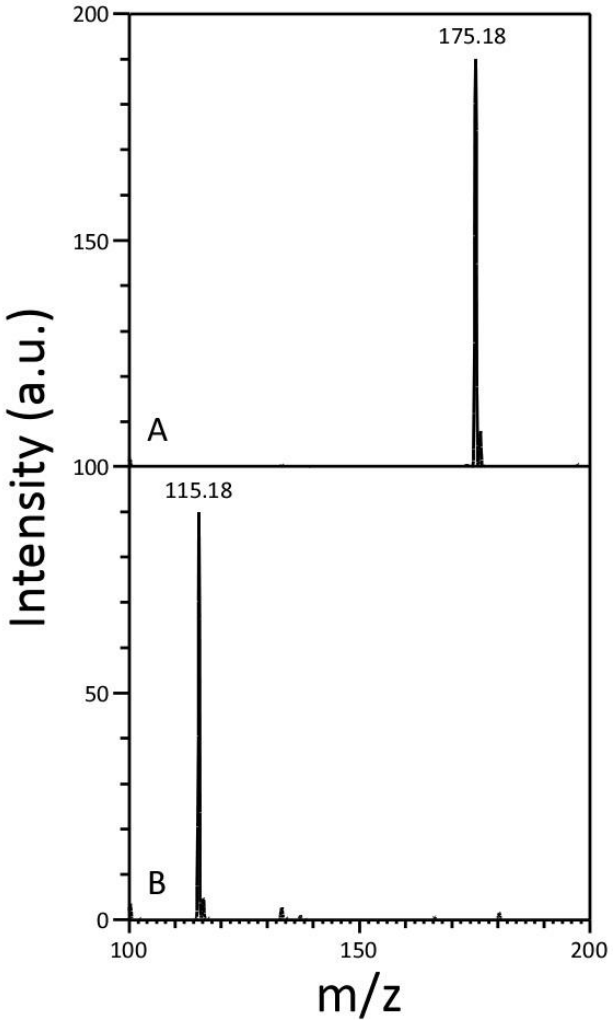

Figure C1: Mass spectra of a solution containing D-arginine and NaOH (pH 12.3) that was measured **(A)** before and **(B)** after hydrothermal treatment at 160°C for 72 h. The m/z ratios correspond to D-arginine and (R)-ornithine-lactam, respectively

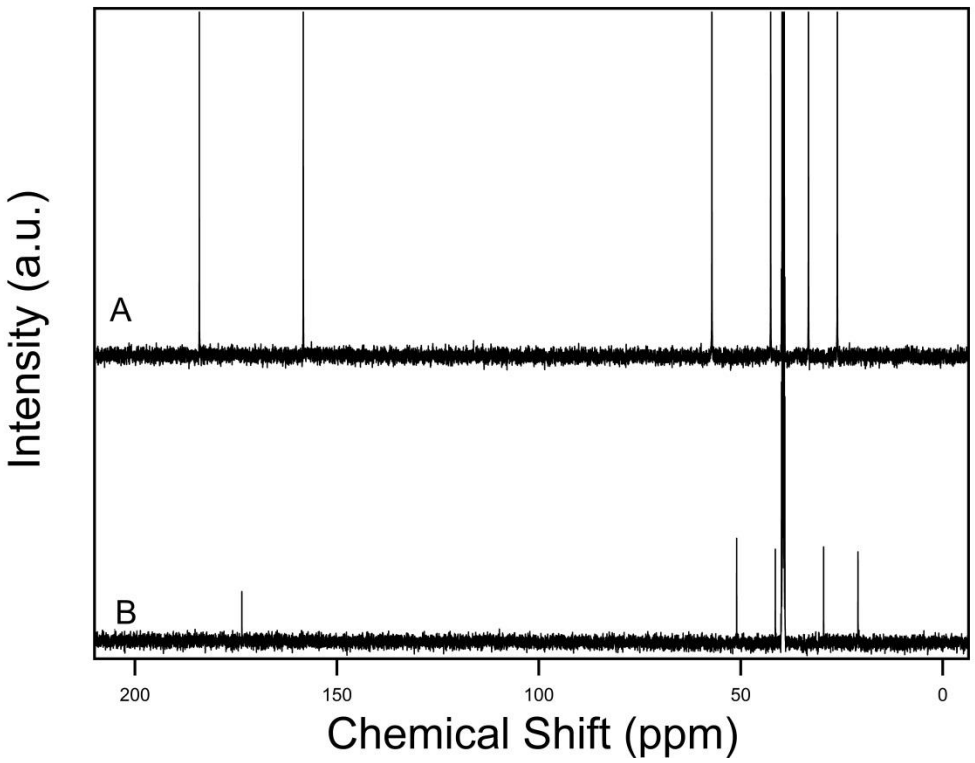

Figure C2: ^{13}C-NMR spectrum in DMSO of **(A)** D-Arg and **(B)** organics that were extracted from a solution containing D-arginine and NaOH (pH 12.3) after heating at 160°C for 72 h. The pattern matches that of ornithine-lactam (see **Figure C3**).

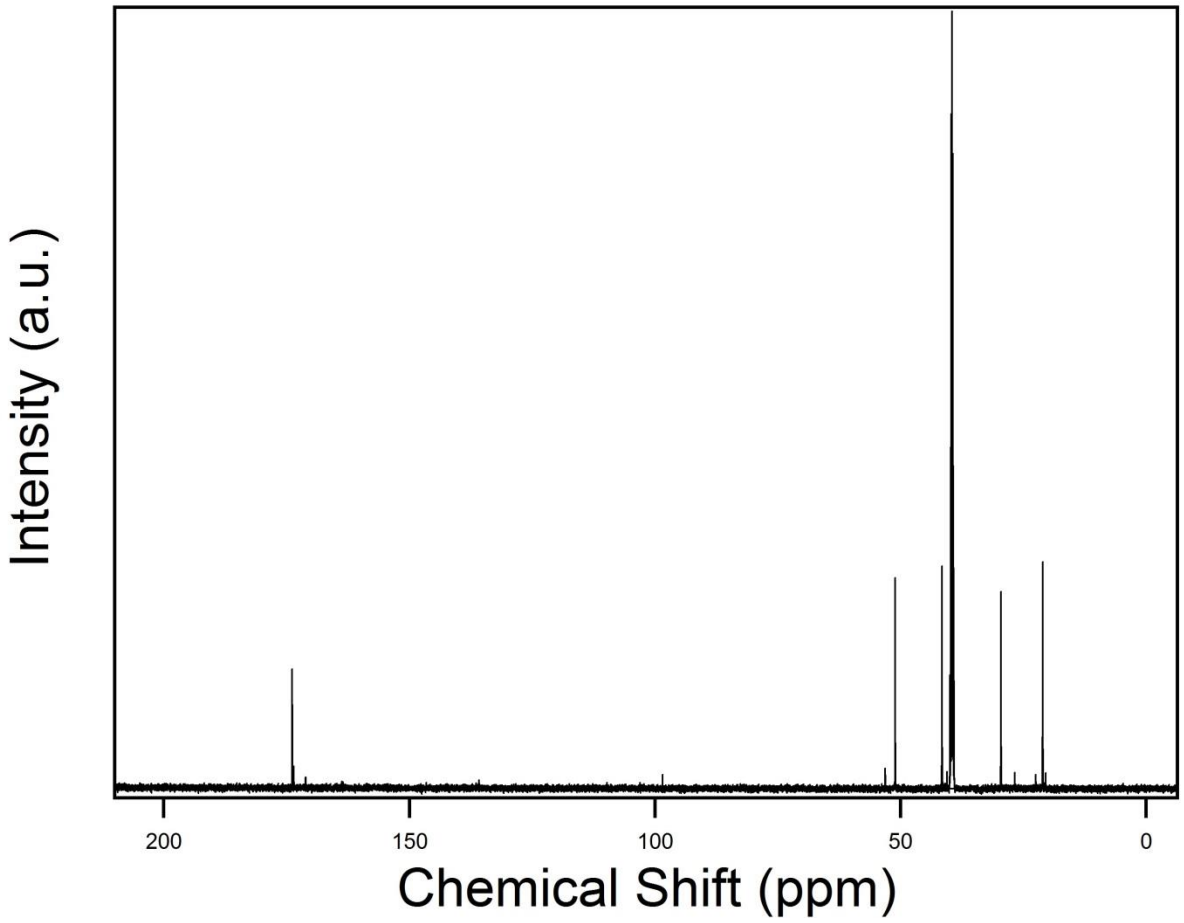

Figure C3: ^{13}C-NMR spectrum of ornithine-lactam (R/S-OL) in DMSO. The reagent was purchased from AK Scientific Inc. to confirm the product of D-Arg. thermal decomposition.

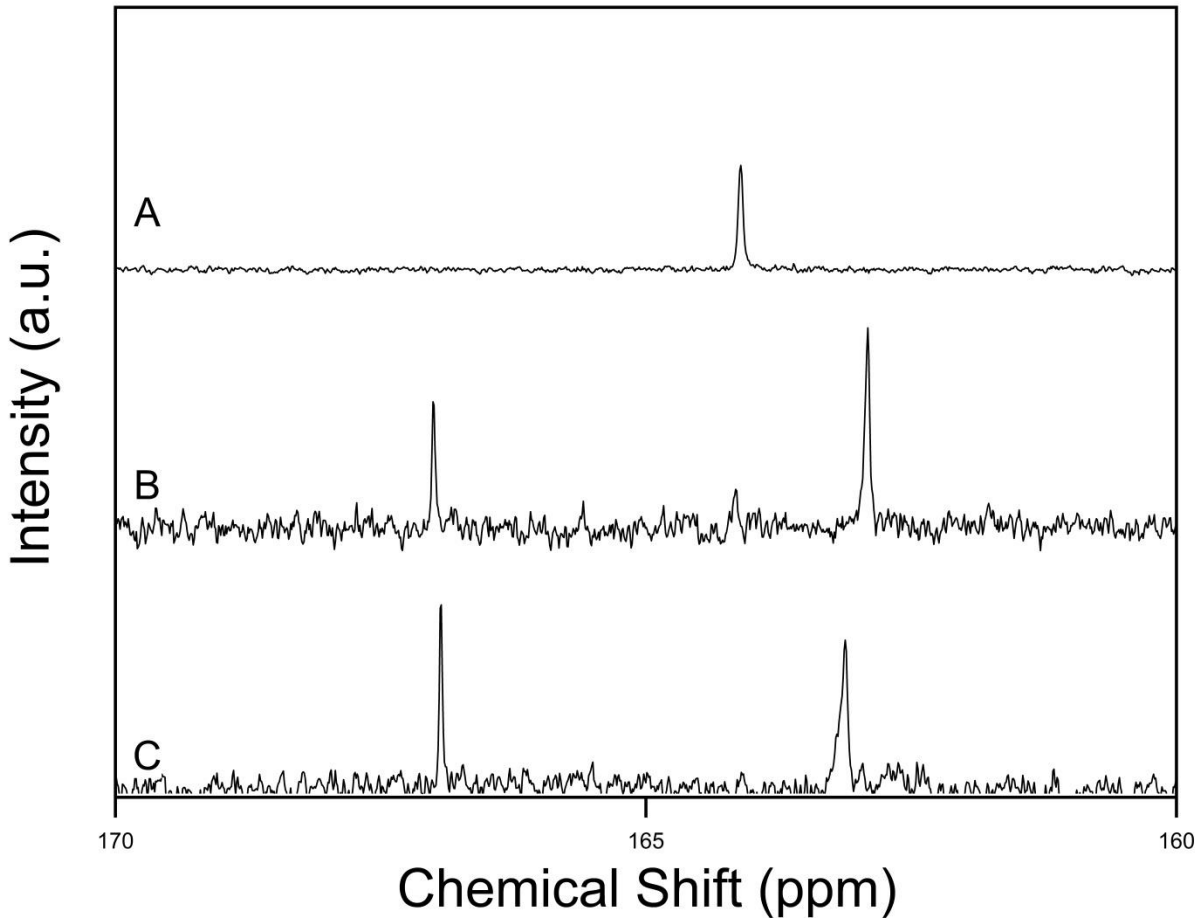

Figure C4: ^{13}C-NMR spectrum of urea measured in alkaline solution **(A)** without heating (i.e. as received reagent from EMD Chemicals Inc.), and after hydrothermal treatment at 160°C for **(B)** 4 h and **(C)** 8 h. The final product of urea decomposition is carbonate.

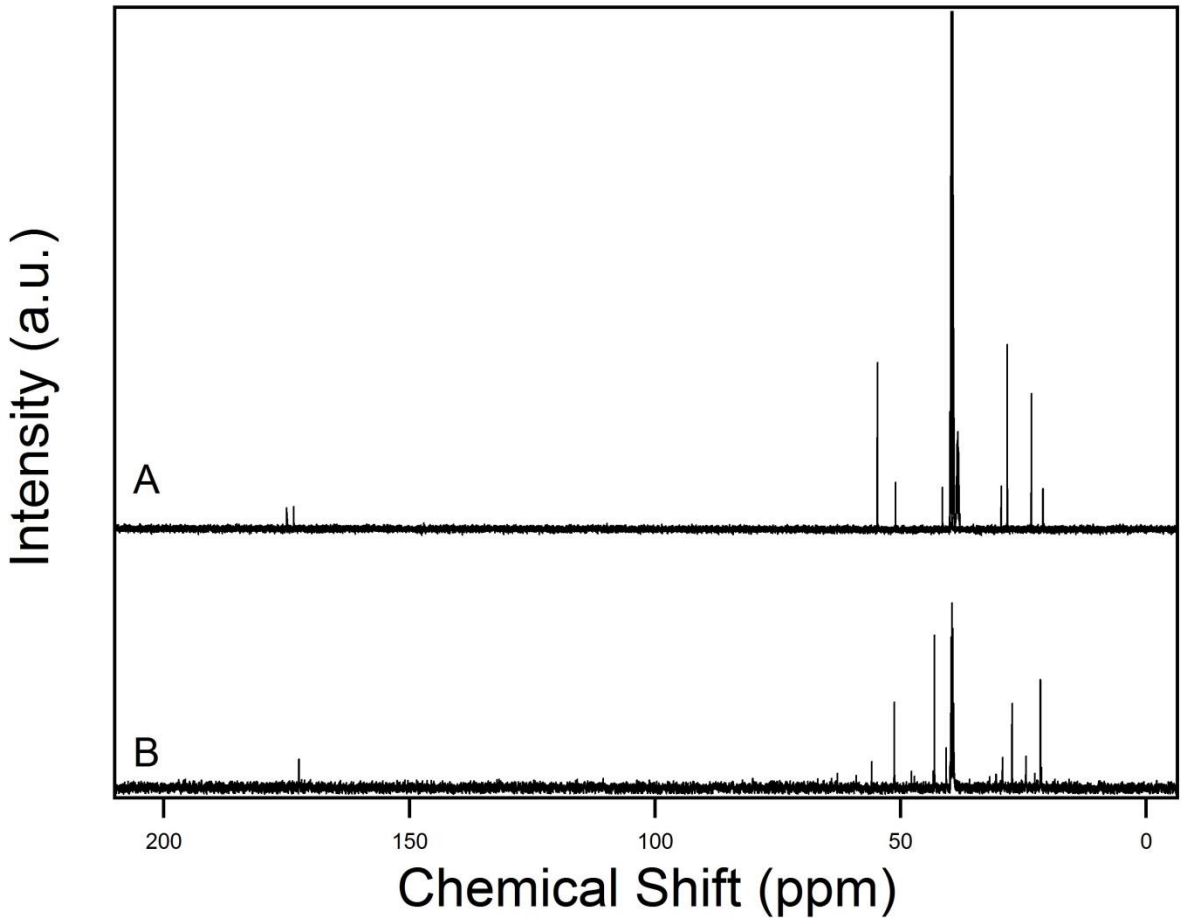

Figure C5: ^{13}C-NMR spectrum of D-ornithine measured in alkaline solution **(A)** without heating (i.e. as received reagent from Sigma Aldrich), and **(B)** after hydrothermal treatment at 160°C for 8 h. The pattern matches that of ornithine-lactam (see **Figure C3**).

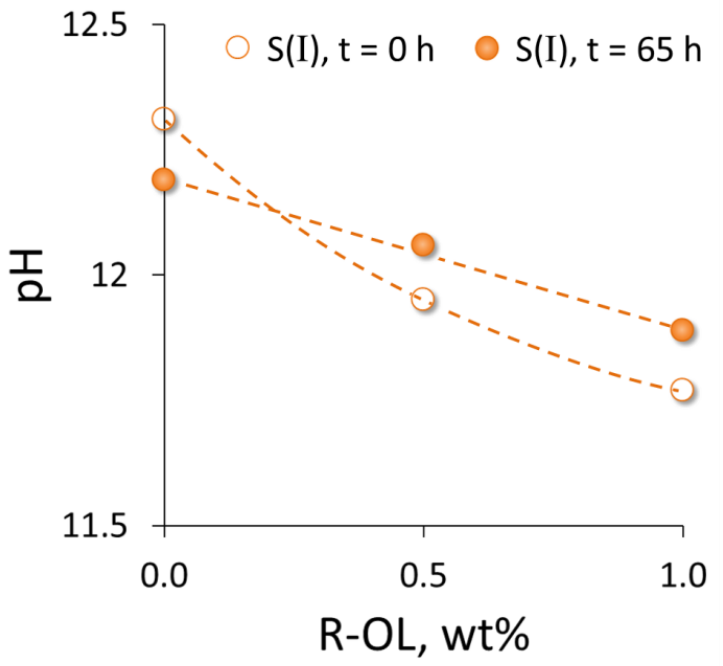

Figure C6: Measurements of pH for silicalite-1 growth solution S(I) prior to (pH_i, open symbols) and after (pH_o, solid symbols) hydrothermal treatment at 160°C for 65 h as a function of R-OL weight percentage.

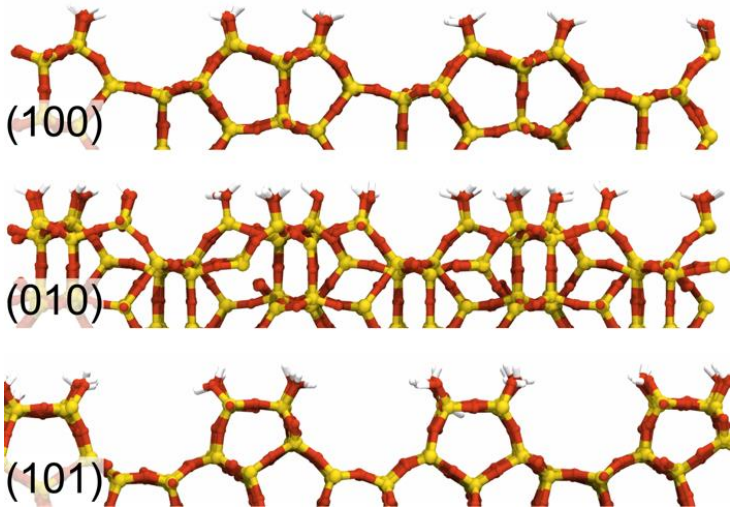

Figure C7: Model (hkl) surfaces of silicalite-1 used in the USMD simulations to investigate R/S-OL adsorption.

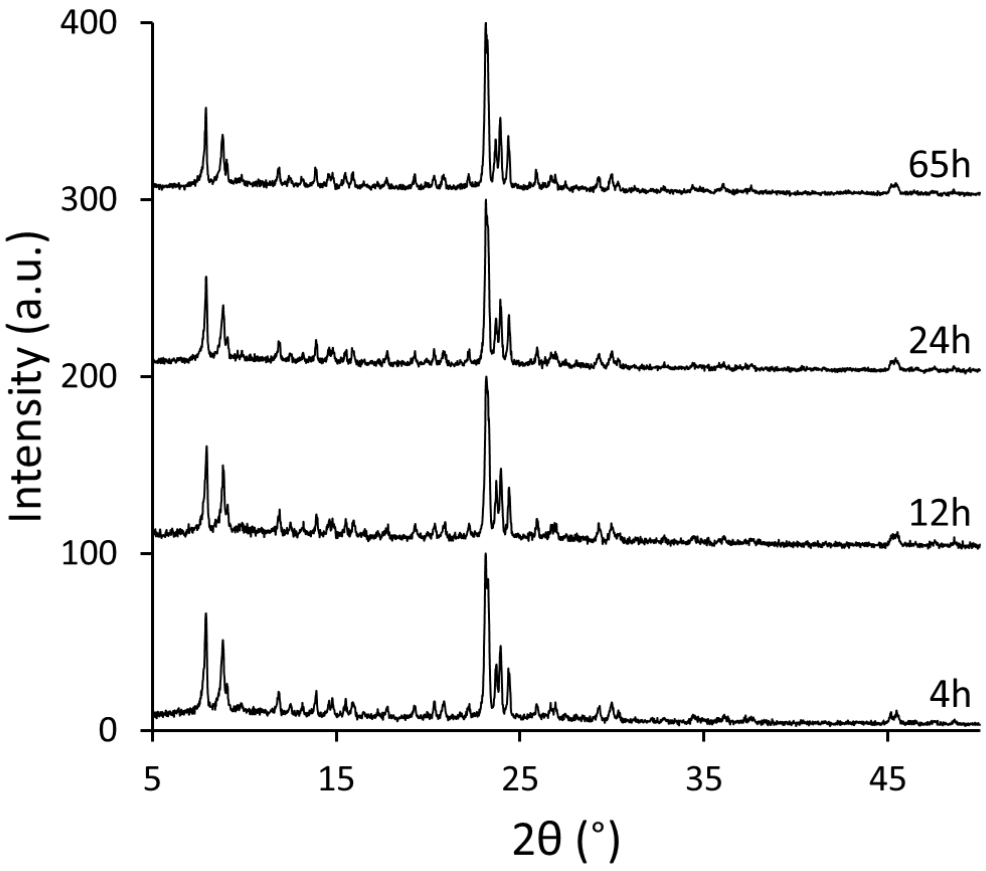

Figure C8: Powder XRD patterns of extracted solids from S(II) growth solutions after 4, 12, 24, and 65 h of hydrothermal treatment at 160°C.

Growth modification of ZSM-5. The effect of R-OL on ZSM-5 (MFI type) crystal morphology and size was assessed by bulk crystallization studies in both the absence of modifier and in the presence of varying R-OL weight fraction. We added aluminum sulfate ($Al_2(SO_4)_3$) to solution S(II)' to make an initial gel Si/Al ratio of 50. The majority of aluminosilicate species are in the form of nanoparticle precursors. ZSM-5 crystals produced from growth solution S(II)' (containing Al) in the absence of modifier exhibit a typical ZSM-5 morphology (**Figure C9A**). A systematic study of varying modifier content (**Figure C9C**) reveals little change in crystal thickness, while crystal length increases monotonically with increasing D-Arg concentration. The aspect ratio of length over thickness increases with increasing modifier concentration (**Figure C9B**). This agrees with the observations for silicalite-1 crystals synthesized in solution S(II).

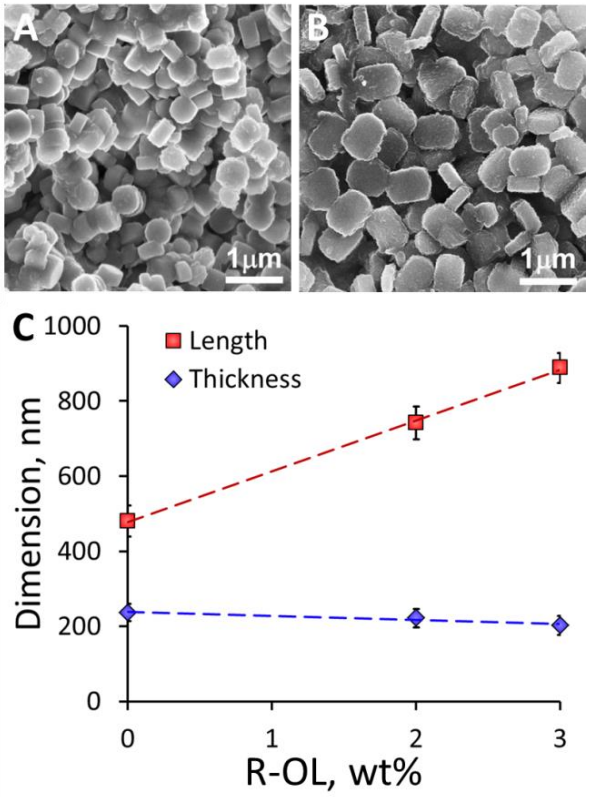

Figure C9: Effect of R-OL on the morphology of ZSM-5 crystals SEM of ZSM-5 crystals prepared **(A)** control (absence of D-Arg) and **(B)** 3 wt% D-Arg. **(C)** Plot of crystal length and thickness of ZSM-5 crystals as a function of modifier concentration

Appendix D

Chapter 5 Supplementary Information

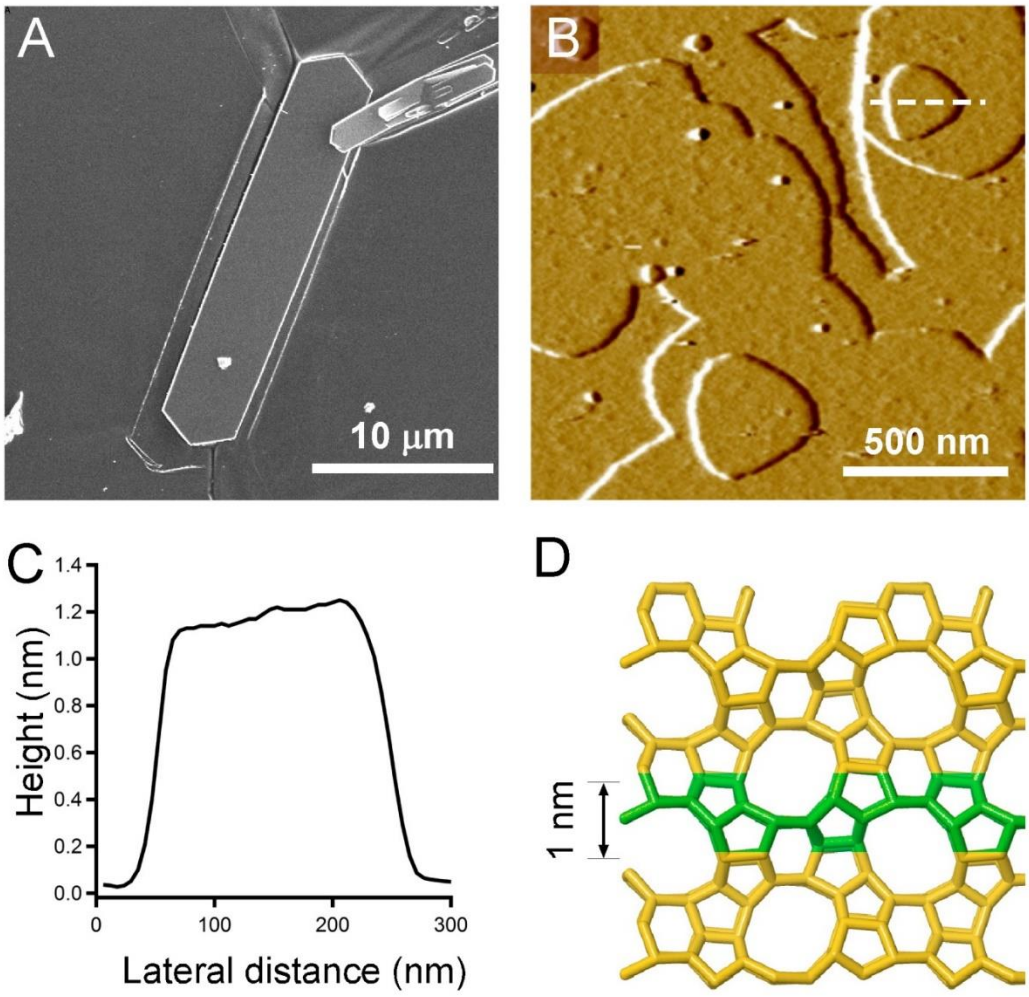

Figure D1: Representative silicalite-1 crystal used as a substrate **(A)** SEM of crystals. **(B**) AFM image of a silicalite-1 (010) substrate. **(C)** Height profile of steps on the crystal substrates,. **(D)** Schematic of a (100) surface showing the pentasil chains in green,

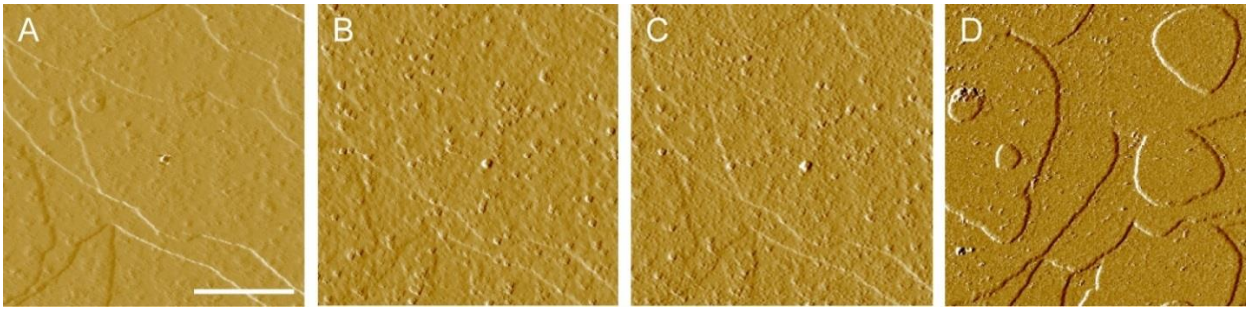

Figure D2: Time-elapsed AFM images in contact with solutions with TEA-nanoparticle solution taken at the following times: **(A)** 1 h, **(B)** 7 h, and **(C)** 17 h. **(D)** AFM image of a different sample after 17 h of AFM imaging. Scale bar equals 500 nm.

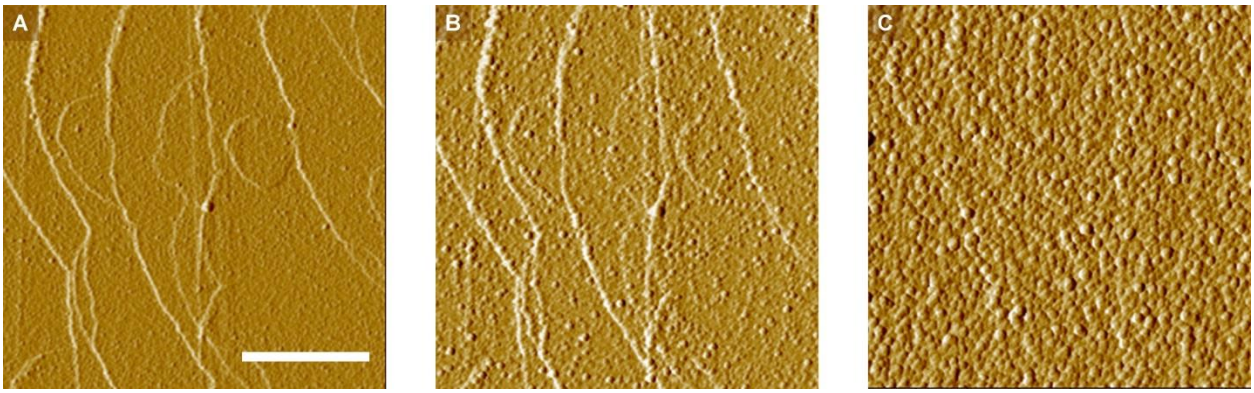

Figure D3: Time-elapsed amplitude AFM images of a silicalite-1 (010) surface in contact with a TBA-nanoparticle solution heated at 60 °C for the following times: **(A)** 1 h**, (B)** 7 h, and **(C)** 17 h. Scale bar equals 500 nm.

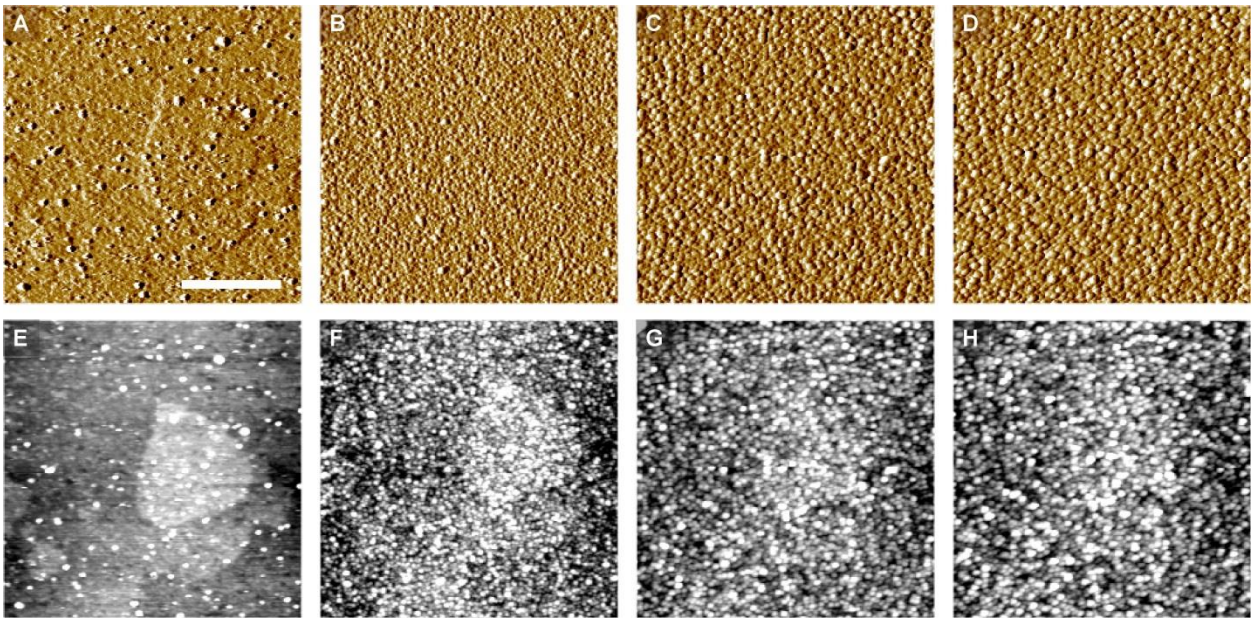

Figure D4: Time-elapsed AFM images (A – D) and corresponding height mode images (E – F) of a silicalite-1 (010) surface in contact with a TPA-nanoparticle solution for the following times: **(A)** 1 h, **(B)** 7 h, **(C)**13 h, and **(D)** 17 h. Scale bar equals 500 nm.

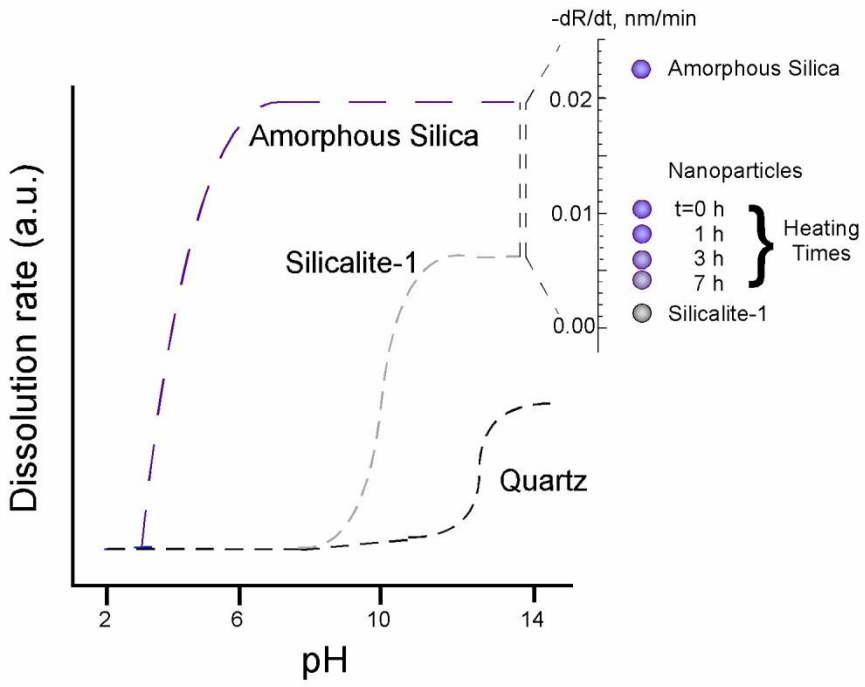

Figure D5: Dissolution rate as a function of solution pH for various silicates reproduced from Rimer et al.[128]. The inset contains a comparison of the dissolutions rates for TPA-nanoparticles pre-heated for various times to amorphous silica and silicalite-1

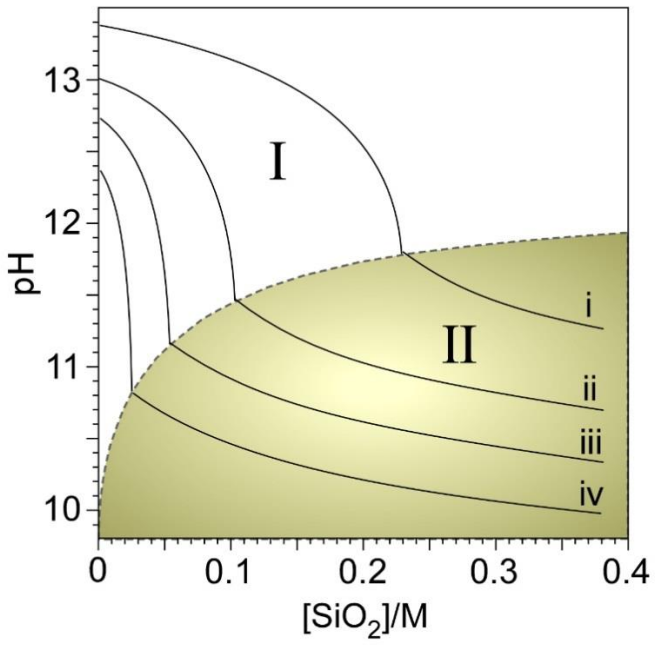

Figure D6: Silica phase diagram for silicalite-1 synthesis adapted from Rimer et al.[128]. The solid lines are reported measurements for TEOS addition to growth solutions containing molar ratios x TPAOH:H_2O with x =(i) 40, (ii)18, (iii)9, and (iv) 4.

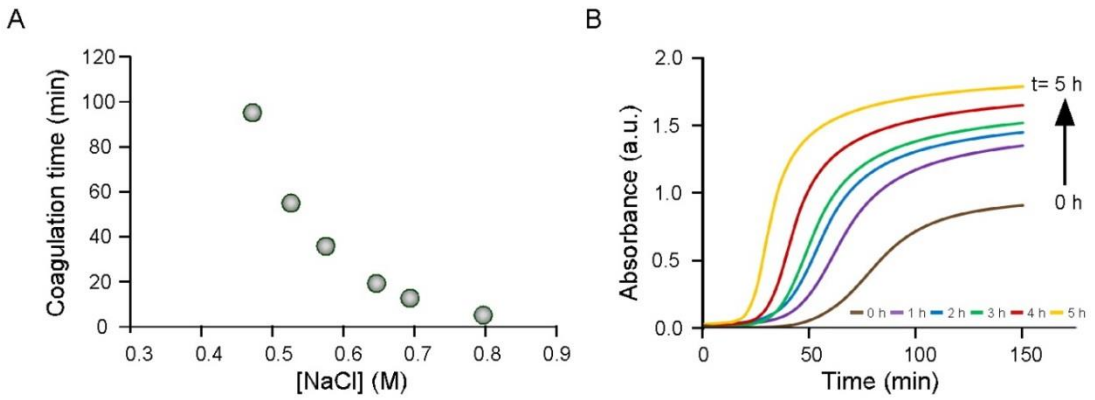

Figure D7: Colloidal stability assay for a TPA-nanoparticle solution. **(A)** Coagulation time for as-synthesized nanoparticles as a function of salt concentration. **(B)** Turbidity measurements at salt concentration (0.53 M NaCl) pre-heated for various times

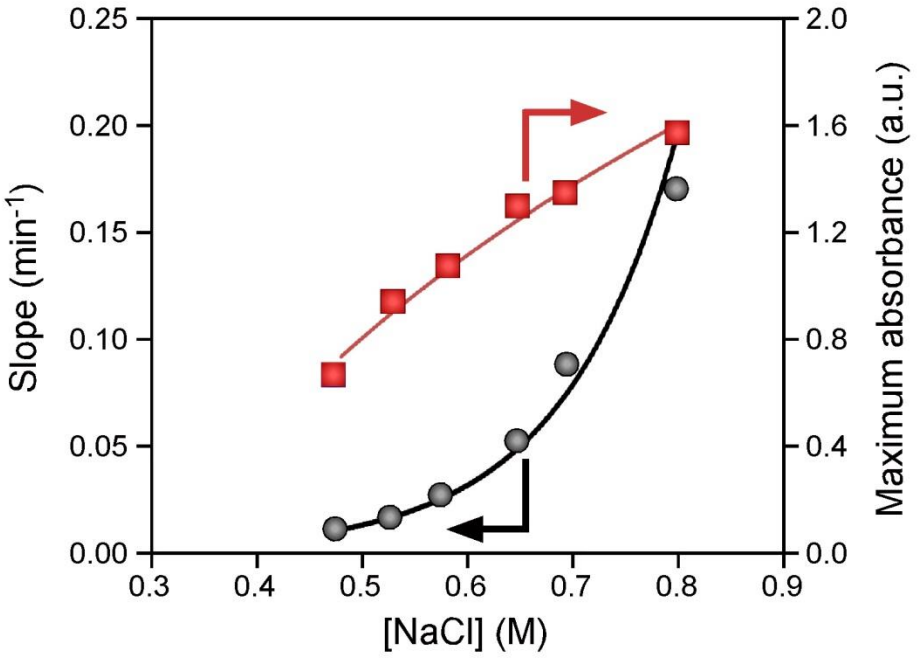

Figure D8: Analysis of turbidity measurements to assess the colloidal stability of a TPA-nanoparticle growth solution using various concentrations of NaCl. (right axis) The slope of the linear region of increasing UV-Vis absorbance. (left axis)

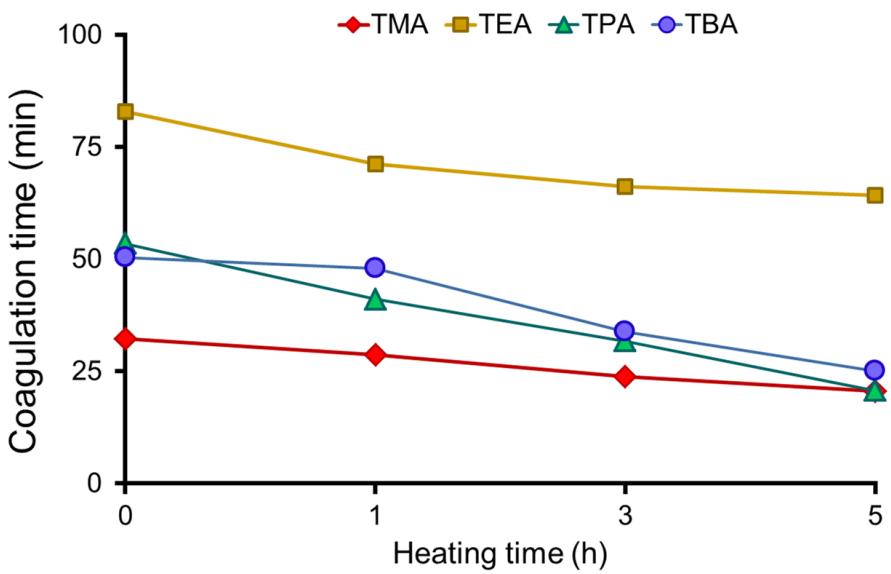

Figure D9: Coagulation time of TAA-nanoparticle solutions heated at 60 °C for various times. The colloidal stability test was performed at a fixed concentration of salt (0.53 M NaCl). Solid lines are interpolated to help guide the eye.

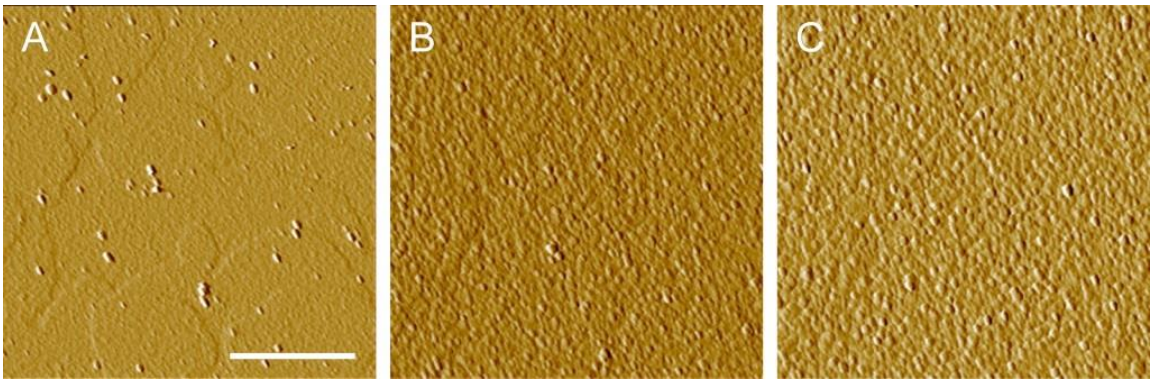

Figure D10: Time-elapsed AFM images during *in situ* growth measurements using solutions containing TPA-nanoparticles and 0.5 wt% TBPO. Images were taken at the following discrete times: (**A**) 1 h, (**B**) 9 h, and (**C**) 17 h. The scale bar equals 500 nm

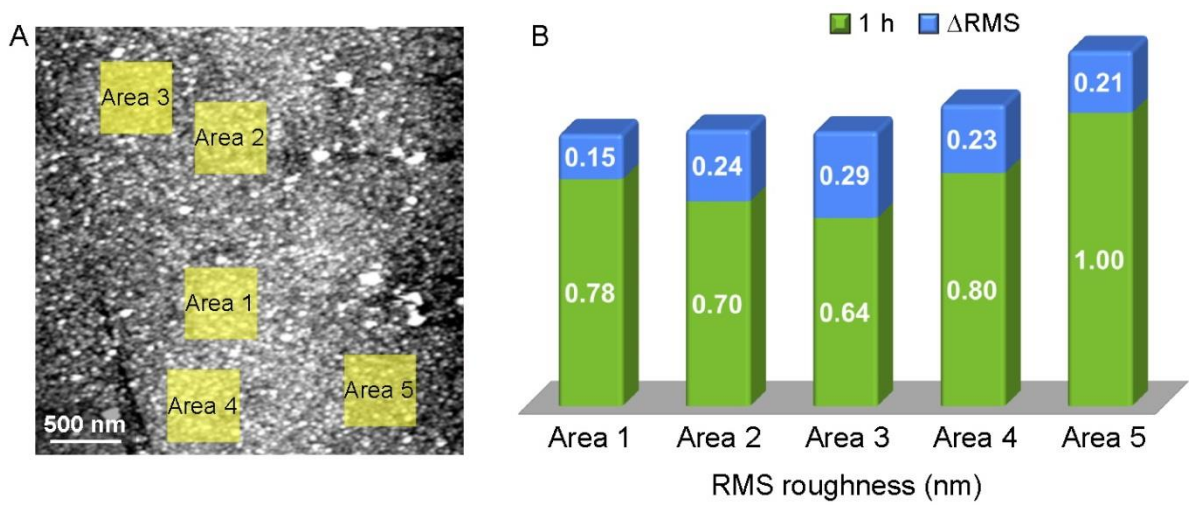

Figure D11: Roughness measurement during *in situ* experiments with TPA. (A) AFM height mode image. (B) RMS roughness after 1 h (green). The net change in RMS roughness over a 17 h period (blue) is plotted as ΔRMS = RMS(17 h) – RMS (1 h).